

Radiation Damage to the
diamond-based Beam Condition
Monitor of the CMS Detector at the
LHC

Zur Erlangung des akademischen Grades eines
DOKTORS DER NATURWISSENSCHAFTEN
von der Fakultät für Physik des
Karlsruher Instituts für Technologie (KIT)

genehmigte

DISSERTATION

von

Dipl.-Phys. Moritz Guthoff
aus Darmstadt

TAG DER MÜNDLICHEN PRÜFUNG: 24.01.2014
REFERENT: PROF. DR. WIM DE BOER
KORREFERENT: PROF. DR. THOMAS MÜLLER

Contents

1. Introduction	7
2. The LHC and the CMS Detectors	11
2.1. The Large Hadron Collider and the CERN accelerator complex	11
2.1.1. LHC injector chain	11
2.1.2. LHC Layout	12
2.1.3. Beam parameters from 2010 to 2013	13
2.1.4. The LHC Beam Loss Monitoring System.	13
2.2. The Compact Muon Solenoid	14
2.3. The Beam Monitoring Systems of CMS	17
3. Particle Detection	19
3.1. Particle interactions with matter	19
3.1.1. Charged particle interactions	19
3.1.2. Neutrons interactions	21
3.1.3. Photon interactions	21
3.2. Diamond as particle detector	22
3.2.1. Properties of diamond	22
3.2.2. CVD diamond growth	24
3.2.3. Signal generation in diamond detectors	26
3.2.4. Electric interface	27
3.2.5. Defects in diamond	29
4. The Beam Condition Monitor (BCM2/1L)	33
4.1. The BCML detectors	33
4.1.1. pCVD detectors	33
4.1.2. sCVD detectors	33
4.1.3. BLM detectors	35
4.2. Electronics	35
4.2.1. Wiring and grounding	36
4.2.2. Tunnel Card - front-end readout electronic	36
4.2.3. BCM2 HV filter boxes	40
4.2.4. DAB64x Card - back end electronics	42
4.3. Noise tests with readout electronics	44
4.3.1. Spike filter for display	46
4.4. Beam abort thresholds	47
4.4.1. Modification of beam abort thresholds due to efficiency loss.	49
4.5. Hardware failures and beam aborts	49
5. A selection of beam condition measurements using BCML.	51
5.1. Typical measurements during LHC operation	51

Contents

5.2.	Long beam loss events	53
5.2.1.	Collimator scan 2011	53
5.2.2.	High vacuum beam loss events.	55
5.2.3.	Background calculations from BCM2 and BCM1L	57
5.3.	Short beam loss events	59
6.	Monte Carlo simulations with FLUKA	67
6.1.	Introduction to FLUKA	67
6.1.1.	Combinatorial Geometry	67
6.1.2.	Event generator	68
6.1.3.	Scoring	69
6.1.4.	Radiation damage estimators	69
6.2.	The CMS FLUKA geometry	72
6.3.	Normalization	78
6.4.	Simulation of proton proton collisions in CMS	78
6.4.1.	Online availability of simulation results	79
6.4.2.	Radiation environment at locations of the BCML detectors	82
6.4.3.	Radiation damage to silicon detectors and comparison with measurements	85
6.5.	Activation of material during one fill.	88
6.6.	Effects on beam background due to new beam pipe design.	88
7.	Studies of Radiation Damage to the installed BCM Diamonds	95
7.1.	Radiation damage of diamond	95
7.1.1.	Charge trapping	95
7.1.2.	Polarization	98
7.2.	Simulation of polarization	100
7.2.1.	Electric field calculations	100
7.2.2.	Simulation of TCT pulses	101
7.2.3.	Simulated decrease of CCD with polarization buildup	104
7.3.	Decrease of signal efficiency of the BCML detectors with increasing integrated luminosity	106
7.3.1.	Normalization of data to instantaneous luminosity.	106
7.3.2.	Observed decrease in signal strength.	107
7.3.3.	Radiation damage constant	111
7.4.	Signal decrease in Neutron irradiations.	116
7.4.1.	Beam line description	116
7.4.2.	Measurement setup and data taking	117
7.4.3.	Data analysis	117
7.4.4.	Conversion to 24 GeV protons and comparison with BCML results . .	118
7.5.	Turn on behavior	119
7.6.	Rate dependency of signal efficiency	121
7.7.	Charge collection distance (CCD) measurements.	125
7.7.1.	Measurements of un-irradiated diamonds	125
7.7.2.	CCD measurements after removal from BCM2	126
7.8.	Measurements using the transient current technique (TCT)	128
7.8.1.	Measurement setup	128
7.8.2.	Un-irradiated diamond	130
7.8.3.	Measurements of sCVD_2011 after irradiation	131

7.8.4. sCVD_2011 after surface treatment	139
7.8.5. Measurements of sCVD_2012 after irradiation	141
7.9. Limitations of the simulation model, and possible improvements	142
7.10. Potential defects responsible for trapping	142
7.11. Conclusions on radiation damage analysis	145
8. Summary and outlook	147
8.1. Summary	147
8.2. Outlook	149
Appendices	165
A. Beam abort thresholds	167
B. Parametric fits to signal decrease	169
B.1. Alternative fit functions	169
B.2. Fit to simulated decrease of active volume	170
B.3. Fit to decrease of sCVD detector signal of BCML	171
B.3.1. Prediction of signal strength at 300 fb^{-1}	172
B.3.2. Operation up to 3000 fb^{-1} (HL-LHC)	173

Chapter 1.

Introduction

One of the biggest science experiments world wide, the Large Hadron Collider (LHC) [Eva08], located at the “Centre Européenne pour la Recherche Nucléaire” (CERN), Geneva, Switzerland, leads the world of particle physics to a new frontier. It is designed to collide protons at a center of mass energy of 14 TeV. It pushes the limit of energy concentrated in a single particle collision far beyond of what was previously achieved. This opens many new possibilities to search for elementary particles, not observed so far, and to find new physics beyond the standard model.

The LHC is a synchrotron particle accelerator with 27 km circumference. Most of the time, two counter rotating proton beams are accelerated and brought into collision at four different interaction points, where the four main LHC experiments are located: ALICE, ATLAS, CMS and LHCb. In addition, there are two independent smaller experiments: TOTEM, located at the same interaction point as CMS, and LHCf, located at the same interaction point as ATLAS. For several weeks at the end of a one year operation, the LHC switches to the collision of heavy ion particles, or heavy ions with protons. In 2010 and 2011, lead ions were brought into collision, and in 2013, protons were collided with lead ions.

The LHC has completed a very successful operational Run 1, starting in 2010, until mid 2013. In 2010 and 2011, the LHC operated at 7 TeV center of mass energy, where an amount of 6.3 fb^{-1} of integrated luminosity was delivered. In 2012, the beam energy was increased to 8 TeV center of mass energy, where about 25 fb^{-1} of integrated luminosity was delivered. This gave sufficient accumulated data for the two multi purpose experiments, ATLAS and CMS, to independently discover the Higgs boson, which was announced on the 4th of July, 2012 [Cha12]. Although this marks the exciting highlight of the past years, many other fascinating discoveries and interesting measurements were made by all of the LHC experiments. CMS, for example, was also able to discover a new composite particle, the Ξ_b^{*0} [Cha12a], and CMS and LHCb were able to discover and measure the branching fraction of the decay of the B_S^0 to $\mu^+ \mu^-$ [Cha13, Aai13].

Each LHC beam stores an energy of 350 MJ under nominal conditions. This amount of highly focused energy has a huge damage potential. If the beam hits solid material, a hole would be burned into the structure. Figure 1.1 shows the result of a test, where a 450 GeV LHC proton beam was shot on a copper target [Kai05]. Above a beam intensity of about 5×10^{12} protons, a hole was burned into the material. This is even a fairly low intensity, as the LHC normally operates at beam currents of $O(10^{14})$ protons.

The beam directly hitting the vacuum chamber would of course be a catastrophic event. Although this is extremely unlikely, there are other scenarios where the high intensity beam is of great danger. In a beam loss event, where only a certain fraction of the beam particles interact with matter, like collimators, the vacuum chamber, or gas particles, high energetic particle showers can create damage to any system along the beam line. For the LHC, a beam loss monitor (BLM) system is in place, which automatically deactivates (dumps) the



Figure 1.1.: Copper targets irradiated with a 450 GeV LHC beam to show the damage potential of the beam. The locations marked A,B,C,D are irradiated with different intensities, which are as follows: A: 1.3×10^{12} , B: 2.6×10^{12} , C: 5.3×10^{12} , D: 7.9×10^{12} protons. The plate shown was about 4.7 cm deep inside a target consisting of several layers of various target materials [Kai05].

beam if high rates are measured [Deh02]. Its main purpose is to protect the superconducting magnets of the LHC from intense heat dissipation due to beam loss events, which would lead to a quench of the superconductivity.

The BLM system of the LHC does not cover the parts of the beam line inside the experimental caverns, as it is the responsibility of the experiments to monitor for beam losses produced there. In CMS, the Beam Condition Monitor 2 (BCM2) was developed to fulfill this purpose, with a major contribution from the Institute of Experimental Nuclear Physics at the Karlsruhe Institute of Technology [Mül11]. Additionally, the BCM1L detector is operated for redundancy, forming together with BCM2 the BCML system, where the L stands for “leakage” due to the operational configuration as a leakage current detector. The system is designed to protect the silicon tracking detector of CMS from catastrophic beam loss events. The current generated in silicon detectors could be so intense that the electronics would get damaged. This happens only at intense levels of particle rates that would not occur in typical LHC operational conditions, but only in extreme cases of machine induced background. The BCML system is in place to deactivate the LHC beam before dangerous levels of particle rates can build up.

The BCM2 detector utilizes the same electronics as the LHC BLM system, but due to the confined space inside CMS the 1 m long ionization chambers could not be used. Instead artificially grown chemical vapor deposition (CVD) diamonds are used as detectors, aligned in rings around the beam pipe. Figure 1.2 shows the picture of one of the BCM2 diamond detector modules.

Diamond material studies go back several decades, mostly performed on natural diamond. Only since the development of the CVD process to artificially grow diamond in the early 1980s, diamond has been considered a reasonable material for particle detection. As an insulator, diamond has almost no free charge carriers, however the mobility of the charge carriers for electrons and holes, is very good. This makes diamond an excellent choice where very fast detectors are required. Diamond is commonly considered as solid state ionization chamber. Typically, the diamond is equipped with metal electrodes on both surfaces, and an electric field is applied over the diamond bulk. An ionizing particle passing through the

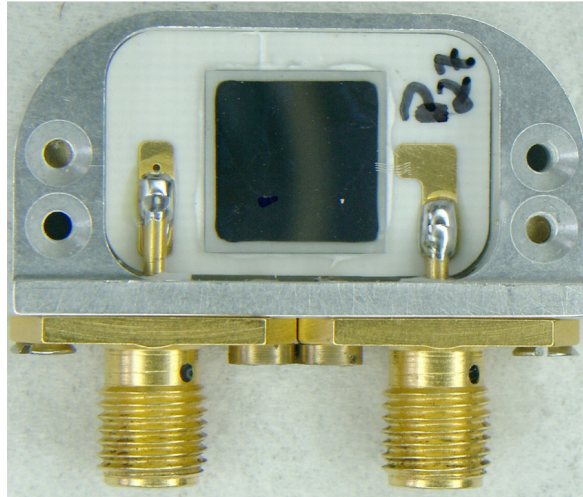


Figure 1.2.: BCM2 detector package showing the $1 \times 1 \text{ cm}^2$ poly-crystalline diamond. [Mül11]

detector creates electron hole pairs. These charge carriers drift along the electric field, which can be measured as detector current.

Diamond detectors have several advantages and disadvantages compared to silicon detectors, which are the usual alternative. Diamond has a very low dark current due to its wide band gap. During irradiation, the dark current does not increase, as it is the case for a silicon detector. Therefore, a diamond detector does not require cooling and represents a niche in applications where cooling cannot be provided. Diamond is also considered to be more radiation hard than silicon. One of the main arguments in favor of diamond is the higher displacement energy. Also, in silicon, heavy nuclear fragments are created during irradiation, which are very damaging. In diamond, this is not the case [Boe09]. The apparent disadvantage of diamond is its price. Due to the high cost of CVD diamonds, it is not a financially viable option to build a full tracking detector with diamond sensors. Single-crystalline diamond sample can only be produced in sizes smaller than $1 \times 1 \text{ cm}^2$, making it difficult to cover a big surface. Poly-crystalline diamonds are grown in wafers, making it possible to manufacture bigger diamond plates. Unfortunately, due to their poly-crystalline nature, they are inhomogeneous, with regions of reduced sensitivity. This is not ideal for pixel or strip tracking detectors, where a uniform response is desired.

The radiation hardness of diamond detectors has been widely studied by various research groups. The RD42 collaboration [RD42] focuses on the development of diamond tracking devices and analyzes the radiation damage to diamond. Test beam irradiations were performed with various types of particle beams at different energies. Both types of available CVD diamonds, single-crystalline and poly-crystalline, were studied. The change in charge collection was measured in laboratory measurement to benchmark the performance of the irradiated diamonds. A general high radiation hardness and a good agreement between single-crystalline and poly-crystalline diamonds was found. Other studies, e.g. by M. Pomorski [Pom08], show that the diamond can polarize due to irradiation, leading to a deformation of the electric field and by that to a potential decrease in charge collection.

This thesis focuses on the measurements following the initial BCM2 commissioning and covers these three major parts:

- The operation of the BCML detector system: Since the start of the LHC, and with it

the start of the operation of BCM2, several modifications were done to the detector system. Certain features of the system were studied. This is summarized in chapter 4. During the LHC Run 1 operation (from 2010 until 2013), a lot of data was taken while the beams were in collisions. Several interesting beam loss events were investigated. These events are shown and analyzed in chapter 5.

- FLUKA Monte Carlo simulations of the CMS detector: The first study of the radiation environment in CMS was done in 1995 [Huh95] and constantly updated since then. The latest major improvement was done during the design of BCM2, where FLUKA was an important tool to predict the performance of the detector [Mül11]. All these studies were focused on nominal LHC parameters. For this work, simulations were performed at the operational condition of 2011 (3.5 TeV beam energy) and 2012 (4.0 TeV beam energy). These simulations are not only of great interest for the whole CMS community, but also give important parameters for the data analysis. The results are presented in chapter 6.
- The most important part of this thesis deals with radiation damage effects on diamond. Many studies with test beam irradiations of diamond detectors were performed in the past, but the BCML detector is one of the first using diamond sensors in an extremely strong hadronic radiation environment. Predictions of the survivability of the BCM2 detectors were based on the RD42 irradiation results [Mül11]. For the work presented in this thesis, the radiation damage was studied with data obtained during normal operation, showing a strong decrease in signal efficiency already at relatively low particle fluences. Test beam irradiations of diamond detector samples were performed using the same readout electronics as used in BCML. The signal decrease measured in BCML operation was compared to the test beam irradiation. Also, a laboratory analysis was performed on diamond samples removed from the system. The charge collection distance of the irradiated detectors was measured. Measurements using the transient current technique (TCT) gave interesting insights into the electric field effects in irradiated diamonds. The findings about the performance of BCML detectors under irradiation and an analysis of the radiation damage to diamond as detector is presented in chapter 7

Chapter 2.

The LHC and the CMS Detectors

2.1. The Large Hadron Collider and the CERN accelerator complex

The Large Hadron Collider (LHC) is a synchrotron particle accelerator with a circumference of about 27 km located at CERN, Geneva, Switzerland [Eva08]. Two hadron beams are accelerated in two separate rings and brought into collision in four interaction points (IP). Protons are accelerated to a maximum energy of 7 TeV per particle, or alternatively, lead ions up to 2.76 TeV per nucleon. In order to bend the particle beam on its circular orbit, 1232 superconducting dipole magnets with a maximum magnetic field of 8.33 T at top energy are used. Magnets with higher multipole fields are installed to focus the beam and perform higher order corrections. In total over 8000 superconducting magnets are used to operate the LHC.

Under nominal conditions 2808 bunches per beam are circulating, where each bunch contains 1.15×10^{11} protons. At 7 TeV this corresponds to 362 MJ stored in each of the two beams. To ensure a safe operation with beam storage times of over 10 hours, various devices to monitor the beam condition are installed in the tunnel. For the scope of this thesis the instruments related to beam losses and machine protection are of importance, therefore only those will be introduced in the following chapter, after a general introduction of the injector chain and the LHC.

2.1.1. LHC injector chain

The performance of the LHC is highly depending on the pre-accelerators. All pre-accelerators have to perform well enough, not to deteriorate the beam properties like the bunch charge or the emittance. The bunch charge is a limiting factor mostly at low energies and hence a problem in the injectors, however it is important to keep the bunch intensity as high as possible, since it is crucial for the later luminosity performance.

The accelerator complex of CERN is shown in figure 2.1. Protons are sourced at LINAC2, accelerated to an energy of 50 MeV and injected into the Proton Synchrotron Booster (PSB), which consists of four independent synchrotron rings. In the PSB the particles are accelerated to an energy of 1.4 GeV and all four lines are injected to the Proton Synchrotron (PS). In the PS the particles are ramped up to 26 GeV. Afterwards they are injected to the Super Proton Synchrotron (SPS) which brings the particles up to their LHC injection energy of 450 GeV. When using heavy ions LINAC3 and LEIR, as first synchrotron, are used before injection to the PS, from where they follow the same chain as the protons.

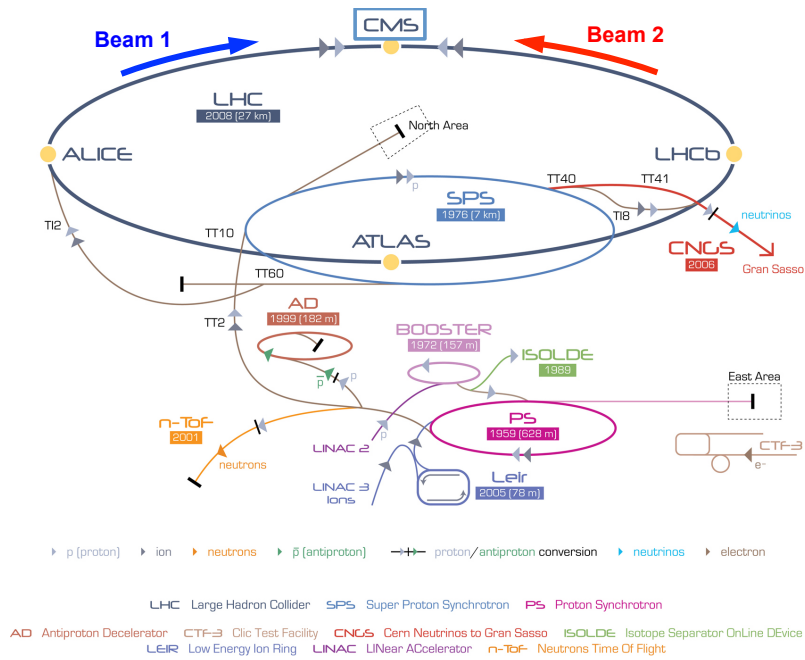


Figure 2.1.: The CERN accelerator complex. The protons used in the LHC are first accelerated by the LINAC2, the PSB, the PS and the SPS before injected to the LHC. Shown also is the definition of beam 1 (clockwise) and beam 2 (counter clockwise).

2.1.2. LHC Layout

The LHC is shaped as octagon with eight arc sections and eight long straight sections (LSS). The arcs contain the main dipole magnets and define the bending radius of the machine. Each LSS is dedicated to one purpose as schematically shown in figure 2.2. Beam 1 circulates clockwise and beam 2 circulates counter clockwise. The four main experiments are located in IP1 (ATLAS), IP2 (ALICE), IP5 (CMS) and IP8 (LHCb). Whereas ATLAS and CMS are the two multipurpose high energy experiments which are designed to take a peak luminosity of $\mathcal{L} = 1 \times 10^{34} \text{cm}^{-2} \text{s}^{-1}$. LHCb is specialized in B-physics and ALICE is the dedicated heavy ion experiment. The interaction region (IR) four hosts the RF cavities, responsible for the particle acceleration, and other beam instrumentation of the LHC. In IR3 and IR7 the collimation system is installed. This system absorbs particles in the beam halo, which would otherwise impact in the superconducting magnets due to a too large momentum or position offset with respect to the core of the beam. After several hours of data taking in collisions, the luminosity has decayed so much that the beams have to be renewed. The beams have to be disposed in a controlled way into the so-called beam dump, which is located in IR6. The beam dump is a 7 m long steel coated graphite block with $\sim 900 \text{ t}$ radiation shielding blocs, into which the circulating beam is deflected in case of a beam abort signal. The trigger signal to dump the beam can either be sent form the operator at the end of a successful fill or by a protection system (e.g. the BLM system of the LHC or BCML system of CMS) measuring a potential threat for the machine or the experiments.

2.1. The Large Hadron Collider and the CERN accelerator complex

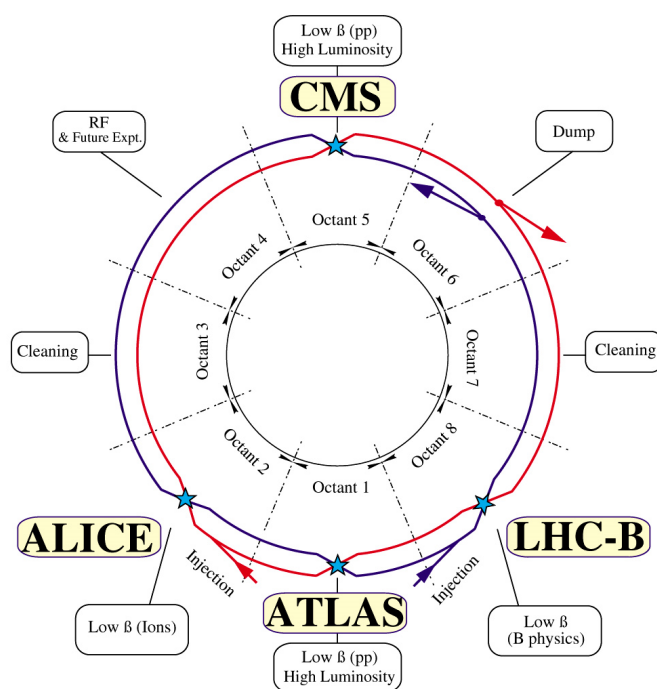


Figure 2.2.: The layout of the LHC, defining the octagonal shape with its eight interaction regions [Eva08].

2.1.3. Beam parameters from 2010 to 2013

During the LHC Run 1 from 2010 until 2013, the full potential of the LHC could not yet be exploited. The beam parameters were different from the design values. Table 2.1 compares the nominal design values with the parameters used during normal operations. Values achieved during machine development periods are excluded. Only every second bunch slot was filled and the bunch spacing was twice the nominal value. Therefore the machine could only be filled with half the number of bunches. On the other hand, the bunch current was higher than the nominal value, thus about 70 % of the nominal peak luminosity was reached in 2012.

2.1.4. The LHC Beam Loss Monitoring System.

The loss of even a small fraction of the beam particles could create a particle shower strong enough to quench one of the superconducting LHC magnets. A beam loss monitoring (BLM) system is in place to detect secondary shower particles, originating from high beam losses. Above a pre-defined threshold, the LHC beams are automatically dumped to prevent magnet quenches. Moreover, the data readings from the BLM detectors allow the observation of local aperture limitations and various other effects involving beam particle losses. It is used to observe beam losses created in collimator scans and aperture scans during machine commissioning.

Mainly, 1 m long gaseous ionization chambers are used as detectors. Figure 2.3 shows a picture of such a BLM tube attached to a dipole magnet. About 3700 BLM tubes are in use around the LHC ring. Additionally, about 280 secondary emission monitors are used.

In the experimental caverns of the LHC experiments no BLM detectors are installed. Here

Parameter	design	2010	2011	2012
Proton energy [TeV]	7	3.5	3.5	4
Number of bunches	2808	368	1380	1374
Bunch spacing [ns]	25	150	50	50
Protons per bunch [10^{11}]	1.15	~ 1.2	~ 1.4	~ 1.5
Peak luminosity (IP1 & IP5) [$\text{cm}^{-2}\text{s}^{-1}$]	10^{34}	$\sim 2 \times 10^{32}$	$\sim 3.5 \times 10^{33}$	$\sim 7 \times 10^{33}$
β^* [m]	0.55	3.5	1.5 / 1	0.6
Events per bunch crossing	19.02	~ 3	~ 15	~ 30
Full crossing angle [μrad]	285	200	240	290
Beam current [A]	0.584	~ 0.08	~ 0.348	~ 0.371
Stored beam energy [MJ]	362	~ 24.8	~ 108	~ 132
RF frequency [MHz]	400.8	400.8	400.8	400.8
Revolution frequency [kHz]	11.245	11.245	11.245	11.245

Table 2.1.: A selection of the LHC beam parameters comparing nominal parameters with operational values of Run 1. The design values are taken from [LHC04]. Values for 2010 - 2013 are typical values achieved in normal operation (excluding machine development periods).

it is the responsibility of the experiments to monitor the beam losses. In CMS the BCML system is in use as transparent extension of the LHC BLM system. More details about the working principle of the BLM system can be found in chapter 4.

2.2. The Compact Muon Solenoid

The Compact Muon Solenoid (CMS) experiment is one of the two multi-purpose experiments at the LHC. CMS is designed as a barrel, symmetrically around the interaction point (IP), with both ends closed by disk shaped end-cap detectors. Figure 2.4 shows the layout of CMS. For an optimal particle identification, CMS is built in the typical sub-detector layout with tracking and calorimetry inside a high solenoidal magnetic field and muon detection outside the magnet.

Magnet The solenoid magnet is the heart of CMS. It has a superconducting NbTi coil with a diameter of 7m over a length of 13m. The design magnetic field 4 T, however it is operated at 3.8 T. The high magnetic field is needed to achieve a good resolution in the tracker measurement of the particle momentum. The magnet covers not only the tracker, but also the calorimeters, as placing the solenoid in front of the calorimeters would massively decrease the energy resolution.

Tracker The CMS tracking system consists of two parts, the pixel and the strip tracker. It measures the trajectories of all charged particles generated in the collisions. It covers the pseudo-rapidity region up to $\eta = 2.4$.

The vertex detector, a silicon pixel detector with three barrel layers at radii between 4.4cm and 10.2cm and two end-cap discs per end, is responsible for tracing the origin of every charged particle. A high spacial resolution is needed to separate particle originating from different primary collisions, and to recreate the travel path of short lived particles, by



Figure 2.3.: A beam loss monitor tube installed at a dipole magnet.

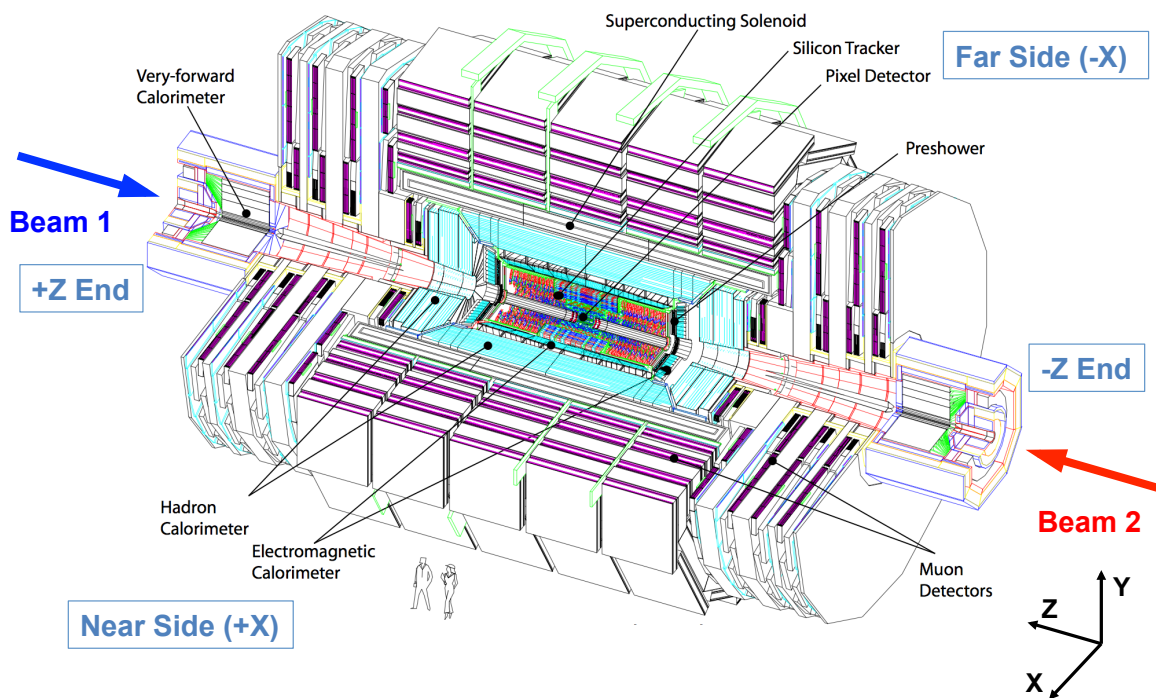


Figure 2.4.: The CMS experiment and its subdetectors [Cha08]. A coordinate system (in CMS convention) and the beam directions were added.

reconstructing the origin of the secondary particles. The measures resolution in x is $12.7 \mu\text{m}$ and in z is $32.4 \mu\text{m}$ [Kha10].

The strip tracker is divided in four parts: the tracker inner barrel (TIB) with four detection layers, the tracker inner disk (TID) with three discs per end, the tracker outer barrel (TOB) with six detection layers and the tracker end cap (TEC) with nine discs per end. The strong magnetic field of 3.8 T enables the tracker to measure the particle charge and momentum. The resolution for the transverse momentum at $p_T = 1 \text{ GeV}$ is about 0.7%.

Being the inner most detector, the tracker is the most exposed detector towards beam loss particles. The tracker is only switched on, if the LHC has declared “stable beams” and if the beam monitoring systems show no signs of increased beam background.

Electromagnetic Calorimeter The electromagnetic calorimeter (ECAL) is made of PbWO_4 scintillating crystals with an avalanche photo diode (APD) readout. The ECAL covers a pseudo-rapidity region up to $\eta = 3$. It measures the energy of electrons and photons with high precision. This is especially important for the analysis of different decay channels of the Higgs boson, like $H \rightarrow \gamma\gamma$, $H \rightarrow ZZ$ or $H \rightarrow WW$.

A part of the ECAL is the preshower detector, installed in front of the calorimeter end-caps. It consists of two layers of lead absorber with high resolution silicon strip detectors. Its main function is to detect photons with high spacial resolution in order to identify π^0 decays [Bar07].

Hadronic Calorimeter The hadronic calorimeter (HCAL) is a sampling calorimeter designed to measure the energy of hadronic jets and neutral hadrons. It is constructed of layers of brass absorbers and plastic scintillators. It is also composed of a barrel and an end-cap detector. The end-cap calorimeters reach up to $\eta = 3$. Additionally, the very-forward calorimeter (HF) is installed at about $Z = \pm 11.15 \text{ m}$, covering up to $\eta = 5$. In the quartz fibers are used as detectors, which placed inside copper absorbers.

CASTOR CASTOR is a 1.5 m long cylindrical shaped quartz tungsten calorimeter located at $Z = -14.3 \text{ m}$. It covers the η range from 5.1 to 6.6. The layers are aligned under 45° with respect to the beam. Photomultiplier tubes detect Cherenkov light created in the quartz layers. CASTOR was only installed on the -Z end. It was removed after the 2011 run, since it cannot handle the high rates at the operational luminosity in 2012 and would have only created a highly damaging radiation field. It was reinstalled after the 2012 proton operation to be available for the heavy ion run.

Muon systems The muon systems play a very important role in the physics program of CMS. One decay channel of the Higgs boson is into two Z bosons, which decay into four leptons. A four muon decay is a very clear event with basically no background. The muon chambers are placed outside the CMS main magnet and therefore in the return field of the solenoid. Detection layers are stacked with iron yoke, which accommodates the return field of the solenoid.

There are three independent muon systems: The Drift Tubes (DT), which form the barrel part of the muon detectors, has four layers with yoke iron in between covering up to $\eta = 1.2$. In the muon end-caps a different system, the Cathode Strip Chambers (CSC), is used, covering up to $\eta = 2.4$. The third muon system uses Resistive Plate Chambers (RPC), which are installed additionally to the DTs and the CSCs in the barrel and in the end-cap regions. It

has a better timing resolution and segmentation compared to the CSC or the DT systems. The RPCs provide complementary information and provide a trigger on events involving muons.

Trigger systems At nominal LHC conditions, the bunch crossing frequency is 40 MHz, with 19 primary proton-proton collisions per bunch crossing. The number of detector channels in CMS is far too numerous to be recorded every occurring collision. For measuring physics processes that occur with a very low cross-section, the high number of collisions is needed to gain enough statistics. A triggering system is set up to initiate a readout of the CMS sub-detectors, if certain trigger criteria are met.

The level-1 trigger is the first stage to reduce the data rate from the initial 40 MHz to approximately 30 kHz. Different sub-systems can send a level-1 trigger event, these are in particular the calorimeter trigger, the muon trigger and different technical triggers. If the global trigger system accepts the trigger condition, a readout signal is sent to all CMS sub-detectors. The sub-detectors store events in a 3.2 μ s pipeline, and if the event is accepted, the data is sent to the high level trigger system. The high level trigger performs a preliminary analysis on every event accepted by the level-1 trigger. The events are further filtered by applying various cuts and the event frequency is reduced to roughly 100 Hz. One event in CMS has a file size of about 1 MB, leading to a final data rate of about 100 MB/s, which is stored for the full physics analysis.

2.3. The Beam Monitoring Systems of CMS

Several independent systems are used to monitor the beam properties in CMS. The main purposes are the measurement of the instantaneous luminosity and the machine induced background, as well as the active protection from dangerous beam loss events. The beam monitoring systems of CMS are described below.

BPTX The beam pickup for timing experiment (BPTX) is technically the same as a beam position monitor at the LHC, where four measurement buttons collect the induced charge created by passing bunches. The signals of all four measurement buttons are added to give a combined signal. No x/y position information is given, but the signal is used to measure the precise moment in time, when the incoming bunches arrive at CMS. One of these pickup measurements per beam is placed upstream of CMS at 175 m distance from the interaction point. The signals are measured and processed by a 5 giga samples oscilloscope. The signal information is used in various parts of CMS. Simple checks, like the number of bunches filled in the LHC, are performed. The time difference between two colliding bunches is calculated and used to predict the Z position of the collisions before stable beams are declared. This is an important feedback to the LHC control room, as a high time difference would suggest problems with the beam and a refill of the beams could be considered. The BPTX signals are also used to provide gating for the background and luminosity measurements performed by the BHC and the BCM1F detectors.

BSC/BHC The Beam Scintillating Counters (BSC), later upgraded to the Beam Halo Counters (BHC), is a monitoring and triggering device for CMS. It uses scintillating tiles placed on the front face of the HF detector at $Z = \pm 10.9$ m, with almost full ϕ coverage. The original detector, the BSC, was composed from parts of the OPAL end-cap calorimeters. Details of

the construction can be found in [Bel07]. In the early running period of the LHC, it was used as minimum bias trigger, beam background monitor and for luminosity measurement. In 2011 the particle rates were too high and the detector saturated, leading to false measurements at high luminosities. The BSC was still used in low luminosity phases and during the heavy ion runs. In 2012 the detector was upgraded to the BHC by replacing the scintillator tiles with smaller $10 \times 10 \text{ cm}^2$ scintillators to reduce the number of particles per channel. More detector channels were used to compensate for the reduced sensitivity. Unfortunately, the dynamic range of this detector is not suitable for post long shutdown 1 operation and the system is now replaced with a new Cherenkov based directional detector for measuring the machine induced muon halo background.

BCM1F The Beam Condition Monitor “Fast” system is a fast particle counter, equipped with single-crystal diamond detectors placed at $Z = \pm 1.8 \text{ m}$ away from the interaction point. Four detector packages per end are aligned around the beam pipe at a radius of about 5 cm. A detector package includes, next to the diamond sensor, a preamplifier and an analog optohybrid to transmit the measured signals optically to the back-end electronics, placed in the service cavern. The signals are usually discriminated and counted with a scalar module. Also available is a time to digital converter to analyze the timing distribution of the particles hitting the detector, and an analog to digital converter to sample the raw data and analyze the signal shapes. Details can be found in [Bel10].

BCML The Beam Condition Monitor “Leakage” is the beam protection system at the LHC. The system was originally designed to consist only of the Beam Condition Monitor 2 (BCM2), which uses poly-crystalline diamonds in a leakage current readout, placed at $Z = \pm 14.4 \text{ m}$ away from the interaction point. The sensors of the BCM1L system, which are also poly-crystalline diamonds placed at $Z = \pm 1.8 \text{ m}$ at a radius of about 4.5 cm, were included in to the BCM2 readout electronics after the BCM1L electronics were abandoned due to high noise. The overall system was then called BCML. The readout electronics is a current measurement device identical to the LHC beam loss monitor electronics (see section 2.1.4). The BCML system is therefore a transparent extension of the LHC BLM system. This is the main detector system used in the analysis of this thesis, and is thoroughly explained in chapter 4.

Chapter 3.

Particle Detection

3.1. Particle interactions with matter

High energetic particles interact with matter in different ways. Charged particles, hadrons and leptons, interact almost entirely via ionization. Neutral hadrons only interact with nuclei. Photons interact via various interaction processes with the atomic shells or the nuclei. A quick introduction to the physics of the different types of interactions is given, where the main focus lies on the interactions relevant for the work of this thesis.

3.1.1. Charged particle interactions

Only charge particles create ionization. When passing through any kind of material electrons are kicked out of their shell and the material gets ionized. The high energetic particles loses a small amount its energy. The amount of energy lost dE per unit length dx is described by the Bethe equation [Dem05]:

$$-\frac{dE}{dx} = \frac{n_e z^2 e^4}{4\pi\epsilon_0^2 m_e c^2 \beta^2} \cdot \left[\ln \left(\frac{2m_e c^2 \beta^2}{\langle E_b \rangle \cdot (1 - \beta^2)} \right) - \beta^2 \right], \quad (3.1)$$

where n_e is the electron density, z is the charge number of the ionizing particle, e the elementary charge, ϵ_0 the vacuum permittivity, c the speed of light in vacuum, $\langle E_b \rangle$ the mean excitation energy and $\beta = v/c$, where v is the speed of the particle.

The Bethe equation is incorrect for electrons, as they get scattered significantly, which is neglected in the Bethe equation. Additionally radiative effects are more significant, which are described in the following.

The second effect for charged particles is the energy loss due to bremsstrahlung. Especially light charged particles like electrons get scattered while traveling through matter and thereby receive a negative acceleration. The energy loss due to this radiative effect increases with particle energy. Above energies of O(100 MeV) it becomes more relevant than ionizing effects. The energy loss of an electron in material due to radiative effects is given by [Dem05]:

$$\left(\frac{dE}{dx} \right)_{rad} = \frac{4n_a Z^2 \alpha^3 (\hbar c)^2 E_e}{m_e^2 c^4} \cdot \ln \frac{a(E)}{Z^{1/3}}, \quad (3.2)$$

where E_e is the kinetic energy of the impinging electron, n_a the atom density of the material, Z_e the charge of the nuclei of the material, α the fine structure constant and $a(E)$ a numerical factor governing at which maximum impact parameter the electron is sufficiently scattered to produce radiative energy losses.

Figure 3.1 shows the ionization and radiative energy loss of an electron in diamond and silicon as function of electron energy [Kuz06]. At about 1 MeV the energy loss is minimal. Hence a particle of roughly this energy is called “minimal ionizing particle” (MIP).

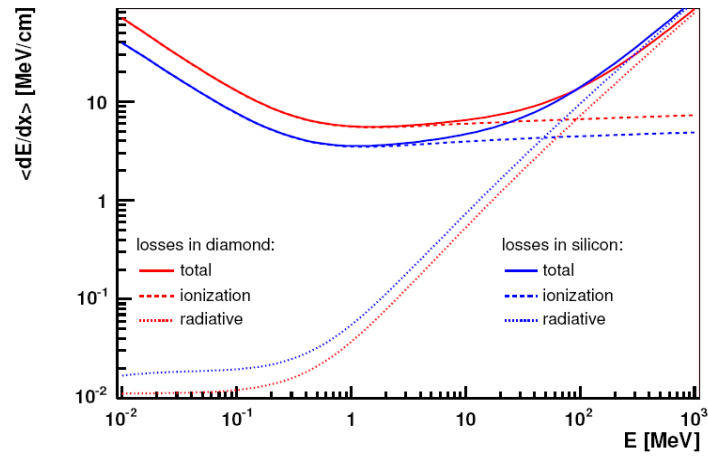


Figure 3.1.: Energy loss of an electron in diamond and silicon due to ionization and radiative losses [Kuz06]

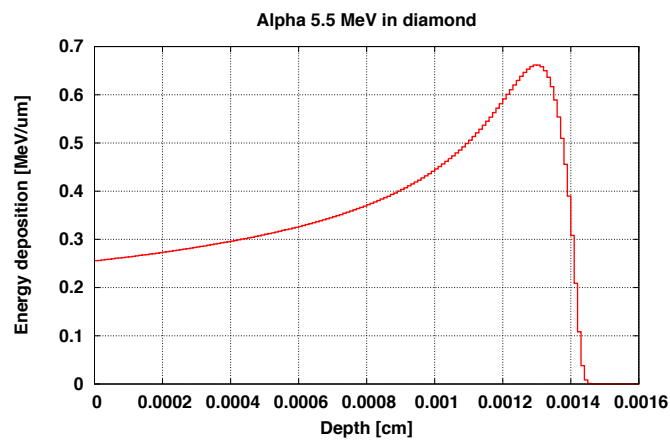


Figure 3.2.: FLUKA monte carlo simulation of the energy deposition of a 5.5 MeV α particle in diamond.

α particles have a low range because they lose their energy fast. A FLUKA simulation was performed to show the energy deposition of an α particle with energy of 5.5 MeV in a piece of diamond. Figure 3.2 shows the deposited energy as function of depth. The highest deposition of energy is in a depth of about $13 \mu\text{m}$, shortly before the particle is stopped, since the amount of ionization increases with reduced particle energy.

3.1.2. Neutrons interactions

Neutrons interact only with nuclei, since they cannot interact with the electrons in the shell via Coulomb interaction. The probability for an interaction is much lower than for charge particles.

Most interactions of neutrons with nuclei are elastic. They lead to a transfer of momentum to the nucleus. The neutron loses energy and gets scattered. Neutrons lose their energy in multiple elastic scatterings and eventually thermalize. The amount of energy transferred to the nucleus E'_N depends on the mass of the scattering nucleus m_N , the neutron mass m_n , the initial energy of the neutron E_n and the angle θ under which the nucleus is scattered with respect to the direction of the incoming neutron. The energy transfer is given by equation 3.3 [Dem05].

$$E'_N = \frac{4m_N \cdot m_n}{(m_N + m_n)^2} E_n \cos^2 \theta \quad (3.3)$$

Ideal for neutron thermalization is hydrogen, as it has the nucleus with the lowest mass and the transfer of energy is maximized. If the neutron hits a proton directly ($\theta = 0$), all the energy of the neutron is transferred to the proton. Materials used for neutron thermalization are hydrogen rich materials, such as water, concrete (contains water) or organic materials like polyethylene or paraffin.

With lower neutron energies the cross-section for neutron absorption increases, at thermal energies it is most significant. Some materials have an especially high neutron capture cross-section. The binding energy excites the nucleus and a photon is emitted, when the nucleus falls back into ground state. Heavy nuclei can undergo fission due to the excitation. Elements with high neutron absorption are for example helium-3, lithium-6 and boron-10. These materials are either used as detector material to enhance the neutron detection probability or as part of neutron shielding to improve the absorption of thermal neutrons.

3.1.3. Photon interactions

Energy deposition of photons is only to a minor amount direct energy deposition. Often charged particles are created, which deposit their energy via ionization.

The important interaction processes of photons with matter are [Dem05]:

- Elastic scattering (Rayleigh- and Thompson scattering)
- Inelastic scattering: The photon scatters at an electron and transmits energy. The scattered photon has a higher energy due to its lower energy. The electron received a partial amount of the photon energy, which is usually sufficient to kick it out of its shell. The process is called Compton effect.
- Absorption in electron shell: The photon transmits all its energy to an electron in the atomic shell and gets destroyed. The electron is kicked out of its shell and has the energy of the photon minus the ionization energy.

- Pair production: Photons with sufficient energy can create a particle-antiparticle pair. For conservation of momentum a heavy nucleus takes part in this process, which takes up the momentum of the photon. Above a photon energy of ~ 1 MeV it is energetically possible to create an electron-positron. Pair production is the dominant process above a photon energy of ~ 100 MeV.
- Photo-nuclear interactions: The photon is absorbed by a nucleus, which changes to a higher energetic excited state.

3.2. Diamond as particle detector

3.2.1. Properties of diamond

Configurations of Carbon Carbon has in its outer L-shell two electrons in the s -orbital, and two of the three p -orbitals are filled with one electron. The orbitals do not create molecular bonds directly, but a linear combination of the orbitals is formed, either in a so-called sp -, sp^2 - or a sp^3 -hybridization.

In the sp^3 -hybridization all p -orbitals are combined with the s -orbital, forming four sp^3 -orbitals in a tetrahedral shape, which are all filled with one electron. They have an angle of 109.5° in between each other. This is the carbon configuration in diamond.

In the sp^2 -hybridization two of the p -orbitals are combined with the s -orbital, forming three sp^2 -orbitals, which are oriented in one plane, with an angle of 120° in between each other. The sp^2 -orbitals can form a strong covalent bond, whereas the remaining p -orbital can only form a weak π -bond. This is the carbon configuration in graphite.

In the sp -hybridization only one p -orbital is combined with the s -orbital, forming two sp -orbitals pointing in opposite directions. This occurs in nature for example in alkyne.

Crystal structure of diamond The orbitals of carbon in diamond are in sp^3 -hybridization. They form a face-centered cubic lattice with a basis of two carbon atoms. One atom is at the $(0,0,0)$ location and one atom is at the $(\frac{1}{4}, \frac{1}{4}, \frac{1}{4})$ location. Figure 3.3 shows a picture of the diamond crystal lattice. This configuration is also called “zincblende” structure, named after the mineral zinkblende (or sphalerit). In zincblende the basis has two different atoms, whereas in diamond both basis atoms are the same.

Classification Natural diamond is classified according to its impurities. The existing diamond classifications are summarized in figure 3.4 [Mil13]. Most important for the classification is the nitrogen content. Nitrogen rich diamonds are type I. The according sub-type defines whether the nitrogen atoms are isolated (type Ib, nitrogen C-centers), in pairs (type IaA, nitrogen A-centers), or in bigger clusters (type IaB, nitrogen B-centers). Type II diamonds are nitrogen free, where boron rich diamonds are classified as type IIb. Diamonds used for particle detection have a very low amount of impurities and are therefore classified as type IIa diamonds.

Material properties Both, artificial and natural diamond, are expensive materials. However, diamond offers unique properties, which makes it advantageous over alternative materials. In table 3.1, the properties of diamond as solid state detector material are compared with silicon, which is the more commonly used material for particle detectors.

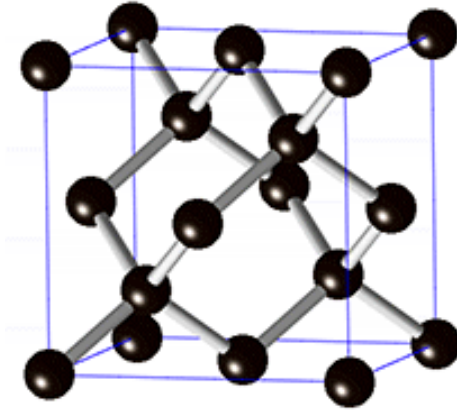


Figure 3.3.: One unit cell of the diamond lattice: face-centered lattice with a two atom basis [Wik05].

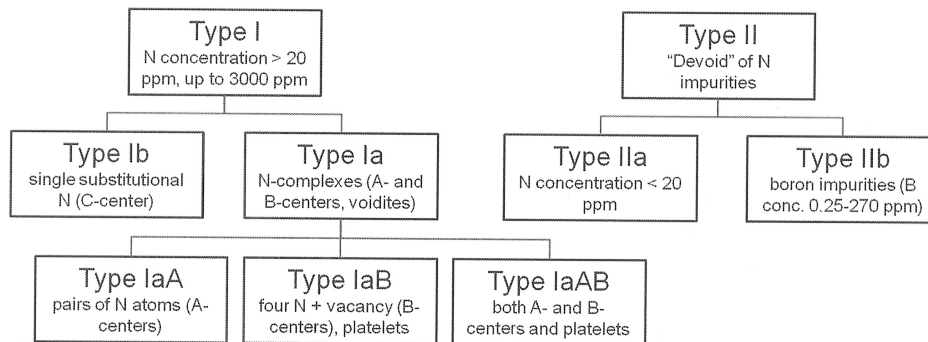


Figure 3.4.: Schematic representation of the different types of diamond [Mil13]. Diamonds used for particle detection are usually type IIa, since this type has the lowest amount of impurities.

Material property	Diamond	Silicon
Density [g/cm ³]	3.52	2.32
Dielectric Constant	5.7	11.9
Resistivity [Ω cm]	$10^{13} - 10^{16}$	2.5×10^5
Thermal Conductivity [W cm ⁻¹ K ⁻¹]	20	1.5
Thermal Expansion Coefficient [K ⁻¹]	0.8×10^{-6}	2.6×10^{-6}
Breakdown Field [V cm ⁻¹]	10^7	3×10^5
Band width [eV]	5.45	1.12
Electron-Hole Pair Creation Energy [eV]	13.2	3.62
Electron Mobility [cm ² V ⁻¹ s ⁻¹]	1800-4500	1350
Hole Mobility [cm ² V ⁻¹ s ⁻¹]	1200-3800	480
Radiation Length [cm]	18.8	9.4

Table 3.1.: Material properties of diamond and silicon [Ohl10]

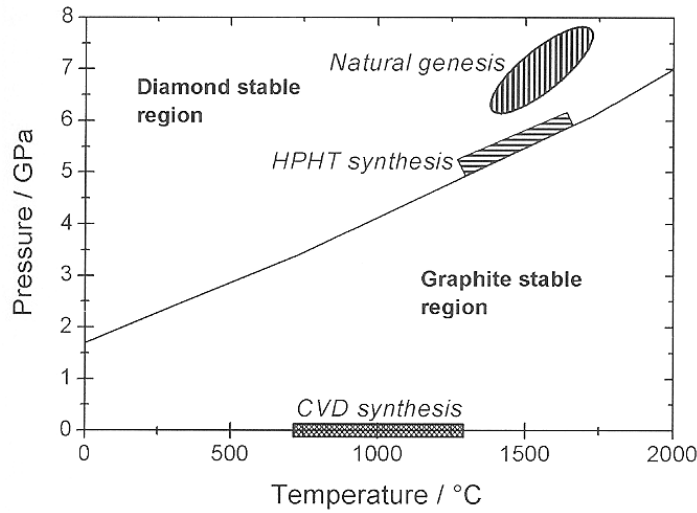


Figure 3.5.: Phase diagram of carbon [Mil13]. Regions for natural genesis, HTHP synthesis and CVD synthesis are indicated.

Diamond has, in contrast to silicon, a wide band gap and hence is considered to be an insulator. This leads to less electron hole pairs produced by ionizing particles, giving a lower signal. The advantage of the wide band gap, on the other hand, is the very low dark current. Thus, no cooling is required for a diamond detector. Even with irradiation, the dark current does not increase, in contrast to silicon, where a great effort has to be made for proper cooling. Another reason for diamond being a good particle detector is its high charge carrier mobility and hence its fast signals, making it suitable as timing detector.

3.2.2. CVD diamond growth

A common method to create artificial diamond is the high-temperature-high-pressure (HTHP) technique. HTHP diamonds usually have a high contamination of nitrogen, which is why they are not suitable as particle detectors. Artificial diamonds used for particle detection are created via chemical vapor deposition (CVD). The phase diagram of carbon is shown in figure 3.5. While HTHP synthesis tries to copy the natural genesis of diamond, CVD

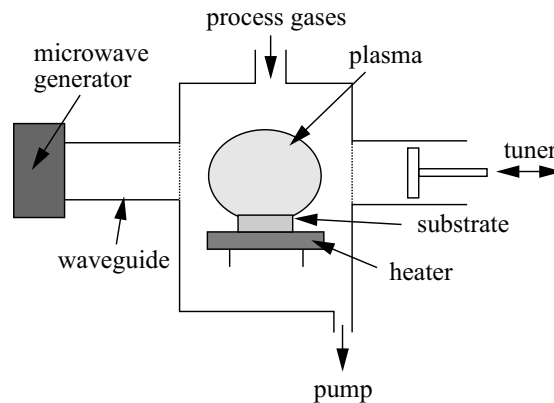


Figure 3.6.: Microwave plasma chemical vapor deposition [May00].

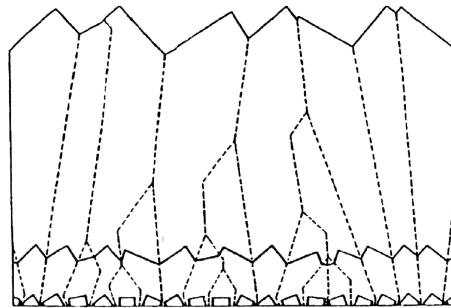


Figure 3.7.: Sketch of a pCVD grain structure [Asm02].

diamonds are created in a metastable state under low pressure.

In the CVD process, methane gas is heated to a plasmatic phase and split into free carbon and hydrogen. The heating is provided via a hot filament, a plasma arc or via microwave plasma. The latter is mostly used for detector grade CVD diamond. Figure 3.6 shows a conceptual drawing of a microwave plasma CVD. The substrate is moved into the “floating” ball of plasma. The plasma is not in contact with other material and has therefore very low contamination with impurities.

The surface of the diamond is usually terminated with an hydrogen atom. In the CVD synthesis these hydrogen atoms are split off and form H_2 molecules with the hydrogen from the methane plasma. Free carbon atoms can now form a bond with the carbon atoms on the diamond surface, which happens in sp^3 -hybrid configuration, four covalent bonds, which is the configuration of diamond. The CVD is very complex and more details can be found in [May00].

The CVD grown diamonds exist in different types, depending on the preparation of the substrate they are grown on. Usually, diamond is grown homo-epitaxially, which means it is grown on a diamond substrate. Two types of homo-epitaxial diamonds exist: single-crystalline (abbreviated sCVD) and poly-crystalline (abbreviated pCVD). For a pCVD diamond, diamond powder is applied to a carrier substrate. While the seed grains grow, some of them get bigger and some grains disappear. With increasing thickness of the diamond the grain size also increases, but the grain structure never disappears. Finally, the major bulk consists of column like grains. Figure 3.7 shows a schematic drawing of the polycrystalline grain structure. The lattice orientation of the diamond in the different grains are

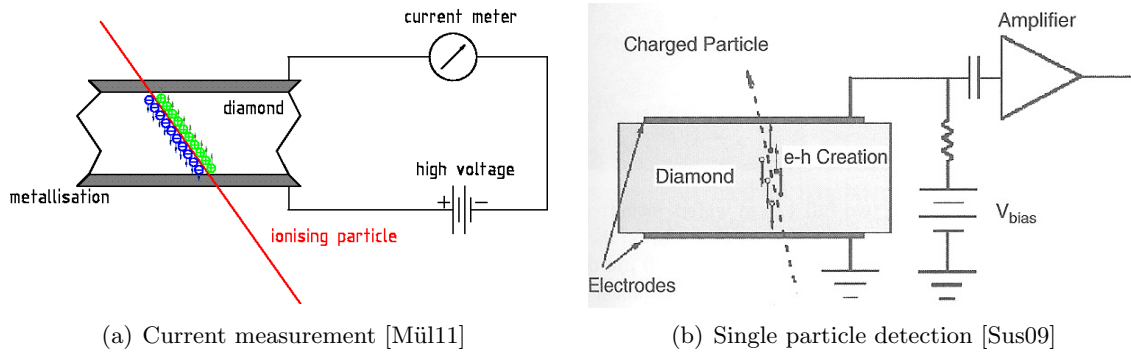


Figure 3.8.: Schematic setup for a diamond detector. Figure (a) shows the working principle of a current measurement device (like BCML). Figure (b) shows the working principle of a detector, where pulses generated by single particles are amplified and measured (like BCM1F).

completely random. sCVD diamonds are usually grown on HTHP diamonds, which are of single-crystalline nature. The CVD diamond grown on the HTHP diamond maintains the single-crystalline structure, i.e. one crystal orientation for the whole diamond piece. They also feature a low concentration of nitrogen. The disadvantage is the maximum achievable size of sCVD diamonds, which are usually of $5 \times 5 \text{ mm}^2$.

Recent efforts have shown success in creating hetero-epitaxial CVD diamond. Here, the diamond is grown on a non-carbon substrate. Most successful is the growing of diamond on a layer of iridium, hence they are called DOI (diamond on iridium) detectors [Ber09]. DOI diamonds can be grown in wafer size, like pCVD diamonds, and have a homogeneous structure. The number of crystal defects is higher than in sCVD, but the crystal structure is almost sCVD-like.

3.2.3. Signal generation in diamond detectors

Diamond is commonly called a solid state ionization chamber. The working principle is similar to a gaseous ionization chamber. The diamond is metallized on both surfaces. A high voltage is applied to the metallization resulting in an electric field in the diamond bulk, usually around a field strength of $1 \text{ V}/\mu\text{m}$. If an ionizing particle passes through the diamond bulk electron-hole pairs are created by ionization. The average ionization energy in diamond is about 13.2 eV [Can79]. The charge carriers drift along the electric field, which is the current that is measured. A minimal ionizing particle (MIP) creates on average 36 electron-hole pairs per μm of diamond it passes through [Can79]. Figure 3.8 shows two principal configurations of a diamond detector readout electronic. Either the current induced is directly measured with a sensitive current measurement device, or pulses created by single particles are amplified and measured.

The charge carriers created inside the diamond bulk material drift until they are stopped by a local defect, the surface of the diamond, or, in case of poly crystalline diamonds, by a grain boundary. The average drift length of the charge is called the charge collection distance (CCD). In fact, the CCD is the sum of the average drift lengths for electrons and for holes.

The CCD is related to the charge collection efficiency (CCE) by the relation:

$$CCD = CCE \cdot d = \frac{Q_{coll}}{Q_{ind}} \cdot d, \quad (3.4)$$

where Q_{ind} is the charge induced by the ionizing particle and Q_{coll} the charge collected by the detector electronics. The CCD and the equivalent CCE are the most important parameters for the quality of a diamond detector. A good quality sCVD diamond has a CCE of 90% - 100% and reaches this value at fairly low electric fields ($\sim 0.2 \text{ V}/\mu\text{m}$).

The CCD is not a material parameter since it cannot be bigger than the thickness of the diamond. The average drift length for an infinite diamond is often referred to as the mean free path (MFP). This term might be misleading, since the charge carriers undergo scattering while they drift through the bulk, hence their path is strictly speaking not "free". The distance until the charge is trapped will be called MFP here as well, since this is an already established term.

The value of MFP can be converted to a CCD for a given thickness d of diamond using the following equation [Dol08]:

$$CCD = \sum_{k=e,h} MFP_k \left[1 - \frac{MFP_k}{d} \left(1 - e^{-\frac{d}{MFP_k}} \right) \right] \quad (3.5)$$

3.2.4. Electric interface

To apply an electric field to the diamond an electrode has to be attached to the diamond surface. It is important to have a good mechanical and good electrical connection. Commonly a metal layer is applied to the diamond. Connections between a metal and a semi-conductor can either be a Schottky or an ohmic contact. The band structure of both types of contacts is shown in figure 3.9.

A Schottky contact is a rectifying contact, created if the work function of the metal Φ_m is greater than the work function of the semi-conductor Φ_s . When brought in contact the electrons on the semi-conductor have a higher energetic level and float into the metal, leaving positive charge at the surface. This charge buildup equalizes the fermi levels. The potential barrier formed has the height of the difference in work functions, although in reality this can be different due to the properties of the metal semi-conductor bond. If a negative voltage is applied to the metal, electrons float into the barrier, reducing its height. The current can flow in this direction. If a positive voltage is applied, the barrier increases and only a low current flows, due to charge carriers tunneling through the barrier.

Ohmic contacts are non-rectifying, They are formed, if the work function of the metal Φ_m is smaller than the work function of the semi-conductor Φ_s . Electrons drift into the semi-conductor until the fermi levels are in equilibrium. No potential barrier is formed and the charge can drift in both directions.

Ohmic contacts are created in diamond, if the electrode metal forms a carbide binding with the diamond. Metals typically used are titanium and chromium. Usually an additional metal layer (e.g. gold) is used to protect against corrosion and provide a layer where a bond-wire can be connected.

An alternative to a metallization is a graphitic contact, which are also ohmic contacts. One way is to create a layer of graphite by heating the diamond surface with an high energetic laser. Another way is to sputter carbon atoms in the diamond surface, which creates a layer of diamond-like-carbon (DLC). DLC is pure carbon, where the orbitals exist in a mixture of

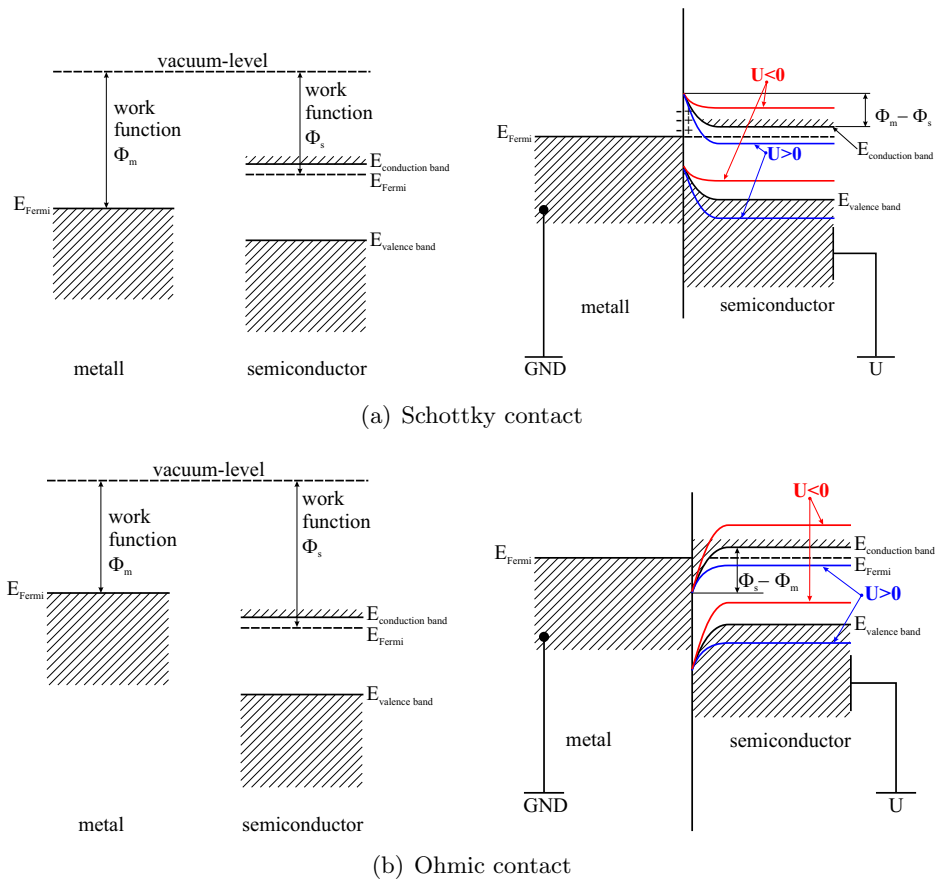


Figure 3.9.: Band structure of Schottky and ohmic contacts [Bol06].

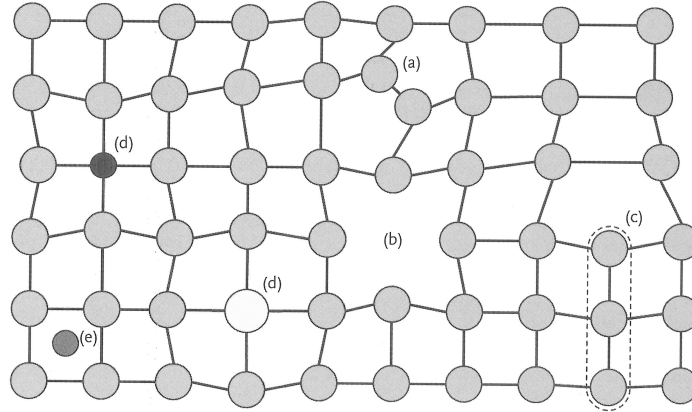


Figure 3.10.: Examples for different types of defects in diamond [Mil13]. (a) Self-interstitial, (b) vacancy, (c) edge dislocation (linear defect), (d) substitutional atom, (e) foreign interstitial.

sp^2 - and sp^3 -configurations. DLC is conductive but maintains some mechanical properties of the diamond. This is a good electrical connection between electrode and diamond. Graphitic contacts have a relatively high surface resistivity, destroying the fast signals of the diamond. It is necessary to apply an additional layer of metal, which is not necessary for the electrode-diamond contact, but reduces the surface resistivity.

3.2.5. Defects in diamond

Lattice defects Like in any other crystal different types of defect exist. Usually those are point or line defects, figure 3.10 summarizes the most common types [Mil13].

Point defects are not extended in any dimension. In single vacancies the crystal lattice is in its normal state, except one atom is missing. Self-interstitials have an additional atom at one single point in the lattice. Other point defects involve impurities. Those can either be substitutional atoms, or foreign interstitials.

Line defects extend along one dimension. A prominent example is the edge dislocation, where one layer of atoms ends. Two dimensional defects are layers of defective crystal lattice. Grain boundaries in pCVD diamonds can be classified as such.

Defects can have various effects on the electrical properties of diamond. They can either act as charge carrier traps, recombination traps, or they can generate charge carriers. The effect of the defect is given by its location in the band structure, as shown in figure 3.11 [Oh99].

A defect with an energy level in the middle of the band gap could potentially trap both, electrons and holes. These recombination traps annihilate charge carriers and therefore reduce the of charge collected. Recombination traps occur in silicon, but are normally not an issue in diamond. Charge generating defects act in the reversed process. From the defect level an electron is excited into the conduction band and the missing state is filled by an electron from the valence band, generating a free electron hole pair. Even in irradiated diamond the dark current is very low, i.e. such charge generating defects do not exist in relevant numbers. An example of high dark current in diamond are the so called “erratic dark currents”, which occur mainly in pCVD diamonds. Those appear only above a certain electric field applied to the diamond, which is different from sample to sample and it is different for both polarities

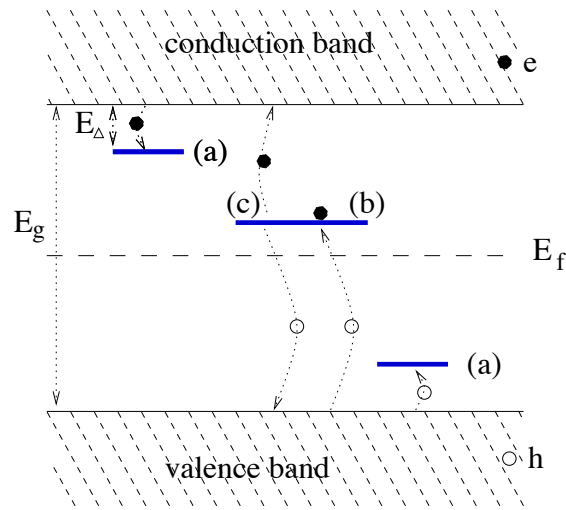


Figure 3.11.: Trapping (a), recombination (b) and generation (c) of charge at defect levels in the band gap of a semi-conductor. E_f is the fermi energy, E_g the band gap and E_{Δ} the depth of the trap level [Oh99].

of the HV. Erratic currents do not appear immediately, it can take several hours before they can be measured. It is unclear how these erratic dark currents are exactly created, but they pose a significant problem for diamond detectors, especially if they are operated in a current readout, like the BCML system.

Defects close to the conduction band act as donors. Defects close to the valence band act as acceptors. In certain applications it is desired to create such defects, which is achieved by doping. Substitutional atoms are injected into the crystal lattice. In a Group IV material, like diamond or silicon, acceptors are usually created by doping with a Group III element and donors are created by doping with a Group V element. Acceptor doping in diamond is commonly achieved with boron. The energy level is 0.37 eV above the valence band [Sus09]. Nitrogen would be an obvious candidate for a donor. However, the ionization energy of 1.7 eV is far to big to be a useful donor. Attempts to create a shallow donor were made with various elements, e.g. phosphorus or sulfur, but a real breakthrough has not been achieved yet [Sus09].

In a diamond detector acceptor and donor levels act as charge traps, which is not desired. Free electron charge carriers can be trapped in donor levels, holes can be trapped in acceptor levels. These carriers do not contribute to the signal any more, hence those traps lower the average drift length (CCD). If such a trap is already filled, it cannot catch an additional charge carrier and is therefore passivated. With time more and more traps can be filled with charge carriers and the CCD increases. This process is commonly referred to as “pumping” or “priming”, it is observed in almost every diamond detector.

Neutral traps, like vacancies or self-interstitials, can also trap charge carriers, which charges the defect. This fixed space charge can lead to a deformation of the electric field and to a decrease in signal efficiency. This process is called “polarization” and will be discussed in detail in chapter 7.

Macroscopic defects During the growth and the post-processing of the diamond, defects in the form of macroscopic defects can be created. The biggest problem during the growth are graphitic inclusions. At localized areas the formation of diamond did not work properly and the carbon is in graphitic configuration. If these inclusion form a line through the whole bulk, both electrodes of the detector are connected via an ohmic connection and high currents are measured, if a HV is applied. Even small graphitic inclusions can lead to inhomogeneities in the diamond bulk.

A method to detect tension in the crystal lattice of sCVD diamonds is to take cross-polarized pictures. Polarized light is being sent through the diamond and a polarizer is placed in front of the camera in an angle of 90° with respect to the polarized light. Tension in the diamond changes the direction of the polarization of the light and after the analyzing polarizer these parts will be visible. Figure 3.12 shows some example pictures of sCVD samples taken with cross polarized light. Often tensions in the corners of the diamond are visible. Localized defects show up as stars.

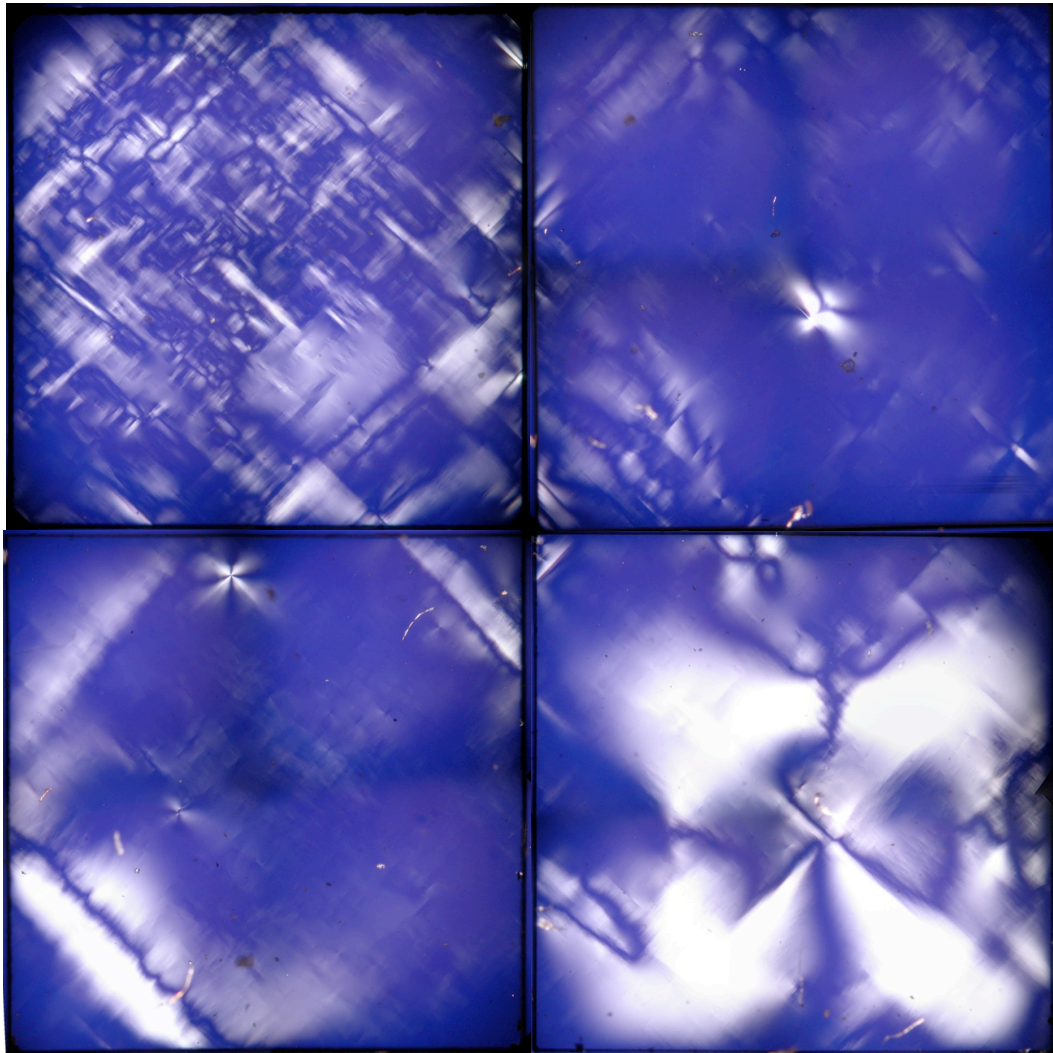


Figure 3.12.: Cross-polarized pictures of four different sCVD diamond samples. The top-left diamond shows general tension over the whole surface. The top-right sample shows a generally low amount of tension, except a defective spot in the center. The bottom-left diamond shows tension is the corners, seen as the light band spanning between the edges. The bottom-right picture shows a strong defect with high tension in the lattice spanning over the whole diamond.

Chapter 4.

The Beam Condition Monitor (BCM2/1L)

In this chapter the Beam Condition Monitor “Leakage” (BCML) is introduced. The original system, the Beam Condition Monitor 2, is described in high detail in [Mül11]. The focus of this chapter lies in the modifications done to the system and the operational experience.

4.1. The BCML detectors

4.1.1. pCVD detectors

In the BCML system mostly pCVD diamonds with a size of $10 \times 10 \times 0.4 \text{ mm}^3$ are used. The diamonds are metallized with $9 \times 9 \text{ mm}^2$ pads of a tungsten/titanium alloy. BCM1L and BCM2 detectors are packaged in different ways.

Each BCM1L diamond is packaged with a BCM1F diamond in to a single module. A picture of the modules is shown in figure 4.1(a). Four of these packages are aligned around the beam pipe at each end of CMS at $Z = \pm 1.8 \text{ m}$, giving a total of 8 BCM1L channels. Figure 4.1(b) shows a picture of the view into the CMS pixel volume, where the installed BCM1F and BCM1L packages are visible.

The BCM2 diamonds are glued on a small PCB using Staystick 472, a non-conducting thermoplastic adhesive. The diamond is bonded to the PCB on both sides, where a hole in the PCB allows the bonding on the back side. The PCB sits inside a small aluminum detector box with two SMA connectors. The cores of the SMA connectors are each connected to opposite sides of the diamond. The shielding of the SMA is connected to the aluminum housing. A picture of this diamond package is shown in figure 1.2. The BCM2 location is located at $Z = \pm 14.4 \text{ m}$.

Two half-wheels are the carrier for the BCM2 modules. Figure 4.2(b) shows such a half-wheel, where two inner detectors and four outer detectors are visible. Both half wheels are mounted on the support bars, holding also the TOTEM T2 detector, just in front of the CASTOR table. The two wheels are closed around the beam pipe to place the inner ring of detectors to within 5 cm to the beam.

4.1.2. sCVD detectors

At the location of the “BCM2 +Z inner near” detector, an additional detector module is placed and a sCVD diamond is used, shown in figure 4.3. The original sCVD was installed when the system was built, but it was replaced after 2011 with a new sCVD detector. The original sCVD detector is referred to as sCVD_2011, as it received all its fluence in 2011. The replacement detector is called sCVD_2012, as it was used in 2012.

The sCVD_2011 is approximately $4 \times 4 \text{ mm}^2$ with $460 \mu\text{m}$ thickness. It is metallized with a circular electrode of 2.9 mm diameter. Unfortunately the exact metal used is unknown, but

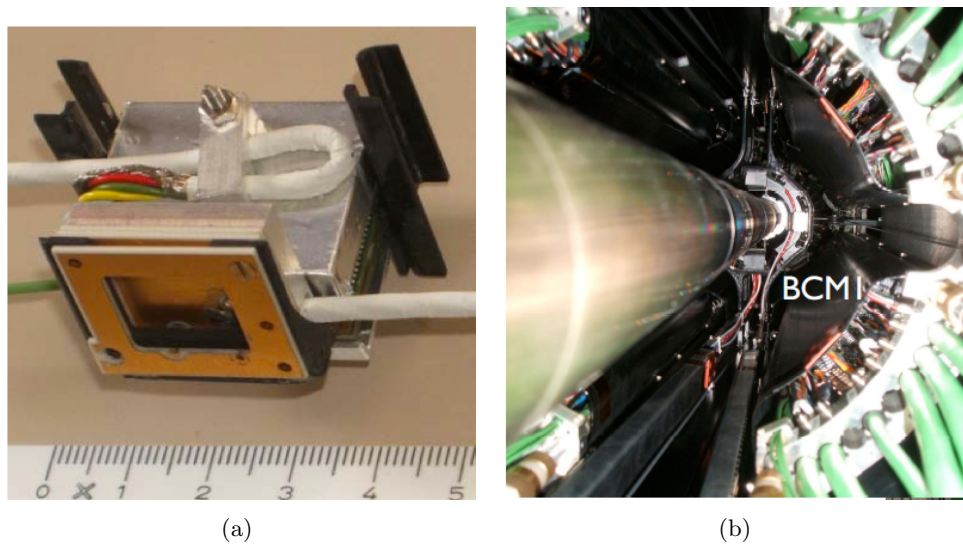


Figure 4.1.: Figure (a) shows a picture of the BCM1 module including BCM1L (module facing the front) and BCM1F (module in the back). Figure (b) shows a view from the tracker bulk head into the pixel volume. The BCM1 modules are aligned around the beam pipe with the ones on the top, below and on the side are visible.

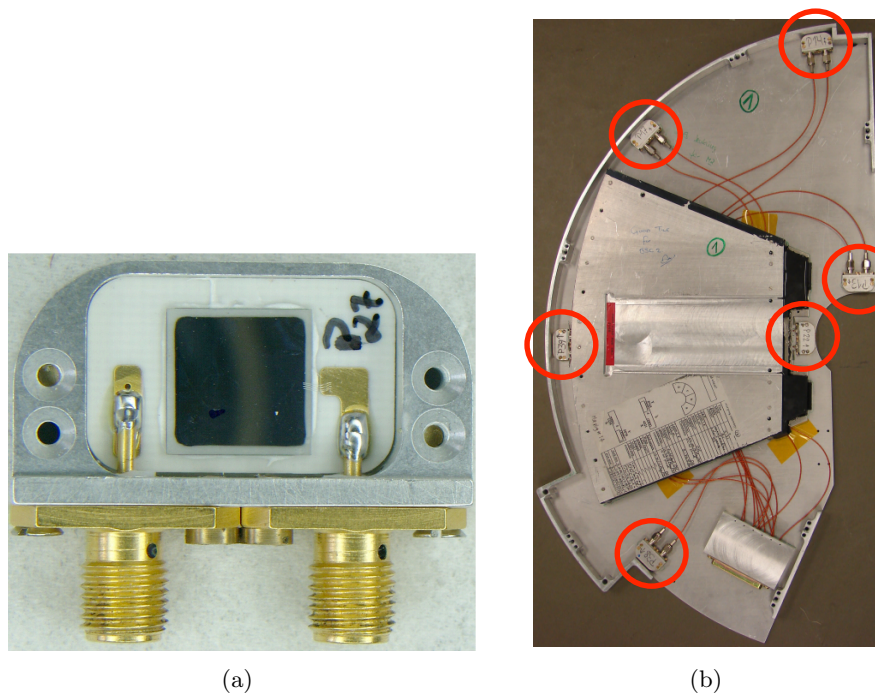


Figure 4.2.: Figure (a) shows a picture of an opened BCM2 detector module, where the $1 \times 1 \times \text{cm}^2$ diamonds visible. Figure (b) shows the mounting structure, a so called half-wheel with the detectors marked. Two such half-wheels form one BCM2 location.

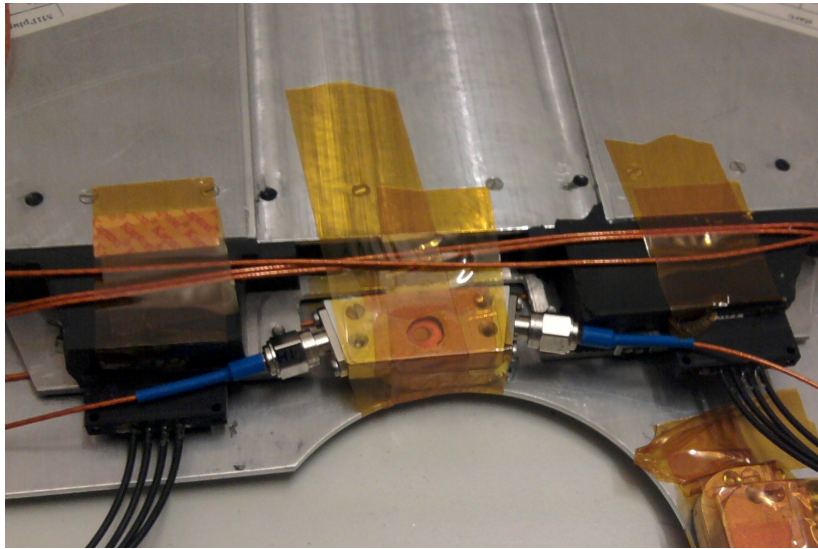


Figure 4.3.: Picture of the sCVD installed in the BCM2 wheel. The sCVD module has a trapezoidal shape with the SMA connectors on the side. It is taped on top of a normal BCM2 detector at the location of BCM2 +Z inner near.

the last layer seems to be gold. Therefore it is likely that a chromium gold electrode was used.

The sCVD_2012 is approximately $5 \times 5 \text{ mm}^2$ with $410 \mu\text{m}$ thickness. It has a $4 \times 4 \text{ mm}^2$ Cr/Au metallization. The charge collection efficiency before irradiation was $\sim 85\%$, which is relatively low for a sCVD diamond.

4.1.3. BLM detectors

At the start 2012, two ionization chambers of the type in use at the LHC were connected to the BCML readout. One ionization chamber was installed on each CASTOR table on both ends of CMS. The tube is directly behind the BCM2, roughly at the same radius as the BCM2 diamonds on the outer location. Figure 4.4 shows the picture of an installed BLM tube. The BLM tube does not suffer from saturation at the particle rates at which it is subjected. Also no radiation damage is expected. Since the BLM tubes are in the same readout system, they are ideal detectors to compare the data with the diamond signals.

4.2. Electronics

An schematic overview of the electrical connections of the BCML system is shown in figure 4.5. The “tunnel card” front-end electronics are located in different places for the BCM2 and the BCM1L systems. BCM1L uses one tunnel card located in the service cavern, whereas the BCM2 tunnel cards are located in the experimental cavern on the HF platform, two tunnel cards per end. The BCM2 tunnel cards use a modified power module to supply the tunnel cards, which are powered by $+8 \text{ V}$ and -8 V DC from the CAEN power supply. The purpose of this modification is to have the ability to remotely switch the power to the tunnel cards on or off. The BCM1L tunnel card uses an LHC default power module, which includes an AC/DC converter. The power module is connected to a normal 220 V AC power outlet. The tunnel cards are connected via optical data transmission to the back-end electronics, the so called

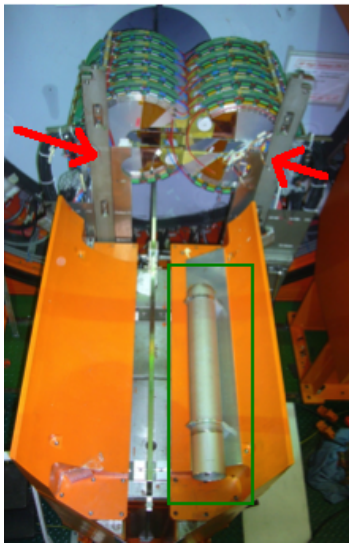


Figure 4.4.: Picture of one of the BLM tubes installed on the castor table, marked by the green square. It is placed directly behind BCM2. The BCM2 wheels are not present on this picture, but one can see the vertical support bars to which the wheels are mounted, marked by red arrows.

DAB cards. The measured data is processed in the DAB cards, where also the conditions for a beam abort is checked and the signal to dump the beams is generated when an abort condition is met.

Various details of the electronic components are described in more detail in the following sections.

4.2.1. Wiring and grounding

The grounding of the BCML system is always at the location of the tunnel card, hence it is different for BCM1L and BCM2. BCM1L is grounded in S1, while the BCM2 is grounded on the HF platform. The wiring scheme for BCM1L is shown in figure 4.6, and for BCM2 in figure 4.7. BCM1L has also a HV filter circuit located close to the sensors (at PP0 on the tracker bulk head), which is shown in figure 4.6(b). The filter box of BCM2 was modified at the start of 2012, the modifications are explained in detail in section 4.2.3.

4.2.2. Tunnel Card - front-end readout electronic

The readout electronics, the so called "tunnel cards", are radiation hard current measurement devices with 8 independent input channels, featuring zero dead time and high dynamic range [Eff06]. The measurement range reaches from 2.5 pA to 1 mA. The tunnel cards were developed as front-end electronics for the beam loss monitoring (BLM) system of the LHC, where they are placed in the LHC tunnel, hence the name tunnel card. The cards used in the BCML system are almost identical. The working principle of the tunnel cards is described in the following.

Measurement principle The tunnel card is an implementation of a current to frequency converter (CFC). The schematic principle is shown in figure 4.8. The detector current dis-

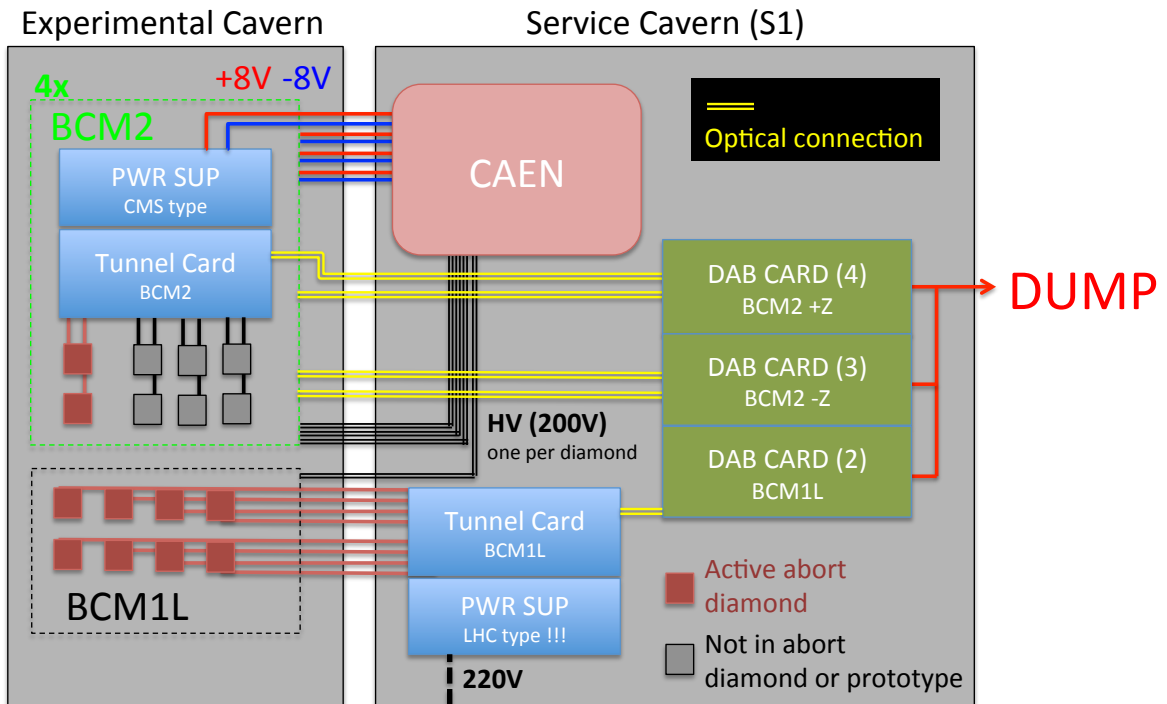
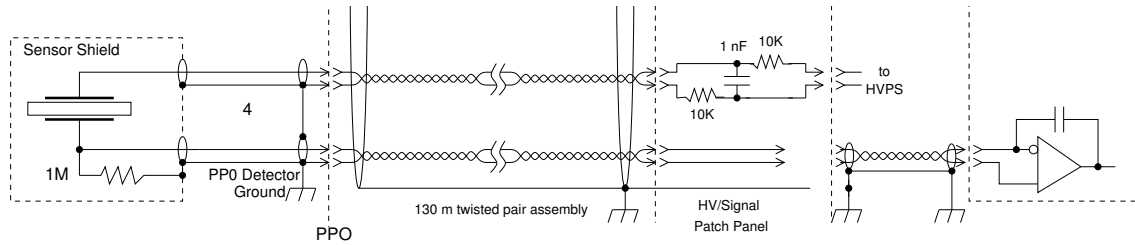
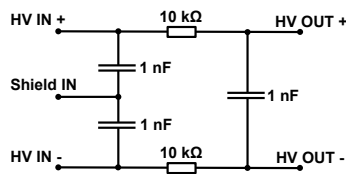


Figure 4.5.: Schematic overview of the BCML system configuration. In BCM1L all 8 diamonds are connected to one single tunnel card located in the service cavern. The BCM1L tunnel card uses a LHC type of power module, which is supplied by 220V AC. Each of the four BCM2 tunnel cards, located at the HF platform in the experimental cavern, are connected to two diamonds, which are active in the triggering of a beam abort. The rest of the channels are outer detectors, prototypes or connected to the BLM ionization chambers. The BCM2 tunnel cards use a custom power supply which is supplied by the CAEN with +8V and -8V DC. The CAEN power supply, used for low and high voltage, and the back-end electronics (DAB cards) are placed in the service cavern.



BCM1_L Cabling and Grounding Scheme
January 26, 2007

(a) BCM1L cabling



(b) BCM1L HV filter

Figure 4.6.: BCM1L detector grounding scheme. Additionally to the cabling shown in figure (a), BCM1L has a HV low-pass filter, located close to the sensor, shown in figure (b).

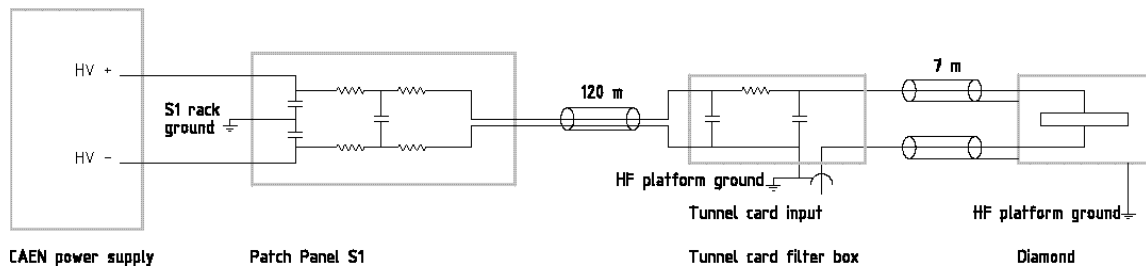


Figure 4.7.: BCM2 detector grounding scheme [Mül11]. The filter box is described in more detail in section 4.2.3.

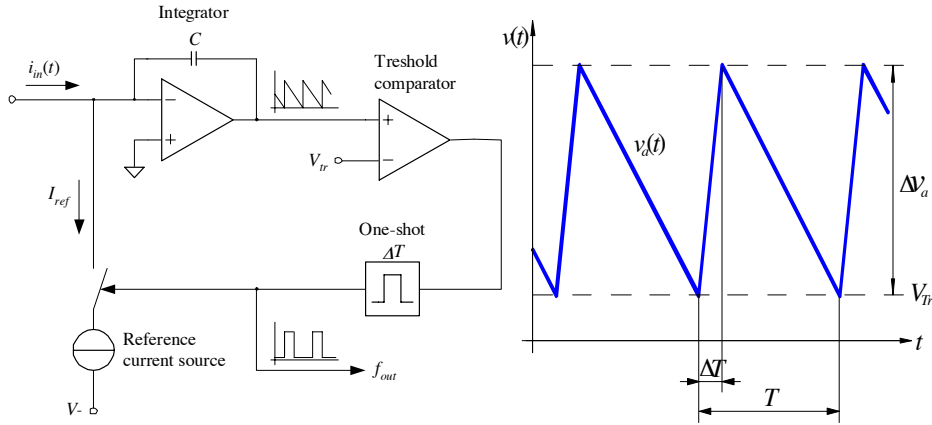


Figure 4.8.: Schematic principle of the current to frequency converter (CFC) in the tunnel cards [Gsc02]. The feedback capacitor gets discharged by the detector current. A comparator checks if the voltage falls below a certain value and initiates a recharge. Every time the capacitor is recharged it counts as one CFC pulse.

charges a capacitor via an integrator circuit. Once the voltage of the capacitor drops below a certain threshold the capacitor gets recharged by a current source. If this occurs, it counts as one CFC count. The number of CFC counts per unit time is proportional the detector current. Additionally an analog to digital converter (ADC) measures the voltage of the capacitor every $40 \mu\text{s}$. By calculating the difference between the measured value and the value measured in the previous reading the current is calculated. The ADC value and the CFC value are combined every $40 \mu\text{s}$ to the final measured value. The ADC thereby extends the dynamic range to lower current values.

The tunnel card does not support negative currents. If negative currents occur the tunnel card can be put in a false state, preventing proper functioning. To avoid negative currents at all times, an offset current of 10 pA is internally created. Due to production tolerances this offset current cannot be set up in a precise way. The tunnel card regulates it internally. When the tunnel card is switched on, it slowly increases the offset current until it measures a 10 pA current. A negative current can occur when the tunnel card is switched on, before the correct offset is reached. In this case only zero values are measured for all running sums. It can take several minutes until the tunnel card is stabilized.

Every two minutes the tunnel card performs a self calibration. Due to production tolerances, the absolute ADC values corresponding to a voltage of the capacitor when fully charged or discharged are unknown. For the proper summing of CFC and ADC readings it is necessary to know how many ADC values one full capacitor discharge corresponds to. The tunnel card remembers the maximum and the minimum ADC value. This is used to calibrate the “weight” of one CFC pulse, which happens every 2 minutes. A mis-calibration can lead to a small change in measured value, the so called calibration jumps. These calibration jumps are only observed in some of the channels. They are an inconvenience because they lead to unphysical jumps of the data, but the jumps are only very low so they do not lead to any problem for the proper abort functionality.

The measured value is transmitted to the back-end electronics via a gigabit optical link (GOL). Every tunnel card has two redundant optical transmitters, sending the data of all 8 channels every $40 \mu\text{s}$.

Reset The tunnel cards are equipped with different possibilities to reset the electronics: A button on the front of the tunnel card, a differential input line on the front of the card, a HV trigger line and an automated reset 2 min. after the tunnel card was switched on.

If the tunnel card is switched on it can happen that it starts up in a false state. In order to rectify this, if it happened, the tunnel card performs an automated reset 2 minutes after it was switched on. Additionally to the eight current measurement channels, the tunnel card also has a HV input with monitoring and control features. In the LHC BLM system the HV, used for all eight connected detectors, is fed to the tunnel card via this HV input. By setting different HV levels various test features of the tunnel card can be activated. If a voltage above 386 V is applied for longer than 15 minutes the tunnel card resets. More details about these test features can be found in [Mül11].

The differential input is not used in BCM1L or in BCM2. The only way to restart the BCM1L tunnel card is via the button on the front of card. The HV input of the BCM1L tunnel card is not connected and therefore this reset function is not available.

The button in front of the tunnel card cannot be used with BCM2, since the cards are not accessible at all times. In BCM2 the HV input is directly connected to one of the HV channels from the CAEN. By activating this HV channel the reset can be initiated.

The reset is electronically initiated by a relay in the tunnel cards used for the LHC. CMS uses a custom modification of this reset mechanism, where a MOSFET replaces the relay, because a relay would not work properly in the magnetic field present on the HF platform.

Powering of the tunnel cards Tunnel cards require the different LV supplies with +5 V, +2.5 V and -5 V. Each tunnel card is connected to a customized power supply module. A standard power supply module, as also used in the LHC BLM system, includes an AC/DC converter and voltage regulators to create the correct voltages. A tunnel card crate is equipped with a transformer to change from the 220 V AC of a normal power outlet to 8 V AC, which is fed to the power supply modules. The BCM1L crate is located in the service cavern and uses this default powering scheme. The disadvantage is that the power cannot be controlled remotely, which is not a problem for BCM1L since the service cavern can be accessed at any time. The BCM2 tunnel crates are located inside the experimental cavern, which cannot be accessed easily. A remote control of the tunnel card power was needed. The power supply modules for the BCM2 tunnel cards do not include the AC/DC converter, only the voltage regulators. Also, the transformer is not needed. Two low voltage DC power lines feed the power module. A +8 V and -8 V low voltage is supplied by the central CAEN power supply located in the service cavern.

4.2.3. BCM2 HV filter boxes

The long HV cables of about 120 m running from S1 to the HF platform potentially introduce noise to the system. A filter was implemented during the set up of BCM2 to remove any noise from the HV line. A filter box installed directly at the inputs of the tunnel cards contains this filter and acts as an adapter to connect the diamond sensor and provide the proper grounding. A picture of how the filter boxes are installed is shown in figure 4.9. They are mounted directly on the BNC input of the tunnel cards. They are connected to the back plane of the crate via short cables. From the backplane a connection is made to the power supplies in the service cavern and to the diamond detectors.

The circuit is shown in figure 4.10. As shown in [Mül11] a high detector current would drain the capacitor in this filter and the HV provided to the diamond drops, especially with

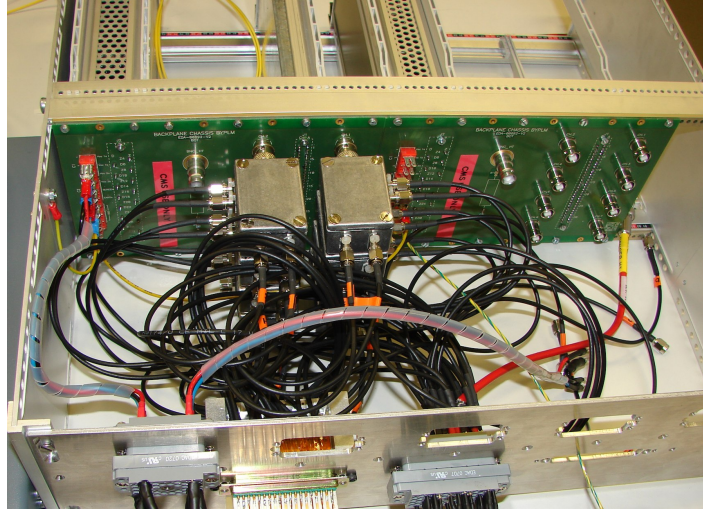


Figure 4.9.: Picture of the HV filter boxes installed in the back part of the BCM2 tunnel card crate. The filter boxes for only one of the tunnel cards are yet installed. The filter boxes stick directly to the BNC inputs of the tunnel cards. They are connected via short cable to the back plane of the crate, from where the connection goes further either to the diamonds, or the service cavern.

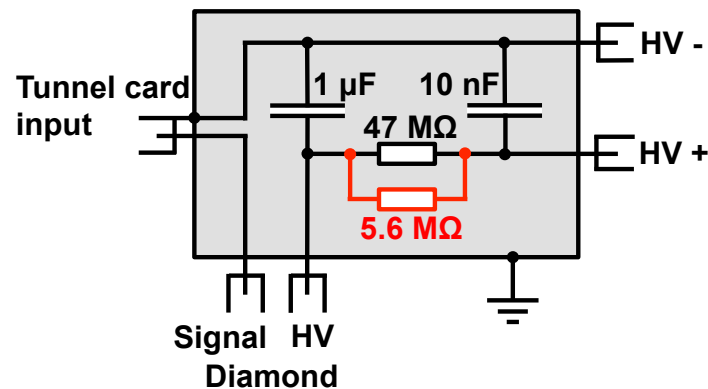


Figure 4.10.: Electrical circuit of the HV filter box used in all BCM2 channels. In the beginning of 2012 the filter was modified by adding a resistor (marked in red) to prevent a discharge of the $1\ \mu\text{F}$ capacitor. The total resistivity reduced to $5\ \text{M}\Omega$, the low pass cutoff frequency changed from $4.3\ \text{mHz}$ to $31.8\ \text{mHz}$.

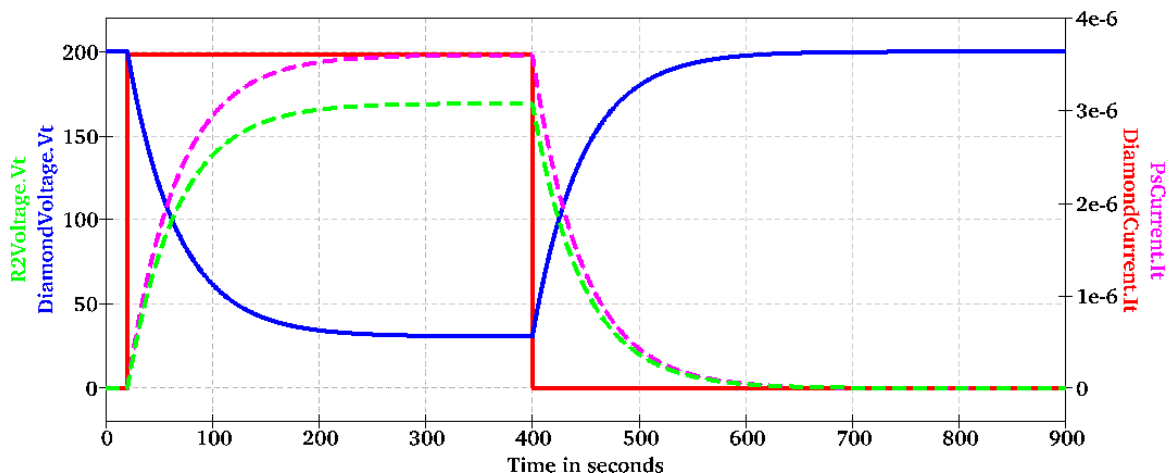


Figure 4.11.: Simulation of the voltage drop for a BCM2 detector current of $4\ \mu\text{A}$ before the filter was changed [Mül11]. If the detector current is switched on the capacitor slowly discharges leaving only $\sim 40\ \text{V}$ of bias HV for the diamond.

a current close to the beam abort threshold. This becomes significant and the full protection efficiency is not guaranteed. A simulation of the voltage drop for a detector current of $4\ \mu\text{A}$ is shown in figure 4.11. In order to prevent this case, an additional abort threshold was introduced. In [Mül11] it was suggested to reduce the $47\ \text{M}\Omega$ resistor to prevent the voltage drop make this safety abort threshold obsolete. This change was implemented in the beginning of 2012. As shown in figure 4.10 an additional resistor with $5.6\ \text{M}\Omega$ was soldered in parallel to the $47\ \text{M}\Omega$ resistor so the resulting resistivity was $5\ \text{M}\Omega$. The cutoff frequency of the low pass changes from $4.3\ \text{mHz}$ to $31.8\ \text{mHz}$, which still provides a very good filtering, but the discharge of the capacitor is less pronounced.

4.2.4. DAB64x Card - back end electronics

Every $40\ \mu\text{s}$ a current reading is transmitted via the GOL to the DAB64x cards [Jon04], which is a general purpose PCB used in the whole beam instrumentation of the LHC.

The data is processed by forming the so called successive running sums. In total there are 12 different running sums with different lengths. For each running sum, the number of previous data readings are summed up. Table 4.1 shows the length of the available running sums. With a new value added in to the running sum the oldest value is erased. Not every running sum is updated on each $40\ \mu\text{s}$ reading. Shorter running sums are used to update the higher running sums. Table 4.1 also shows how often a running sum is updated. A beam abort threshold can be configured on each running sum. If the value of one running sum exceeds its abort threshold the beam dump signal is asserted.

The data is read out for monitoring purposes at a frequency of $1\ \text{Hz}$. When the readout is triggered the highest value of each running sum measured since the last readout is recorded. This is implemented to show the measured values of a short event, which happened in between two read outs. During a more-or-less constant situation, the values measured in the tunnel card have a Gaussian distribution. Since the maximum value is reported, it does not correspond to the mean of the values, but to the upper tale. With higher running sums, the width of the distribution decreases and the difference between the actual average of the detector current and the reported value decreases. Above running sum 8, the noise is so far

Running Sum number	40 μ s steps	integration time [ms]	refresh 40 μ s steps	refresh time [ms]
RS 1	1	0.04	1	0.04
RS 2	2	0.08	1	0.04
RS 3	8	0.32	1	0.04
RS 4	16	0.64	1	0.04
RS 5	64	2.56	2	0.08
RS 6	256	10.24	2	0.08
RS 7	2048	81.92	64	2.56
RS 8	16384	655.36	64	2.56
RS 9	32768	1310.72	2048	81.92
RS 10	131072	5242.88	2048	81.92
RS 11	524288	20971.5	32768	1310.72
RS 12	2097152	83886.1	32768	1310.72

Table 4.1.: All running sums calculated in the DAB cards [Zam06].



Figure 4.12.: Picture of the USB readout together with the tunnel card electronics and a power supply module for the tunnel card [Mül11].

reduced that the measured values are realistic.

The full stream of 40 μ s data cannot be saved. In case of a beam abort, a buffer containing the last 2048 values of this data stream is read out and saved. This so called “post-mortem data” offers valuable information to analyze the beam loss event responsible for the beam dump. Such post-mortem data set is not available for the BCML channels, as they have not yet caused a beam abort due to an actual beam loss.

More details about the working principle of the readout electronics can be found in [Zam06].

USB readout box

A readout box is available which can substitute the DAB card readout. It can be connected to a PC via USB, hence its referred to as “USB readout box”. One tunnel card can be connected via an optical link. A program is available for the Windows operating system to control the USB readout box. It can display the status information of the tunnel card and forms the runnings sums, which can be read out at a configurable readout frequency. The USB readout box is ideal to test the performance of the tunnel cards or test detectors in the lab. It was also used for the current measurement in test beam irradiations. The readout frequency of the USB box can be configured and is not fixed at 1 Hz, as it is with the DAB cards. The default is to read out every 0.4s, but it can be as low as every 0.1 s. A picture of the USB box together with the tunnel card is shown in figure 4.12.

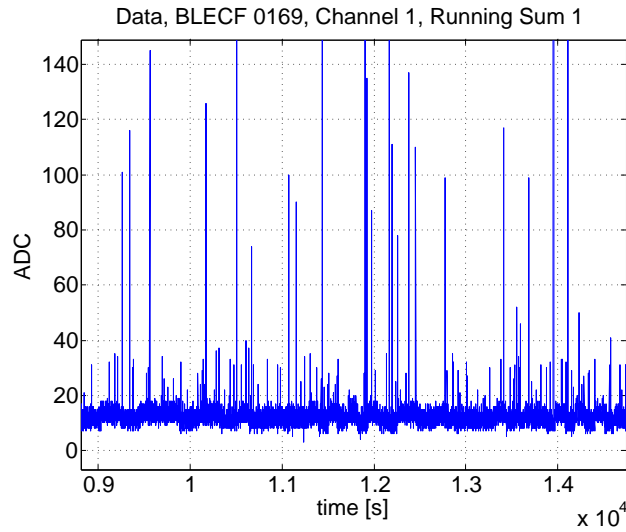


Figure 4.13.: Running sum 1 data of one channel showing noise spikes. An input current of 3 nA was applied to the channel.

4.3. Noise tests with readout electronics

The readout electronics was designed to be dead time free with a high dynamic range. Those features are important for a beam loss monitor. As described in section 4.2, this is achieved by combining a current to frequency converter (CFC) measurement with an ADC measurement. During the combination of the data from both measurements, a mis-match can occur which results in a wrong data value in the 25 kHz data stream from the tunnel card to the back-end electronics. When the running sums are calculated this mis-match shows up as a spike in the data of running sum 1. Since it is only one isolated false $40 \mu\text{s}$ value, the size of the spike is reduced in the higher running sums, where only relatively low normal values are added. In the longest running sums the spike is not visible any more, since the wrong value is averaged with many correct values. Figure 4.13 shows the running sum 1 data of an example channel for several minutes, where a 3 nA input current was applied to the channel. Clearly visible is the baseline, which is the normal data reading. Many spikes are about 20 ADC values high. Additionally there are spikes visible which are much higher, but not as often.

These noise spikes were first observed during the commissioning of the BCM2 detector and a preliminary analysis is shown in [Mül11]. A more comprehensive analysis of the noise was needed, since it was not known if the height of the noise peaks would increase with higher detector currents. Due to the danger of asserting a beam abort because one of these spikes exceeds the beam abort threshold a detailed analysis of the spike behavior was performed. For this test the USB readout box was used. The feature of configuring the readout speed was used to compare the occurrence of spikes with a 1 s readout period and a 0.4 s readout period.

The input of the tunnel card is connected to a current source, which was a battery with a resistor in series to control the amount of current. The current could be varied by changing the value of the series resistor. The running sum data was recorded over several hours to get enough spikes to obtain an approximate measurement of their frequency.

To analyze the data every recorded value is histogrammed and normalized to the number data reading per hour. This way the height and the probability of occurrence of the spikes

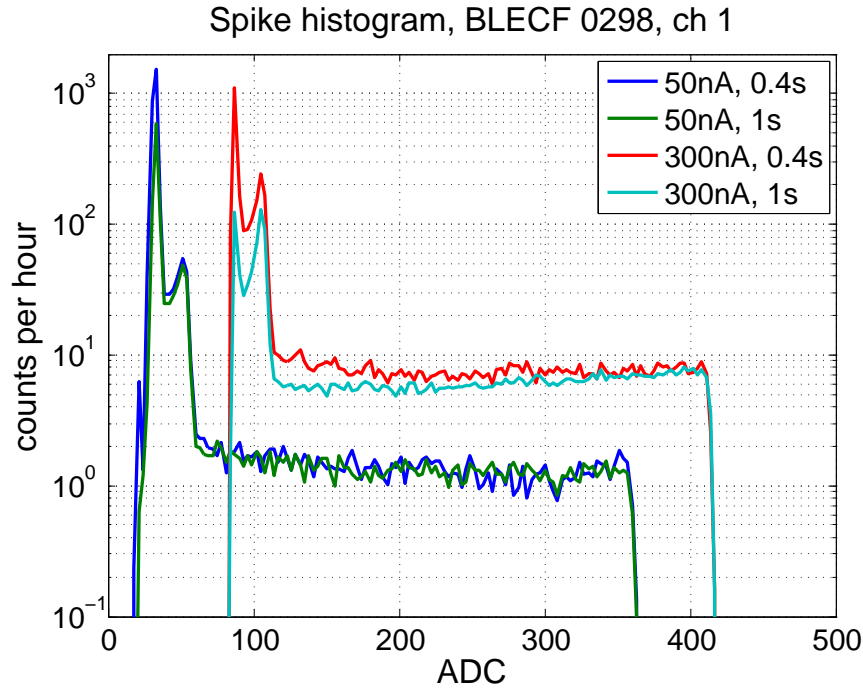


Figure 4.14.: Histogram of the running sum 1 data for one channel with a current source attached, showing the occurrence of noise-spikes. The data was measured with two different values for the input current and two different readout speeds. Spikes can have a magnitude between the correct readout values and a maximum spike height added to the normal readout value. The readout speed does not influence the number of spikes. The number of spikes increases linearly with input current

is displayed.

Figure 4.14 shows the histogram of the running sum 1 data for a measurement comparing two different input currents with two different readout speeds. Each histogram shows two peaks at low values, which are about 20 ADC values different. The peak on the left of every histogram is the highest since it is the normal read out value for the given input current, 30 ADC for 50 nA and 85 ADC for 300 nA. Due to noise the values of running sum 1, the ADC values are significantly higher than one would expect. This is more pronounced with lower input current and therefore the measured ADC value does not scale properly with the input current. The second peak is due to a certain kind of data spikes which are quite numerous, but always have a very low amplitude. Due to their low amplitude, they do not pose a problem.

Above these low values, many entries can be found, which can have a wide range of ADC values. For the measurement with 50 nA input current they can be as high as about 360 ADC values. For the 300 nA measurements they can be about 415 ADC values high. The height of the spike is equally distributed up to this maximum level. No spikes were found above that level. If the normal current value of 30 ADC for 50 nA and 85 ADC for 300 nA is subtracted, a general spike maximum of 330 ADC counts was found for this particular channel of this tunnel card. This level of maximum height is different in other tunnel cards and it even differs between channels of one card. The occurrence of the spikes is not affected by the readout

Tunnel card installed at	BCM1L	BCM2 -Z top-far	BCM2 -Z bottom-near	BCM2 +Z top-near	BCM2 +Z bottom-far
channel 1	328	147	314	345	113
channel 2	311	102	314	105	100
channel 3	275	102	326	166	139
channel 4	343	112	350	353	127
channel 5	247	104	205	88	135
channel 6	318	112	332	128	139
channel 7	193	109	330	58	84
channel 8	335	134	288	147	134

Table 4.2.: Maximum height of spikes for the tunnel cards installed in BCML.

speed. Only the number of good data points are reduced. If a spike happens, it will be the reported value overwriting the correct measurement.

With higher input current the number of spikes increases. The occurrence increased by around a factor of 6 when the current was changed from 50 nA to 300 nA. Hence the number of spikes increases approximately linearly with the input current. For the 300 nA measurement a slight decrease in spike occurrence is observed with slower readout speed. This is due to the fact that the chance of having two spikes in one readout period is increased, in which case only the higher spike of both is visible.

As explained earlier the spikes occur when data from the ADC is mis-matched with the data from the CFC. This can happen when the measurement capacitor is being recharged. The number of recharges, which corresponds to the number of CFC pulses, increases linearly with input current and therefore the chance of having a spike increases linearly with input current as well.

The height of the spikes does not increase with higher current, except for the increase due to a higher base line. Therefore there is no added danger of firing a false beam abort. The maximum height of the spikes poses a limit of the minimal abort threshold that can safely be configured, which is mostly relevant for running sum 1. This is important to consider if abort thresholds are modified.

The tunnel cards installed in the system were checked for the height of the spikes. The maximum spike height for all channels of the tunnel cards installed until the end of 2012 can be found in table 4.2. The maximum values were calculated from several days of data with and without beam.

If a new tunnel card is installed the spike limit should be evaluated before setting the abort threshold close to the recommended limit. If the need for very low thresholds under the recommended limit is required the tunnel cards have to be hand selected for suitable maximum height of the spikes.

4.3.1. Spike filter for display

The running sum 1 data is important information and is constantly displayed in the control room of CMS. It is also part of the so called "Background 3" number which is published to the LHC and displayed in OP Vistars, the online status display of the LHC¹.

One solution of improving the data quality would be a faster readout cycle. The number

¹<http://op-webtools.web.cern.ch/op-webtools/vistar/vistars.php>

of spikes would not be reduced, but the number of good values would be increased. Unfortunately the readout speed of the production system is fixed to 1 s and this cannot be changed.

With the increased luminosity in 2011, the detector current in the BCML sensors increased and the spikes became very numerous. A data filter was implemented to reduce the number of spikes on the displays. Important is to preserve any data spike that is due to an actual beam loss signal. The algorithm works by the following steps:

1. Potential spikes are selected by applying a 3rd order median filter to the data of running sum 1. The data value is compared with the preceding and the succeeding value. The median value of these three is used as filtered value. To achieve this the data stream has to be delayed by one second, which is not a problem for the displays. The filtered data is subtracted from the unfiltered data and if the difference is above a certain threshold this readout second is flagged as potential spike. This is done for every channel separately.
2. The data of potential spikes in running sum 1 is compared with running sum 2. A spike occurs only in one $40\ \mu\text{s}$ readout, which means the data of running sum 2 has the same size. A beam loss event, longer than $40\ \mu\text{s}$ shows an increase in running sum 2 compared to running sum 1. If this is the case, the spike is not filtered and the original data is kept.
3. Since a beam loss event shorter than $40\ \mu\text{s}$ would look exactly like a fake spike it would still be flagged as spike after step 2. A significant beam loss event would be detected by many channels and not only one. The data, which is flagged as a spike is compared with the data from neighboring sensors. If a potential spike is found in at least two channels, the data is not filtered.
4. If a data point is flagged as spike after step 2 and 3, the spike is replaced with the median filtered value calculated in step 1.

This filter decreases the number of spikes drastically. Unfortunately the filter fails when the number of spikes get too numerous. With two successive spikes the median filter cannot detect the spikes any more. The constant monitoring of the running sum 1 data is not possible any more. Since the normal values are also dominated by noise, this is not a big loss. Beam loss events, which have greater amplitudes than the height of the spikes, can still be seen clearly.

4.4. Beam abort thresholds

The BCML system is designed to protect the CMS inner detector against short duration ($\leq 40\ \mu\text{s}$) dangerously high beam losses, and longer-term ($\leq 83\ \text{s}$) high beam background conditions that can result in problematic conditions for data taking and an increased dose to the inner detector region. An additional medium-time scale threshold is needed specifically for the BCM2 to guarantee a high detector efficiency, corresponding to an upper limit on the leakage current drawn by the detector.

The original setting for the abort thresholds are motivated [Mül11] and the necessary modifications are explained.

Running Sum 1 - $40\ \mu\text{s}$ integration threshold:

The $40\ \mu\text{s}$ integration abort threshold is calculated based on the tracker community's damage tolerances studies:

- 10^9 MIPs/cm² per "short-loss", is the damage threshold defined by the tracker community.
- $40\ \mu\text{s}$ is the shortest loss period measured by the BLM electronics.
- A safety factor of 1000 is included for the threshold corresponding to a threshold set to 10^6 MIPs/cm²/ $40\ \mu\text{s}$.
- For 10^6 MIPs a measured charge of 1.21 nC charge collection is expected in the used pCVD detectors (assuming a CCD of $210\ \mu\text{m}$). In $40\ \mu\text{s}$ this corresponds to a current of $30.2\ \mu\text{A}$.
- An even more conservative value of $10\ \mu\text{A}$ (= 2050 ADC counts) was chosen.
- This abort threshold was modified after significant radiation damage was observed, see section 4.4.1.

Running Sum 10 - 5.2 s integration threshold:

The 5 s integration abort threshold protects the detector against capacitor discharge in the BCM2 HV filter box, to maintain a high detector efficiency:

- A maximum current of $0.9\ \mu\text{A}$, corresponding to 26 M ADC counts (averaged over 5 s) is chosen as the threshold limit.
- In the beginning of 2012 the filter boxes were modified to remove the danger of capacitor discharge as described in figure 4.10. The RS 10 abort threshold was removed on 15th August 2012 [Dab12].

Running Sum 12 - 83.9 s integration threshold:

The 83 s integration abort threshold is calculated based on an increased beam background activity compared to the expected particle flux at nominal CMS luminosity, averaged over 83 s:

- 290 nA, 126 M ADC counts. This was well above the expected rate at that time with the intention to increase it with higher luminosity.
- Due to the increasing instantaneous luminosity of the LHC, the measured signal in the BCM2 detectors was getting close to the first defined abort threshold. Of course it is not desired to dump the beams due to signals generated by collision products and an increase of the abort threshold was necessary.
- With the introduction of BCM1L in the abort threshold, the threshold philosophy was redefined: The abort threshold should be based on three times the expected signal at nominal LHC luminosity given by data driven extrapolations. The thresholds of the new BCM1L channels were defined this way, and the BCM2 thresholds were modified on 29th August 2011 [Dab11a].
- The fills chosen for the data driven extrapolation of the first modification, were #2000 for the BCM2 sensors and #2040 for the BCM1L sensors. A linear fit was applied to the correlation between signal and luminosity for each channel and an extrapolation of the signal to $3 \times 10^{34}\ \text{cm}^{-2}\text{s}^{-1}$ was made based on this fit.
- With this new method every channel received its own abort threshold.
- Due to increasing radiation damage it was necessary reevaluate the optimal abort threshold in 2012. The details are described in section 4.4.1.

4.4.1. Modification of beam abort thresholds due to efficiency loss.

Due to radiation damage, the detector efficiency of the BCML sensors decreased and with it the level of protection. The abort thresholds introduced in chapter 4.4 were lowered to ensure the desired protection. A modification of the abort thresholds has to be approved by the collaboration and can't be done often. The thresholds were modified once in 2011 and once in 2012. The modifications are documented in [Dab11a, Dab12]. In 2011, the modification was rather motivated by a need to increase the abort thresholds, since the detector current during normal operation was getting dangerously close to the running sum 12 threshold. The data driven method to obtain the running sum 12 threshold (see chapter 4.4) compensates the radiation damage the detector received so far, because it purely calibrates the threshold to the measured signal with respect to instantaneous luminosity. The data driven extrapolation needs to be re-done when the detectors have lost some amount of signal strength.

Since the running sum 1 threshold is based on an expected detector performance, it cannot be directly calibrated during operation. It is assumed that the signal of the un-irradiated detectors is as expected and the relative loss in signal strength is used to compensate the radiation damage. In 2012, after a total integrated luminosity of 16 fb^{-1} , a compensation for the reduction in signal strength measured so far was introduced for the abort threshold on running sum 1. Details about the signal loss are later explained in chapter 7.3, figure 7.11(b). BCM1L lost $\sim 30\%$ of its signal strength and BCM2 inner on +Z lost about 60%. Both groups of detectors still fulfilled the requirements for an abort threshold of 10^6 MIPs/cm^2 ($= 30.2 \mu\text{A}$) with their initial abort threshold of $10 \mu\text{A}$. The signal strength of BCM2 -Z was reduced by 80% and the abort threshold current was lowered to $7.2 \mu\text{A}$ ($= 1476 \text{ ADC}$) to maintain the abort conditions of 10^6 MIPs/cm^2 .

The full history of the abort thresholds for each channel can be found in appendix A.

4.5. Hardware failures and beam aborts

No beam loss events have been significant enough to cause a beam dump initiated by the BCML system so far. In a few number of incidents a beam dump was asserted because of a hardware failure. This was intended by design, since, with the system not fully working, the protection of CMS cannot be guaranteed. All hardware incidents, which may or may not have resulted in a beam dump, are summarized below.

Tunnel card failure A spontaneous reset of a tunnel card happened with two tunnel cards, where in total 3 beam dumps were asserted. The cards function correctly after the incident and so the first time the card was not deactivated, causing a second beam dump a day later. The second tunnel card with the same symptomatic problem was immediately replaced. The reason for this spontaneous reset is not fully understood and the error could not be recreated in the lab. A single event upset (SEU) could have been the reason, possibly related to the MOSFET reset transistor. This hypothesis is supported by the fact that this type of reset never happened with the LHC BLM system, where the MOSFET is not used.

Low voltage power supply One LV power supply module in the CAEN power supply was damaged and slowly went into under-voltage. This resulted in the tunnel cards losing their power and shutting down, which resulted in a beam dump. Due to a change in the firmware of the DAB cards, it was not possible at first to deactivate the affected channel in the abort

and a beam dump was caused twice over two days. Eventually the affected channels were deactivated in the abort until the LV module could be replaced.

HV power supply A HV power supply module developed a fault. The HV was still being provided but the internal monitoring electronics was not functioning. It did not result in a beam dump since the presence of the HV is not a condition for the beam permit. The damaged module was immediately replaced.

HV missing In one incident, the HV of BCM2 was not switched on due to a human error. No beam dump was asserted. The missing HV was spotted a few hours into the fill and immediately reactivated. It would be desirable to have a hard-wired check for the presence of the HV and dump the beam if the HV would be missing. Technically there is no easy solution with enough flexibility needed to configure the correct channels and HV levels, hence it is not yet available.

Diamond / Signal In a spurious event the current measured in one BCM1L channel increased suddenly by a large amount. The beam was dumped properly once the current reached the abort threshold. The event is not fully understood. Shortly before, a failure of the BCM1F channel at the same location was observed. It is likely that this error was caused by the BCM1F module and affected the BCM1L channel since both detectors share some parts of the electronics. With the upgrade of BCM1F in long shutdown 1, the BCM1L will be more decoupled, making such events less likely.

S1 cabling The cabling of the BCML electronics in the service cavern is quite exposed. Accidentally a cable, responsible to give the timing impulse to read out the data was damaged and no monitoring data was available. The cable was replaced as soon as the error was spotted. Only the monitoring readout was affected and the beam abort system was still fully functioning, hence no beam abort was asserted. Several cables running in front of this rack are beam abort sensitive. If such a cable would become damaged, the beams would be dumped. A safe handling of this rack is very important, especially during beam time.

Chapter 5.

A selection of beam condition measurements using BCML.

Although the BCML systems main purpose is the protection and the automatic beam abort, it has unique features that make it also interesting as a monitoring device. While most of the measured signal is due to collision products there is also a component of signal from machine induced background. To first order the signal measured in the BCM detectors is linear with collision rates, or luminosity. The measurement of this would be of interest, but unfortunately the requirements for a relevant luminosity measurement are higher than what the BCM system can provide. The measurement of particle rates from machine induced background is also of interest. Here a precise measurement is not really necessary, but rather a confirmation of proper running conditions is needed. Due to much lower rates of machine induced background compared to luminosity a measurement is quite difficult. In case of increased background rates, representing poor LHC conditions, a good measurement is possible, since in this case the signals are significant. This chapter will give an overview of the possibilities for online monitoring with the BCML system.

5.1. Typical measurements during LHC operation

During a typical LHC fill the proton or ion beams are brought into collisions. The immediate instantaneous luminosity, the maximum value for this fill, depends on the beam intensity and beam optics. The beam intensity is usually low in the beginning of a year and then ramped up by increasing the number of bunches and the bunch charge. Also the β^* value can be decreased to obtain a higher instantaneous luminosity. Even at the same beam configuration the luminosity can vary due to differences in emittance. While the fill progresses the beam quality deteriorates. The intensity decreases due to beam losses and luminosity burn off and the emittance increases due to collective effects. This leads to a decrease in luminosity and the fill is dumped by the operator when the luminosity is decreased to about 50% of its maximum value. The instantaneous luminosity and the measured detector currents of the BCML detectors is shown in figure 5.1 for a typical LHC fill, where fill number 2624 was chosen as an example. The signal of all BCM2 inner and all BCM1L channels are averaged. The signals measured at the different detector locations vary due to the different flux of charged particles. Also the radiation damage the detectors have received, and hence the signal output, is different. A comprehensive analysis of the signal output level is given in chapter 7. The signal of the BCML detectors is generated almost entirely by collision products, hence it is proportional to the luminosity, and the BCML signals decrease with time due to decrease in luminosity. In the logarithmically plotted signals (figure 5.1(b)) one can observe a small increase in signal before the beams are brought into collisions and high signals are measured. These readings are due to machine induced background. By comparing

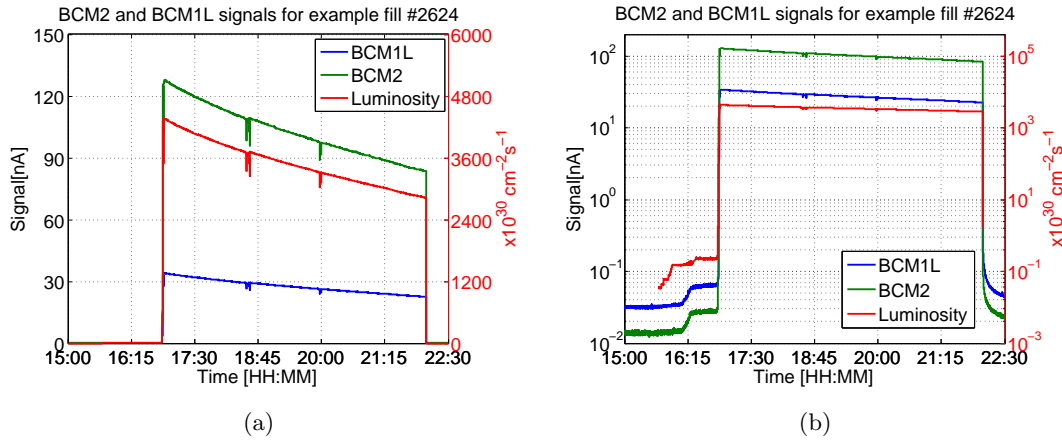


Figure 5.1.: Signal of BCM2 and BCM1L detectors during an example fill (fill #2624) and the Luminosity for this fill measured by the HF detector. Figure (b) shows the same data on a logarithmic scale.

the detector readings before and after the beams are brought into collision one can see that the signals due to machine induced background are several orders of magnitude lower than the signal due to collision products.

Machine induced background particles come from three different types of beam losses:

1. **Inelastic beam gas:** Beam particles interact inelastically with residual atoms inside the vacuum chamber. These interactions produce particle showers in CMS if they originate somewhere in the long straight section, and even up to the arcs.
2. **Elastic beam gas:** Beam particles scatter elastically with residual gas. The scattered beam particles interact with the TCTs at IP5 as this is the aperture limitation at CMS. The particle shower due to elastically scattered beam particles is therefore localized at one point.
3. **Beam halo:** Beam halo particles are beam particles with a high transversal momentum. They are usually caught by the betatron cleaning, but some particles might escape the system and can hit the TCTs at IP5 producing particle showers inside CMS.

A different source of background is the collision induced background. This type of background refers to a flux of particles which are secondary particles of collision products, but not wanted in the detector. These can be for example out-of-time hits due to short term activation or albedo neutrons. Hits in the muon chambers due to particles scattered around in the experimental cavern can be classified as collision induced background. This type of background is usually proportional to luminosity. Activation can build up and increased signals could be measured at later moments of a fill, hence be a non linear effect with luminosity. Due to the long integration time of $40 \mu\text{s}$ of the shortest integration duration of the BCML electronics the signals from direct collision products and collision induced background cannot be separated. An evidence for increased signals due to activation towards the end of a fill could not be measured, since the non linearities with particle rate in the BCM detectors are much more significant (see chapter 7.6).

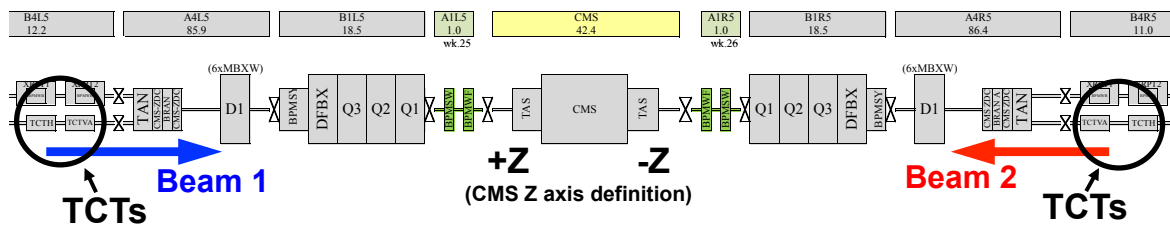


Figure 5.2.: Location of the tertiary collimators (TCT) in the long straight section (LSS) at IR5. The TCTs are 147.5 m away from the interaction point on the incoming beam line.

5.2. Long beam loss events

A beam loss event is considered as “long” if it lasts longer than 1 s. The signal measured of this event can easily be plotted as function of time. A running sum should be chosen, which is significantly shorter than the event, in order not to smear out the shape of the event.

5.2.1. Collimator scan 2011

During the machine commissioning in 2011 a collimator scan with the tertiary collimators (TCT), located ± 147.5 m away from IP5, was performed. Figure 5.3 shows the definition of the beam orientation with the CMS Z axis. Beam 1 enters CMS on the positive end (+Z), and Beam 2 enters CMS from the negative end (-Z). The collimators are moved step by step closer to the beam and the beam losses are measured. When the beam losses are high the collimators scrape the beam and the relative position of the collimator towards the beam axis is known. The beam losses produced in the collimator scan last several minutes. Since the TCTs are the last collimators before CMS the beam losses produced there generate strong particle showers inside CMS. Beam losses produced there pose the biggest threat for CMS. Beam losses originating further upstream from the TCTs are highly suppressed by the shielding provided by the TCTs.

In figure 5.3 the signals from BCM1L and BCM2, averaged over one side, as well as the positions of the collimators for this collimator scan is plotted. A high value of the collimator position means the collimator is open, as the collimators are moved in the position value decreases. When the collimator scrapes the beam signals are clearly seen in BCM2 and BCM1L. BCM1L detects about the same signal on +Z and on -Z if the collimators are moved on either side. This is as expected, since there is no significant material between the +Z and -Z positions of BCM1L that could absorb particles or produce new secondary particles. BCM2 detects signals almost only downstream (on the opposite end of where the event happened). On the upstream side the beam pipe geometry does not create strong particle showers in the BCM2 inner location and the measured signal is very low. On the downstream side an electromagnetic particle shower can develop in front of the BCM2 detectors and produce high signals. This behavior is expected from FLUKA simulations of machine induced background [Mül11]. There was no correlation in signals from horizontal or vertical detectors with respect to horizontal or vertical collimator movement found. The detected particle shower develops horizontally and vertically, and hence signals are always measured in every detector aligned around the beam pipe.

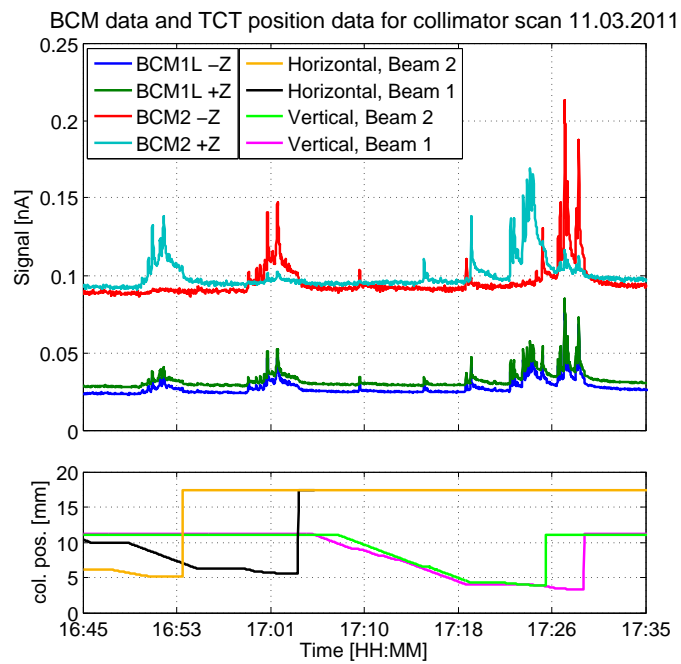


Figure 5.3.: During this collimator scan the TCTs were moved in until they scraped the beam. The lower plot shows the position of the TCTs. The upper plot shows the BCM1L and BCM2 data averaged over one side. When the TCT scrapes the beam the BCM detectors measure beam losses. BCM1L +Z and -Z measures the same for beam 1 and beam 2. BCM2 measures a high signal downstream.

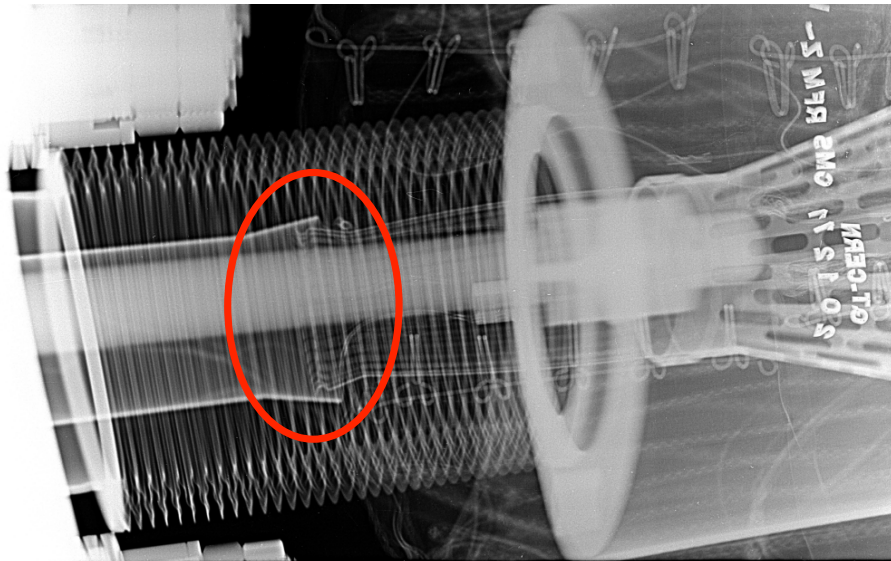
5.2.2. High vacuum beam loss events.

If the vacuum inside the beam pipe at IP5 is worse than normal values, an increased number of collisions of beam particles with residual gas particles occur. Secondary particles hit the beam pipe and surrounding heavy material and produce particle showers inside CMS. Background events related to vacuum usually last several minutes, until the vacuum system was able to restore nominal operating conditions.

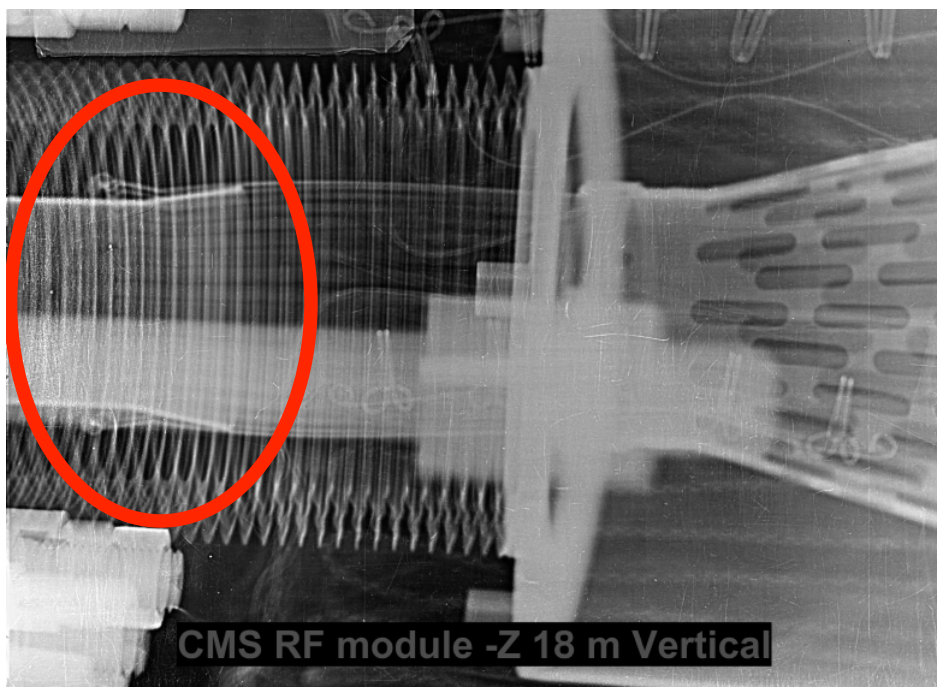
Events of bad vacuum happened several times during 2010 and 2011 at CMS. At 18.3 m away from the interaction point on the right end of CMS is an interconnect of beam pipes. The electrical connection between the different parts of the beam pipe is provided by RF fingers, small metal stripes attached to one beam pipe pushed over the other. Instead of being on the outside of the beam pipe they were pushed inside providing only a bad electrical contact. An X-ray picture taken from this connections is shown in figure 5.4(a). With higher beam currents the image current in the beam pipe also increases. Above a certain beam intensity the connection sparked which leads to the emission of large number of electrons. Beam particles interacted with this electron cloud, resulting in high beam losses. The electrical connection was repaired in the beginning of 2012, as seen on the X-ray picture (figure 5.4(b)). The fingers are now correctly placed outside of the beam pipe.

The first observed event with bad vacuum was during fill 1440 (25th OCT 2010), see figure 5.5. BCM1L was included into the system only on 2011, but at this moment the USB test readout (see chapter 4.2.4) was connected to the BCM1L diamonds and hence BCM1L data is available. Figure 5.5 shows the BCML data for this fill together with the vacuum pressure close to CMS. The measured signal increases significantly during the time of high vacuum pressure. The vacuum pressure increases and decreases fast resulting in a structure of spikes lasting several seconds. The electron cloud produced by sparks get reabsorbed within seconds. The spikes can also be observed in the signal of the BCM detectors. Unfortunately the BCM1L readout had some data loss and not all spikes are recorded for BCM1L.

During 2011 many fills had bad vacuum around 18.3 m on the right end of CMS, especially at high beam intensities. The RF-fingers were repaired in the beginning of 2012 and since then no vacuum problems have been observed close to CMS. The most severe event happened in fill 2208 on the 13th Oct 2011, around 1:08 am. The vacuum reached a pressure of 6.8×10^{-6} mbar. Figure 5.6(a) shows the data of BCM2 together with the offline luminosity for this fill. In BCM1L the measured signal was about five times higher than the luminosity. The beam was not dumped since the high spike was not long enough to reach high values in running sum 12. About 50% of the abort level was reached. If the beam intensity would have been at nominal level a beam dump would have occurred. Figure 5.6(b) shows a zoom in on the high peak of the event together with the vacuum pressure at 18.3 m on the right end of CMS. The signal shape of the BCML detectors is the same as the shape of the vacuum pressure. Before a background event creates dangerous levels of particle fluences the data taking efficiency of CMS is reduced. Background particles traverse the pixel detector in parallel to the detector plane and create huge number of hits. These so called PKAM events have a very long readout time. This creates a very long dead time for CMS. Figure 5.6 shows the data taking efficiency for fill 2208. During the high spike of background the data taking efficiency was reduced to almost zero. From experience in 2011 the data taking efficiency is affected when the pressure increases above 10^{-8} mbar.



(a) The RF fingers should be outside the beam pipe for a proper electrical connection of the beam pipe elements. Either due to mistakes during installation or due to underestimated thermal expansion the RF fingers were pulled back too far and moved inside the beam pipe when the two beam pipe elements were pushed back together. The proper electrical connection was not guaranteed and at a high image current through the beam pipe sparks occurred, which degraded the vacuum. This led to very high beam losses.



(b) After repair the RF fingers are correctly placed around the adjoining beam pipe.

Figure 5.4.: X-ray pictures of the RF fingers at beam pipe connection at 18.3 m away from the IP at CMS before and after repair.

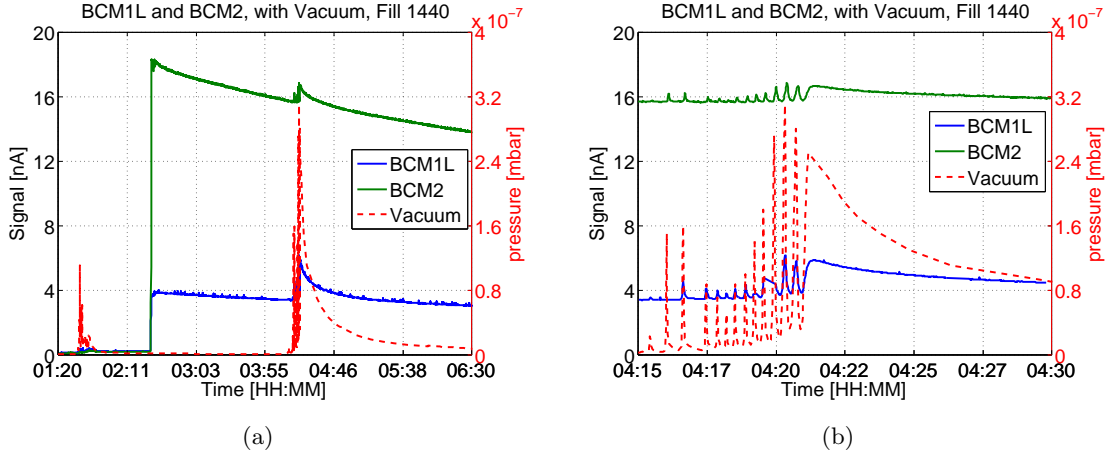


Figure 5.5.: Signal measured in BCM2 and BCM1L for fill 1440, together with the vacuum pressure measured 18.3m on the -Z end of CMS. The vacuum suddenly degraded creating an increased amount of beam gas background. An increase in signal was measured in the BCM detectors.

5.2.3. Background calculations from BCM2 and BCM1L

In order to discriminate the small signal of machine induced background one can make use of two detectors with different sensitivities towards collision rates. The signal in the BCM detectors during collisions is the sum of the signal coming from collision products and the signal due to machine induced background. The sensitivities of BCM1L and BCM2 towards those components are different. BCM2 measures about 6 times higher value from collisions than BCM1L, while the background signal is roughly the same. The different sensitivities are parameterized as:

$$S_{BCM1L} = S_{background} + S_{collisions} \quad (5.1)$$

$$S_{BCM2} = S_{background} \cdot c_b + S_{collisions} \cdot c_p \quad (5.2)$$

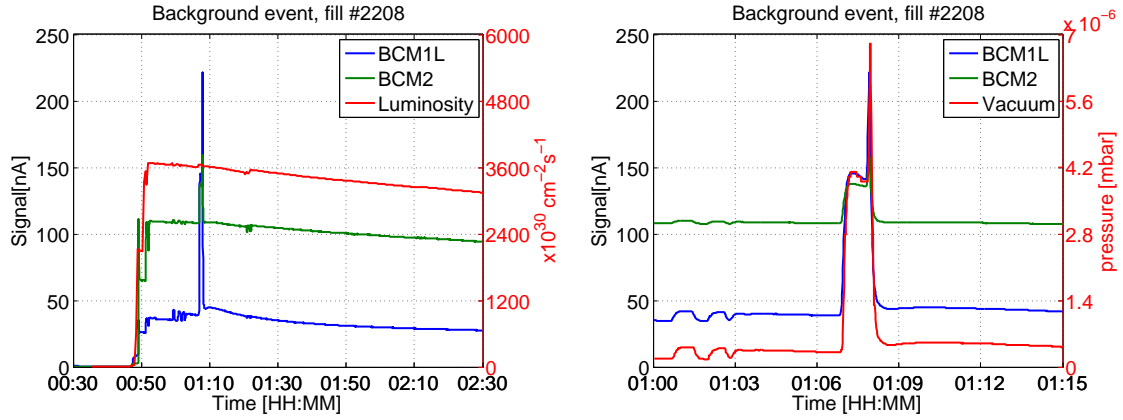
S_{BCM1L} and S_{BCM2} are the signals measured with each detector. $S_{background}$ and $S_{collisions}$ are the components of the BCM1L signal arising from collision products and machine induced background. c_b is the sensitivity of BCM2 towards background and c_p the relative sensitivity towards collision signals relative to the sensitivities of BCM1L. Equations 5.1 and 5.2 can be solved for the background and the collision signal separately:

$$S_{background} = \frac{S_{BCM2} - S_{BCM1L} \cdot c_p}{c_b - c_p} \quad (5.3)$$

$$S_{collisions} = \frac{S_{BCM2} - S_{BCM1L} \cdot c_b}{c_p - c_b} \quad (5.4)$$

This way the machine induced background, and the collision rates, can be directly calculated from the signals of BCM1L and BCM2 if the relative sensitivities are known. For a good separation of the signal components c_b and c_p should be different. If they are the same, both signals have the same shape and a separation of signal components is not possible.

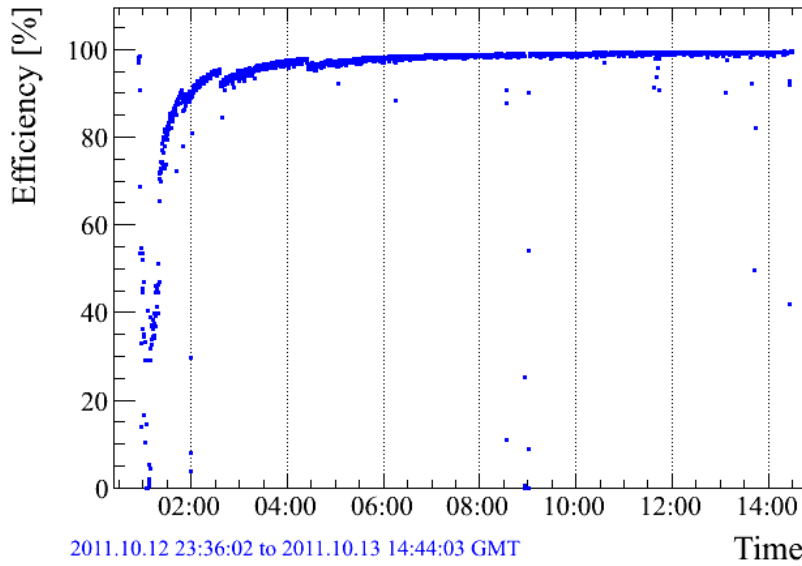
The calculated signal components are in the units of the detector measurement. In case of the BCM1L detector the detector current can be converted to the actual flux of MIP particles.



(a) BCM2 and BCM1L signals together with luminosity

(b) Zoom in to spike event. BCM2 and BCML signals together with vacuum pressure

Fill 2208 Datataking Efficiency



(c) Data taking efficiency of CMS during the bad vacuum event. The plot is taken from official CMS web based monitoring.

Figure 5.6.: Measurements during the worst vacuum pressure observed so far close to CMS during operation. The pressure in fill 2208 spiked up to 6.8×10^{-6} mbar. Figure (a) shows the BCM2 and BCM1L data for this fill together with the instantaneous luminosity. Figure (b) shows a zoom in to the spike of the data together with the vacuum pressure at 18.3 m on the right end of CMS. During the highest values of the beam background the CMS data taking efficiency was decreased to almost zero as seen in figure 5.6(c).

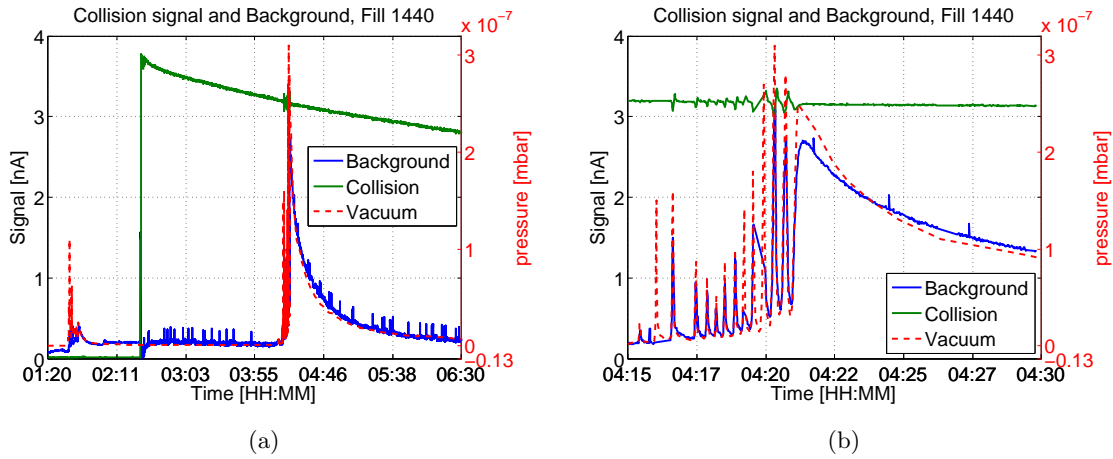


Figure 5.7.: From the BCM2 and BCM1L data of the vacuum bump event in fill 1440 the background and collision signals were calculated using equations 5.3 and 5.4. The axis of the vacuum pressure is moved so the pressure curve matches the background signal. Figure (b) shows a zoom in to the time of the vacuum spikes. There is a clear correlation between background signal and vacuum pressure. The collision signal shows no increase during high vacuum.

Figure 5.7 shows the background calculation for fill 1440 which had an event of bad vacuum and hence high beam background, described already in section 5.2.2. The calibration coefficients used for this calculation are $c_b = 0.465$ and $c_p = 4.88$. The calculated collisions signal shows only the normal decrease luminosity signal without contamination of background. The background signal tracks shape of the pressure curve. Some vacuum spikes are not visible in the background data due to missing data points.

For CMS the primary detector for determining the machine induced background rates is the BCM1F detector, but this method of extracting background rates from BCML provides an additional measurement. This method can be applied to any set of two detectors, which are placed at different locations and hence have a different response to collision products and background. Unfortunately due to radiation damage (see chapter 7) a constant recalibrating was necessary and the results were not fully reliable. If radiation stability problems are solved in the future this method could be used more reliably.

5.3. Short beam loss events

A beam loss can have a wide range of duration. The readout frequency of the beam monitoring detectors is 1 s. The BCM2/1L system can exploit the different running sums (see chapter 4.2.4) to analyze the timing structure of a beam loss event with a duration shorter than 1s. A very common type of short beam loss event at the LHC has a duration of the order of 1 ms. These events are commonly referred to as UFOs (unknown falling objects) [Bae11]. Although the origin could never be proven distinctively it is believed that dust particles, dropping from the inside wall of the vacuum chamber, fall into the beam and become evaporated. These events happen several times per fill around the LHC. Many times the beam loss event was large enough to trigger a beam dump. The abort thresholds of the LHC BLM systems were increased to avoid too many beam dumps due to UFOs[Neb11]. A plot showing

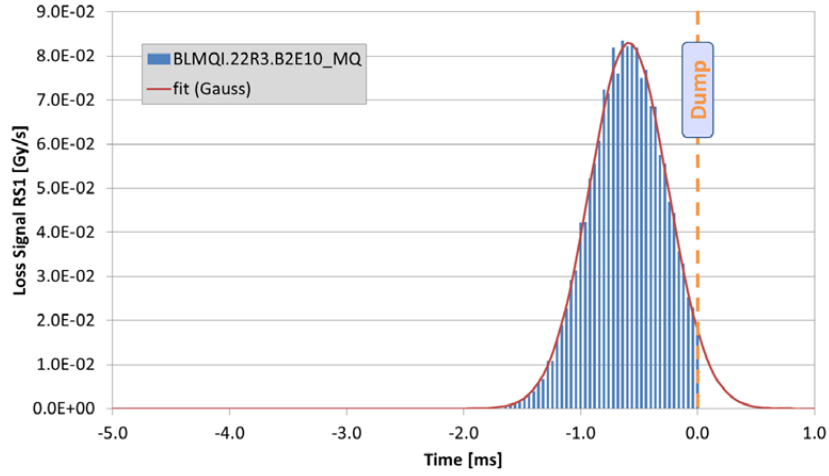


Figure 5.8.: Profile of an example UFO event measured with the LHC BLM system. The beam was dumped on running sum 5. Therefore the post mortem data was available and this profile based on the $40 \mu\text{s}$ data could be shown. The event has the typical gaussian shape of a UFO. [Bae11]

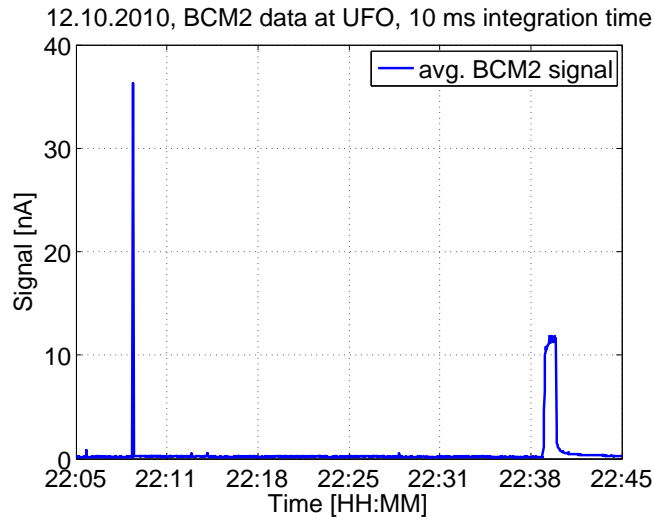


Figure 5.9.: The average running sum 6 signal of all BCM2 inner channels round the UFO event. The strong signal of the UFO is seen as one single spike. Since the LHC was in squeeze mode at this moment there was no significant signal due to collisions. The fill was dumped shortly after the beams were brought into collisions due to reasons unrelated to the UFO.

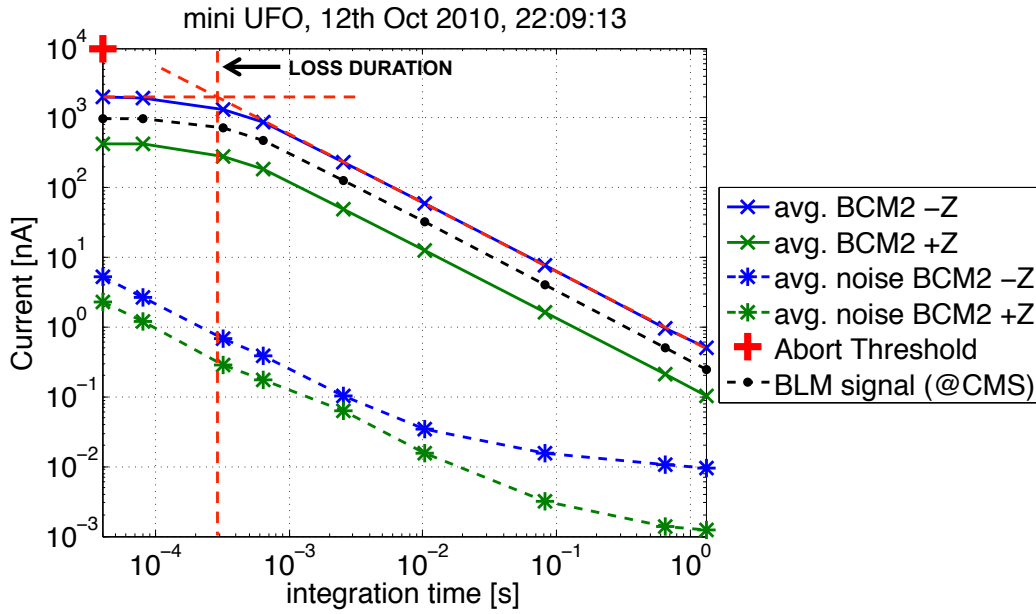


Figure 5.10.: The BCM2 data of different integration times between $40 \mu\text{s}$ and 1.2 s for the second the UFO occurred on 12th October 2010 at 22:09:13. The signal from the diamonds on the +Z and the -Z end are averaged. A BLM detector close to CMS is also plotted. When the integration time gets longer than the event the measured values go down. This way a rough timescale of the event can be determined, in this case $\sim 0.3 \text{ ms}$.

such an event, as measured with the BLMs of the LHC, can be found in figure 5.8. The shown event triggered a beam abort and hence post mortem data was available to analyze the exact beam shape. The event shows the typical gaussian shape of UFOs. Several times an LHC experiment triggered a beam dump due to a UFO event close to the experiment. In CMS this has never happened. Only three significant UFOs were found at CMS during 2011 and 2012, they were all below the threshold for a beam abort. The first event happened on 12th Oct 2010 at 22:09:13. The average running sum 6 signal ($\sim 10 \text{ ms}$ integration time) is shown in figure 5.9. The UFO is shorter than one readout second and shows up as one single spike. This UFO happened while the LHC was in squeeze mode. The plot also shows higher signals about 30 minutes later, when the beams were brought into collisions. This fill was dumped shortly after due to reasons unrelated to the UFO.

Timing calculation: Since the UFOs have not triggered a beam dump no post mortem data is available. The running sum information can be used to analyze the timing structure of the event. The readout of BCM2, as explained in chapter 4.2.4, gives the maximum value found in one readout second. This is true for all integration time windows (running sums). A significant UFO exceeds the usual data in all running sum and the data obtained for the readout second of the event belongs to the UFO. The signal of all running sums of the readout second where a UFO happened is plotted in fig. 5.10 as a function of the integration time. This shape of signal as function of running sum is typical for a UFO.

A precise calculation of the duration of the UFO can be done the following way:

1. If the integration time is larger than the beam loss event the total charge Q of the event

is deposited within this time window and hence independent of the integration time. The current I as function of the integration time t is then given by:

$$I(t) = \frac{Q}{t} \quad (5.5)$$

This hyperbolic relation visualized in a double logarithmic plot as a linear decrease, as seen in figure 5.10 above an integration time of 1 ms. By fitting equation 5.5 to the data points above 1 ms the total charge Q of the event is obtained.

2. If the pulse is significantly longer than $40 \mu\text{s}$ one can assume that the current does not change much within these $40 \mu\text{s}$. The current measured in running sum 1 ($40 \mu\text{s}$ integration) is then a measurement of the height of the pulse.
3. As shown in figure 5.8, UFOs are shaped gaussian. The function of the gaussian shape is:

$$I(t) = \frac{Q}{\sqrt{2\pi\sigma^2}} e^{-\frac{(t-t_0)^2}{2\sigma^2}}, \quad (5.6)$$

where t_0 is the time of the maximum and σ^2 the variance. For the current at $t = t_0$, which is the current measured in running sum 1 (I_{RS1}), we get:

$$I(t_0) = I_{RS1} = \frac{Q}{\sqrt{2\pi\sigma^2}} \quad (5.7)$$

4. The FWHM of the gaussian curve can be calculated by solving equation 5.7 for σ :

$$FWHM = \sigma \times 2\sqrt{2\ln 2} = \frac{Q}{I_{RS1}} \times \frac{2\sqrt{2\ln 2}}{\sqrt{2\pi}} = \frac{Q}{I_{RS1}} \times 0.9394 \quad (5.8)$$

Table 5.1 shows the results for the timing analysis for each BCM2 inner channel. The average measured duration (FWHM) is $278 \mu\text{s}$, which is roughly three turns. The highest signal was measured in BCM2 -Z inner top, where running sum 1 reached $2.54 \mu\text{A}$ which is about 25 % of the beam abort threshold. The number of equivalent MIP particles traversing the detector during the event can be calculated from the deposited charge, assuming $200 \mu\text{m}$ CCD and 36 e/h-pairs per μm :

$$\#MIPS = \frac{Q}{1.602 \times 10^{-19} \frac{\text{C}}{\text{e/h-pair}} \times 36 \frac{\text{e/h-pair}}{\mu\text{m}} \times 200 \mu\text{m}} \quad (5.9)$$

From table 5.1 the average number of MIPS measured was 315733, with a maximum value measured of 661307 MIPS.

Location of the UFO: Figure 5.11 shows the signal of the BLM detectors around CMS during the UFO event. Signals were measured on both sides of CMS mostly on beam 1. It is likely that the UFO happened around the Triplet left of IP5 (+Z end of CMS) on beam 1 which points towards CMS. This is consistent with the fact that BCM2 measured a higher signal on the -Z end, downstream of the UFO. The BCM2 detectors downstream of a beam loss event usually measure a higher signal since the particle showers are stronger.

BCM2 detector	Q [fC]	I_{RS1} [μ A]	$FWHM$ [μ s]	MIPs per event
-Z inner top	763	2.54	282	661307
-Z inner far	648	2.24	272	562032
-Z inner near	549	1.78	290	475908
-Z inner bottom	444	1.44	289	384846
+Z inner near	85	0.3	267	73396
+Z inner top	87	0.3	274	75238
+Z inner far	182	0.64	267	157721
+Z inner bottom	155	0.52	282	134623

Table 5.1.: Properties of measured signals during UFO event on 12th Oct 2010 at 22:09:13.

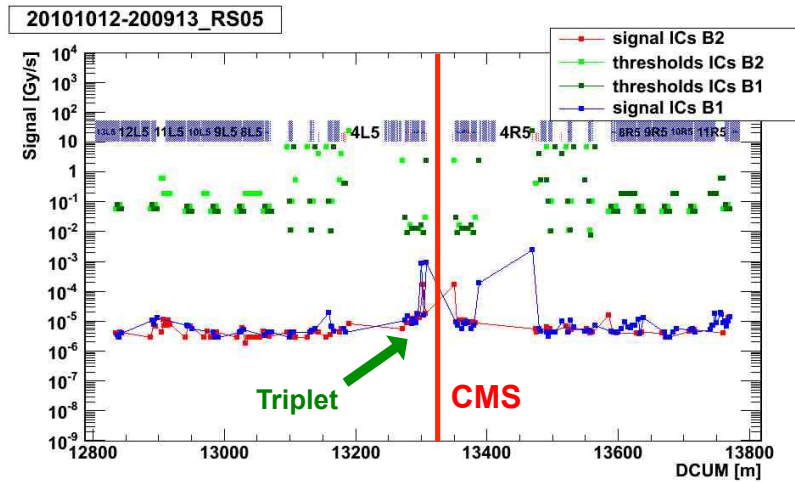


Figure 5.11.: The running sum 5 signal of the beam loss monitors of the LHC at the second of the UFO. High signals were measured on both ends of of CMS, mostly on the beam 1 side. It is likely the UFO happened on beam 1 on the left hand side of CMS at the Triplet. The particle shower propagated through CMS, which is consistent with the fact that BCM 2 signals were higher on the -Z end, which is on the right hand side of CMS.

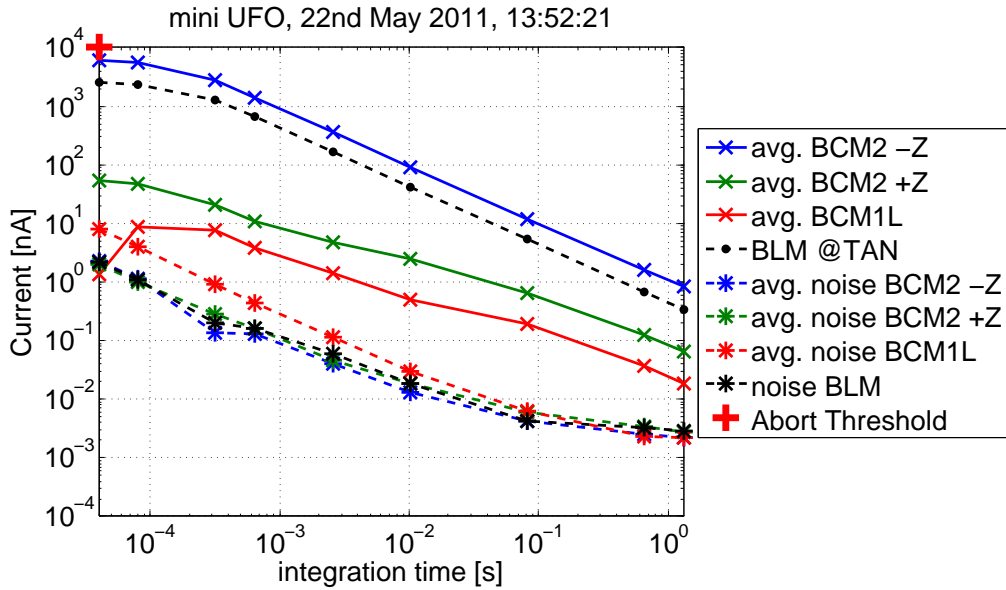


Figure 5.12.: The BCM2 data of different integration times between $40 \mu\text{s}$ and 1.2s for the second the UFO occurred on 22nd May 2011 at 13:52:21. The signal from the diamonds on the +Z and the -Z end are averaged. A BLM detector located at the TAN on the -Z end shows the same timing structure. The signal measured in BCM1L and BCM2 +Z are small and do not show the same timing structure as the BCM2 on -Z. It is likely that they have not been in the direct particle shower of the UFO.

Other UFOs: Two additional UFO events with significant signal were found. It is likely that more events happened, but, as there is no automated monitoring, only if someone spots an unusual spike on the online displays UFO events are discovered.

Figure 5.12 shows the measured signal of the UFO event on 22nd May 2011 at 13:52:21, and table 5.2 the results of the timing calculation. The highest signal reached 93% of the abort threshold, measured in BCM2 -Z inner top. The BCML and the BCM2 +Z detectors had a significantly lower signal. These detectors measured also a signal component with longer duration as seen by the shoulder at about 10 ms in the timing plot (figure 5.12). Only the signals from BCMLs on -Z were significant enough for a proper timing analysis. This UFO was shorter than the first with one. The measured duration (FWHM) of the event was $143 \mu\text{s}$.

Figure 5.13 shows the measured signal of the UFO event on 18th April 2012 at 09:39:47, and table 5.3 the results of the timing calculation. The UFO timing structure was measured in all BCML detectors with an average event duration of $437 \mu\text{s}$. The highest signal reached 18% of the abort threshold, measured with BCM1L. The presented data was not corrected for radiation damage and the actual MIP flux was likely significantly higher than measured, especially in BCM2 -Z.

BCM2 detector	Q [fC]	I_{RS1} [μ A]	$FWHM$ [μ s]	MIPs per event
-Z inner top	1381	9.33	139	1197096
-Z inner far	742	4.97	140	643359
-Z inner near	825	5.3	146	715240
-Z inner bottom	701	4.48	147	607781

Table 5.2.: Properties of measured signals during the UFO event on 22nd May 2011 at 13:52:21.

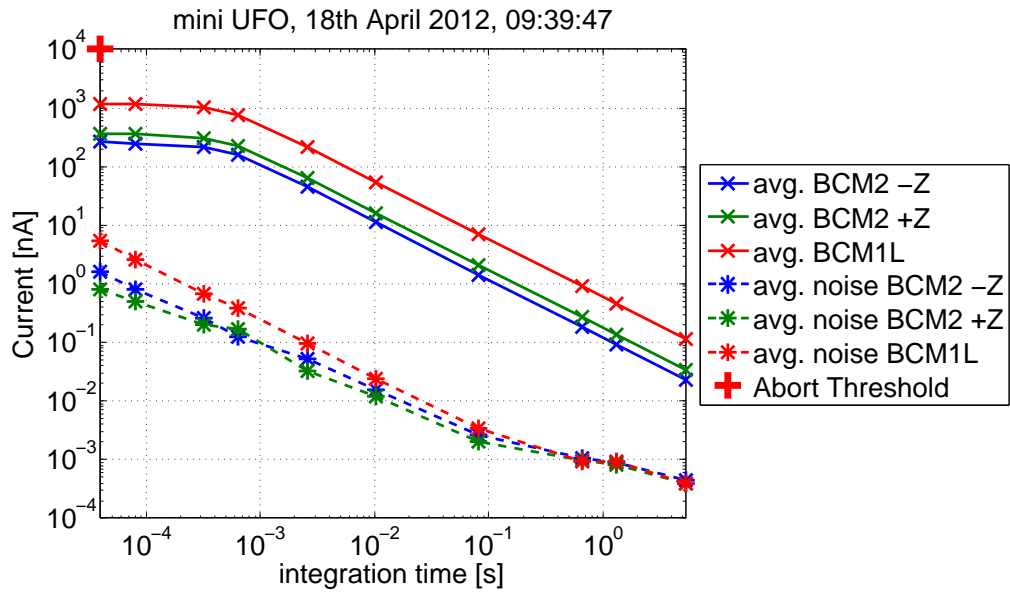


Figure 5.13.: The BCM2 data of different integration times between 40 μ s and 1.2s for the second the UFO occurred on 18th April 2012 at 09:39:47. The UFO timing structure is visible in all BCML detectors.

Detector	Q [fC]	I_{RS1} [μ A]	$FWHM$ [μ s]	MIPs per event
BCM1L -Z far	543	1.16	439	470512
BCM1L -Z up	589	1.21	456	510467
BCM1L -Z near	421	0.93	426	365158
BCM1L -Z down	446	0.95	443	386468
BCM1L +Z far	816	1.66	461	707839
BCM1L +Z up	334	0.68	461	289592
BCM1L +Z near	407	0.84	456	353062
BCM1L +Z down	864	1.8	451	749442
BCM2 -Z inner top	159	0.38	391	137480
BCM2 -Z inner far	113	0.28	383	98170
BCM2 -Z inner near	95	0.2	447	82398
BCM2 -Z inner bottom	93	0.19	447	80278
BCM2 +Z inner near	95	0.2	444	82119
BCM2 +Z inner top	118	0.26	430	102610
BCM2 +Z inner far	242	0.53	432	210222
BCM2 +Z inner bottom	207	0.46	424	179360

Table 5.3.: Properties of measured signals during the UFO event on 18th April 2012 at 09:39:47. The UFO signal was measured in all BCML channels. The measured duration (FWHM) of the event was 437 μ s on average. BCM1L measured the highest signal reaching 18% of the abort threshold. It is likely that the actual MIP flux was higher since the detectors had already experience radiation damage at the time of the UFO event.

Chapter 6.

Monte Carlo simulations with FLUKA

For a physics experiment like CMS the understanding of the radiation environment is of great interest: It is necessary for the evaluation of the detector performance, effectiveness of shielding or to assess radiation damage. Monte Carlo simulations have been done for CMS with various simulation tools. FLUKA[Bat06, Fer05] is one of these tools used to understand the particle rates inside CMS and in the whole experimental cavern.

FLUKA offers the possibility to predict radiation damage to semi-conductor detectors. The number of dislocations created in the material can directly be calculated. The number of dislocations cannot directly predict the performance of a detector. But the damage potential of any radiation environment can be scaled to the damage potential of any particle type and energy. With this scaling, the results from irradiation tests can be converted to the expected effects of the particle environment in CMS.

The main purpose of the work in this chapter is to compute the radiation environment at the BCML detectors for the CMS running conditions of 2011 and 2012. In particular the expected detector signal was estimated and the radiation damage to the BCML detector was predicted. Nevertheless a thorough explanation of the FLUKA simulations of CMS and some of its applications is given.

6.1. Introduction to FLUKA

FLUKA is a particle physics simulation toolkit. In FLUKA single events are simulated, initiated by a primary particle or collision-event. In case of the CMS simulation a proton-proton collision is used as primary event. All particles are transported until they are destroyed or fall under a predefined cutoff. Typically it is not used for the purpose of recording single events and studying the tracing of single particles. The output is usually averaged over all simulated primary events and normalized per primary event.

6.1.1. Combinatorial Geometry

A FLUKA geometry is created by mathematically combining basic geometric shapes. These shapes are called bodies and they can be finite objects such as spheres, boxes, cones, etc. or infinite elements such as planes or infinite cylinders. Bodies are combined using a + and a - operator to form a complex element, the so called region. The + operator acts like an AND, the region of two bodies connected by a + consists out of the space which is inside both bodies. The - operator subtracts the inside of the body from the rest, which is like the + operator, but the outside of the volume is used. The | operator is like an OR and its used to create one region out of several separate building blocks. Figure 6.1 visualizes how regions are formed.

There are limitations on the complexity of the geometries that can be created, as there are limitations on the number of elements that can be used. The computing time will also

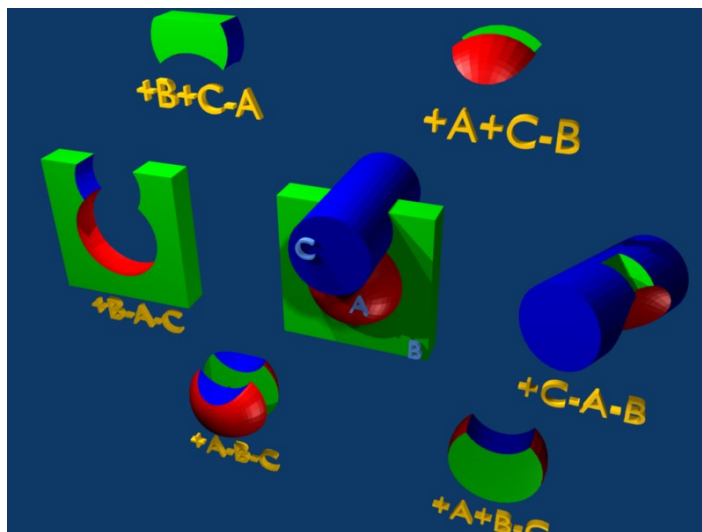


Figure 6.1.: Example of the combinatorial geometry in FLUKA using three bodies: A, B and C. Various regions are created by using the + and the - operator in different ways to combine the bodies. [FBC11]

increase with a higher number of geometry elements. Since overlapping regions or volumes without a defined region lead to a crash of FLUKA, it is also very difficult to create complex geometries that are bug free. FLUKA geometries are therefore always simplifications of the reality. It is important, that the correct material composition and the material densities are chosen so that the total weight is correct. The major elements have to be correctly included for calculations involving particle shower cascades. For activation studies, it is also important to include trace elements that have the potential to get highly activated.

Every region is assigned a material. Cut-off parameters and biasing can also be configured per region. Some scorings are region based and have to be connected to a certain region.

Lattice

A feature of the FLUKA geometry is the Lattice function. If a region is defined as lattice, instead of filling this region with a material, a piece of geometry, implemented at a different position, is copied to the lattice. This is defined by a transformation which can be both rotations and translations. In the simulation this is handled by shifting particles entering the lattice region via the defined transformation into the fully defined region. There the particle is transported, and finally moved back again via the transformation.

6.1.2. Event generator

As event generator DPMJET-III [Roe00] is used to create the primary proton-proton and lead-lead events. DPMJET also supports any nucleus-nucleus, hadron-nucleus and photon-nucleus interactions. It is directly linked into the FLUKA code and hence the default event generator for high energetic hadronic interactions in FLUKA. It is based on PHOJET 1.12, PYTHIA 6.115 and LEPTO 6.5.1.

6.1.3. Scoring

A scoring is a user-defined output of the simulation. A certain scoring routine is called when a particle matches the conditions for this scoring.

A concept that is used in many of the scorings routines is the so called track length estimation. In this case the path length of a particle passing through a scoring volume is recorded. The track length is normalized to the detector volume, resulting in a fluence value per unit area. This method is more suitable than e.g. counting particles, as it properly weights particles that have a steep angle, only scrape the detector volume, or get destroyed or created in the middle of the scoring volume.

Many different types of scoring routines, or so called ‘estimators’, are available in FLUKA, however only the ones that are used for this work are described:

- **USRBIN:** This is the most often used FLUKA estimator. The volume of interest is overlaid with a binning mesh that can be Cartesian, in cylindrical coordinates, or as a special case bound to a geometry region. This scoring is used to obtain particle fluences by calculating the track length density, or dose like values by scoring the energy deposition. Usually the obtained 3D data is projected to two dimensions and shown as a 2D flux map.
- **USRTRACK:** This estimator is a pure track length scoring, which is assigned to a certain region. The output is a differential fluence in energy, which makes this estimator useful for obtaining energy spectra. This estimator has to be assigned to a region and cannot be scored at an arbitrary location.

Scorings are configured with a generalized particle type. For fluence scorings this can be either a simple selection of the particle or particle group (such as charged hadrons, all neutral, etc.), which is scored, or a special unit of measure where every particle is weighted according to a predefined function (for example: ambient dose equivalent, 1 MeV neutron equivalent, etc.). Also “dose like” scorings are generalized particle types, which are for example: dose, energy deposition, non ionizing energy loss, etc.

6.1.4. Radiation damage estimators

Non Ionizing Energy Loss - NIEL

While ionizing energy loss is the dominant contribution of the energy deposition from charged particles, it does not lead to significant radiation damage in silicon or diamond detectors. The non-ionizing energy loss (NIEL) is associated with nuclear interactions, which causes lattice defects and hence radiation damage.

The stopping power $S = dE/dx$ of a material can be expressed as the sum of energy loss transferred to electrons (ionizing, S_i) and energy transferred to nuclei (non-ionizing, S_n):

$$S = S_n + S_i = \frac{dE_n}{dx} + \frac{dE_i}{dx}. \quad (6.1)$$

The Lindhard partition function $\xi(T)$, depending on the kinetic energy T , gives the fraction of the total stopping power $S(T)$ that goes into the non-ionizing part, which goes directly into the calculation of the NIEL:

$$\xi(T) = \frac{S_n}{S}. \quad (6.2)$$

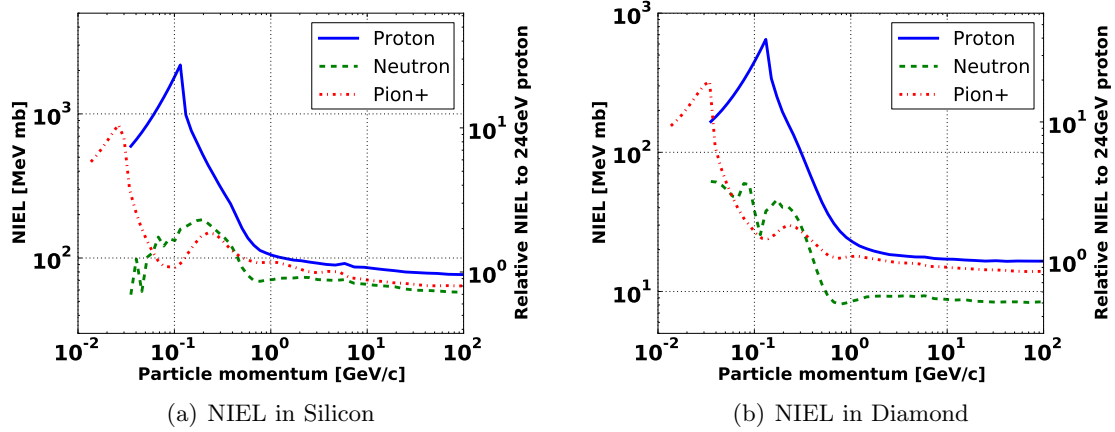


Figure 6.2.: Non Ionizing Energy Loss (NIEL) of various particles at different energies in a piece of silicon, and a piece of diamond. [Gut13]

The NIEL is usually expressed as stopping power in units of $keV\ cm^2/g$ or as NIEL cross section in units of $MeVmb$. In FLUKA the NIEL stopping power is not simulated, but rather the deposition of energy due to non-ionizing interactions in units of GeV . To convert to the NIEL cross-section in units of $MeVmb$ the following formula was used:

$$\sigma_{NIEL}[MeVmb] = \frac{NIEL[GeV] \cdot u[g/mol]}{d[cm] \cdot \rho[g/cm^3] \cdot N_A[mol^{-1}]} \cdot 10^3[MeV/GeV] \cdot 10^{27}[mb/cm^2], \quad (6.3)$$

where $NIEL$ is the FLUKA simulated number, u is the molar mass, N_A the Avogadro constant, d the thickness of the detector and ρ the density of the material.

A FLUKA simulation was performed where protons, neutrons and pions of kinetic energies between 1 MeV and 100 GeV are shot on a detector piece made of silicon or diamond at a size of $10 \times 10 \times 0.4\ mm^3$. The NIEL inside the detectors was scored and converted to a NIEL cross-section using equation 6.3. The results are shown in figure 6.2 [Gut13].

1 MeV neutron equivalent in silicon

The 1 MeV neutron equivalent in silicon (1 MeV-n-eq) is a measure of particle flux, where every particle is weighted by its NIEL cross-section in silicon relative the NIEL cross-section of a 1 MeV neutron in silicon, which is by definition 95 MeV mb. This gives the particle the weight of its potential to create radiation damage in a silicon detector. This definition 1 MeV-n-eq flux is implemented in FLUKA as generalized particle type, which makes the estimation of radiation damage to a silicon detector very easy, even if no silicon is implemented in the FLUKA geometry.

Displacements per Atom

Displacements per atom (DPA) is a direct measure for the radiation damage to a given material. It states how often, on average, an atom in the material was displaced due to impacting particles. For example a DPA of 10^{-22} means that one atom of a sample of 10^{22} atoms was displaced from its lattice site. The DPA value is directly related to the number of

created Frenkel pairs, which are crystallographic defects, where interstitial atoms are located near vacancies in the crystal lattice.

Compared to the NIEL as a measure of radiation damage, DPA is more accurate, since it does not count phonon interactions, but only the type of interactions causing a lattice defect. In addition DPA takes recombination of defects (Frenkel pairs) into account, so this study is considered to be an improvement to the previous NIEL study.

The DPA routine was recently added into version 2011.2 of FLUKA. A brief introduction of the implementation will be given here, so that the basic mechanisms and parameters are introduced. More detailed information can be found in [Fas10].

To calculate the number of Frenkel pairs, FLUKA uses the theory of Norget, Robinson and Torrens [Nor75]:

$$N_F = \kappa(T) \frac{\xi(T)T}{2E_{th}}, \quad (6.4)$$

where N_F is the number of Frenkel pairs, $\kappa(T)$ the displacement efficiency, T the kinetic energy of the primary knock on atom, $\xi(T)$ the Lindhard partition function and E_{th} the lattice displacement threshold energy. In the following paragraphs, a short explanation will be given on how FLUKA calculates these quantities.

Displacement efficiency $\kappa(T)$ This compensation factor takes several effects into account, such as forward scattering in the displacement cascade and the recombination of Frenkel pairs due to overlap of different branches in the collision cascades. The number of remaining defects has been approximated to fit molecular dynamics simulations.

Lattice displacement energy E_{th} This is the average displacement energy over all crystallographic directions, and measured with dedicated experiments or lattice simulations. For the studies presented here the threshold energy used for diamond is $E_{th} = 43.3$ eV, which is the average over all lattice directions from [Koi92]. Typical values for silicon are between 21 and 25 eV. In the simulation a value of 25 eV is used, which is the FLUKA default value for silicon. Apart from being a parameter for the number of generated Frenkel pairs, it is also a parameter for $\xi(T)$ where it sets the lower limit for the restricted energy loss.

The DPA values obtained in a simulated irradiation of a piece of diamond at a size of $10 \times 10 \times 0.4$ mm³ are shown in figure 6.3. Protons, neutrons and pions of kinetic energies between 1 MeV and 100 GeV are simulated. Also shown is a comparison with a piece of diamond of the size $10 \times 10 \times 0.001$ mm³. This is an unrealistic thickness for a detector, but it shows in the higher energetic regime a lower DPA. In the thicker piece secondary particles can create further displacements where as in the thin detector the secondaries escape. The curves of the charged particles kinks down at low energies since the particles are completely stopped by ionizing energy deposition. In the simulation of the 1 μ m thin detector even at lowest energies the particles are not completely stopped. [Gut13]

24 GeV proton equivalent in diamond

For silicon it is standard practice to convert a fluence by any particle to an equivalent fluence of 1 MeV neutrons using the NIEL scaling. This is more comprehensive than quoting a number of NIEL when quantifying the radiation damage to a silicon detector. FLUKA calculates the

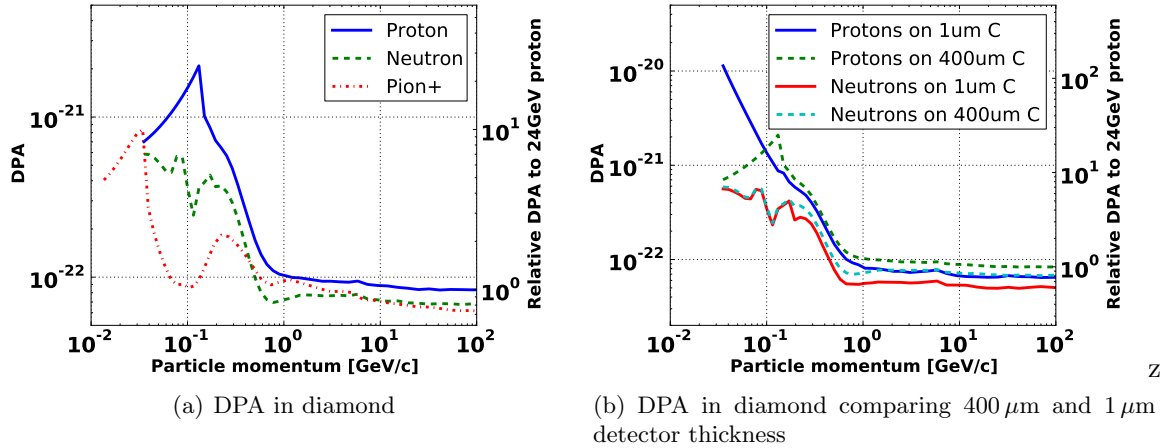


Figure 6.3.: Displacements per atom (DPA) of various particles at different energies in a piece of diamond. [Gut13]

1 MeV neutron equivalent directly since this is implemented as a generalized particle type (see section 6.1.3).

There is no such comprehensive flux equivalent scoring for diamond in FLUKA, but the DPA in a piece of diamond can be scored. The number of DPA is not intuitive and the calculation of a standardized equivalent flux is desirable. For diamond most experimental data is available for irradiations with 24 GeV protons. These are therefore chosen as the particle for the normalization. From the simulation of irradiation a DPA scaling number of $DPA_{norm} = 8.924 \times 10^{-23}$ per $\text{proton}_{24\text{GeV}}/\text{cm}^2$ was calculated. The 24 GeV proton equivalent flux is then calculated for any simulation, where the $DPA_{simulation}$ was scored in diamond:

$$Flux_{24\text{GeV}-p-eg} \left[\frac{24\text{ GeV protons}}{\text{cm}^2 \times s} \right] = \frac{DPA_{simulation} \left[\frac{1}{s} \right]}{DPA_{norm} \left[\frac{\text{cm}^2}{24\text{ GeV protons}} \right]}. \quad (6.5)$$

Here it is assumed that the $DPA_{simulation}$ result is normalized to a rate per second. This number can also be given as a total number of displacements resulting in a equivalent fluence in units of $[24\text{ GeV protons} / \text{cm}^2]$. This fluence will be called “24 GeV proton equivalent in diamond”, which will be referred to as 24 GeV-p-eg. This method of simulating the equivalent fluence will be used later in chapter 7 to compare the observed radiation damage in the BCM detectors to test beam irradiations.

6.2. The CMS FLUKA geometry

A FLUKA model describing the CMS geometry in a simplified way was first developed by Mika Huhtinen [Huh95]. Since then, several people made custom changes to study particular regions of interest. The newest publication of results with an updated geometry was done by Steffen Müller [Mül11].

Since the last publication of data, several details to the geometry have been updated to improve the data quality at specific locations. Especially to improve the radiation environment at the BCML locations several things have been modified. The modified parts are described in this section together with a general overview of the features of the CMS geometry.

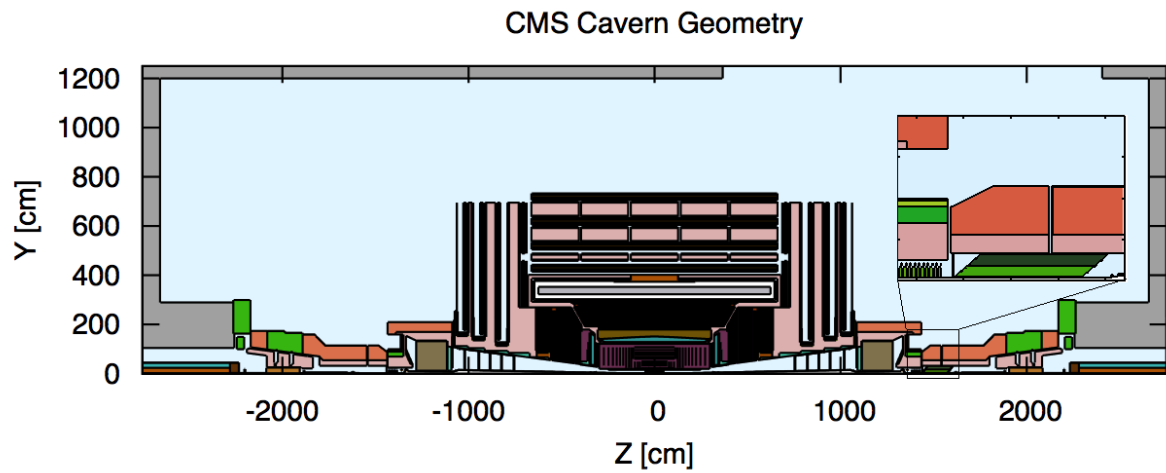


Figure 6.4.: FLUKA geometry of the CMS detector including a zoom in to the forward region, where Totem T2, BCM2 and CASTOR is placed.

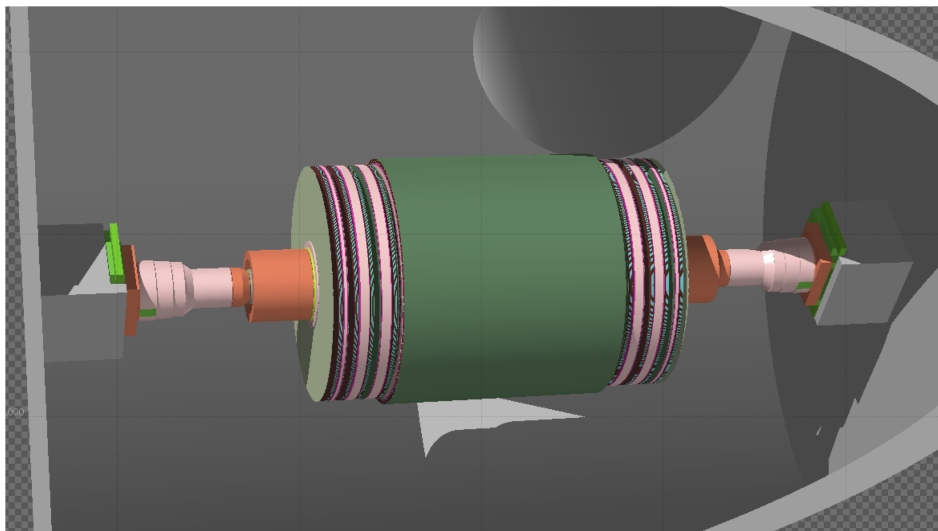


Figure 6.5.: 3D representation of the CMS geometry. While most of the geometry is symmetric in ϕ the blockhouse is an exception to this. The cavern was enlarged for this picture to get a better view.

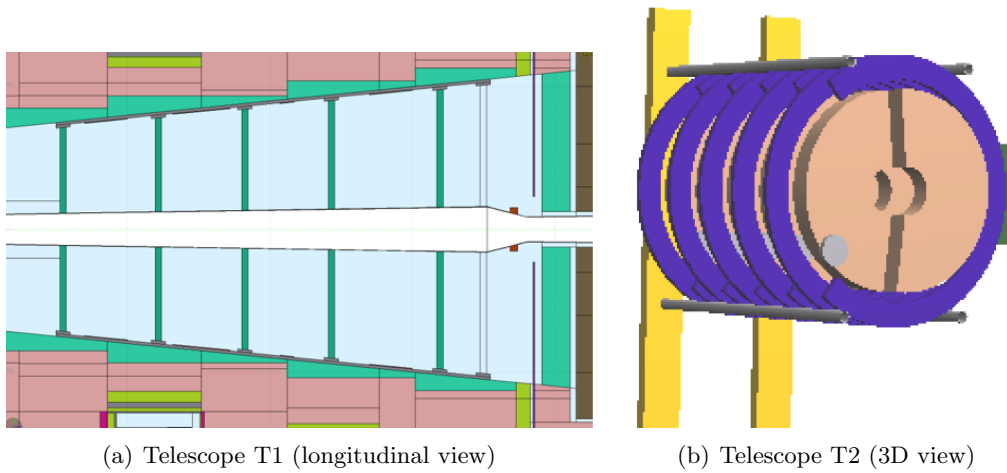


Figure 6.6.: TOTEM forward telescopes implemented in the CMS FLUKA model.

In order to understand the particle rates inside the CMS detector and in the whole experimental cavern, the complete detector and the experimental cavern have to be simulated. To reduce the necessary running time to obtain results with small statistical error the geometry is symmetric in Z and in ϕ with certain exceptions. The Z -symmetry is implemented by using the FLUKA lattice option. Only the positive end of the cavern is modeled and the negative end is a mirror picture of it. Excluded from this lattice is the region describing the CASTOR detector and the shaft, which are both only present on one end of the detector as shown in figure 6.4. A 3D picture of the CMS geometry is shown in figure 6.5.

An overview of all major modifications done to the simulation that influence and improve the simulation results connected to the BCM detectors is given here.

TOTEM Geometry The TOTEM Experiment [Ane08] is dedicated to the measurement of the total pp (proton-proton) cross section with the luminosity independent method and to study elastic scattering and diffractive processes at the LHC in combination with the CMS experiment. To achieve an optimum forward coverage for charged particles inelastically produced by the pp collisions in IP5, two tracking telescopes T1 and T2, are installed on both side of IP5 in the pseudo-rapidity region $3.1 \leq \eta \leq 6.5$. The telescope closest to the interaction point (T1, centered at $Z = 9$ m) consists of Cathode Strip Chambers (CSC), while the second one (T2, centered at $Z = 13.5$ m) uses Gas Electron Multipliers (GEM) [TOT04]. The newly included TOTEM FLUKA geometry was modeled in collaboration with F. Ravotti.

The T1 telescope fits in the space between two conical surfaces, the forward beam pipe and the inner envelope of the flux return yoke of the CMS end-cap. Each telescope consists of five planes of CSCs, equally spaced along the z coordinate. A detector plane is composed of six CSC wire chambers covering roughly a region of 60° in ϕ ; however, in the geometry model, the T1 CSC wire chambers are considered to be ϕ -symmetric. The chambers are composite structures, sandwich panels of standard glass-epoxy laminate (G10) with a core of honeycomb, and are flushed with a gas mixture Ar/CO₂ (50/50%). In the FLUKA model, an average material combining the previous three constituents in the proportion 20/60/20%-weight respectively, for a total mass of 25 kg. Each of the five detector planes, plus a sixth frame, which supports patch panels for the connectivity of the services, are fixed separately to conical aluminum rails. The rails, which serve as mechanical support structure, have a

total weight of 200 kg. In the simulated geometry, this support structure is modeled by a thin ϕ -symmetric conical surface of equivalent mass. Finally, in the peripheral region between the CSC planes, a series of support plates host the cathode readout electronics. These plates are also included in the FLUKA model as concentric rings of metal and electronic material (Al/Cu/FR4) with a thickness chosen to maintain the total mass equivalent to 30 kg/ring. The T1 model is shown in figure 6.6(a).

The T2 telescopes are installed inside the forward shielding of CMS between directly in front of BCM2. In each T2 arm, 20 semi-circular GEM planes, with overlapping regions, are interleaved on both sides of the beam pipe to form 10 detector planes of full azimuthal coverage. The GEMs are mounted as pairs with a back-to-back configuration. For the purposes of the FLUKA geometry, the paired chambers are modeled as a unique one with double thickness as shown in figure 6.6(b). The material budget of T2, minimized by using low-Z construction materials and honeycomb structures in the manufacturing the mechanical support, has been finely reproduced in the FLUKA model. The material definition of the GEM chambers takes into account the real detector structure: three GEM amplification stages realized by three perforated and Cu-clad polyimide foils (1.6%_w) supported by honeycomb plates (42.3%_w). The GEM foils are then separated by a 3 mm drift space followed by two 2 mm deep charge transfer regions and a 2 mm charge induction space, as show in detail in [Ane08]. These drift spaces are flushed with a gas mixture Ar/CO₂ (70/30%) that constitutes the rest of the material budget (56.1%_w). The front-end electronics of the GEM detector is mounted at the periphery of the chamber, on a concentric printed circuit board named “horseshoe card” after its geometrical shape. Since in the same spatial region, the cooling lines and the readout board are also located, an equivalent region made of different materials is used. The “horseshoe cards” of the 10 detectors of one T2 telescope half arms are connected to the so-called “11th card” which provides the interface to the outside world and is also present in the simulated FLUKA model. Finally, the FLUKA geometry of T2 also includes the detector support structures, two massive bars, on which also BCM2 is mounted, and four small cylindrical tubes, made of stainless steel, see fig. 6.6(b). T2 is not modeled ϕ -symmetrically, but more detailed, and is therefore one of the exceptions to the general ϕ -symmetry of the FLUKA CMS geometry.

The CASTOR Detector The CASTOR calorimeter is located exactly behind the BCM2 wheels and is therefore one of the most influential parts of CMS on the radiation environment at the BCM2 location. In the model used in previous studies [Mül11], CASTOR was a simple tungsten cylinder, where the density was matched to the overall weight of the active volume of CASTOR. In order to be only present on one end, a user routine modified the material composition according to whether the particle was within the normal (positive) region or the (negative) lattice region.

The new model of CASTOR is implemented with two concentric cylindrical layers which are cut with an angle of about 45° along the Z-axis in order to reproduce the shape of the high-Z material sampling plates:

- The inner cylinder has a radius from 4 cm to 18 cm and represents the active volume of the detector. It is composed of an average material made of 95.2% tungsten and 4.8% quartz. An equivalent material with the density of 12.88 g/cm³ has been used to describe the total mass of the active volume that is about 1682 kg.
- The outer cylinder reaches the ultimate radius of 31.8 cm and simulates the external stainless steel support skeleton. The density of 1.029 g/cm³ was chosen to match the

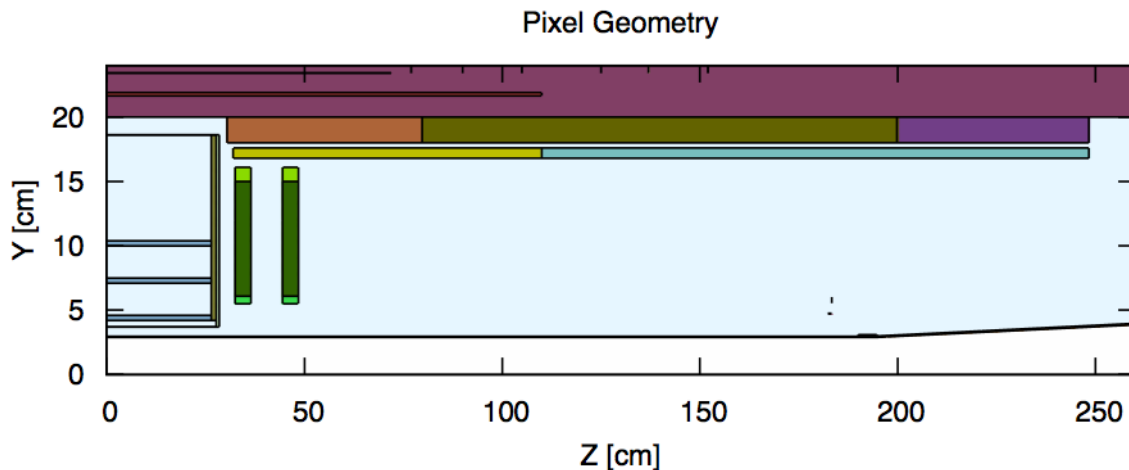


Figure 6.7.: FLUKA geometry of the CMS pixel detector.

weight of about 300 kg.

The CASTOR volume has now been removed from the lattice definition and a real region on the negative end was included. In the normal CMS definition of positive and negative ends CASTOR, as well as the shaft are located on the negative, or “minus” end of the CMS detector. In the used FLUKA model CASTOR is located at positive Z values since the shaft is likewise implemented on this end, which means the definition of the Z axis follows the definition of the LHC, which is opposite to the CMS definition. The corresponding detector volume at negative Z is instead replaced by air. For configurations without the CASTOR detector installed (like the proton run during 2012) CASTOR can be deactivated in FLUKA by configuring “air” as material for this region.

Pixel The mechanical design and material budget of the CMS barrel pixel and forward pixel detectors can be found in [Ams09]. The FLUKA pixel detector model was updated and now includes next to the central barrel and detector and the forward disks: the inner and outer shielding, the end flange, power and signal cables, the supply tube, the supply box and the service cylinder. A schematic geometry of the CMS pixel detector for FLUKA simulation is given in figure 6.7. The central barrel detector consists of three layers at the mean radii of 4.4, 7.7 and 10.2 cm, with a length of 53 cm. The central barrel region is defined by the inner and the outer shielding at radii of 3.7 and 18.6 cm extending over the full barrel length of 57 cm. The signal and power cables run parallel to the modules along the z-direction. They are fed through the spacing in the end-flange and they radially distributed until connect to the Printed Circuit Boards. The barrel pixel detector is completed by two forward pixel disks on each end, located along the beam axis at $Z = \pm 34.5$ cm and $Z = \pm 46.5$ cm, extending from 5.87 cm to 14.5 cm in radius. The total mass of pixel detector is about 66.4 kg. The chemical compositions of all used materials correspond to the mechanical design and material budget [Ams09]. The new pixel FLUKA geometry was included in the CMS geometry in collaboration with I. Kurochkin.

Preshower The preshower detector is installed in front of the endcap electromagnetic calorimeters. It consists of two detection layers consisting of a lead absorber followed by a silicon

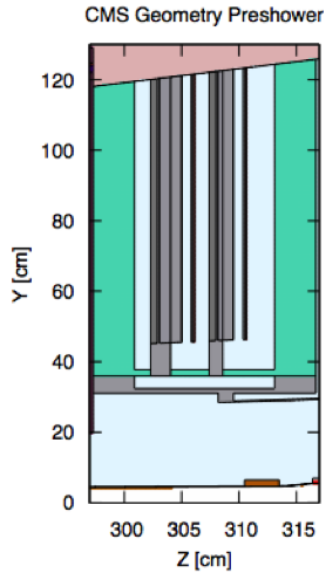


Figure 6.8.: FLUKA geometry of CMS preshower detector.

sensor. A cooling screen is attached to the lead layer consisting of aluminum tubes filled with cooling water. In front and behind the two detection layers is a 3.6 cm thick layer of paraffin. In the FLUKA geometry polyethylene is used as material, since this material was already implemented and the differences between paraffin and polyethylene are negligible. The previous model of the Preshower detector was based on drawings from an early design stage. An update to fit the actual installed version was performed for the purpose of a detailed study of the radiation environment at the Preshower detector position, see section 6.4.3. A picture of the geometry can be found in figure 6.8. The FLUKA model consists of layers of material confined in R by two cones with η of 1.653 and 2.6. The cooling screen is composed of an average material with a density of 2.93 g/cm^3 consisting of 70% Aluminum and 30% C_6F_{14} cooling liquid. The support cone made out of aluminum under the detection layers is implemented as well.

BCM2 For the BCM2 diamond detectors at $Z = 14.39 \text{ m}$ a layer of Aluminum was included in front of and behind them to represent the support structure. This modification has a rather low influence on the over all CMS radiation simulation, however for specific interest in the BCM2 region this more detailed model was implemented to gain a more realistic results at lower energies. The Aluminum layers range from 3 to 33 cm and are 1 mm thick facing the interaction point and 2 mm behind the diamonds.

Magnetic field The map used as input for FLUKA is extracted from CMSSW. The latest version of the magnetic field (CMSSW version 5.01) is used. The version of the magnetic field used by all previous runs were based only on simulations, the newer version of the field incorporates findings from cosmic ray data. Especially in the forward regions the newer model is more realistic. The field definition is, like the geometry, symmetric in ϕ and ranges in Z from 0 to 1600 cm and in R from 0 to 900 cm. The data is available in resolution of 2.5 cm bins.

6.3. Normalization

The output of the FLUKA simulation is always normalized per primary particle, in case of the CMS simulation: per primary proton-proton collision. Results should be normalized either to values per unit time at a given instantaneous luminosity, or normalized to a integrated luminosity. This is done by multiplying with the number of inelastic collisions which are calculated for a given luminosity by:

$$\#collisions = \sigma_{inelastic} * luminosity.$$

The luminosity can be either an integrated value giving a total number of collisions, or instantaneous giving a collision rate, usually per second. The inelastic collision cross section $\sigma_{inelastic}$ used for the simulated beam energies are:

- 3.5 TeV beam energy: $\sigma_{inelastic} = 73.5 \text{ mb}$
- 4.0 TeV beam energy: $\sigma_{inelastic} = 74.7 \text{ mb}$
- 7.0 TeV beam energy: $\sigma_{inelastic} = 80 \text{ mb}$

The $\sigma_{inelastic}$ value for 3.5 TeV and 4.0 TeV was measured by the TOTEM collaboration [TOT11, TOT12]. For 7.0 TeV no measurements exist yet. The numbers for $\sigma_{inelastic}$ predicted by various Monte Carlo event generators range from $\sim 75 \text{ mb}$ to $\sim 90 \text{ mb}$ [Bel13]. One generator that was tuned to results from LHC is the EPOSLHC [Pie13]. This generator should give a reliable number and predicts 79.95 mb for 7 TeV beam energy.

Given the statistical precision of the simulation and the systematical errors due to the coarse geometry description a precise value for $\sigma_{inelastic}$ down to the 1 % level is not necessary and the used values are well justified.

6.4. Simulation of proton proton collisions in CMS

Previously published simulation results of radiation environments in CMS are available for the nominal LHC configuration, or at injection energy. For this work simulations were performed with parameters matching the 2011 and the 2012 LHC running conditions. For the 2011 simulation using 3.5 TeV beam energy the CASTOR detector was included in the simulation. For the 2012 simulation using 4.0 TeV beam energy CASTOR was deactivated by setting the material definition of the CASTOR volume to air. A simulation run is also performed with 7.0 TeV beam energy used by various sub-detector groups for the prediction of their detectors after long shutdown 1. The geometry used for this is the nominal geometry described above and the results are only valid in the limitations that no major modifications are done.

Further details of the FLUKA parameters are listed below:

- The set of defaults was applied by using the option PRECISION in the DEFAULTS card.
- Primary proton-proton events are generated by the SPECSOUR card which invokes DPMJET-III [Roe00].
- The cutoff for Neutrons is 0.01 meV. This is the lowest energy handled by the low energy neutron library.

- The cutoff for charged hadrons is 1 keV.
- The cutoff for electrons is mostly 30 keV, and for photons 3 keV. In some regions with high density material they are higher to avoid too high CPU load.

The main scoring used is a USERBIN scoring with cylindrical coordinates over the whole cavern with a 2 cm resolution in Z and in R. There is only one bin in ϕ . A splitting over the ϕ angle is not necessary since the geometry is symmetric. The particle types and groups scored are: All particles, all charged particles, neutral hadrons, charged hadrons, charged hadrons with $E > 20$ MeV, neutrons, neutrons with $E > 20$ MeV, protons, photons, electrons, charged pions, dose, non ionizing energy loss, silicon 1 MeV neutron equivalent, number of inelastic interactions.

The R/Z distribution of all the particle flux over the whole cavern, normalized per cm^2 per second at nominal luminosity ($10^{34} \text{ cm}^{-2} \text{ s}^{-1}$), is shown in figure 6.9. Figure 6.9(a) shows the results from the 2011 run, figure 6.9(b) shows the results from the 2012 run. The increase in particle flux on the positive Z axis of the 2011 run is clearly visible. Particles hitting the CASTOR detector produce many secondary particles that can leak out of the forward shielding and flood the cavern.

6.4.1. Online availability of simulation results

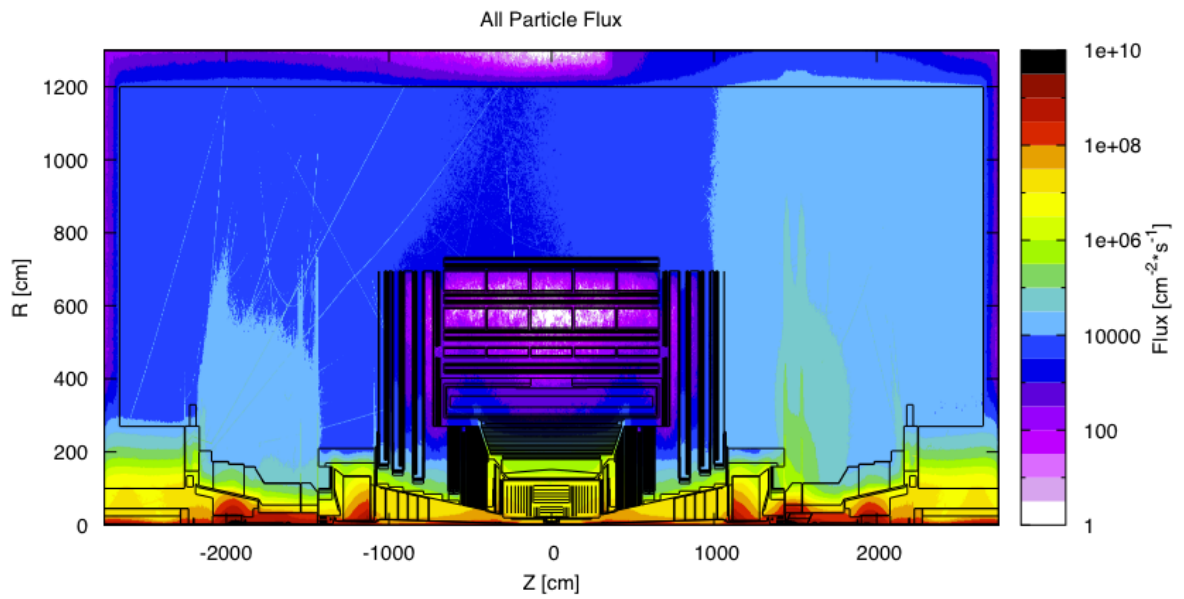
Results of the FLUKA simulation runs are of interest to the whole CMS collaboration. Flux maps obtained in the simulations are made available online. A online plotting tool was developed which enables the user to create customized plots. The aim was to create a plotting software that works similar to the FLUKA internal plotting, so only the FLUKA result files have to be uploaded. USBIN (2D flux maps) results of any FLUKA simulation can be uploaded, and made available, although it is optimized for LHC proton-proton collisions, as the normalization to a certain luminosity (as presented in section 6.3) is calculated. The website is hosted on CERN's AFS services and uses python 2.4.3 to process the data and matplotlib 0.99.1.1 to create a plot.

The Radiation Simulation online Plotting tool (RSP) is available under:

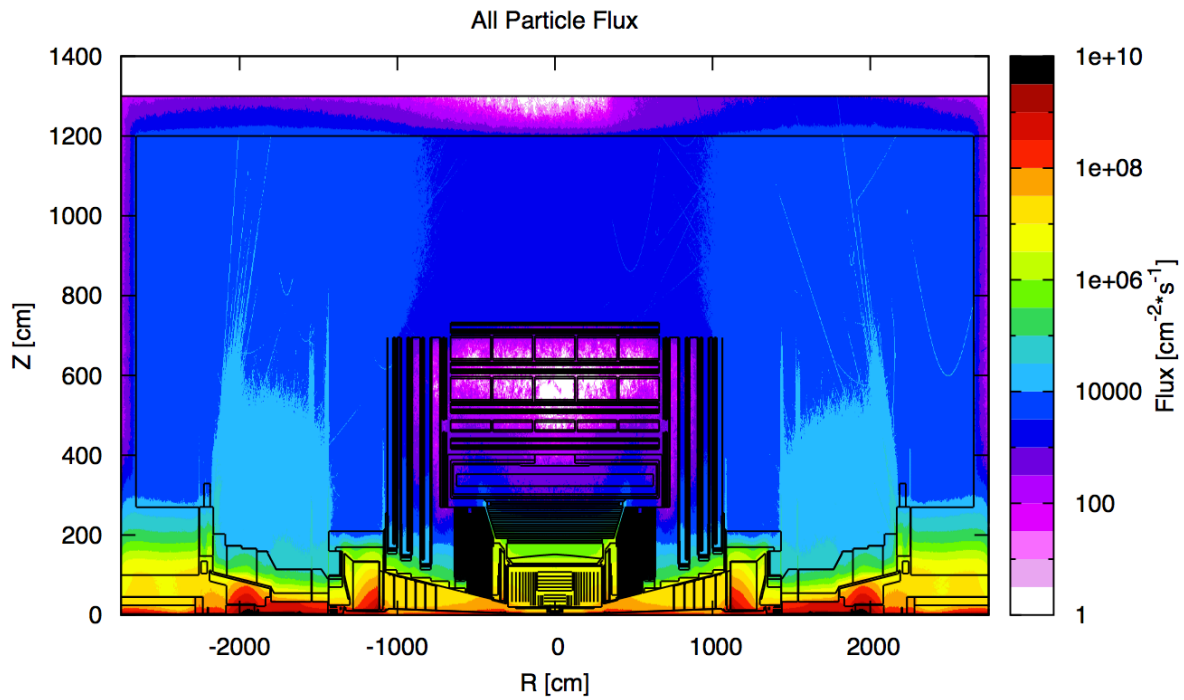
www.cern.ch/cms-fluxmap

The selection of the plot parameters are done in four steps:

1. The simulation run is selected. All results are grouped in the runs with which they were obtained. Different beam energies, geometry variations, or special runs, like activation simulations, can be configured.
2. One of the USBINs of the simulation run can be selected. Usually the different particle types are chosen here, but also different kinds of available binning can be selected.
3. The plot parameters are chosen. Figure 6.10 shows a screenshot of this step. The options are to select the plot range, rebinning, color scale options, and the plot normalization to a certain instantaneous or integrated luminosity.
4. A 1-D projection plot can be created based on the 2-D plot created in the previous step. Also a data value of a single point can be displayed, or the full data set shown in the plot can be downloaded as textfile.



(a) All Particle Flux, 2011 situation



(b) All Particle Flux, 2012 situation

Figure 6.9.: Particle Flux of all particles for nominal luminosity.

6.4. Simulation of proton proton collisions in CMS

Selected simulation run:
CMS_pp_7TeV_FLUKA

[← to step 1](#)

Selected scoring:
All Particles

[← to step 2](#)

Please note that plot is generated from a large raw binary data file, so please be patient, this process could take a few minutes.

step 1
→
step 2
→
step 3
→
plot

[\[↔ click here\] simulation description](#)

step 3: Plot Options

Select plot range:

R min [cm]: <input type="text" value="0.00"/>	R max [cm]: <input type="text" value="1300.00"/>	R rebin: <input type="text" value="1"/>
Φ min [rad]: <input type="text" value="-3.14159"/>	Φ max [rad]: <input type="text" value="3.14159"/>	Φ rebin: <input type="text" value="1"/>
Z min [cm]: <input type="text" value="-2750.00"/>	Z max [cm]: <input type="text" value="2750.00"/>	Z rebin: <input type="text" value="1"/>

Select normalization:

instantaneous [$\mu\text{b}^{-1}\text{s}^{-1}$] (default value: 10'000)

integrated [fb^{-1}] (default value: 1)

[\[↔ click here\] color bar options](#)

Select plot colors features:

color-map min: <input type="text" value="automatic"/>	color-map max: <input type="text" value="automatic"/>	no. of colors: <input type="text" value="automatic"/>
--	--	--

color palette:

spectral

rainbow

normal

[\[↔ click here\] data type](#)

Select data type:

raw data

error data [%]

[← Previous](#)
[Next >](#)
[Reset Form](#)

Figure 6.10.: The Radiation Simulation online Plotting tool (RSP). After selecting the simulation run, and the generalized particle type to plot (Here: “All Particles” of the proton-proton simulation of CMS at 7 TeV beam energy) the user can select the plot range, normalization to a instantaneous luminosity and the limits of the color scale.

Due to the large amount of fluence data produced in the scope of this thesis it cannot all be plotted here, but all results useful for the CMS collaboration is made available via the RSP online tool.

The website and the uploaded FLUKA results are highly appreciated by the CMS collaboration. In the first 8 months since it went online in March 2013 there were about 600 unique users from 24 different countries, more than 10000 hits and almost 1 GB worth of plots downloaded.

6.4.2. Radiation environment at locations of the BCML detectors

The energy spectra of various different generalized particle types at the locations of the BCML detectors were recorded for the 2011 and the 2012 simulation run. The results for the 2011 simulation are presented. They give the most information, as CASTOR was installed in this simulation run. The spectra for each location, comparing the different particle types, are shown in figure 6.11. The flux is normalized per second at nominal luminosity. The “all particles” spectra is recorded as generalized particle type itself, showing that there is not a type of particle, which is missed in the scoring of the single particle types. The neutrons below 20 MeV are not added to the “all particle” scoring, since they have a different binning and cannot be summed with other particles.

The BCM2 spectra at the inner location are similar compared between the +Z end (figure 6.11(a)), and the -Z end (figure 6.11(b)). It has a peak in the high energetic regime around 100 GeV, which is mostly due to direct collision product. The main components are pions and photons. Neutrons and protons peak as well, but they are about one order of magnitude lower in flux. In the spectra of the BCM2 outer location this high energetic peak is suppressed, since the outer detectors are shielded from the interaction point by the HF detector. Below 1 GeV the spectrum consists mostly of electrons and photons generated in electro-magnetic particles originating mostly in the beam pipe elements in front of CMS. The most prominent difference between BCM2 on the -Z and the +Z end, seen in the inner and the outer detectors, is the neutron flux below 1 GeV. The neutron spectrum peaks between 100 keV and 1 MeV in all BCM2 regions. On the -Z end however the neutron peak is roughly two orders of magnitude higher. The only difference between -Z and +Z is the presence of the CASTOR detector on the -Z end. High energetic particles hitting CASTOR create spallation neutrons which reflect back into BCM2.

The high energetic peak of collision products in the BCM1L spectrum is around 10 GeV, which consists, like in BCM2, of mostly photons and pions. The difference in energy of this peak between BCM2 and BCM1L can be explained by the difference in η range. BCM1L is at about $\eta \approx 4.3$, and BCM2 is at about $\eta \approx 6.3$. The absolute momentum of a particle $|p|$ in high energy collisions is related to the η by:

$$|p| = p_T \cosh \eta \quad (6.6)$$

A particle at $\eta = 6.3$ has about 7.5 higher energy than a particle with the same transversal momentum at $\eta = 4.3$. The two high energetic peak in BCM1L and BCM2 are formed by particles of roughly the same transversal momentum, just with a different forward boost.

Figure 6.12 compares directly the different locations for neutrons, photons and charged particles separately. The neutron spectra (figure 6.12(a)) show clearly the increase on -Z compared to +Z due to the CASTOR effect. The BCM2 inner detectors have slightly more thermal neutrons (below 1 eV). The charge particle spectra (figure 6.12(b)) is almost the same comparing BCM2 on -Z (with CASTOR) and +Z (without CASTOR). Only at rather

6.4. Simulation of proton proton collisions in CMS

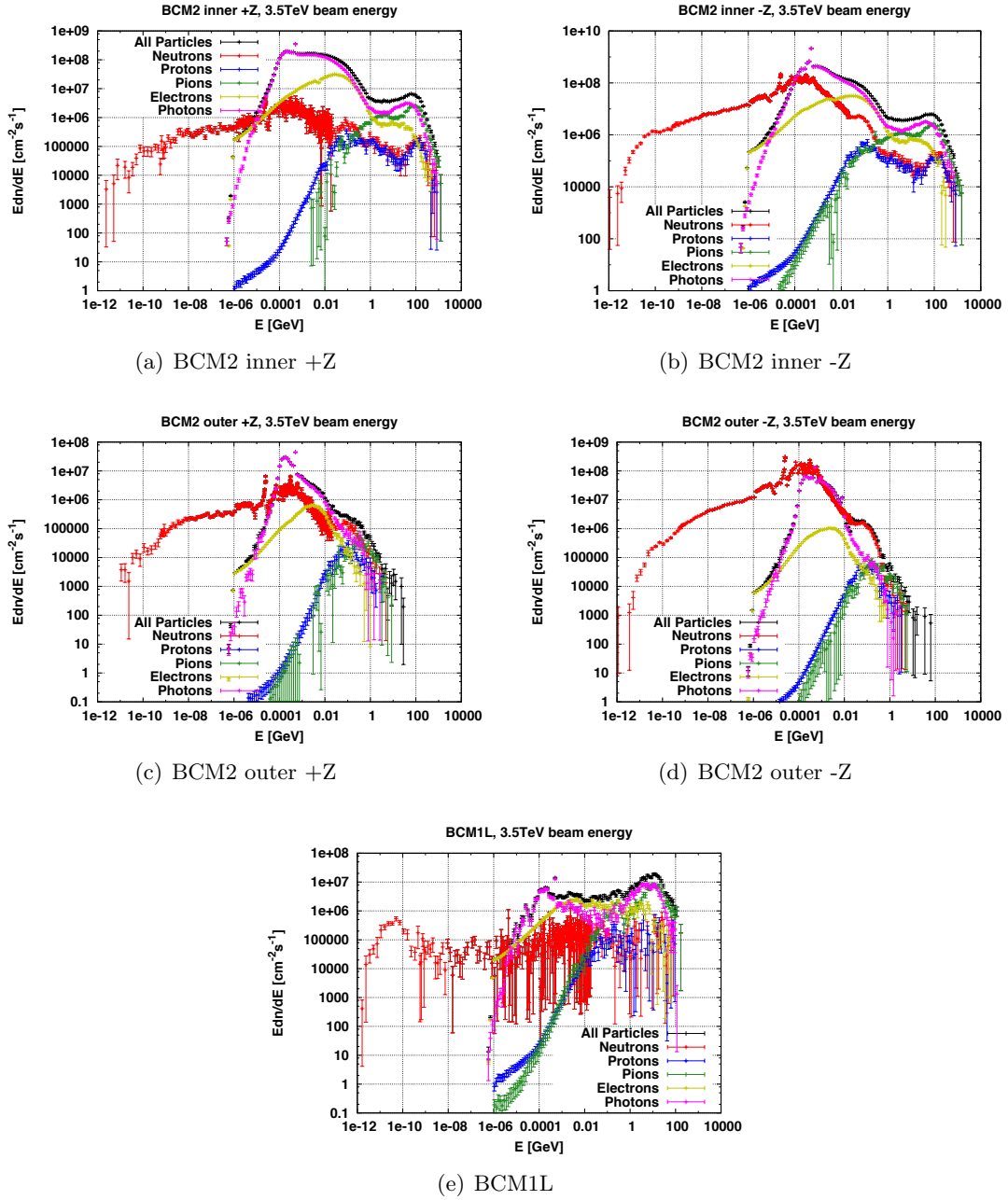


Figure 6.11.: Particle energy spectra at the BCM1L locations at 3.5 TeV beam energy. The data is normalized to the flux per second at nominal luminosity. For each detector location, the spectra of the different particle types are grouped together to show the composition of the radiation environment. Neutrons below 20 MeV are not included in the “all particle” flux due to a different binning structure

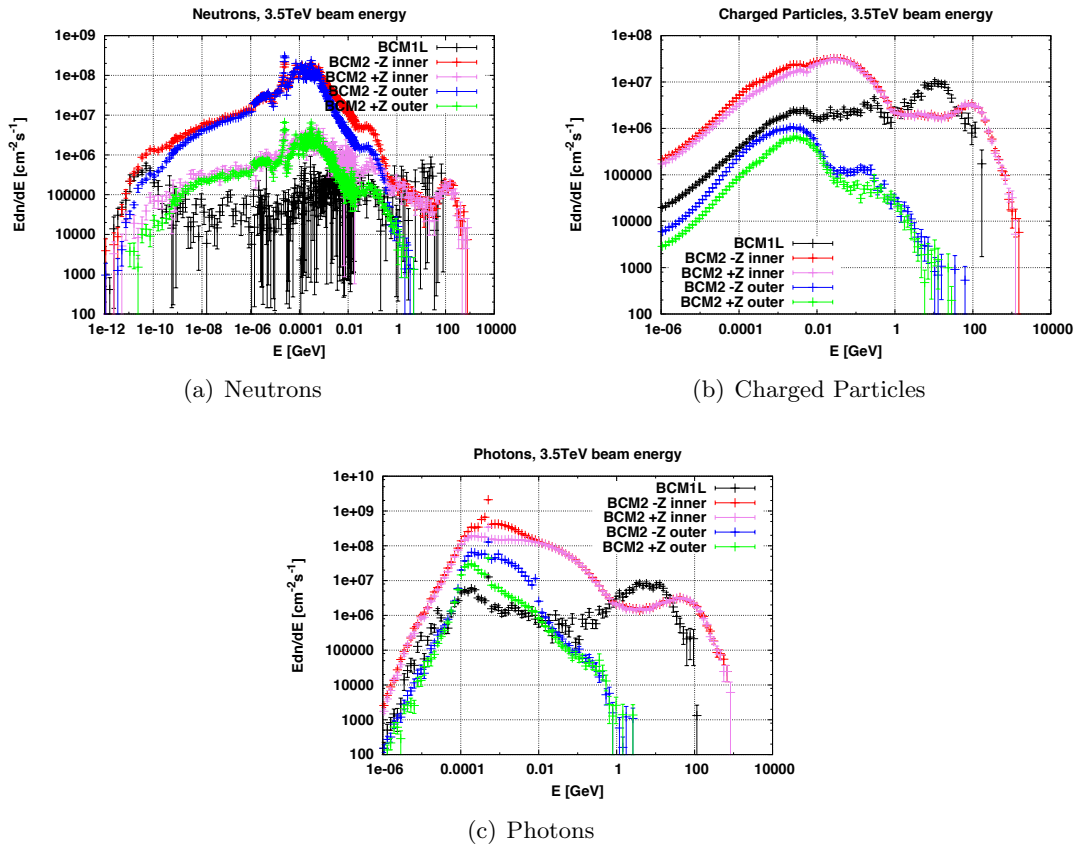


Figure 6.12.: Particle energy spectra at the BCML locations at 3.5 TeV beam energy. The data is normalized to the flux per second at nominal luminosity. The spectra of each particle location are grouped in one plot for different particle types to show the difference in radiation environment between the different locations.

Detector	Signal 2011 [nA]	Signal 2012 [nA]	S ₂₀₁₁ /S ₂₀₁₂
BCM1L	48.9 ± 1.6 (3.3 %)	54.1 ± 1.4 (2.6 %)	0.904
BCM2 inner -Z	267.5 ± 8.1 (3.0 %)	245.7 ± 8.3 (3.3 %)	1.089
BCM2 inner +Z	219.6 ± 8.5 (3.9 %)	262.1 ± 14.1 (5.3 %)	0.838
BCM2 outer -Z	12.6 ± 0.41 (3.3 %)	6.0 ± 0.15 (2.5 %)	2.083
BCM2 outer +Z	5.6 ± 0.19 (3.4 %)	6.4 ± 0.31 (4.7 %)	0.866

Table 6.1.: Expected signal of the BCML detectors at nominal luminosity. The given error is the statistical uncertainty of the simulation.

low energies (below ~ 10 MeV) a slightly higher charged particle flux is visible. As the signal generated in the detectors is mostly due to charged particles, no significant difference is expected between +Z and -Z (for exact numbers see section 6.4.2).

Expected detector signal

The expected detector signal for a given luminosity is calculated by scoring the total energy deposition Q_{ind} in the diamond. Using the average ionization energy of 13 eV the number of electron hole pairs or the charge per second can be estimated.

$$Signal[A] = Q_{ind}[eV]/13 eV \times e[C] \times \#collisions[s^{-1}] \times CCE, \quad (6.7)$$

with e being the elementary charge. A CCE of 40 % is assumed, which is a realistic number for pCVD diamond detectors of the used quality. Table 6.1 shows the results of the expected detector response at nominal luminosity for the 2011, 2012 and nominal scenarios.

Radiation damage prediction

In the previous study by S.Müller[Mül11], the displacement per atom (DPA) scoring was used to predict the lifetime of the BCM2 system. This study was only performed for 7 TeV beam energy without the CASTOR detector present. It was assumed that the early LHC period at intermediate beam energies and the presence of CASTOR would not significantly contribute to the radiation damage of the diamond detectors.

The prediction of the number of displacements does not directly reveal the radiation damage in terms of reduced detector performance. The DPA is however a scaling method that allows any particle to be weighted to reflect its damage potential compared to a reference particle type. The mixed field particle flux at the BCML detector locations can be converted to the 24 GeV proton equivalent as described in section 6.1.4.

In the newly performed simulation runs, new results for DPA scorings are obtained for the 2011, 2012 and nominal conditions. The results of the equivalent fluence per fb⁻¹ of integrated luminosity is shown in table 6.2. The equivalent fluence can be compared with irradiation studies to predict the detector performance after a certain amount of integrated luminosity.

6.4.3. Radiation damage to silicon detectors and comparison with measurements

One available benchmark of the CMS simulation is the comparison of the predicted radiation damage to the silicon detectors in CMS, and the measurement of their bulk leakage, which increases with the amount of radiation damage. In several subdetectors of CMS, silicon

Detector	24 GeV prot.-eq. 2011 [$\text{cm}^{-2}/\text{fb}^{-1}$]	24 GeV prot.-eq. 2012 [$\text{cm}^{-2}/\text{fb}^{-1}$]
BCM1L	$3.39 \times 10^{12} \pm 4.13 \times 10^{11}$ (12.2%)	$3.58 \times 10^{12} \pm 3.06 \times 10^{11}$ (8.6%)
BCM2 inner -Z	$2.59 \times 10^{14} \pm 5.27 \times 10^{12}$ (2.0%)	$1.05 \times 10^{13} \pm 5.10 \times 10^{11}$ (4.9%)
BCM2 inner +Z	$9.03 \times 10^{12} \pm 5.52 \times 10^{11}$ (6.1%)	$1.00 \times 10^{13} \pm 5.10 \times 10^{11}$ (5.1%)
BCM2 outer -Z	$1.94 \times 10^{14} \pm 2.52 \times 10^{12}$ (1.3%)	$4.68 \times 10^{12} \pm 1.52 \times 10^{11}$ (3.2%)
BCM2 outer +Z	$3.83 \times 10^{12} \pm 1.82 \times 10^{11}$ (4.7%)	$4.49 \times 10^{12} \pm 1.48 \times 10^{11}$ (3.3%)

Table 6.2.: Equivalent fluence of 24 GeV protons at the locations of the BCM1L detectors for an integrated luminosity of 1 fb^{-1} calculated by scoring the DPA in the diamond and rescaling to the DPA of 24 GeV protons. The given error is the statistical uncertainty of the simulation.

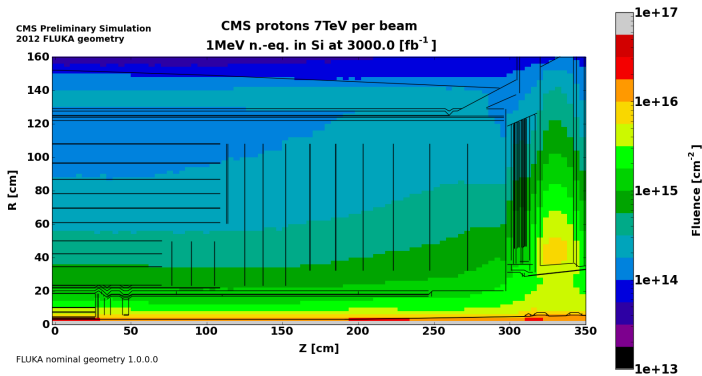


Figure 6.13.: Simulated 1 MeV neutron equivalent in the Tracker and Ecal region for 7 TeV beam energy normalized to 3000 fb^{-1} .

detectors are used. FLUKA simulations are used to predict the radiation damage to the silicon detectors by compiling the 1 MeV-n-eq (see section 6.1.4) fluence. The 1 MeV-n-eq was scored in a USRBIN scoring over the whole of CMS. Figure 6.13 shows the result of this scoring over the area of the Tracker and the ECAL.

The simulated 1 MeV-n-eq fluence predicts the fluence for a given luminosity. For the prediction of leakage current in silicon detectors, the irradiation profile is calculated from the FLUKA results with the actual luminosity profile. The temperature of the sensors also has to be taken into account, to properly account for the annealing effects.

Figure 6.14 shows an example, where these results were used to predict the leakage current due to radiation damage in the preshower detector[Barn13]. The preshower geometry was updated in the scope of the upgrades to the CMS geometry presented in this thesis. predicted leakage current matches well measured data.

A second example is the leakage current in the silicon strip tracker. In figure 6.15 the measured leakage current is plotted as function of simulated fluence for modules located at different radii [Bart13]. The modules more distant have a lower leakage current, and a lower fluence value. The linear correlation shows that the FLUKA simulation relates well to the inflicted radiation damage.

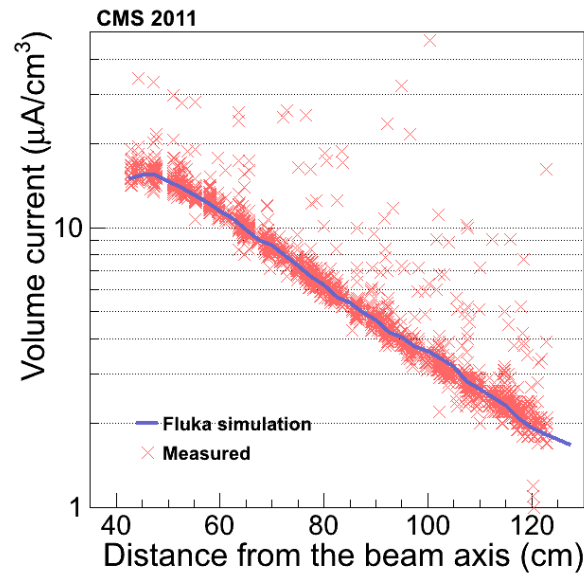


Figure 6.14.: Measured leakage current in the Preshower silicon detectors together with predictions based in the FLUKA simulated 1 MeV-n-eq[Barn13]

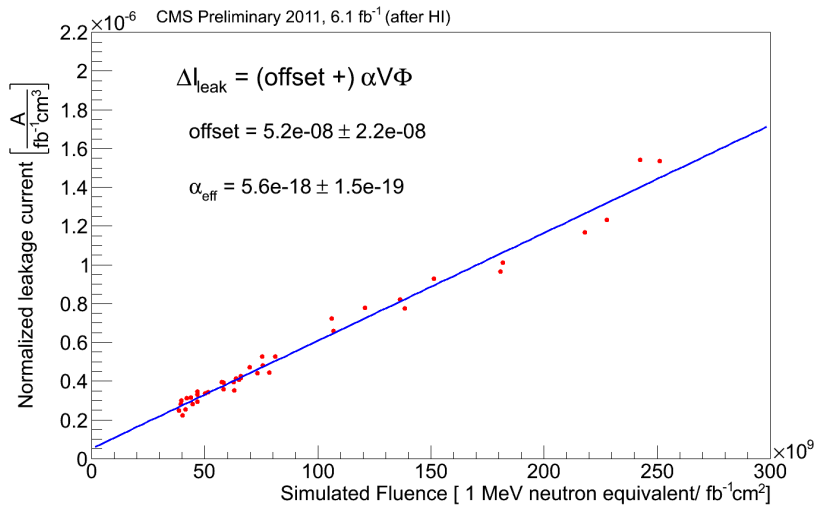


Figure 6.15.: The measured leakage current as function of simulated fluence for modules located at different radii. A linear correlation is found between the leakage current and the simulated fluence. [Bart13]

6.5. Activation of material during one fill.

Usually the signal contribution due to radioactive decay of material surrounding detectors used in CMS is negligible. During a fill very short-lived nuclei could accumulate and contribute to the measured signal. It was shown that this activation partially explains the afterglow effect measured in the BCM1F detectors [Mül11]. As the buildup of radioactivity during a fill would lead to an increased signal towards the end of a fill, the signal contribution due to activation was simulated. The used FLUKA configuration is summarized here:

- A beam energy of 4 TeV was used. An instantaneous luminosity of $5 \times 10^{33} \text{ cm}^{-2}\text{s}^{-1}$ was assumed, which corresponds to 3.75×10^8 collisions per second. A collision time of 10 hours was used. This configuration was used as an approximation of a typical fill of 2012.
- The electro-magnetic cascades were deactivated for prompt radiation (direct collision products), for decay products the usual cut-offs were used. This is the standard approach for activation simulations.
- All scorings were done at the following times after the start of the fill: 1 minute, 2 hours, 4 hours, 6 hours, 8 hours, 10 hours (end of fill). Additionally at times after the fill: 1 second, 5 seconds, 10 seconds.
- At any of these scoring times the energy deposition per second was scored for all BCML detectors. Additionally a map of the activity (in Bq/m^3) and the charged particle flux was recorded with low granularity in the whole cavern and with high resolution below 1 m radius.

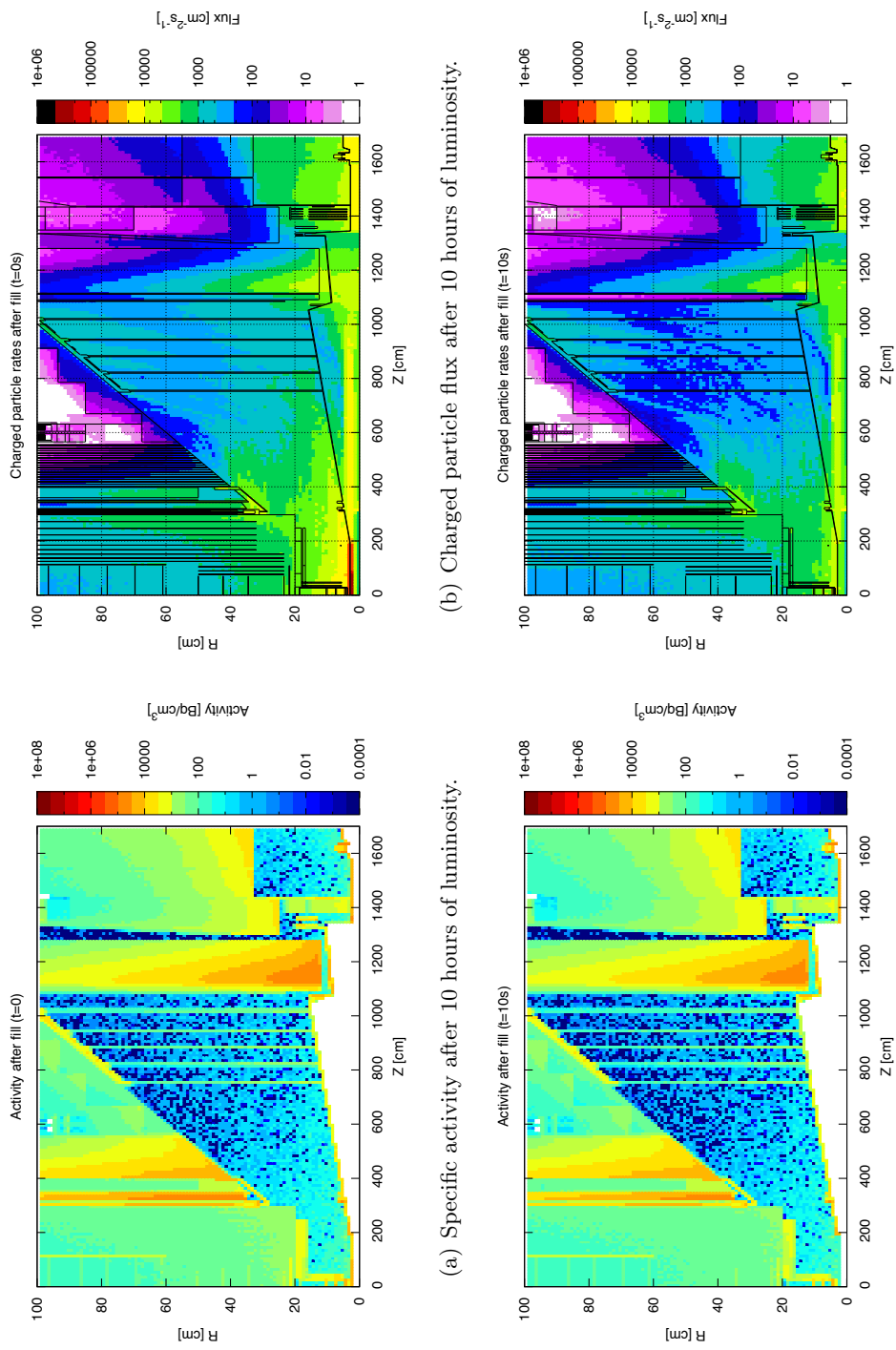
Figure 6.16 shows the specific activity and the flux of charged particles per second due to decay radiation after 10 hours of luminosity and 10 seconds after the end of the fill. Only the parts at low radius are shown as the activation happens mostly there. The activity mostly accumulates at heavy parts, like the calorimeters and the shielding, but also at the beam pipe. The charged particles flux can be used to estimate detector hits due to activation in any detector in CMS. After 10 seconds of cool down the activation is noticeably reduced. It is very significant at the beryllium part of the central beam pipe, where the activation is almost gone after 10 seconds. The high flux of charged particles around the central beam pipe, where also BCM1L is located, is much reduced.

Figure 6.17 shows the simulated signal due to activation in the BCML detectors during and shortly after the fill. Most of the activation is already built up in the first minutes. A slow increase is observed over the whole fill. This is probably not happening in reality, as a constant luminosity is simulated, but in reality the luminosity decreases with time. The saturation value for the activation induced signal is about 20 pA for the detectors at the BCM2 inner and the BCM1L locations, but only about 2 pA for detectors at the BCM2 outer location. This is much lower than the signal due to prompt radiation, which is of the order of several hundred nA. The signal disappears quickly after the fill. After 10 seconds the signal is reduced to about one third.

6.6. Effects on beam background due to new beam pipe design.

During Long Shutdown 1 a new central beam pipe is being installed in CMS. The radius of the cylindrical part is reduced from 2.9 cm to 2.2 cm. This will allow the redesign of the

6.6. Effects on beam background due to new beam pipe design.



(a) Specific activity after 10 hours of luminosity.

(b) Charged particle flux after 10 seconds after beam dump.

(c) Specific activity 10 seconds after beam dump.

(d) Charged particle flux 10 seconds after beam dump.

Figure 6.16.: Simulated activation build up during a typical LHC fill. The specific activity in Bq/m^3 and the charged particle flux due to radioactivity is shown after 10 hours of luminosity and 10 seconds after the luminosity stopped.

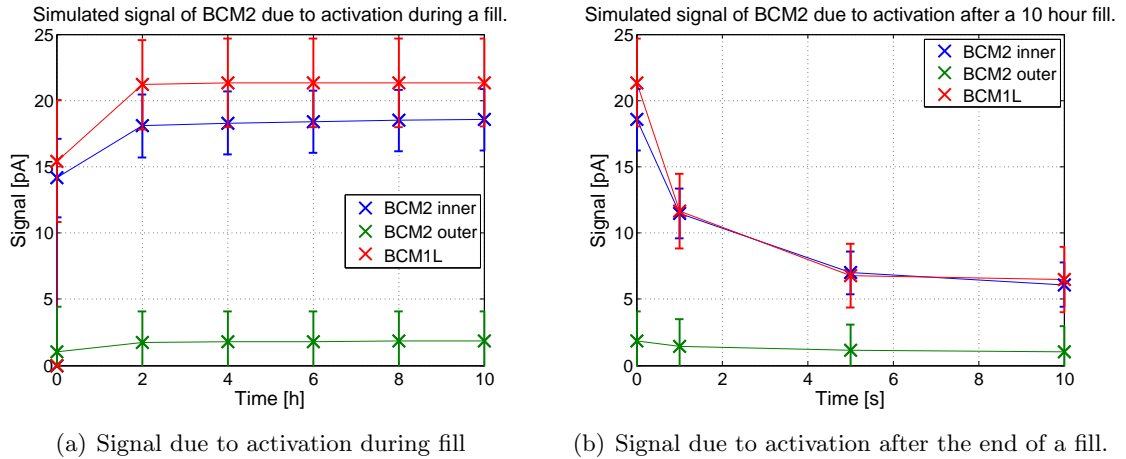


Figure 6.17.: Simulated signal measured in the BCM1L detectors due to radioactivity created during one fill (figure (a)). The signal builds up mostly within the first minute, after 2 hours into the fill the signal due to activation increases only slightly.

Pixel detector with an inner layer at a smaller radius, in order to achieve a better spatial resolution of the CMS Tracker. A major concern was that the new beam pipe design and the pixel detector at a different radius would increase the particle rates in the pixel due to machine induced background. This would lead to higher numbers of so called PKAM, where background particles traverse the detector in parallel to its plane leaving huge number of hits. These events take a long time to read out, which leads to an increase of dead time for the CMS data taking. A comparison simulation study was performed with the original beam pipe and two possible upgrade designs. The study was based on the FLUKA geometry used in [Mül11]. Figure 6.18 shows the differences in the geometry for the old and the new beam pipe design. The cylindrical beryllium part was reduced in radius, as well as the first pixel layer represented by a sheet of silicon. The conical part kept its opening angle, but due to the smaller cylindrical part the transition between cylinder and cone is at a different Z position. A collar used to connect the beryllium with the stainless steel was removed as this is not part of the new beam pipe. The material in the conical part changed from stainless steel to AlBeMet (aluminum-beryllium-alloy) in one upgrade design, or aluminum in the second design.

The machine induced background for inelastic beam gas, elastic beam gas and beam halo was simulated using a SixTrack simulation of the LHC and the MARS code to simulate the particle showers in the long straight section of CMS [Mok09]. All particles hitting the interface plane at 22.6 m away from the interaction point are recorded to file with all their relevant properties. This list of particles is used as input for the FLUKA simulation. The particles are propagated through the CMS geometry and the effects on CMS can be studied.

The relevant scoring parameters are the charged particles, as they create hits in the Pixel detector. Figure 6.19 shows the flux of electrons for the old beam pipe, the new geometry with a AlBeMet cone and the new geometry with the aluminum cone. The flux rates for only one beam is shown. The beam travels from the right side to the left and hence also the background particles. In figure 6.19(a) with the old geometry one can see that in the conical section of the beam pipe many electrons are created. The inner most layer of the Pixel is in the shadow

6.6. Effects on beam background due to new beam pipe design.

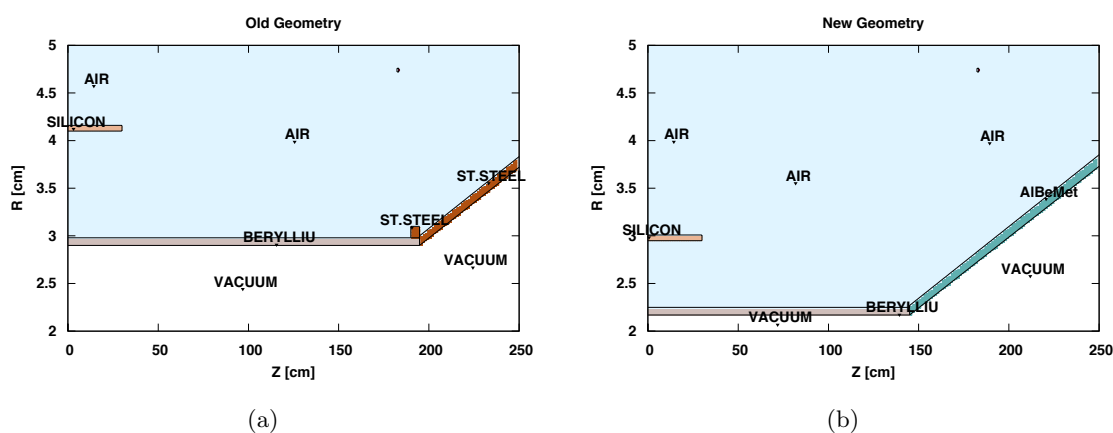


Figure 6.18.: Two versions of the beam pipe as implemented in FLUKA. The upgrade model shown in figure (b) was simulated in two version: one with AlBeMet as material for the conical part, and one with aluminum. This model is a simplification of the actually built beam pipe, which has beryllium up to 2 m in Z.

of this conical part and therefore exposed to a high number of electrons. Figures 6.19(b) and 6.19(c) show the results for the two new beam pipe designs. The electron flux is much reduced in both cases due to the lighter material used for the conical part. Figure 6.19(d) shows the difference between the old model and the AlBeMet model. The red area shows where the flux is higher in the old model, the blue area shows where the new model has a higher flux. The highest difference is around 3-5 cm in R, where the inner Pixel layer is located. An increase in electron flux is visible at the radius of the new beam pipe. In the old simulation there was no material at this radius and therefore also no particle shower.

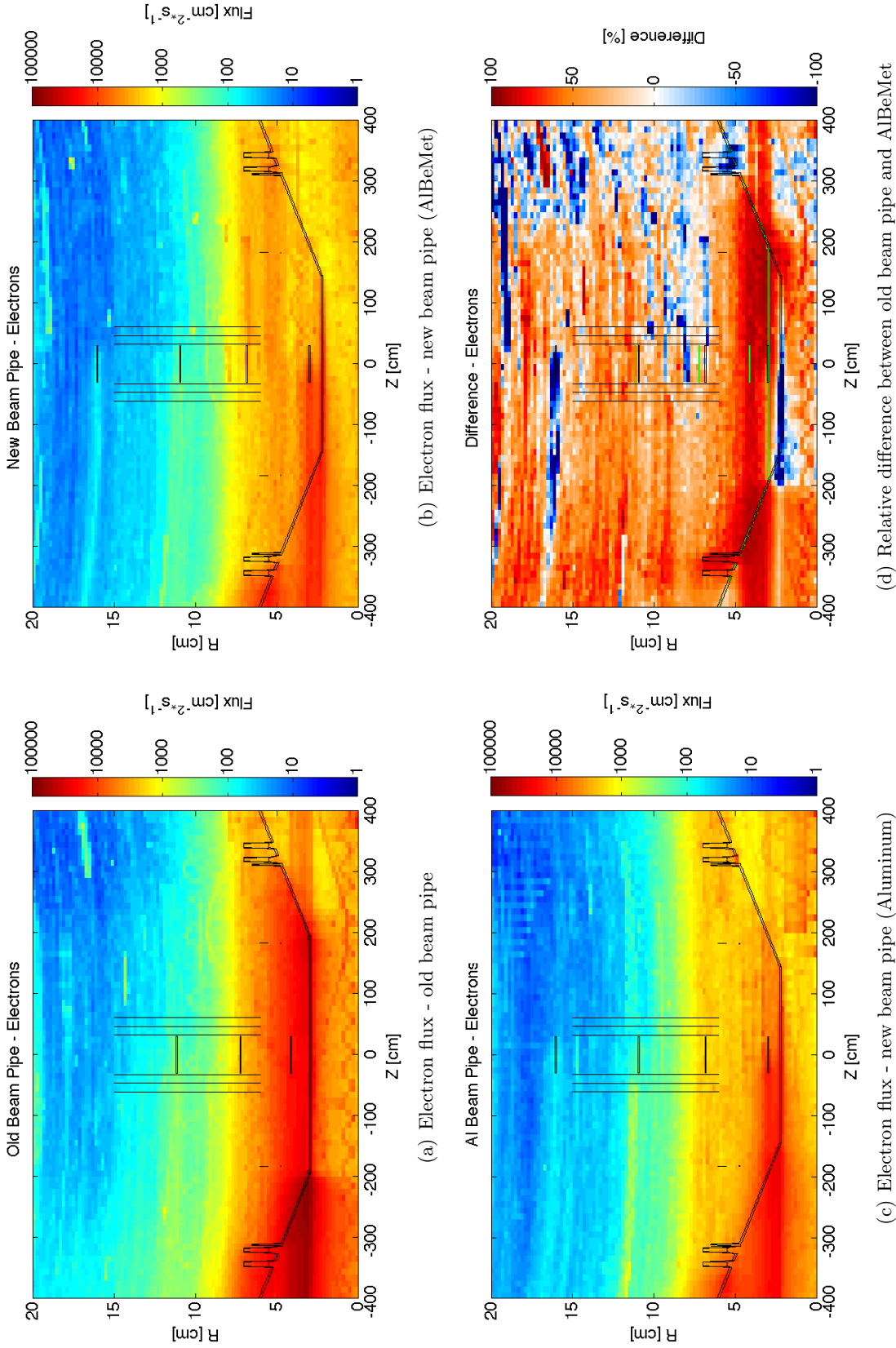


Figure 6.19.: The background particle flux in the pixel detector is mostly due to electrons created in electro-magnetic particle shower at the conical part of the central beam pipe. Figure (a) shows the electron flux due to beam background with the old stainless steel beam pipe. Figure (b) shows the same simulation where the new geometry with an AlBeMet beam pipe is used. Figure (c) shows the same results with an aluminum beam pipe. Figure (d) shows the relative difference between the old beam pipe and the new AlBeMet beam pipe.

6.6. Effects on beam background due to new beam pipe design.

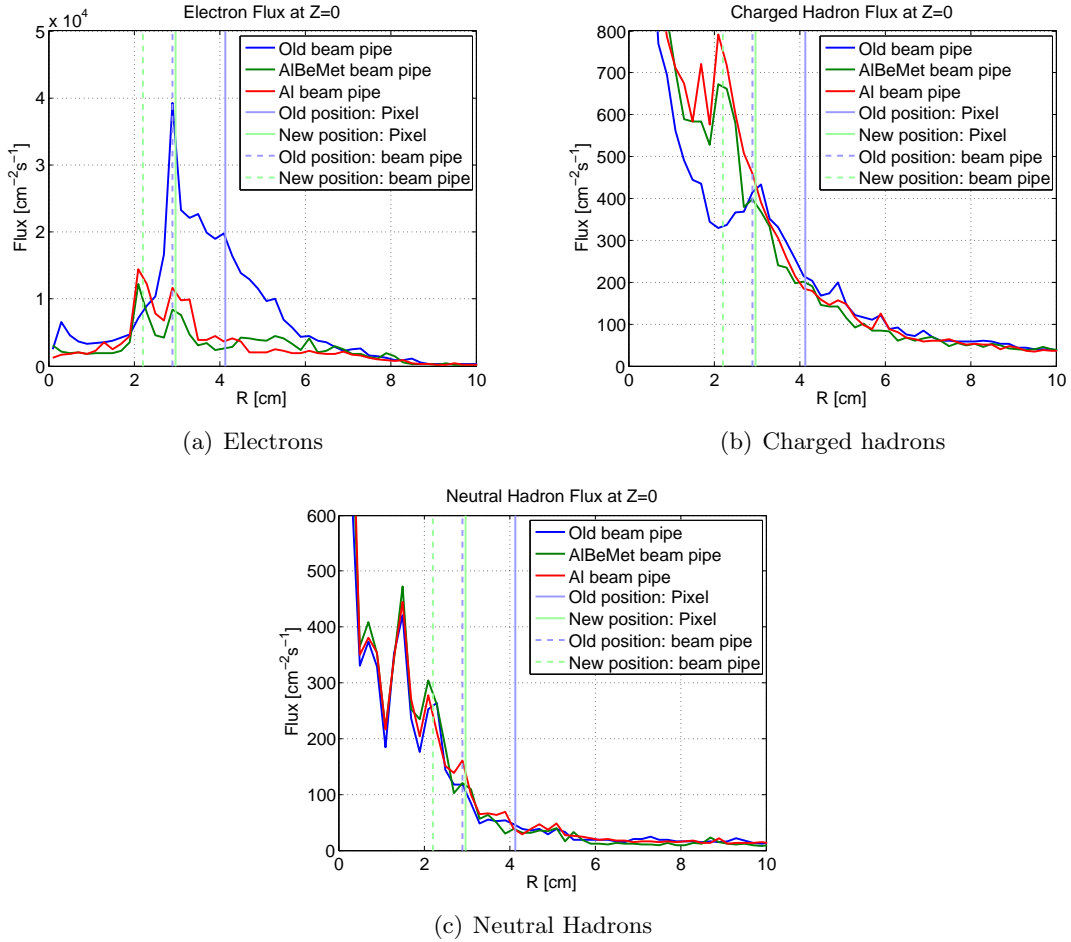


Figure 6.20.: Particle flux of electrons, charged hadrons and neutral hadrons due to machine induced background at $Z = 0$ as function of R . Results for simulations with old beam pipe and new beam pipe in AlBeMet and aluminum are shown. The position in R of the old and the new beam pipe, as well as the position of the old and the new inner most pixel layer is shown. The aluminum and the AlBeMet beam pipes generally show comparable results. The change from the old to the new geometry reduce the electron flux significantly between ~ 3 cm and ~ 6 cm. Only at about 2 cm radius a slight increase is observed with the new geometry, as no material is present in the old geometry at such low radius. The charged hadron fluence does not change above ~ 3 cm. Only an increase is observed below 3 cm, which is not relevant as no detectors are installed at these radii. Comparing the flux at the old and the new position of the inner most pixel layer an increase in charged hadron flux is expected. As the hadronic flux is much lower than the electron flux, which is significantly reduced, this increase does not pose a problem. No difference in neutral hadron flux is observed with any geometry version.

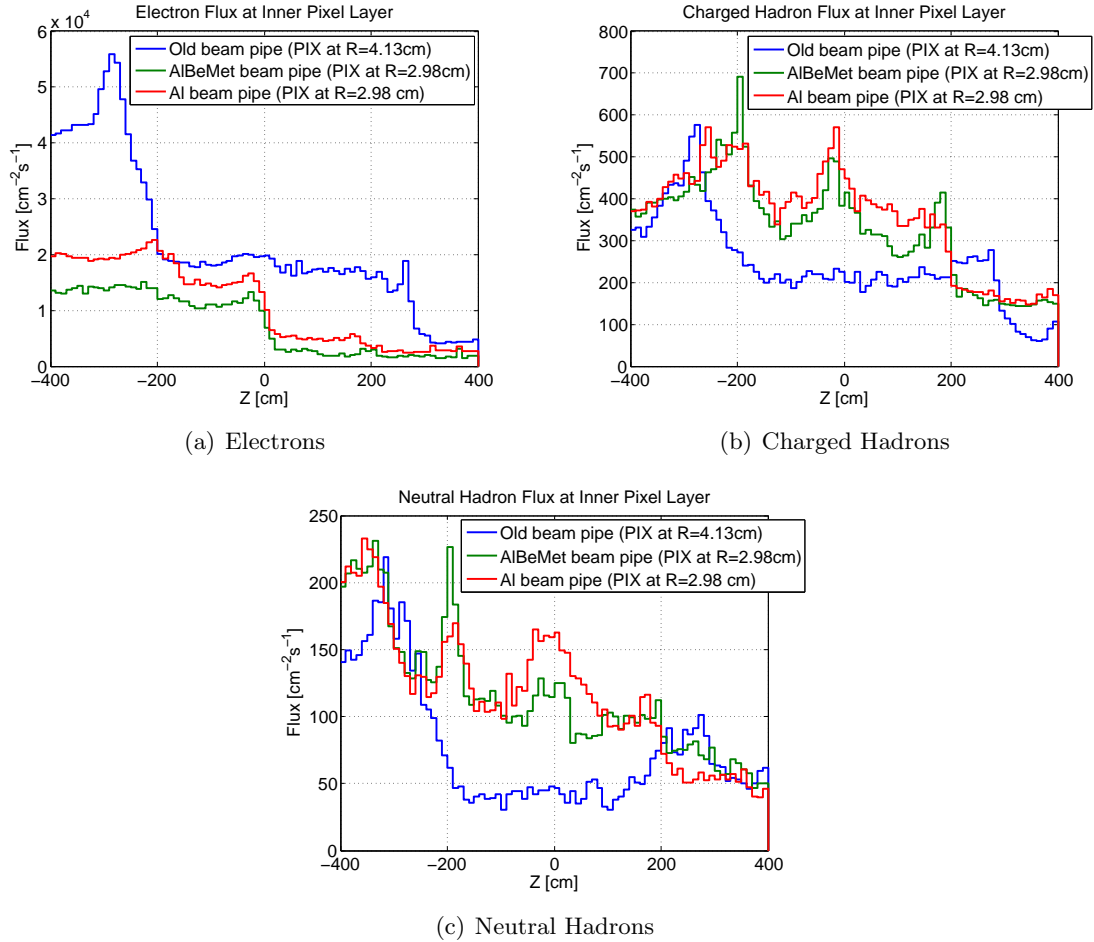


Figure 6.21.: Particle flux of electrons, charged hadrons and neutral hadrons due to machine induced background as function of Z at a radius which corresponds to the location of the inner most pixel layer (4.13 cm in the old geometry, 2.98 cm in the new geometry). Results for simulations with old beam pipe and new beam pipe, either in AlBeMet or in aluminum, are shown. The particle beam travels from positive Z to negative Z . The neutral and the charged hadronic fluence shows an increase by factor ~ 2 due to the decrease of position in R . The electron flux is decreased significantly, which is more dominant than the increase in hadronic flux. Inside the pixel detector volume (at $Z=0$) an increase in electron flux (from right to left) is observed, which is more dominant with the new beam pipe geometry. More high energetic particles interact inside the pixel and more electrons are created. The resulting flux is still lower than with the original geometry design.

Chapter 7.

Studies of Radiation Damage to the installed BCM Diamonds

The radiation hardness is one of the key arguments for the usage of diamond detectors. The performance of the BCML sensors in an intense radiation field is analyzed and presented in this chapter. It is one of the first hands on experiences with diamond detectors in a damaging environment and high particle rates. The change in signal efficiency is analyzed and compared with expectations, and the implications for the operation are shown. Polarization, the origin of the signal decrease, is analyzed in laboratory measurements.

7.1. Radiation damage of diamond

Diamond detectors are usually considered more radiation hard than silicon detectors. Diamond has, in comparison to silicon, a higher displacement energy, which is the amount of energy needed to kick an atom out of its position, making the production of a defect less likely. Secondly, carbon has a lighter nucleus than silicon. Carbon disintegrates under irradiation mostly into α -particles and light nuclei, while fragments of silicon are quite heavy, mostly it disintegrates into manganese, aluminum, sodium and neon. These heavy secondary nuclei are quite damaging and responsible for most of the produced defects [Boe09]. These considerations only take the production of defects into account. The performance of a detector under irradiation is also influenced by the other effects like radiation hardness of the contacts or electric field effects.

Radiation damage to diamond detectors has been studied extensively by various people including the RD42 collaboration [RD42, RD42a, Kag10]. An overview of the expected performance under irradiation will be given here.

7.1.1. Charge trapping

Under irradiation, the mean free path (MFP) of the charge carriers decrease, as more traps are generated inside the diamond, which leads to an increased charge trapping.

The number of defects N increases linearly with the fluence Φ :

$$N(\Phi) = N_0 + k_N \times \Phi \quad (7.1)$$

where k_N is a constant defining the number of traps generated per unit of fluence and N_0 the number of defects in the un-irradiated diamond.

The trapping time τ is inversely proportional to the number of defects N in the lattice:

$$\tau \sim \frac{1}{N} \quad (7.2)$$

By combining equations 7.1 and 7.2 one obtains:

$$\frac{1}{\tau(\Phi)} = \frac{1}{\tau_0} + k_t \times \Phi, \quad (7.3)$$

where k_t is a constant combining the proportionality of equation 7.2 and k_N , τ_0 is the trapping time in the un-irradiated sensor.

The MFP can be expressed as a function of the drift velocity v_{drift} and the trapping time τ :

$$MFP = v_{drift} \times \tau \quad (7.4)$$

If one assumes a constant drift velocity, equations 7.4 and 7.2 can be combined:

$$\frac{1}{MFP(\Phi)} = \frac{1}{\tau_0 \times v_{drift}} + \frac{k_t}{v_{drift}} \times \Phi \quad (7.5)$$

By combining k_t and v_{drift} into one final damage constant k one obtains:

$$\frac{1}{MFP(\Phi)} = \frac{1}{MFP_0} + k \times \Phi \quad (7.6)$$

Equation 7.6 is the commonly used parameterization for the radiation damage in diamond. The constant k depends on the impinging particle type and energy.

The MFP is not a parameter which can be measured directly. Usually the CCD is measured, which can be converted to a MFP using equation 3.5. If the MFP is smaller than the thickness of the diamond equation 7.6 can be rewritten using only the CCD:

$$\frac{1}{CCD(\Phi)} = \frac{1}{CCD_0} + k \times \Phi \quad (7.7)$$

In figure 7.1 the theoretical decay curves are calculated for a 400 μm thick diamond with an initial CCD of 200 μm and 400 μm . The simplified equation 7.7 is plotted in comparison with the more correct parameterization of the MFP using equation 7.6. The MFP is converted to the CCD for the given detector thickness. The legend gives the initial value of CCD or MFP depending on the used model. The MFP value is calculated for one charge carrier type and the same behavior for both charge carriers is assumed. The CCD includes the drift length of both charge carrier types and is therefore twice as big as the MFP for an infinitely thick detector. An initial CCD of 200 μm corresponds to an initial MFP of about 156 μm . Both curves are almost identical, hence the simplified CCD model is well justified for detectors with an initial CCD of half the detector thickness, like pCVD diamonds (CCE \approx 50%). For an initial CCD of almost the thickness of the detector (here 400 μm) a MFP much higher than the thickness has been assumed to obtain an equivalent CCD. The exact initial MFP is not relevant as long as it is significantly bigger than the thickness, here 10000 μm is used. The MFP model shows a slightly flatter decrease than the CCD model. The highest difference is about 10%, visible around a fluence of $5 \times 10^{15} \text{ cm}^{-2}$. Therefore even for a good sCVD detector, with an initial CCE of almost 100%, the difference of the simplified CCD model is negligible, given the usual uncertainties of measurements in test beam irradiations.

Irradiation studies of pCVD and sCVD diamonds have been performed by the RD42 collaboration. The measured CCD after various irradiation steps with 24 GeV protons is shown in figure 7.2, where a k factor of $0.7 \times 10^{-18} \text{ cm}^2 \mu\text{m}^{-1}$ was measured.

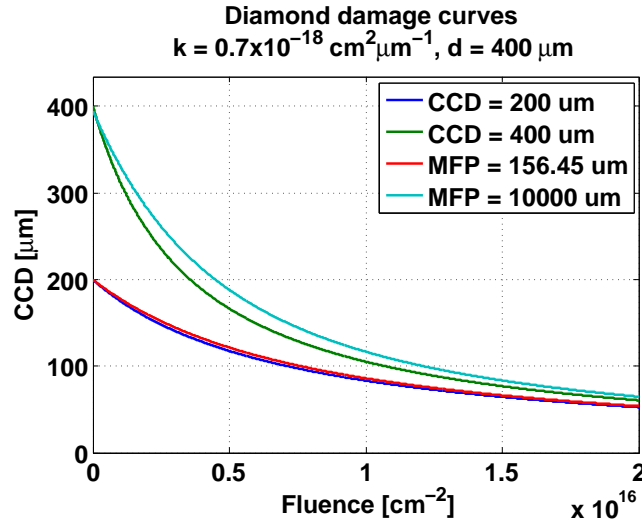


Figure 7.1.: Calculated decrease of charge collection distance (CCD) in a $400 \mu\text{m}$ thick diamond detector for different initial CCD. The simplified parameterization describing an hyperbolic decrease of the CCD is compared with the more correct model calculating a hyperbolic decrease of the mean free path (MFP) and converting it to a CCD value for the given thickness. Both models are similar for an initial CCD of $200 \mu\text{m}$. For an initial CCD of $400 \mu\text{m}$ the MFP model predict a about 10 % higher value than the CCD model, but both curves are fairly similar.

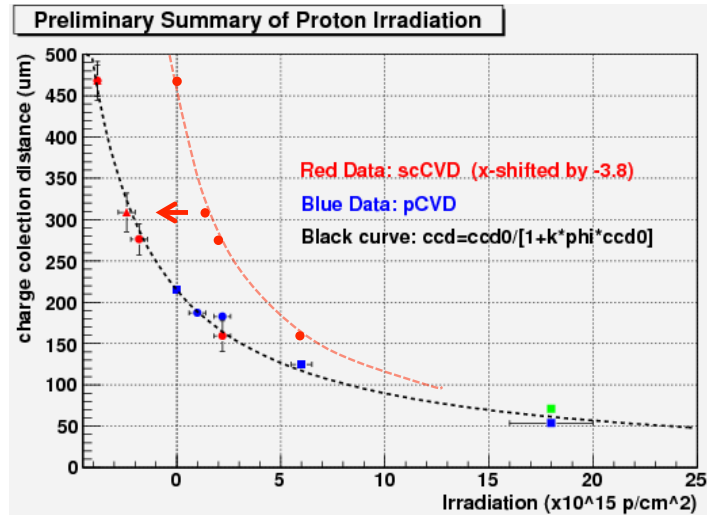


Figure 7.2.: Damage curve measured by the RD42 collaboration for irradiations of diamond with 24 GeV protons. The sCVD data is shifted to the left by $3.8 \times 10^{-15} \text{ p/cm}^2$. With this shift the data of the sCVD and the data of the pCVD lie on the same damage curve. Equation 7.7 is fitted to the data. The obtained damage constant is $k = 0.7 \times 10^{-18} \text{ cm}^2 \mu\text{m}^{-1}$.

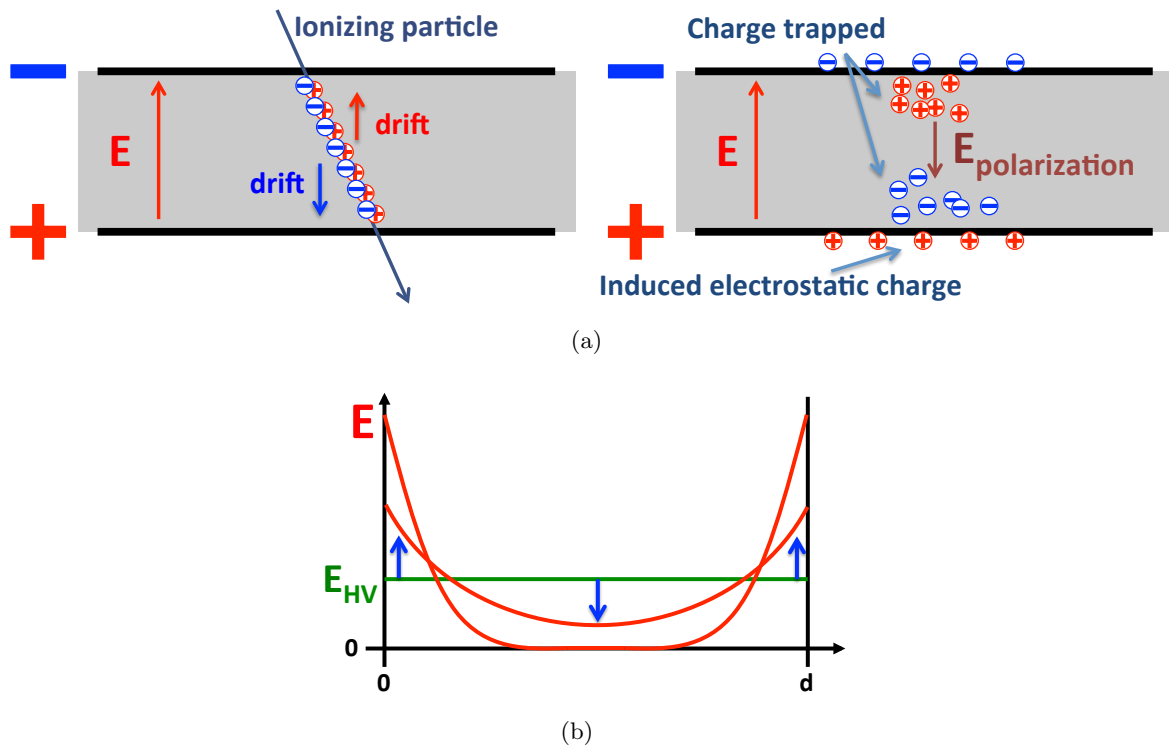


Figure 7.3.: Figure (a) visualizes the charge carrier during particle detection process. Electron-hole pairs are created along the path of the ionizing particle. They are separated by the electric field and drift in opposite direction. The highest hole concentration is at the cathode, the highest electron concentration at the anode. If charge carriers get trapped they form an electric field that counteracts the electric field due to the HV. The space charge in the build creates influenced charge on the electrodes which leads to an increase of electric field close to the electrodes. Figure (b) shows the electric field distribution in the bulk as the diamond polarizes. The integral over the electric field has to be conserved as the HV is externally applied. In the center of the bulk field free regions are created and lead to a decrease of effective detector thickness.

7.1.2. Polarization

Fixed space charge inside the diamond bulk deforms the electric field. This process is called “polarization”. Space charge is created, if charge carriers are trapped at local defects, which can occur inside the whole diamond bulk, or in the interface between diamond and metal electrode. For the explanation of the electric field effect a homogeneous trapping in the bulk is assumed.

The polarization effect is schematically explained in figure 7.3. Ionizing particles traversing the detector create electron hole pairs, which are separated by the electric field. The two types charge carriers drift along the electric field in opposite directions, which is the normal detection mechanism. Holes drift towards the cathode, which results in the highest hole density close to the cathode, and electrons drift towards the anode, which results in the highest electron density at the anode. The amount of trapped charge is proportional to the charge carrier density and hence the holes accumulate at the cathode and the electrons at the

anode. The electric field, formed by the trapped charge, counteracts the applied electric field, leading to an reduced field in the center of the diamond bulk. Since anode and cathode are connected to a current source they will charge up more due to electrostatic induction. The externally applied HV is conserved and so is the integral over the electric field. The reduction of the electric field in the center of the bulk is compensated by an increase in electric field close to the electrodes, shown in figure 7.3(b). The actual shape of the electric field is defined by the distribution of space charge, which itself is depending on the type and distribution of traps, the trapping and de-trapping times, and the rate at which charge carriers are created.

A reduced electric field is usually not a problem as long as the field is high enough to ensure the drift of the charge carriers. CCE measurements of un-irradiated diamonds have shown full charge collection even below $0.2 \text{ V}/\mu\text{m}$. Only when the electric field is almost zero the charge drift is not ensured. A reduction in signal strength occurs, if regions of almost no field are created. Therefore, polarization leads a reduction of the size of the active detector volume.

If polarization is the reason for the decrease of signal strength one can apply different techniques to reduce or even overcome the polarization:

1. **Increase HV:** If the HV is doubled the amount of trapped charge needed to form the same electric distribution is also doubled. With infinite HV reserves the signal could theoretically be completely recovered. In a given stable situation, where the diamond is strongly polarized, the signal output almost doubles, if the HV is doubled.
2. **Alternating HV:** If the HV changes polarity, the charge carriers change their direction of drift and they are trapped on the opposite side of the diamond bulk. If the traps are distributed homogeneously the distribution of the trapped charge will also be homogeneously. If the hole and the electron trapping are the same, they will compensate each other and no electric field deformation will happen. If the trapping for one charge carrier is more dominant a electric field deformation will still occur. However, field free regions cannot occur even in this case, since the whole bulk is charged up. Field free regions have a constant electric field, which requires the region to be free of charge.

The frequency at which the HV has to be flipped depends on the rate the charge is introduced into the diamond. During a measurement using a radioactive source (e.g. for CCD measurements) a frequency of about 0.1 Hz can be sufficient. In high rate environments, switching frequencies of several Hz might be necessary.

3. **Depolarization with light:** As wide band gap material, diamond is insensitive to visible light. Only UV light has enough energy to excite diamond. Charge traps are levels inside the band gap and their distance to the valence or the conduction band is relatively small. Light that does not have enough energy to create ionization can still de-trap the charge and hence remove polarization. Applying light on the diamond removes polarization, but, depending on the particle environment, high amount of light might be needed to clear the polarization.

Polarization can exist in un-irradiated detectors due to charge traps created during growth process, or due to a bad contact between diamond and metal electrodes. A good quality diamond detector does not polarize prior to irradiation. Under irradiation, traps are created inside the bulk material, which can contribute to polarization. It is therefore a radiation damage effect, which may not contribute to the decrease of charge collection efficiency in weak particle field environments, but shows up in an intense radiation field.

The strength of the polarization is influenced by many parameters: Number of traps in the diamond, type of traps, distribution of traps, trapping and de-trapping times, and the radiation environment. In a stable operating situation, a balance between trapping and de-trapping develops. The amount of trapping is defined by the amount of charge deposited in the diamond, hence the strength of the polarization and the strength of the signal is depending on the particle rate environment.

7.2. Simulation of polarization

7.2.1. Electric field calculations

To show in further detail how the electric field changes in a polarized diamond, a more detailed calculation is performed. A simple model is set up, where the strength of trapping and de-trapping is configured. A charge carrier density corresponding to the situation in a MIP environment is assumed to calculate the distribution of trapped charge and the electric field. For a given electric field a signal is calculated that an alpha particle would generate in such a detector. This can be compared to measurements using the transient current technique (TCT).

The calculation of the distribution of the fixed space charge is based on the following assumptions:

1. Calculations are done in one dimension through the diamond bulk. For correct normalization of the parameters a detector size of $1 \mu\text{m}^2$ is assumed.
2. Electrons and holes are generated homogeneously inside the bulk. Due to the electric field they are separated, which means that the hole density is highest at the cathode and zero at the anode with a linear increase. For electrons its vice versa. The linear dependence can be motivated when a charge collection distance of almost the thickness of the diamond is assumed.
3. The trapping mechanism is not simulated. The relative amount of trapping for holes and electrons can be configured. Even for one charge carrier type the strength of the trapping can be varied over the location of the bulk, e.g. to configure a stronger trapping close to the electrodes. The configured number is arbitrary and regulates the fraction of the charge carriers adding to the trapped space charge.
4. Above an electric field of $0.01 \text{ V}/\mu\text{m}$ charge carriers are separated by the electric field, below the induced charge can recombine. The diamond volume with electric field below $0.01 \text{ V}/\mu\text{m}$ is considered inactive. Charge entering the inactive volume is considered as stopped and non existent.
5. Since polarization effects seem to be of a problem much before the CCD reduces significantly, it is assumed that the charge carriers drift through the whole active volume for the estimation of the detector efficiency. For the calculation of the TCT pulse at a later stage the trapping is included.
6. The charge build up is calculated iteratively. Every step an arbitrary number of charge induced and trapped. The amount of charge was chosen small enough to achieve a realistic development of the electric field.

	Electrons	Holes
E_c [V/ μm]	0.578	0.570
v_{sat} [$\mu m/ns$] (Pomorski)	263	157
v_{sat} [$\mu m/ns$] (sCVD_2011)	225	132
β	0.42	0.81

Table 7.1.: Parameters for the parametrization of the drift velocity (equation 7.9). Two values for v_{sat} are given. The measurement of M. Pomorski for unirradiated sCVD detectors[Pom08], and the measurements done with the irradiated sCVD_2011. E_c and β are also taken from Pomorski's measurement.

7. A small fraction of charge is removed every step to simulate the de-trapping. The amount of the de-trapping is a free parameter in the calculation. It is necessary to include this in the simulation to avoid negative electric fields in asymmetric simulations (more trapping of one charge carrier type compared to the other), but reasonable amount of de-trapping does not affect the general outcome of the simulation.

Every iteration step the electric field E is calculated by integrating over the space charge $\rho(x)$ (Gauss's law):

$$E(x) = \frac{1}{\epsilon_0 \epsilon_r} \int \rho(x) dx, \quad (7.8)$$

where ϵ_0 is the vacuum permittivity and ϵ_r the relative permittivity (for diamond $\epsilon_r = 5.7$ is used). The integral over the electric field is conserved by the applied high voltage. A reduction in electric field due to polarization is compensated by additional charge on the electrodes, leading to an increase in electric field by a fixed amount. The field free regions are calculated from the electric field distribution. This is an input for the following iteration step, since the charge cannot drift in these regions.

7.2.2. Simulation of TCT pulses

Once the electric field distribution is calculated, a TCT pulse can be estimated. A model to transport charge through the diamond bulk was established.

The drift velocity v_{drift} as function of the electric field is modeled by the Caughey-Thomas model[Cau67]:

$$v_{drift}(E) = v_{sat} \frac{E/E_c}{(1 + (E/E_c)^\beta)^{1/\beta}} \quad (7.9)$$

v_{sat} , E_c and β are the fit parameters of the model. The used parameters, shown in table 7.1, were taken partially from [Pom08], which is a good parameterization for an unirradiated diamond. Figure 7.4 shows the drift velocity as function of electric field. This parameterization is used to simulate the diamonds sCVD_test1 and sCVD_2012. In section 7.8.3 it will be shown that the mobility of the charge carriers in the sCVD_2011 is lower than the measurements performed with unirradiated detectors. The saturation velocity v_{sat} was lowered for the curves to match the data. Unfortunately only two measurement points were available and hence a proper fit of the model was not possible. This modified parameters are used for the simulation of sCVD_2011.

Important for the signal shape at low fields is also the trapping. Since the trapping process is not modeled, the effects are estimated the following way: The measured CCD as function of HV (see chapter 7.7) was converted to MFP as function of the location in the diamond for

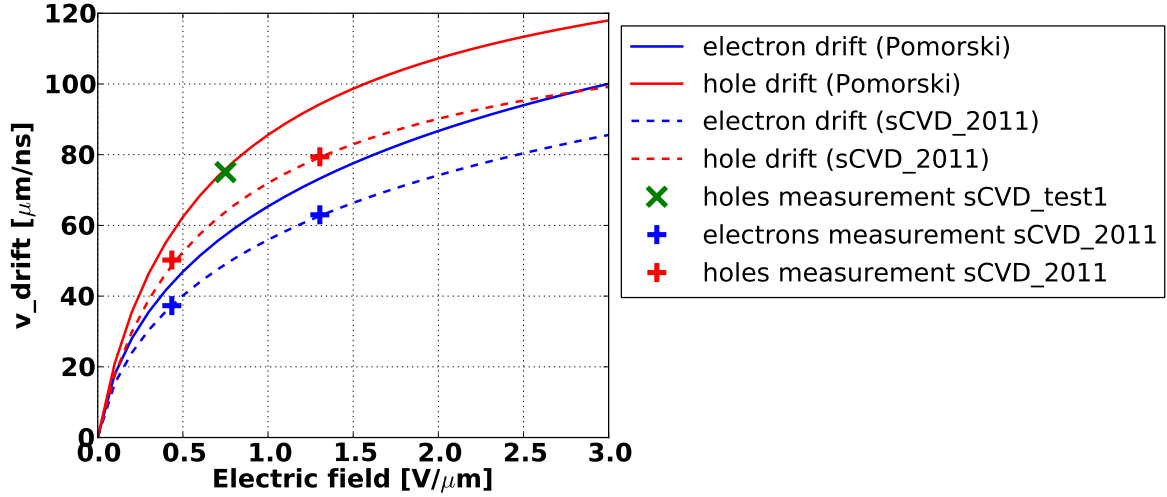


Figure 7.4.: Drift velocity of electrons and holes as function of electric field. The solid lines are the parameterization taken from [Pom08]. For parameterization shown by the dashed lines the saturation velocity was reduced to match the measurements taken with the sCVD_2011 diamond (see section 7.8.3).

a given electric field distribution using equation 3.5. The amount of charge carriers decrease exponentially in case of a constant trapping probability. The MFP as material parameter is the distance where the charged is trapped by half its original amount. Hence the trapping can be calculated by:

$$\delta_f = e^{-\frac{x_{\text{step}} \ln(2)}{MFP}}, \quad (7.10)$$

where x_{step} is the distance of the charge carrier drifted in the iteration step and δ_f the fraction of charge carriers that are still free after the iteration step. The used CCD measurement is from the sCVD_2011 after irradiation (figure 7.32(b)), as this diamond was used for TCT measurements and will be compared with the simulation. The trapping parameters can be easily adapted for any diamond.

Longitudinal diffusion is also relevant, especially for low field regions. The diffusion is described by Fick's second law:

$$\frac{\partial c}{\partial t} = D \frac{\partial^2 c}{\partial x^2}, \quad (7.11)$$

where c is the concentration along x and D the diffusion constant with a dimension of [length²time⁻¹]. For one step in time, the charge in every bin in x is transported separately. The charge in one bin is considered to be distributed in a delta function. The solution of equation 7.11 for a delta function is a gaussian curve:

$$c(x, t) = \frac{Q}{\sqrt{4\pi Dt}} e^{-\frac{x^2}{4Dt}}, \quad (7.12)$$

where Q is the total charge in the initial bin. The diffusion constant D is calculated using the Einstein relation:

$$D = \mu k_B T / q, \quad (7.13)$$

where μ is the mobility of the charge carriers, which is calculated from dividing the drift velocity by the electric field. q is the charge of the particles, which is one, since the simulation

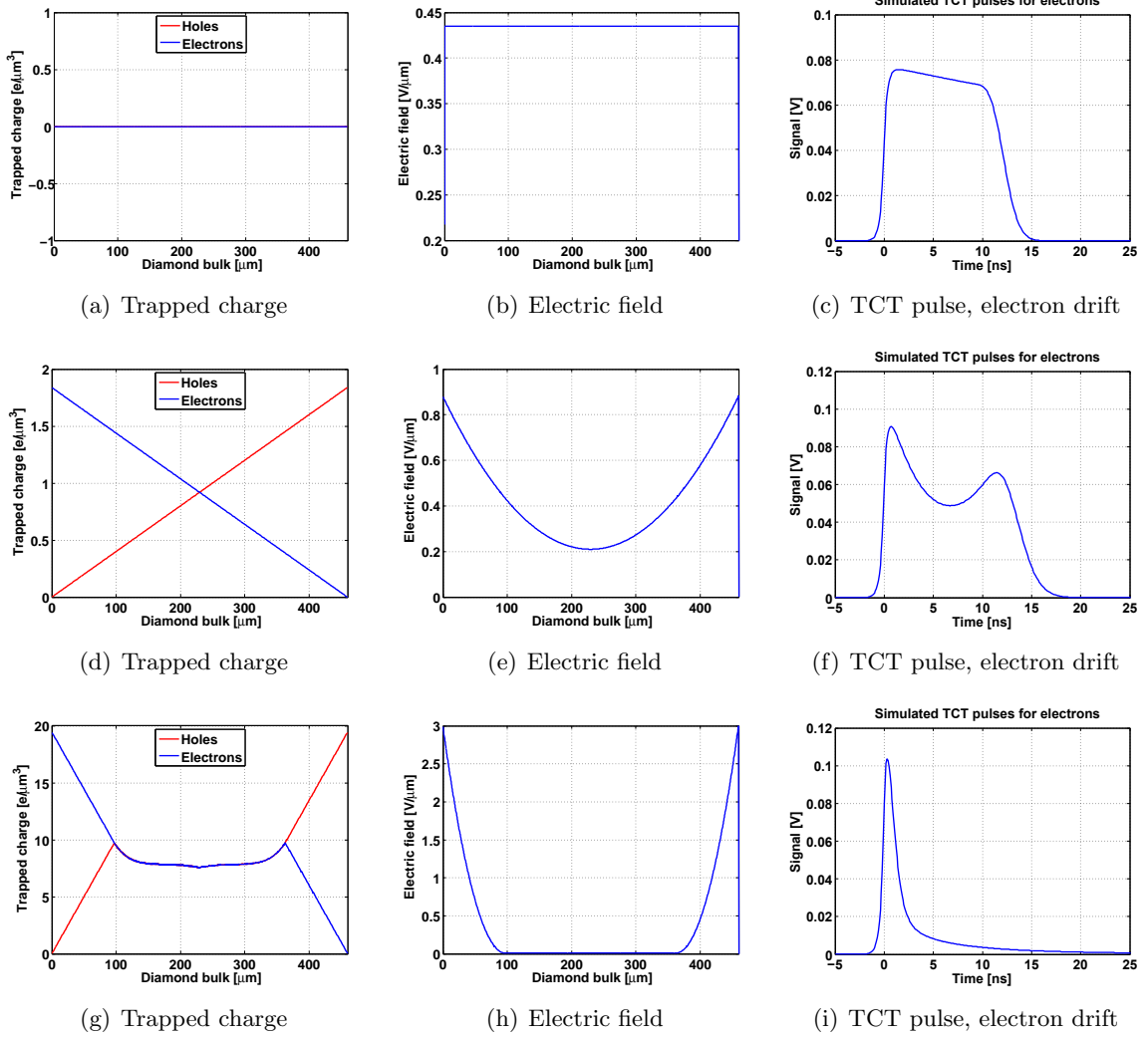


Figure 7.5.: Simulation of space charge, electric field and TCT pulse for an unpolared detector (figures (a) to (c)), a slightly polarized detector (figures (d) to (f)), and a highly polarized detector, where the electric field is reduced to zero in the center of the bulk (figures (g) to (i)). The same amount of trapping for electrons and holes is assumed.

	Section 1	Section 2	Section 3	Total
CCD ₀ [μm]	441	334	258	369
k' [$\text{steps}^{-1}\mu\text{m}^{-1}$]	2.96×10^{-9}	1.32×10^{-9}	0.72×10^{-9}	1.29×10^{-9}

Table 7.2.: Results of all hyperbolic fits shown in figure 7.6

calculates in units of elementary charge. Unfortunately, it was not possible to match the simulation to the measurements, as a stronger longitudinal diffusion was observed. The diffusion constant had to be increased by a factor 30 to match the measurements. Most likely the difference is due to additional effects, which are not taken into account in this simulation, causing the charge cloud to disperse. One effect that could be responsible is the coulomb repulsion of charge carriers against each other.

The charge drift is converted to a TCT pulse, as it would be measured with the detector setup used for this thesis. The current is amplified by 50 dB and converted to a Voltage measured by the Oscilloscope at a 50Ω input impedance. A low pass filter with 1 GHz cut-off frequency was applied to the signal to simulate the bandwidth limitation of the measurement system.

Figure 7.5 shows the result of an example simulation. 2×10^6 iteration steps were simulated. At three different steps the trapped charge and the electric field is plotted. Additionally a TCT pulse was simulated. Figures 7.5(a) to (c) show the situation of an unpolarized detector. There is no charge inside the bulk and the electric field is constant. The TCT pulse is almost a square pulse, only slightly decreasing due to charge trapping. In figures 7.5(d) to (f), the situation is shown, where the electric field is deformed, but no zero field region is created yet. The TCT pulse is deformed due to the low field in the center of the diamond and reveals a double peak. The second peak arises when the charge carriers drift through the high field region on the opposite side of the bulk. In figures 7.5(g) to (i) the results at the end of the simulation is shown. The electric field reached zero in the center of the bulk. The amount of electrons and holes trapped in the zero field region has to be the same, as this region also has to be free of net charge. The TCT pulse is now a single short spike, since the charge is stopped in the zero field region.

7.2.3. Simulated decrease of CCD with polarization buildup

If a diamond detector is operated polarization free, the decrease in CCD due to radiation damage is an effect of the trapping of charge carriers at local defects. In case of polarization buildup, the MFP is not significantly reduced, but, due to the polarization, field free regions are created. The reduction of CCD is therefore a result of reduction of effective detector thickness. The effective detector thickness is calculated for each iteration step of the electric field simulation. Figure 7.6 shows the decrease of the active region as function of iteration steps in the same example simulation as shown in figure 7.5. A hyperbolic fit equivalent to equation 7.7 was applied. The fit does not match the simulation well. The decrease of the simulated data is steeper in the beginning, but is more flat at the latter part, compared to the fit. The simulation was split into three parts and the hyperbolic fit was applied to the parts only, also shown in figure 7.6. The partial fits have lower residuals, but still the shape of the data is not well reproduced. The k factors obtained in the partial fits decrease with higher fluence. A hyperbolic decrease is of course not expected, as the effect responsible for the signal decrease is not described by the trapping model, which would suggest a hyperbolic decrease.

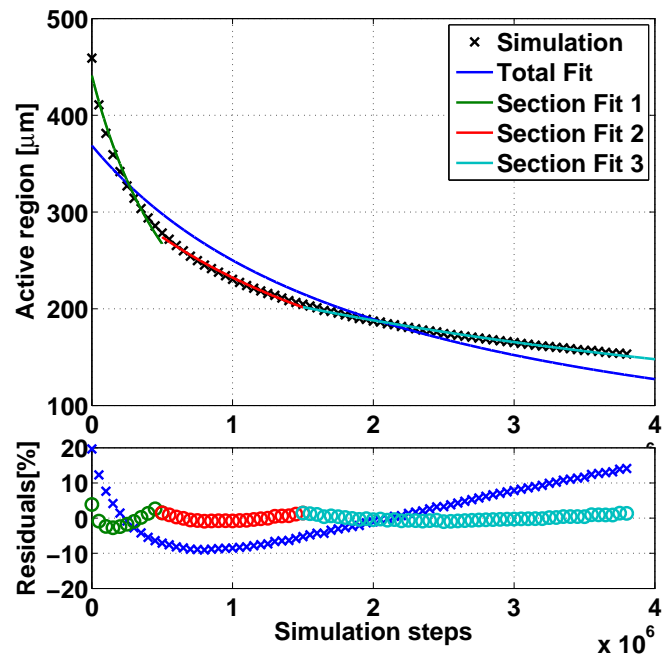
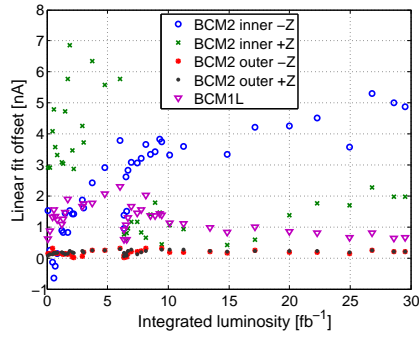
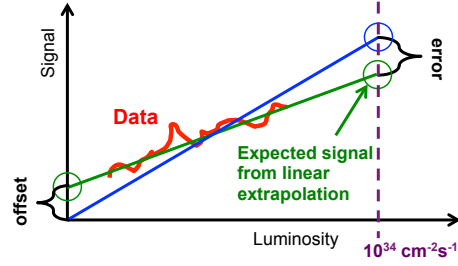


Figure 7.6.: Fits to decrease of active detector volume due to polarization. A hyperbolic fit function is used, which does not describe the data well, indicating a decrease in k factors with stronger polarization. The change in k factors is shown by dividing the data in three parts and fitting the hyperbolic curve to these sections. The k factors decrease with higher fluence.



(a) Offsets of the linear fit to each analyzed fill.



(b) Error estimation based on the offset from the fit.

Figure 7.7.: The offset of the linear fit applied to the data of each fill is plotted as function of the integrated luminosity (figure (a)). It shows a significantly higher value than the noise of the system, which is usually a few pA. This shows that the perfect linearity of the system is not given. For some channels a drift in offset is visible which can be due to a increased non linearity with higher radiation damage, and due to different instantaneous luminosities. The offset can be seen as measure of error to the linear extrapolation of the signal to nominal luminosity. An error value to the extrapolation of the expected signal to nominal luminosity is calculated by extrapolating a zero constrained linear fit to nominal luminosity and using the difference as error estimation.

7.3. Decrease of signal efficiency of the BCML detectors with increasing integrated luminosity

Although diamond detectors should be very radiation hard and no significant degradation of the performance was expected in the first years of LHC operation [Mül11], the signal efficiency of the BCML detectors was monitored. This chapter analyzes and quantifies the decrease of the signal efficiency.

7.3.1. Normalization of data to instantaneous luminosity.

The particles hitting the diamond detectors are almost entirely collision products. The signal from beam background is negligibly small. The detector signal is therefore, to the first order, proportional to the instantaneous luminosity. The collision rates at LHC and hence the signal in the BCML detectors is not constant, but vary over the duration of a fill, as shown in section 5.1. To compare the detector efficiency over all fills the normalization is done the following way:

The data is analyzed on a fill by fill basis. The fills, selected by hand, should be long enough to cover a wide range of luminosity values, there should be no beam loss events giving rates above the normal beam background, and the data taking was checked to be valid for the whole fill. For every selected fill, the data from the BCML detectors is plotted with respect to the official CMS offline luminosity, measured by the HF detector. A linear fit is applied to the data and the expected detector signal at nominal luminosity ($10^{34} \text{ cm}^{-2}\text{s}^{-1}$) is extrapolated.

This method of normalization has certain errors:

7.3. Decrease of signal efficiency of the BCML detectors with increasing integrated luminosity

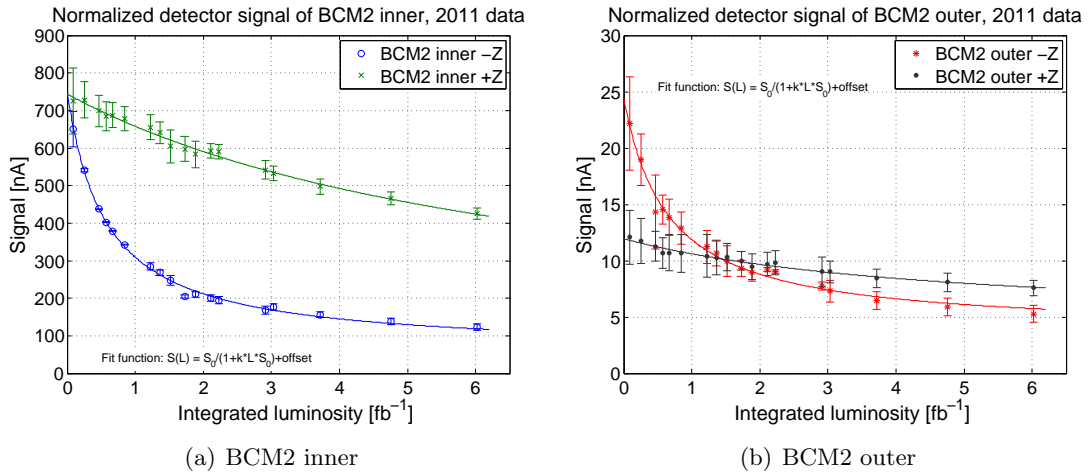


Figure 7.8.: Signal of the BCM2 detectors, averaged per detector group, normalized to a instantaneous luminosity of $10^{34} \text{ cm}^{-2}\text{s}^{-1}$ as function of the integrated luminosity. The highest signal at zero integrated luminosity is measured by the BCM2 inner detectors. The highest radiation damage was observed on the BCM2 on the -Z end. Charged particles are numerous at the inner detectors give a high signal but since they are mostly electrons their damage potential is fairly low. The neutrons flux at BCM2 -Z is very high due to the CASTOR detector is responsible for the high radiation damage, but the signal from the neutrons is quite small.

- The error on the linear fit can be propagated to an error value on the extrapolated value. This error is comparably small.
- The linear fit has a certain offset value, which is not consistent with the linearity of the system. This offset, shown in figure 7.7(a), ranges between -1 nA and 7 nA and is much bigger than the noise values observed during inter-fill periods, which are negligibly small. This offset is a measure of the non linearity of the system. An error value to the extrapolated signal is calculated by constraining the linear fit to a zero offset and extrapolating to the same instantaneous luminosity, where the nominal luminosity of $10^{34} \text{ cm}^{-2}\text{s}^{-1}$ was chosen. This number is used as a worst case systematical error. This is the dominant error of about 10-20%. Figure 7.7(b) visualized how this error is calculated.

The total error on the normalized values for each analyzed fill is obtained from adding both error values in quadrature. The error value can differ significantly from fill to fill. Fills with low instantaneous luminosity have usually a higher error since the extrapolation to nominal luminosity extends over a wide range.

7.3.2. Observed decrease in signal strength.

Although there are 40 BCML channels, many detectors are placed in the same radiation environment due to the Φ symmetry of the CMS detector. The signal from all detectors within one group of the detectors in the same radiation environment is averaged. The five groups are: BCM1L, BCM2 inner +Z, BCM 2 inner -Z, BCM2 outer +Z, BCM2 outer -

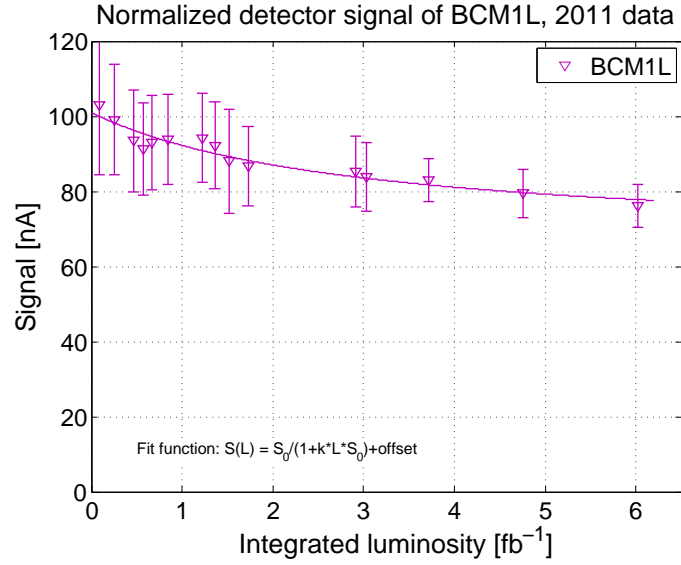


Figure 7.9.: Signal of the BCM1L detectors, averaged per detector group, normalized to a instantaneous luminosity of $10^{34} \text{ cm}^{-2}\text{s}^{-1}$ as function of the integrated luminosity. Only a very small decrease in signal was measured.

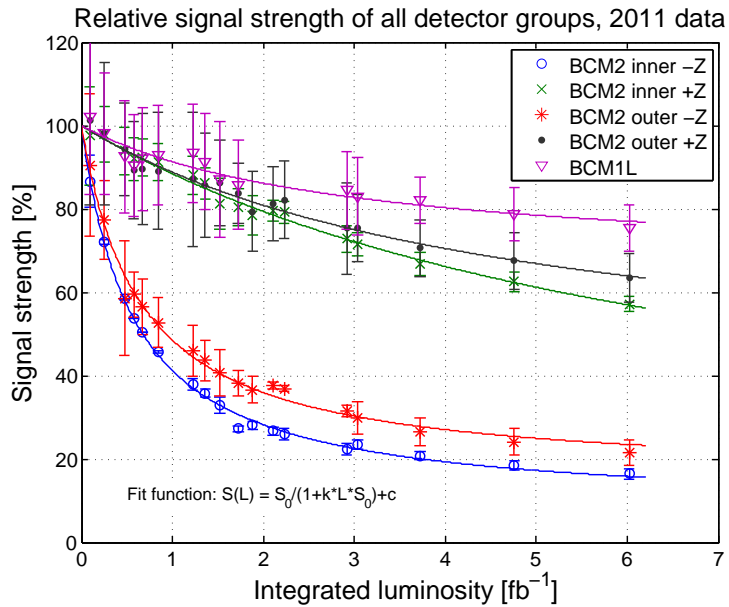


Figure 7.10.: Signal strength of BCM detectors relative to the signal of the unirradiated detectors as function of integrated luminosity for the 2011 running period.

7.3. Decrease of signal efficiency of the BCML detectors with increasing integrated luminosity

Z. BCM2 on -Z and +Z are placed in different radiation environment since the CASTOR detector was installed only on the negative end, giving rise to a higher neutron flux on the -Z end (see chapter 6.4.2)

For every analyzed fill the integrated luminosity over all previous fills is calculated from the CMS offline luminosity. The normalized signal strength for each fill is calculated as described in section 7.3.1 and plotted as function of the integrated luminosity. The data from 2011 for every detector group can be found in figure 7.8 and 7.9. Also plotted is a fit to the data using a hyperbolic function with an offset. This function qualitatively matches the decrease. A more detailed view on the decay function is given in the appendix B. A decrease in signal strength is visible in all detectors. It is most pronounced in BCM2 on the -Z end, for the inner and the outer detectors. The least decrease was observed in BCM1L.

The signal observed in the BCM2 inner detectors at zero integrated luminosity is very similar comparing the detectors on +Z and on -Z (see figure 7.8(a)). Both groups of detectors gave about 700 nA normalized detector current before the radiation damage effects started. The behavior as a function of integrated luminosity is different, since the detectors on -Z receive a much higher neutron flux due to the CASTOR detector mounted behind the BCM2 wheel. Neutrons have a very low interaction cross section and give therefore only a very low contribution to the signal. The signal of the BCM2 outer detectors is lower by roughly a factor of 40, since they are shielded from the IP by the hadron forward calorimeter (see chapter 6.4.2). Here the particles created by CASTOR give a significant signal compared to the low signal from the IP and a difference in BCM2 outer +Z and -Z is visible (figure 7.8(b)).

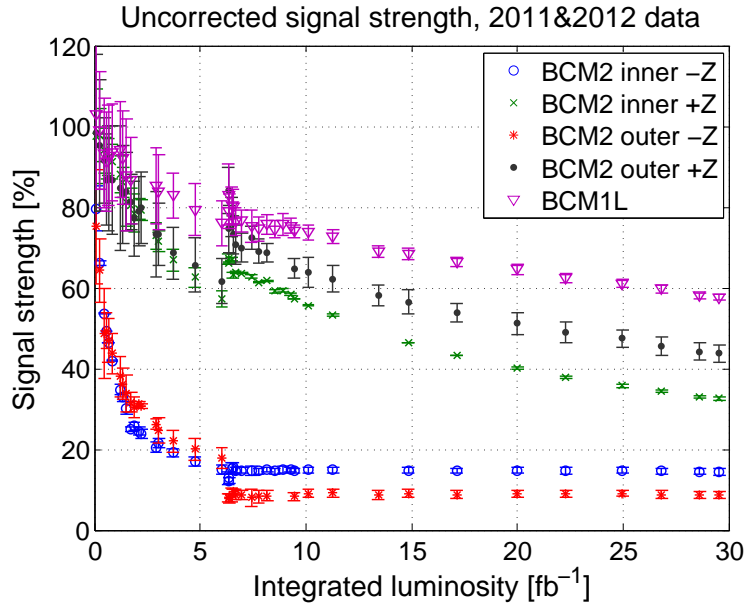
The relative change of the signal strength is plotted in figure 7.10 for all detector groups. For the definition of 100% signal strength the signal of the unirradiated detectors is used. As exact value the number from the fit at zero integrated luminosity is used, since the data points at the beginning have quite high errors. The relative change in signal strength is comparable between inner and outer detectors of BCM2, although the measured detector signal was significantly different.

The simulated neutron energy spectra are presented in figure 6.12(a). The amount of radiation damage is correlated with strength of the neutron fluence. The BCM2 detectors on -Z receive the highest neutron fluence, where also the highest damage is observed. While BCM2 on the +Z end receives an intermediate fluence and experiences an intermediate amount of damage, the BCM1L detectors receive the least amount of neutrons and experience the least amount of damage.

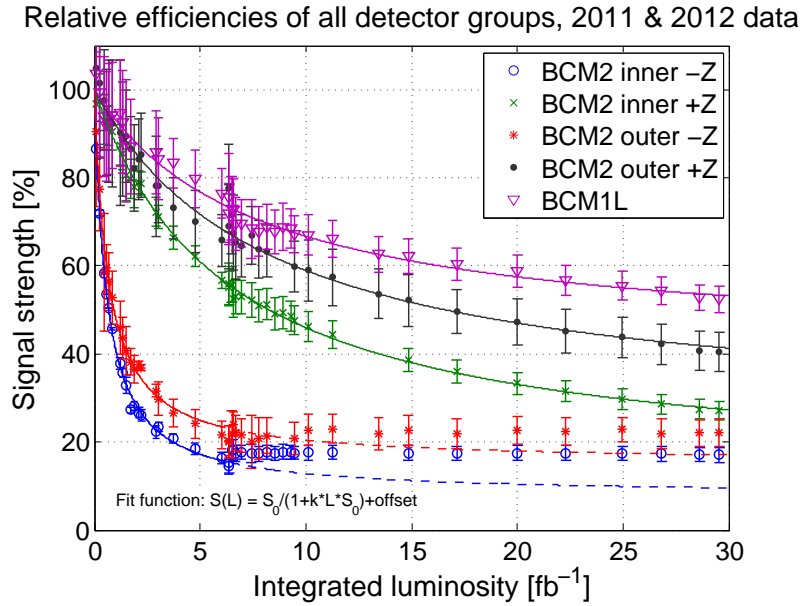
Comparison of 2011 and 2012 data

With the 2012 run the radiation environment changed at the BCML detector locations: The collision energy of the LHC increased from 7 TeV to 8 TeV, giving a slightly (about 10%) increased radiation field at all BCM detectors, for both signal and radiation damage. The CASTOR detector, which was the main source of damaging neutrons for BCM2 -Z, was removed. This resulted in a decrease of albedo neutrons in that location. The amount of radiation damage decreased significantly. Due to the small interaction cross-section of neutrons with the diamond detector the signal rates decreased only slightly due to this.

In order to compare the signal efficiencies of 2012 with 2011, the data has to be corrected. The results for the expected detector signal from the FLUKA simulations for the 2011 and the 2012 case presented in chapter 6.4.2, table 6.1, are used for this. The ratios of the results for both simulation runs give the correction factors to scale the 2012 data to the level of the 2011 data. The statistical error on the simulation gives an additional error on the data points



(a) Signal strength over 2011 and 2012 of the BCML detectors uncorrected for the change in radiation environment.



(b) Signal strength corrected for the change in radiation environment using FLUKA simulation results.

Figure 7.11.: Relative signal strength of BCM detectors as function of integrated luminosity for the 2011 and 2012 running period up to a total of 30 fb^{-1} . The change in radiation environment results in a change in signal compared to luminosity. The 2012 data corrected using FLUKA simulation results, and brought to the same level as the 2011 data. The hyperbolic fit to the data of BCM1L and BCM2 +Z tracks the decrease of the efficiencies of these detectors. The slope of the BCM2 detectors on the -Z end changed significantly. This is shown by extrapolating the 2011 fit to the full axis. A decrease is not measurable any more for BCM2 -Z.

7.3. Decrease of signal efficiency of the BCML detectors with increasing integrated luminosity

for 2012.

Figure 7.11(a) shows the uncorrected data of 2011 and 2012. In figure 7.11(b) the same data is shown, where the data from 2011 is not changed, but the data from 2012 was corrected to match the signal height to the 2011 data. In 2013 only heavy-ion collisions and proton-proton collisions at intermediate energy were done at the LHC and this data is not used. The decrease of the signal efficiency continued in 2012 for BCM1L and BCM2 on +Z. The hyperbolic fit continues to track the decrease of the signal. The detectors of BCM2 -Z did not experience a decrease in signal over 2012. The fit to the 2011 data is extrapolated and does not agree with the data in 2012 any more. This is expected since the CASTOR detector was removed, and with it a significant source of damage. Although the radiation field in 2012 is now comparable between BCM2 on +Z and -Z, the decrease is different. BCM2 on -Z is already heavily damaged in 2011 and is now on the rather flat part of the hyperbolic curve, while BCM2 +Z is still on the steeper slope and therefore showing more degradation with the same amount of particle fluence.

The HV of the diamonds was 200V during the whole time, which corresponds to an electric field of about $0.5 \text{ V}/\mu\text{m}$. The signal can be recovered by increasing the HV, but this was not done since enough signal was still measured for the main purpose of the BCML detector. Also the risk of erratic dark currents increases with higher HV, which can lead to false beam aborts,

Single crystal diamond

At the same location as BCM2 inner on +Z a prototype single-crystalline CVD diamond (sCVD) was installed during 2011. This diamond has a different metallization than the pCVD, as explained in chapter 4.1. This diamond was replaced with a new sCVD diamond in the 2012 run. In figure 7.12 the measured detector current for both sCVD and the regular pCVD diamond installed at the same location is plotted, including the hyperbolic fit. The signal is normalized to the size of a detector with $1 \times 1 \text{ cm}^2$ and $400 \mu\text{m}$ thickness. The initial signal of the sCVD detectors is significantly higher than the signal of the pCVD detector. One can see that the sCVD loses the signal faster than the pCVD. This is expected, since the relative increase in traps is higher in a sCVD compared with a pCVD, which already has many traps in an un-irradiated state and acts like a pre-damaged sCVD diamond. Therefore the pCVD decreases along the rather flat part of the hyperbolic curve.

As earlier mentioned, there is also a difference in the metallization between the pCVD diamond and the sCVD diamonds. The influence of the metallization on the signal loss, comparing two detectors with the same bulk material but different metallization, has not yet been quantified.

7.3.3. Radiation damage constant

The 24 GeV proton equivalent fluence was simulated with FLUKA for all BCML diamond location for 2011 and 2012 as shown in chapter 6.4.2, table 6.2. This can be used to scale the data to be a function of the equivalent fluence. The fluence is not the actual fluence of the mixed particle field, but the given fluence of 24 GeV protons creates the same radiation damage as the particle field the detector is placed in. A different scaling factor is applied for the 2011 and the 2012 data, as obtained with FLUKA.

The CCD of the detectors was measured prior to installation and the signal output can be scaled to a CCD using the signal of the un-irradiated sensor. An initial CCD of $200 \mu\text{m}$ is used for all detectors, which is a reasonable average for pCVD detectors of about $400 \mu\text{m}$

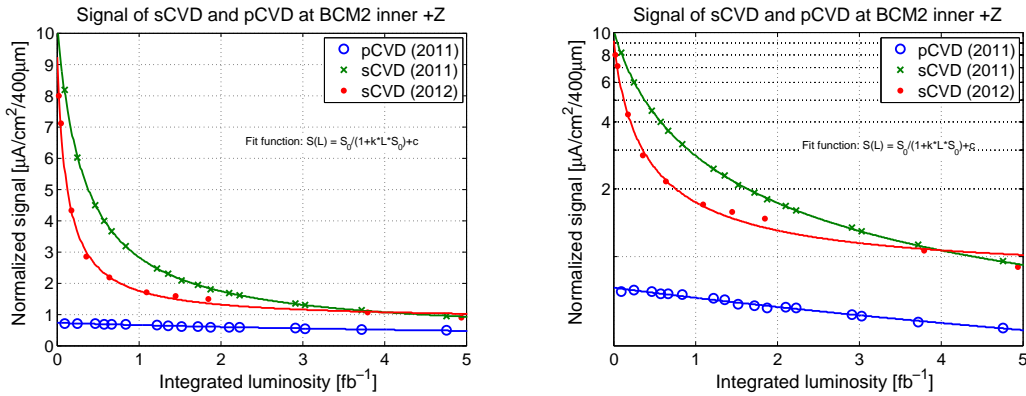


Figure 7.12.: The measured detector current, normalized to detector size, of the two prototype single crystal diamond and a poly crystal diamond at the same location as function of integrated luminosity. The sCVD detectors show significantly more initial signal than the pCVD, but the sCVD signal decreases faster. Both plots show the same data, but the right plots has a logarithmic y-axis to better show the behavior at lower values.

thickness. The signal efficiency is then multiplied with the initial CCD to obtain the the CCD values during the irradiation process.

Scaling the data in this way, it can be visualized as $CCD(\Phi)$. This makes it possible to directly compare the curves with the decay curves expected from testbeam irradiations. Since the equivalent fluence is normalized to 24 GeV protons, the decrease should be the same as the decrease measured in irradiations with 24 GeV protons.

According to studies by RD42, the decrease in CCD as function of fluence is the same for all types of diamond, only the initial CCD differs between a pCVD and a sCVD diamond. The radiation damage constant k of the hyperbolic fit for a given type of impinging particle and energy is always the same for any type of diamond. Figure 7.2 shows the decrease of CCD as function of fluence for irradiation with 24 GeV protons. The damage constant measured in this study is $k = 0.7 \times 10^{-18} \text{ cm}^2 \mu\text{m}^{-1}$.

Figures 7.13, 7.14 and 7.16 show the data scaled to $CCD(\Phi)$ for the pCVD and the sCVD detectors. A hyperbolic fit (equation 7.7) over the full dataset is applied. Also included are fits of the hyperbolic curve over selected parts of the data, where the data was split into three parts. The hyperbolic fit is not a good fit function, as the fall-off of the data is steeper in the first part and in the latter part the reduction is less strong than a hyperbolic decay would imply. The fits to selective parts are closer to the data, as shown by the residuals, but the k factors obtained in the section-fits decrease with higher fluence.

Table 7.3 gives the results of the data fit. The k factors obtained range between 1.79×10^{-17} to 5.91×10^{-17} with an average of 3.8×10^{-17} . Compared the RD42 expectation this result too high by a factor of 58. The results from the sCVD diamonds is 9.22×10^{-16} , which about is factor 1500 higher than the RD42 expectation. There is a significant difference between the pCVD and the sCVD diamond.

The RD42 damage curve is measured in a low rate environment. The detectors are likely to be polarization free, so the decrease in CCD is only due to charge trapping at defects. The much stronger decrease, and the fact that the decrease is not described by an hyperbolic curve, lead to the conclusion that the decrease of signal strength is not due to charge carrier

7.3. Decrease of signal efficiency of the BCM2 detectors with increasing integrated luminosity

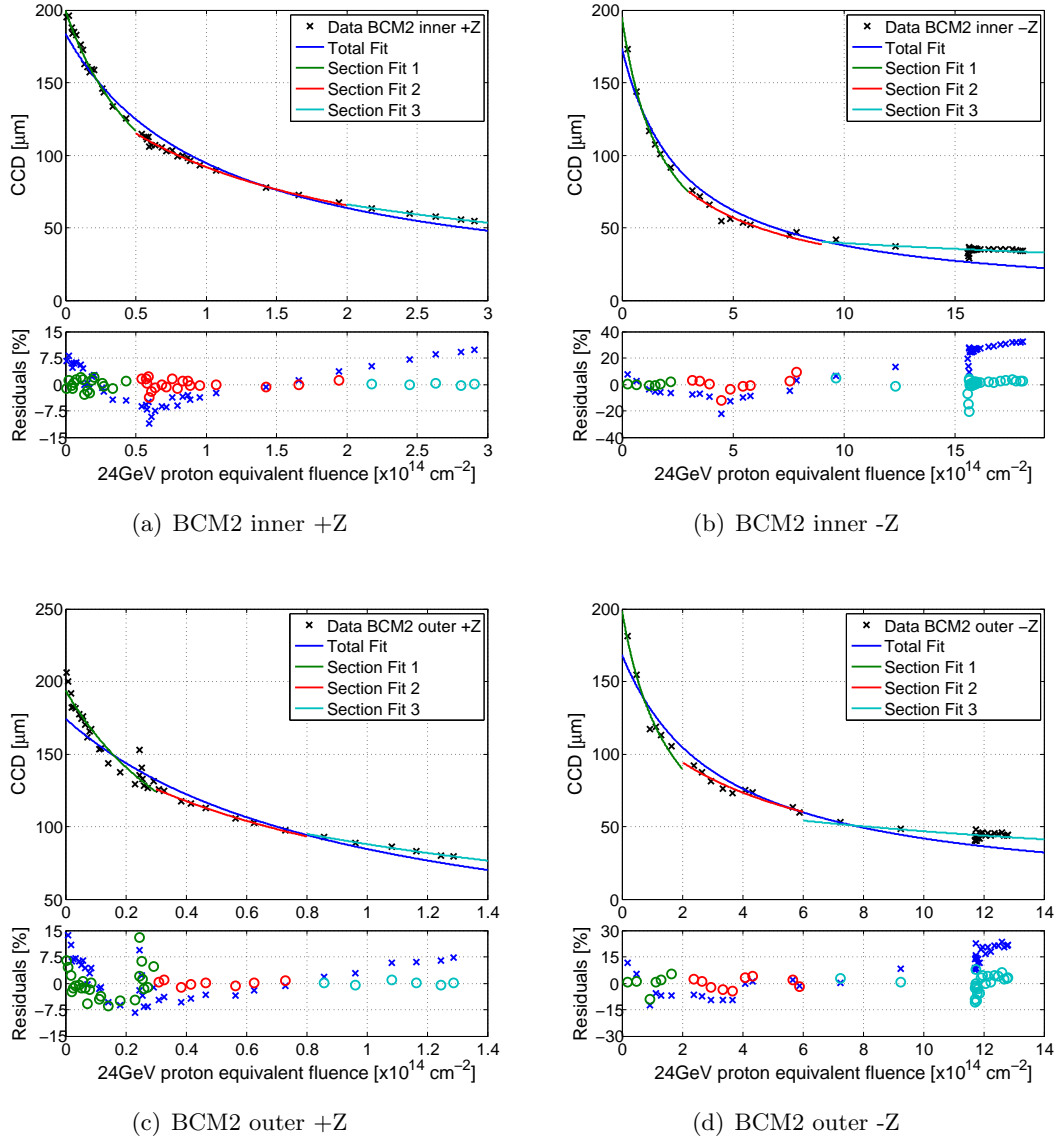


Figure 7.13.: Hyperbolic fit to the data of all BCM2 detector groups. The fit over the total data diverges as seen in the residuals. The data was split in three parts and fits of the same function applied to the partial data.

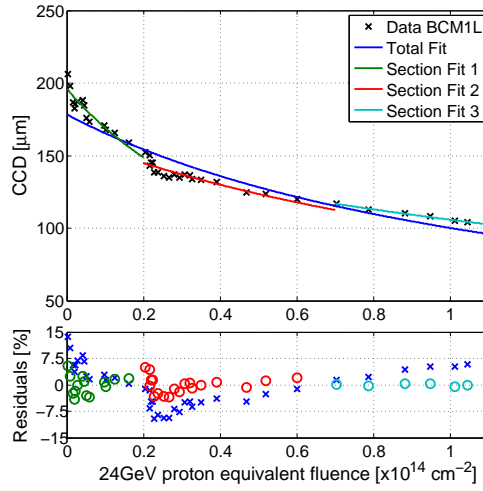


Figure 7.14.: Fits of hyperbolic damage curve to BCM1L data.

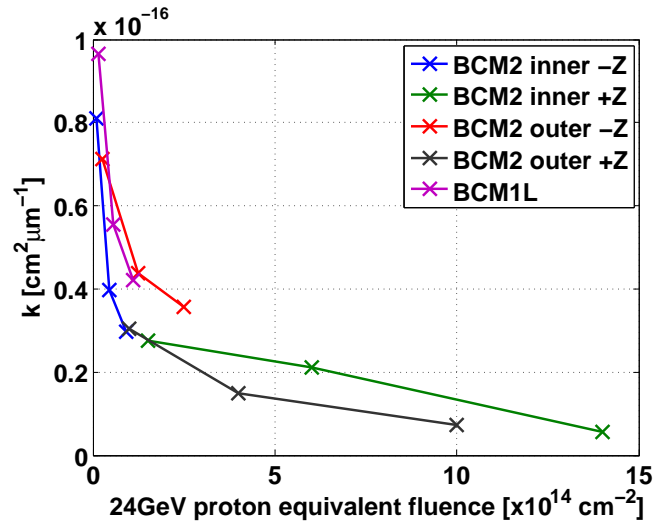


Figure 7.15.: All k factors obtained in partial fits to the BCM1L detectors are plotted as function of the average fluence of the data set where the k factor was obtained from. In every detector the k factors decrease with higher fluence. The difference is more than an order of magnitude between the highest and lowest fluence.

7.3. Decrease of signal efficiency of the BCML detectors with increasing integrated luminosity

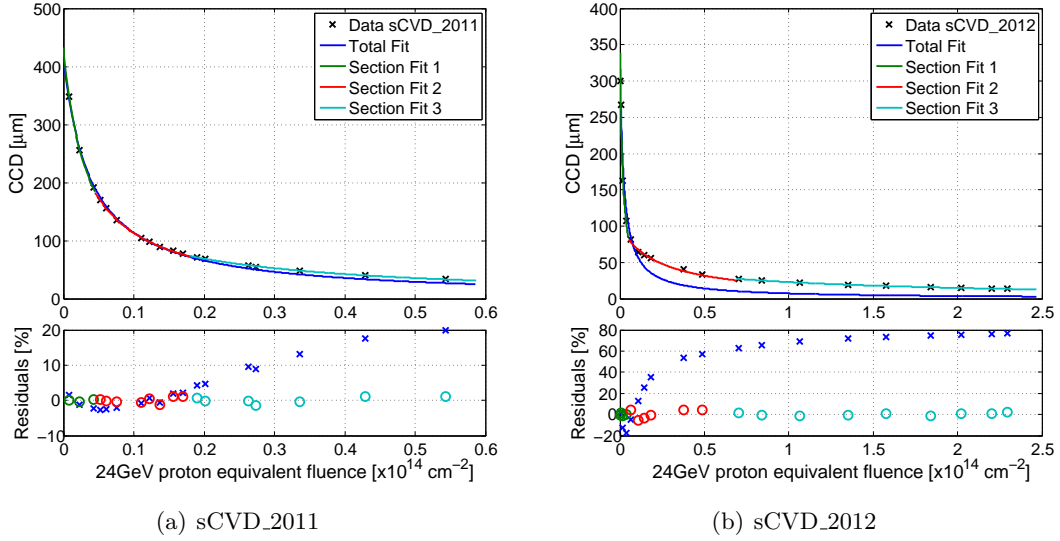


Figure 7.16.: Hyperbolic fit to the data of the sCVD diamonds, where one fit was performed over the total data and three fits to separate parts of the data. The hyperbolic fit clearly diverges from the data, implying that the signal decrease is not purely hyperbolic.

		Section 1	Section 2	Section 3	Total
BCM1L	CCD ₀ [μm]	196.1	163.8	154.6	179.2
	k [cm ² μm ⁻¹]	8.09×10^{-17}	3.97×10^{-17}	2.98×10^{-17}	4.22×10^{-17}
BCM2 inner -Z	CCD ₀ [μm]	194.91	144.0	50.6	173.3
	k [cm ² μm ⁻¹]	2.76×10^{-17}	2.11×10^{-17}	0.562×10^{-17}	2.06×10^{-17}
BCM2 inner +Z	CCD ₀ [μm]	199.8	154.0	125.4	183.6
	k [cm ² μm ⁻¹]	7.11×10^{-17}	4.38×10^{-17}	3.57×10^{-17}	5.02×10^{-17}
BCM2 outer -Z	CCD ₀ [μm]	198.9	132.0	70.9	168.2
	k [cm ² μm ⁻¹]	3.04×10^{-17}	1.50×10^{-17}	0.725×10^{-17}	1.79×10^{-17}
BCM2 outer +Z	CCD ₀ [μm]	194.0	159.3	139.9	175.2
	k [cm ² μm ⁻¹]	9.65×10^{-17}	5.56×10^{-17}	4.22×10^{-17}	5.91×10^{-17}
sCVD_2011	CCD ₀ [μm]	433.2	369.8	184.5	437
	k [cm ² μm ⁻¹]	6.92×10^{-16}	6.14×10^{-16}	4.55×10^{-16}	6.14×10^{-16}
sCVD_2012	CCD ₀ [μm]	338.6	99.1	50.1	336.2
	k [cm ² μm ⁻¹]	1.81×10^{-15}	0.43×10^{-15}	0.237×10^{-15}	1.23×10^{-15}

Table 7.3.: Results of all hyperbolic fits shown in figures 7.13, 7.14 and 7.16. In all channels a decrease in k factor towards higher fluences was measured. The k factors of the sCVD diamonds are significantly higher than the k factors of the pCVD diamonds.

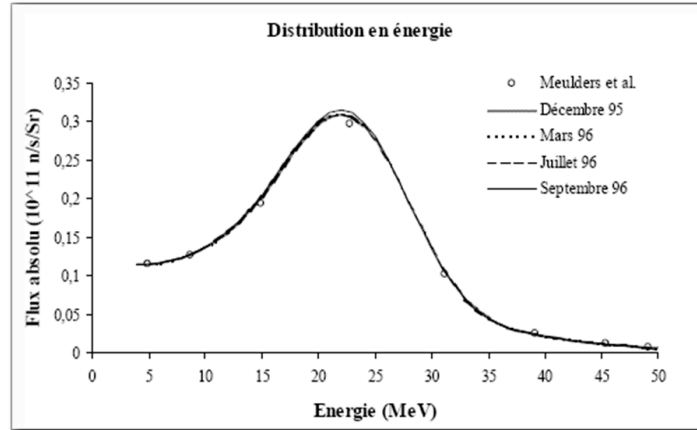


Figure 7.17.: Neutron energy spectrum of the Louvain beam line. [Mil]

trapping. The decrease can however be attributed to the polarization effects, which occur in a high rate environment, like the particle field the BCML detectors are placed in. The decrease of k-factors with higher fluence was already predicted by the simulation of the effective detector volume due to polarization.

7.4. Signal decrease in Neutron irradiations.

As shown in chapter 6.4.2, the main source for radiation damage is induced by low energetic neutrons. To better understand the damage inflicted by low energetic neutrons, a test beam irradiation was performed. Two sCVD diamonds were irradiated at the cyclotron in Louvain-la-Neuve, Belgium.

7.4.1. Beam line description

The cyclotron produces a primary deuteron beam with an energy of 50 MeV, which is sent on a 2 cm thick beryllium target. The neutrons are created by the reaction:



A filter consisting of 1 cm polyethylene, 1 mm cadmium and 1 mm lead is used to reduce the gamma and charged particle contamination and to remove some of the very low energetic neutrons. The resulting neutron energy spectrum is shown in figure 7.17. The spectrum peaks at 23 MeV and has a FWHM of about ~ 15 MeV.

The integrated cyclotron beam current I is recorded during the irradiation. It can be converted to a neutron fluence Φ via the formula[Mil]:

$$\Phi = \frac{10^{14} \times I[\mu\text{A}]}{0.079 \times d^{1.902}}, \quad (7.15)$$

where d denotes the distance of the irradiated object to the outer edge of the filter.

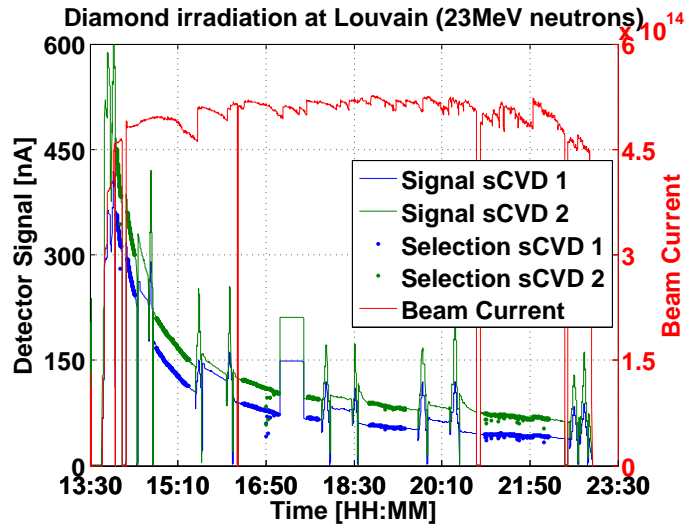


Figure 7.18.: The recorded data of both sCVD diamonds is shown together with the cyclotron beam current. The parts of the data, where the diamonds were in a stable situation at with an applied electric field of $1\text{ V}/\mu\text{m}$ are selected. This data selection is used to calculate the radiation damage constant.

7.4.2. Measurement setup and data taking

The diamonds were aligned in the center of the beam using a laser positioning system. Both diamonds were mounted directly behind each other to place them in the same beam line. The second diamond received slightly less fluence due to the higher distance to the conversion target. Both diamonds were connected to separate HV power supplies and a tunnel card readout system. During the irradiation process, the detector current was recorded for both diamonds. This was possible, because the detector current was well within the dynamic range of the tunnel card. During a proton irradiation it would not be possible to measure the generated current, since the detector current would be extremely high due to ionizing energy loss.

The tunnel card readout happened every 0.4 seconds. During most of the operation, both diamonds were operated at $1\text{ V}/\mu\text{m}$. Occasionally a HV scan was performed. The instantaneous and the integrated beam current was recorded every 3 to 4 seconds by the locally available system.

7.4.3. Data analysis

The data from the beam current measurement and the detector current was merged by assigning to each beam current measurement the detector current value closest in time. The measured detector current is shown in figure 7.18. Also shown is the instantaneous beam current, which is not constant, since the cyclotron is constantly retuned to give the maximum beam current. The times where the diamonds were operated at $1\text{ V}/\mu\text{m}$ are selected to be used for the calculation of the radiation damage constant.

The instantaneous beam current was converted to a flux and the integrated beam current to a fluence value at the diamond locations using equation 7.15. The detector current was normalized to the neutron flux. It was assumed that the detectors collected $\sim 100\%$ of the induced charge at zero fluence, which is a reasonable assumption for sCVD diamonds. The

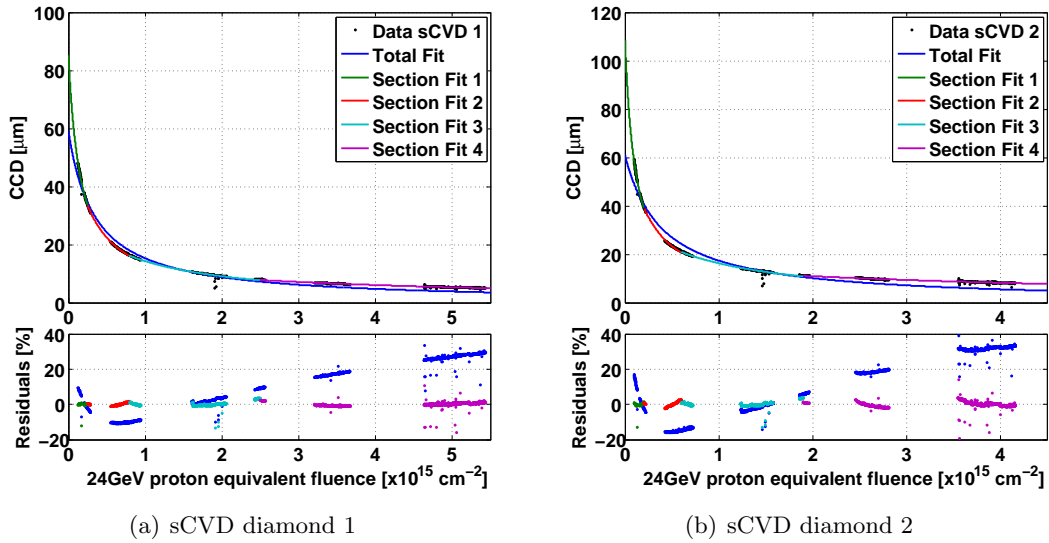


Figure 7.19.: Hyperbolic fit to the damage curve measured in 23 MeV neutron irradiation. Figure (a) shows the data for the sCVD with $60\ \mu\text{m}$ thickness and figure (b) shows the data for the sCVD with $108\ \mu\text{m}$ thickness. A fit over the full data set and fits over partial selection of the data is shown.

signal was divided by its initial signal value and multiplied with the detector thickness to obtain a CCD value. The hereby measured CCD is plotted as function of the neutron fluence. The hyperbolic damage curve (equation 7.7) was fitted to both curves over the full data set, and over selected parts of the data. The selected data and the fits are shown in figure 7.19. The hyperbolic curve does not fit well over the whole data set. The actual signal decay is flatter than the hyperbolic. The fits over selected parts of the data match better, as seen by the lower residuals, since they do not have to cover a wide range of data. The shape of the residuals reveal the same systematic error as already seen in the simulation (figure 7.6) and in the data measured with the BCM system (figure 7.13), indicating a signal decrease due to polarization. The k factors obtained in the fit decrease with higher irradiations. The k factors obtained in the partial fits are shown in figure 7.20 as function of the average fluence of the selected data range.

7.4.4. Conversion to 24 GeV protons and comparison with BCML results

In order to compare the fluence of the test beam with other irradiations and with the CMS radiation environment, the relative damage parameter compared to 24 GeV protons was simulated using FLUKA. The used simulation geometry is the same as the one used to obtain the DPA damage curves shown in chapter 6.1.4. The primary neutron beam was configured with a gaussian distribution in energy with an average of 23 MeV kinetic energy and a FWHM of 15 MeV. The obtained DPA value is 3.6185×10^{-22} , which results in a relative value compared to 24 GeV protons of 4.32.

The results from irradiation with 23 MeV neutrons is converted to the equivalent of 24 GeV protons using this DPA scaling factor. The k factors are plotted as function of fluence in figure 7.21 together with the results from the pCVD and the sCVD detectors of BCML shown in chapter 7.3.3. For different reasons, the results are not directly comparable: The

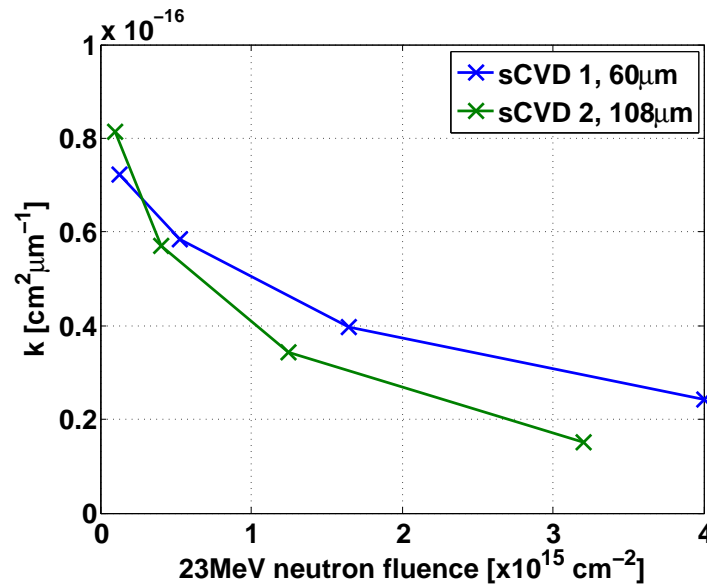


Figure 7.20.: Radiation damage constant obtained from the fits to the partial selections of the data measured during 23 MeV neutron irradiation.

used diamonds are different in type, not only the difference due to being poly-crystalline or single-crystalline, but also the diamonds used in the irradiation are significantly thinner (60 μm and 108 μm). Radiation damage due to trapping is considered independent of the type of diamond, but this is not the case for a decrease in signal efficiency due to polarization. Also the diamond in the neutron irradiations were biased at 1 V/ μm where as the BCML detectors are operated at 200 V, which corresponds to roughly 0.5 V/ μm for all of them. Nevertheless, all results show the downwards trend with higher fluences, and all of them show a significantly higher value for the damage parameter than measured by RD42.

7.5. Turn on behavior

One way to indicate, that the reduction in signal strength is due to polarization, is to analyze non steady conditions. When the LHC beams are brought into collisions, the rate environment changes almost instantly from a low rate environment to a high rate environment. Since the rates are so high at the BCM2 inner and BCM1L locations, the diamond detectors in these locations stabilize immediately. The BCM2 outer detectors are ideal to study the turn on behavior, since they are in a much lower rate environment, but received almost the same damage as their counterparts at the inner location.

As example fill #2242 was chosen, at which the LHC had delivered about 6 fb⁻¹. Figure 7.22 shows the average signal of the BCM2 outer detectors from the -Z and the +Z end together with the instantaneous luminosity. The error band of the BCM data shows the one σ variation within the detector group. All curves are normalized to the signal at the end of the fill to show the relative behavior at the start of the fill. The luminosity is plotted as reference how the signal should look like, if a perfect linearity between collision rate and measured signal would exist. The detectors on -Z and on +Z clearly behave in a different way. BCM2 +Z detectors show a slow increase in signal when the beams are brought into collision. BCM2 -Z detectors show instantly an increased signal, which reduces down to a steady level. BCM2

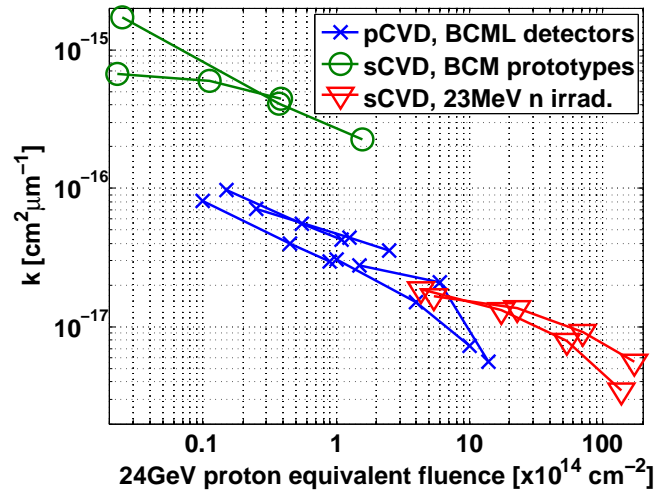


Figure 7.21.: Radiation damage constant as function of 24 GeV-p-eq fluence as measured with the BCML detectors together with the results from the sCVDs installed in BCML, and the measurements in neutron irradiations. All detectors show a general downwards trend, but the very different types of detectors used and operated at different electric fields. The sCVD and pCVD diamonds in BCML were operated at about $0.5 \text{ V}/\mu\text{m}$ and the diamonds used in the irradiation were operated at $1 \text{ V}/\mu\text{m}$. Also the thickness is different. The sCVD and pCVD diamonds in BCML are between $400 \mu\text{m}$ and $460 \mu\text{m}$ thick and the diamonds used in the irradiation were $60 \mu\text{m}$ and $108 \mu\text{m}$ thick. These differences would create a different level of polarization and the k-factors are not expected to match.

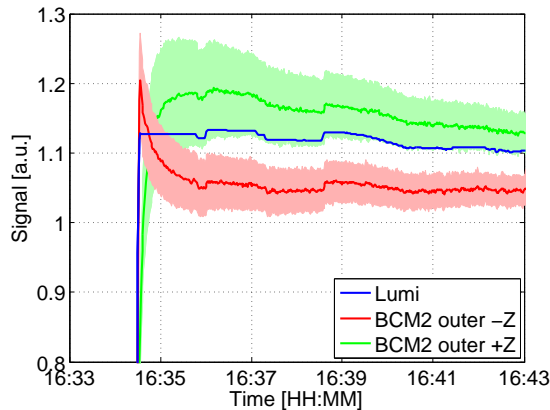


Figure 7.22.: The signal of BCM2 outer detectors averaged on +Z and on -Z is shown at the start of the example fill #2242. The luminosity is plotted as a reference. All curves are normalized to the signal at the end of the fill. The BCM2 +Z detectors received only low amounts of damage show a slow increase towards the expected level, consistent with the well known pumping effect. The highly damaged detectors at -Z lost some of their polarization in the inter-fill period. When the fill starts the signal is higher at first and the polarization builds up over about 2 minutes leading to a decrease in signal.

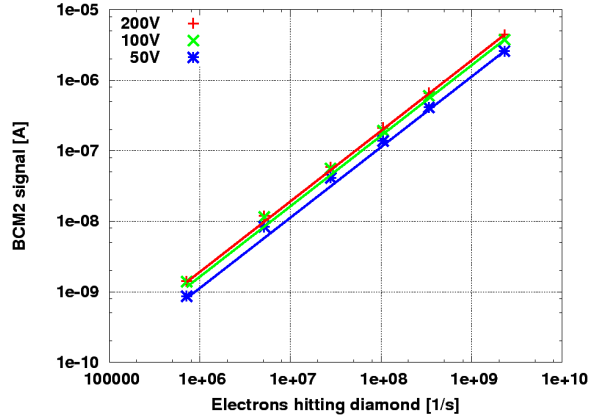
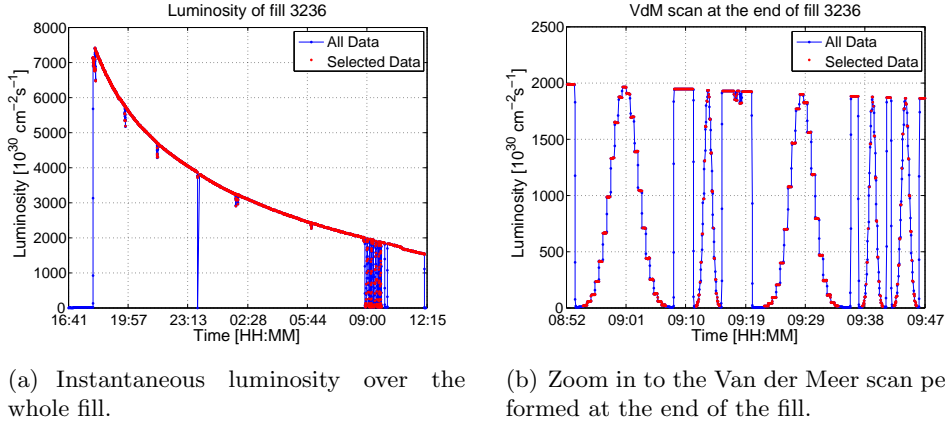


Figure 7.23.: A BCM2 detector was measured in a high rate test beam up to the abort threshold level. At a operating voltage of 50V a slight saturation is visible, but at the operating HV of 200 V the behaviour was linear[Mül11].



(a) Instantaneous luminosity over the whole fill.

(b) Zoom in to the Van der Meer scan performed at the end of the fill.

Figure 7.24.: Instantaneous online luminosity of fill 3236. Data set with one value per lumi-nibble (integrated over 2^{14} orbits = ~ 1.5 seconds) available was used. Only values during stable conditions (marked in red) are used for the analysis.

-Z had received about $1.2 \times 10^{15} \text{ cm}^{-2}$ 24 GeV-p-eq fluence and was reduced to about 15% signal strength, while BCM2 +Z received only about $2.3 \times 10^{13} \text{ cm}^{-2}$ 24 GeV-p-eq fluence and was still at about 60% signal strength. The only slightly damaged detectors on +Z show a typical pumping behavior. Traps responsible for reducing the CCD get filled and passivated, resulting in an increased CCD. The strongly damaged detectors on -Z lose their signal due to the buildup of polarization, which is created by radiation damage induced traps.

7.6. Rate dependency of signal efficiency

As a protection device, the linearity of the signal response of the BCM detectors is very important. This makes a reliable extrapolation towards the high rates at the level of the beam abort threshold possible. Several test beam studies were performed in the design phase of the BCM2 system to test the response of the detectors. These studies, performed with un-irradiated detectors, show a linear response up to the beam abort threshold current at

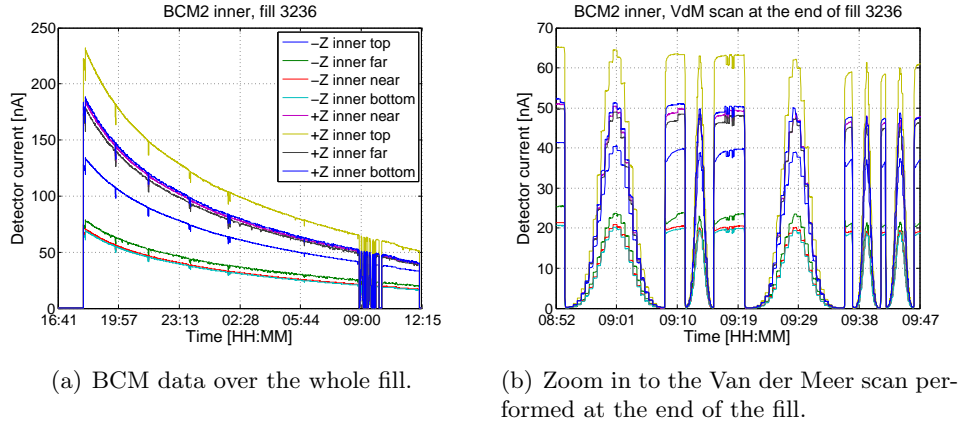


Figure 7.25.: Detector current of BCM2 inner detectors during fill 3236. Running Sum 9 (1.31 s integration) was used.

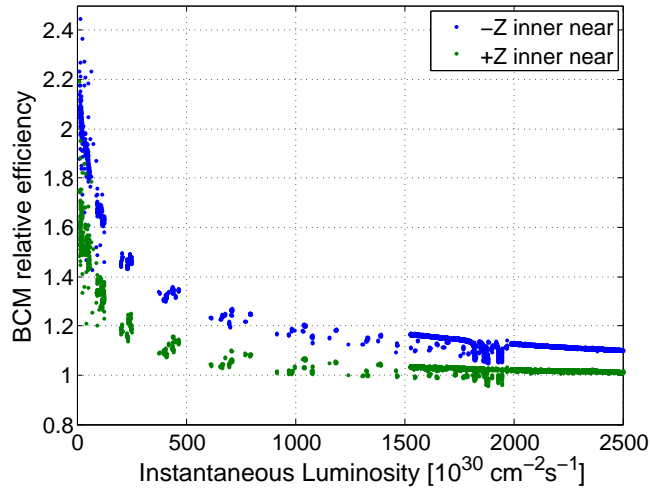


Figure 7.26.: Relative efficiency for two BCM2 exemplary inner detectors, one from the -Z end and one from +Z end. The relative efficiency is calculated by calculating the ration of BCM signal and luminosity and normalizing it to the efficiency at the start of the fill.

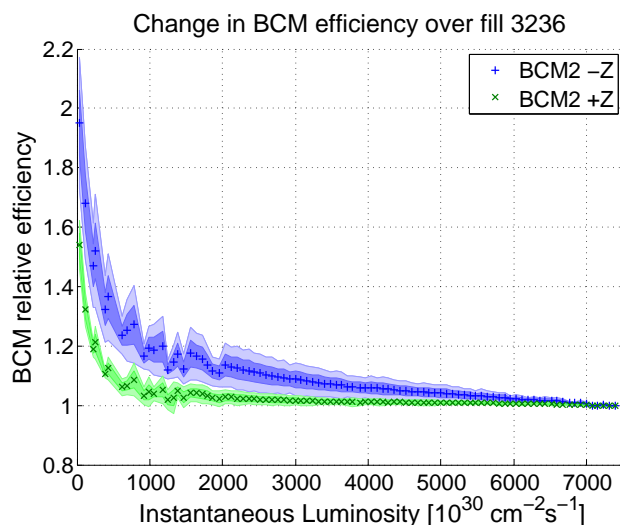


Figure 7.27.: Relative efficiency for BCM2 -Z and +Z, where the average over all four detector within one group was formed. The dark band shows the one σ , the light band the two σ deviation within the detector groups. It shows that the behavior of the +Z and the -Z detectors are clearly different, where the only difference is the much higher radiation damage on the -Z detectors.

the operating voltage of 200 V. At a HV of 50 V a minor saturation was observed [Mül11]. Figure 7.23 shows the result of one of these studies. This section is part of the radiation damage chapter, since a clear difference between highly damaged and less damaged detectors is visible.

Already shown by the offset to the linear fit in chapter 7.3 is, that there is a certain non-linearity of the system. In order to study this more, the data from fill #3236 is used, which was an extremely long fill. Figure 7.24 shows the instantaneous luminosity as a function of time for this fill, measured with the HF detector. Normal fills are dumped by the operator when the instantaneous luminosity has dropped to about half the original value. This fill had a luminosity range from about $7.3 \times 10^{33} \text{ cm}^{-2} \text{ s}^{-1}$ down to $1.5 \times 10^{33} \text{ cm}^{-2} \text{ s}^{-1}$. Additionally a Van der Meer scan¹ (VdM scan) was performed at the end of the fill. This way, many data points are also available from luminosity values of $2 \times 10^{33} \text{ cm}^{-2} \text{ s}^{-1}$ down to zero. The used luminosity measurement is the official online luminosity where one data point per luminibble (integrated over 2^{14} orbits = ~ 1.5 seconds) is available. The offline luminosity would be better to use, since additional correction factors are included, but this is only available every lumi-section (integrated over 2^{18} orbits = ~ 23 seconds), which is not sufficient to make a good matching of the luminosity measurements with the BCM data during the VdM scan. The difference between online and offline luminosity was found to be below 1%, which is much smaller than the needed precision for this analysis. Not every value is used for the analysis. Only luminosity data above $10^{31} \text{ cm}^{-2} \text{ s}^{-1}$ are used since at this low level no signal can be measured with the BCM detectors any more. In addition values with fast changes of more than $5 \times 10^{31} \text{ cm}^{-2} \text{ s}^{-1}$ per lumi-nibble are also omitted. This way only data values from stable conditions are used.

Figure 7.25 shows the rates from the BCM2 inner detectors. Running Sum 9 (1.31 s integra-

¹During a Van der Meer scan the detector response is measured as function of beam separation. This way the beam profile can be measured, which is used for the calibration of the luminometers.

tion) was used for this analysis since this integration time window offers the best compromise between noise level and speed to resolve the fast changes during the VdM scan. In the zoom plot (fig. 7.25(b)) one can observe the turn on behavior also described in chapter 7.5 when the beams are brought into head on collisions after one scan. It takes several minutes for the detectors to stabilize. This shows that the duration of one VdM scan step is not sufficient to measure the exact value of response for this point. A certain difference in efficiency response between the constant luminosity data and the VdM scan data has to be expected.

The data is divided by the luminosity and plotted as function of luminosity, in order to visualize the linearity of the detectors compared to luminosity. A detector with a perfect linearity with respect to luminosity would show a flat curve in this representation. The relative efficiency was normalized to the efficiency at the start of the fill. This way the relative change of detector efficiency as function of rate environment can be visualized. Figure 7.26 shows relative efficiency plot for two exemplary detectors, one from BCM2 at the -Z end and one from the +Z end. It zooms in at lower luminosity values. The part of the data recorded during constant luminosity (above $1.5 \times 10^{33} \text{ cm}^{-2} \text{ s}^{-1}$) has a low level of scattering. The data points from the VdM scan (below $2 \times 10^{33} \text{ cm}^{-2} \text{ s}^{-1}$) are more spread. A jump in curve from the constant luminosity to the VdM scan region is visible, as expected due to the fact that there was not enough time to stabilize the detectors in one VdM step. The VdM scan points show clearly that the increase in signal efficiency continues towards lower particle rates. One might think the increase in detector signal towards later times in the the fill arises from activation of material in the surrounding area of the detector. The efficiency data calculated from data taken during the VdM scan clearly shows that the change in efficiency is caused by a change in luminosity. This slope is traced by every different VdM scans. If activation would have been the reason for the increased signal towards the end of the fill the VdM scan would have showed no change in efficiency since the data points were taken close in time.

All BCM2 detectors show this behavior. In order to visualize this the average of all inner detectors per end was calculated (fig. 7.27). The error bands shows the estimation of the standard deviation in each group, where the dark band shows one σ , the light band the two σ deviation. In addition the data points with similar luminosity points were averaged to reduce the number of points in the plot and create a smoother curve. Figure 7.27 shows that in general, although every single channel behaves slightly different, there is a difference visible between BCM2 on -Z and on +Z, and it is not just an effect of the diamonds being different on average. The detectors from the -Z end have a stronger rate dependency compared to the detectors from +Z, where the only difference between them is the integrated fluence they had received.

At a low rate not many of the traps are filled and the polarization field is less strong. The level of trap filling depends on the ratio of trapping and de-trapping. It is inverse proportional of the de-trapping time, but increases proportionally to the rate of trapping. The trapping rate is increased with higher charge carrier density and hence with the particle rate hitting the detector. This applies to a detector with high damage (many traps) and a detector with low damage (few traps). As the rate increases the traps are filled more and for a low damaged detector the situation with fully filled traps is eventually reached. Above that rate level there is no rate dependency any more. A highly damaged detector should saturate at a higher level of rate environment. The low damaged detectors on BCM +Z indeed show only a very small rate dependency at high luminosities where as the high damaged detectors on BCM2 -Z still show a strong variation in rate.

7.7. Charge collection distance (CCD) measurements.

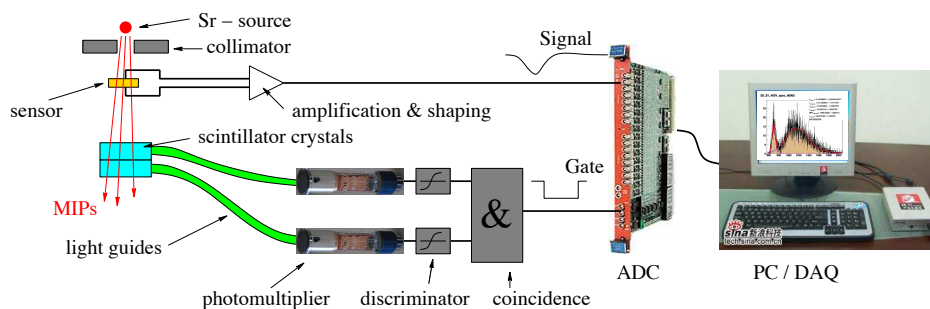


Figure 7.28.: Scheme of the CCD measurement setup.[Ohl10]

7.7. Charge collection distance (CCD) measurements.

Charge collection distance (CCD) or charge collection efficiency (CCE) measurements are performed to analyze the performance of a detector. The measurements presented here were performed in DESY Zeuthen, Germany. The measurement setup is described in detail in [Ohl10], but a short summary will be given here. Figure 7.28 shows the scheme of the measurement setup. β particles from a ^{90}Sr source penetrate the diamond under test and hit two scintillators. The scintillators are in coincidence to reduce noise hits and act as trigger for the data taking of the signal from the device under test. The discrimination of the scintillator pulses allow to trigger only on β particles that have a energy high enough to be close to the energy of a minimum ionizing particle (MIP). The signal of the diamond is amplified and digitized with a shaping ADC. The histogrammed particle spectrum is fitted with a Landau distribution convoluted with a Gauss curve and the most probable value (MPV) is used as benchmark number for the detector efficiency. The system is calibrated by injecting a well defined amount of charge, so that the amount of charge collected with the diamond (Q_{coll}) is exactly known. The CCE and CCD are defined as:

$$CCE = \frac{Q_{coll}}{Q_{ind}} \quad (7.16)$$

$$CCD = CCE * thickness \quad (7.17)$$

The induced amount of charge Q_{ind} is known to be 36 electron-hole pairs per μ for a MIP traveling through diamond.

7.7.1. Measurements of un-irradiated diamonds

Figure 7.29(a) shows the CCD as function of applied high voltage of the diamond sCVD_test1. It shows the typical behavior of an un-irradiated single crystal diamond: Both polarities show the same slope. The CCD saturates at quite low electric fields of about $0.2 \text{ V}/\mu\text{m}$. The saturated CCD is almost as high as the thickness of the diamond (CCE almost 100%).

Figure 7.29(b) shows the CCD of the diamond sCVD_2012 prior to its installation in BCM2. There seems to be no intrinsic problems with polarization as seen by the low saturation field of about $0.2 \text{ V}/\mu\text{m}$. But the CCE measured in saturation at high fields is only about 80% which shows the inferior quality of this diamond sample.

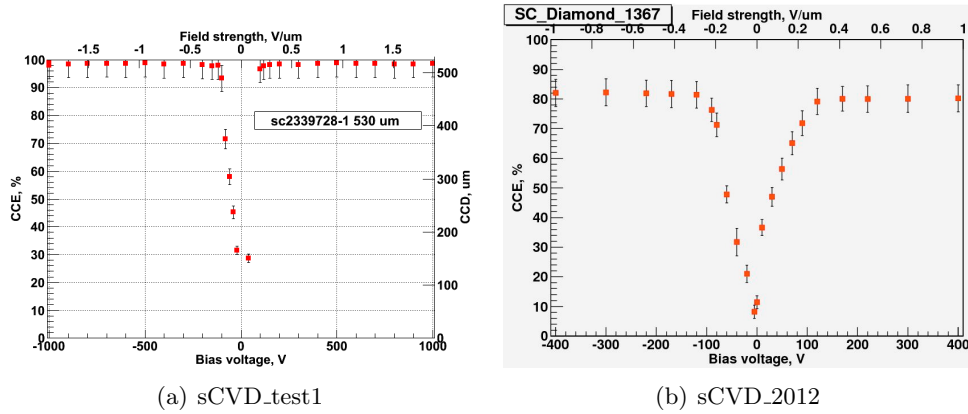


Figure 7.29.: Charge Collection Distance measurements as function of applied electric field for the diamonds sCVD_test1 and sCVD_2012 prior to irradiation. Both diamonds saturate at about $0.2 \text{ V}/\mu\text{m}$. The sCVD_test1 has almost 100 % CCE, but the sCVD_2012 has only about 80 % CCE showing inferior diamond quality.

Diamond	24 GeV-p-eq fluence [cm^{-2}]	CCD ₀ [μm]	CCD prediction [μm]
sCVD_2011	5.69×10^{13}	430	423
BCM2 +Z outer	2.41×10^{13}	150	150
BCM2 -Z outer	1.23×10^{15}	150	133

Table 7.4.: The table shows the fluence received by the three analyzed diamonds calculated by FLUKA converted to 24 GeV proton equivalent. Also shown is the initial CCD prior to irradiation

7.7.2. CCD measurements after removal from BCM2

After 2011 three diamonds were removed from the system: **sCVD_2011** (located at +Z inner near), **BCM2 +Z outer bottom-near** and **BCM2 -Z outer bottom**. Measurements were taken with constant HV and with alternating HV to avoid the buildup of polarization. Results are shown in figures 7.30, 7.31 and 7.32. For both pCVD diamonds measurements with constant HV taken prior to installation were available, which show a CCD of about $150 \mu\text{m}$ at $1 \text{ V}/\mu\text{m}$. Table 7.4 shows the received fluence, the initial CCD and a prediction of the CCD after irradiation for all three diamonds. The received fluence was calculated with FLUKA and converted to 24 GeV proton equivalent. The initial CCD for the sCVD was not known, but for a rough estimation of the expected CCD decrease $430 \mu\text{m}$ was assumed, which is a reasonable number for a sCVD of $460 \mu\text{m}$ thickness. After the irradiation during operation in 2011 it is expected for the sCVD to lose about $10 \mu\text{m}$ CCD, the pCVD from BCM2 +Z outer should not show any difference, and the pCVD from BCM2 -Z outer is expected to have a CCD decrease to about $130 \mu\text{m}$.

Figure 7.30 shows the CCD measurements of BCM2 outer +Z and figure 7.31 the measurements of BCM2 outer -Z. The left plot shows measurements using a constant HV and the right plot shows the results using an alternating polarity HV. The applied alternating HV had a square wave function with a frequency of 0.1 Hz and an edge slope of $50 \text{ V}/\mu\text{s}$. For the low damaged pCVD from +Z no difference before and after irradiation is visible, as expected.

7.7. Charge collection distance (CCD) measurements.

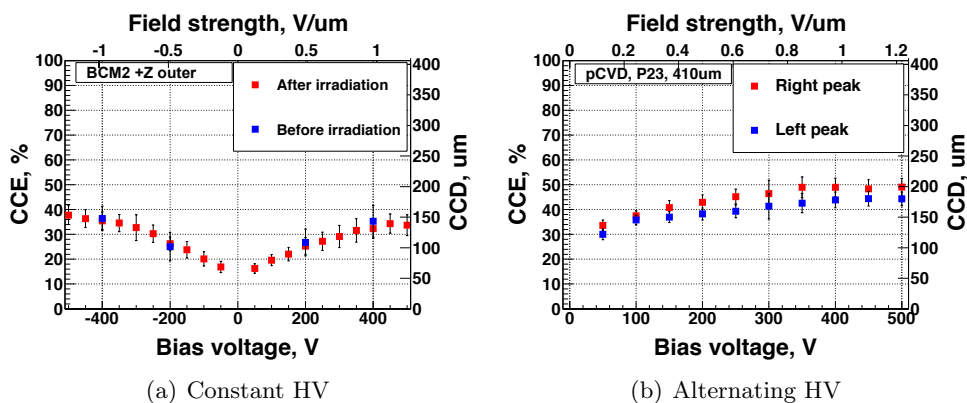


Figure 7.30.: CCD measurements of the pCVD diamond from BCM2 outer +Z.

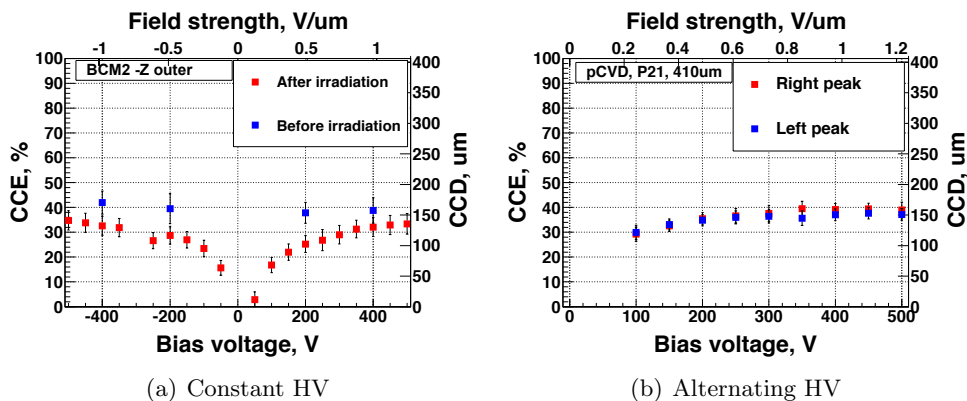


Figure 7.31.: CCD measurements of the pCVD diamond from BCM2 outer -Z.

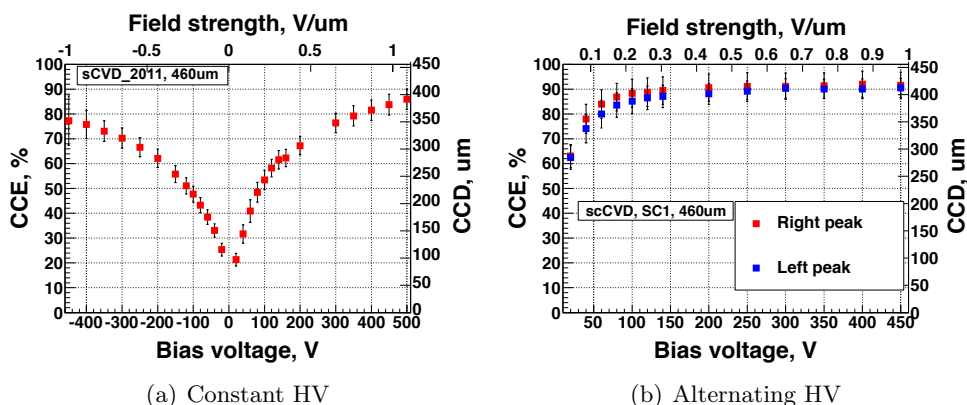


Figure 7.32.: CCD measurements of the sCVD_2011 from BCM2 inner +Z.

The measurement using alternating HV shows significantly higher CCD than the measurements using constant HV indicating a certain amount of polarization in the unirradiated detector. For the high damaged pCVD from -Z a decreased CCD after irradiation is visible especially at lower field strength. At $1 \text{ V}/\mu\text{m}$ the CCD is down to about $130 \mu\text{m}$, which is also consistent expectation. With higher HV the internal field becomes less dominant compared to the applied HV field and the CCD reaches almost the values of the unirradiated state. In the measurement with alternating HV the CCD values are the same as prior to irradiation, indicating that the signal loss is only due to polarization.

Figure 7.32 show the measurements with the sCVD_2011. Unfortunately no measurements prior to installation are available. With a constant HV it is necessary to apply rather high fields ($> 1 \text{ V}/\mu\text{m}$) to reach maximum CCD. Already at low applied field ($\sim 0.5 \text{ V}/\mu\text{m}$) the CCD reaches its maximum value when the alternating HV is used. This shows that the reduced CCD at low fields using constant HV is due to polarization. If the polarization is overcome by alternating HV the CCD saturates at about $420 \mu\text{m}$. Although predictions are based on an estimated CCD_0 this also agrees with the expectation.

In summary the CCD measurements match the expected decrease as predicted by the RD42 damage curve. The reduction in detector signal strength observed in CMS, as shown in section 7.3.2, is higher than the decrease of CCD. Hence the reduction of CCD is not the main reason for the observed signal decrease. The reduced signal was probably attributed to a buildup in polarization. As explained in section 7.1.2, the buildup of polarization can be stronger in an high rate environment. Therefore the signal in an intense radiation field, like in CMS, could be even more reduced than in the CCD measure environment.

7.8. Measurements using the transient current technique (TCT)

The electric field inside a sensor can be determined by the Transient-Current-Technique (TCT): after introducing electron-hole pairs on one side of the detector, e.g. by a radioactive α source, one observes the current generated by the drift of the charge carriers due to the internal electric field of the sensor. This current as function of time is proportional to the electric field as function of distance. By creating the charge carriers either at the cathode or anode the drift from electrons or holes can be observed.

7.8.1. Measurement setup

The measurement setup at the Institute for nuclear particle physics (IEKP) at the KIT is normally used for measurements with silicon detectors [Ebe13]. The readout was adapted to facilitate the data taking as needed for the measurements presented here. A sketch of the setup can be found in figure 7.33. It consists of a Picosecond 5531 bias tee, a MITEQ AM-1309 amplifier, a Tektronix TDS 5104B oscilloscope and a Keithley 2410 as HV source. The amplifier has a 50 dB amplification and a bandwidth of 1 GHz, which is the limiting factor in terms of bandwidth for the whole system. As α source a $3.56 \text{ kBq } ^{241}\text{Am}$ source was used. In addition a $3.56 \text{ MBq } ^{90}\text{Sr}$ source was used to pump the detector. During the measurement both sources were used at the same time. The β particles from the ^{90}Sr source penetrate the thin α source and the diamond. The signals generated by the α particles, which are used to probe the electric field, are significantly higher than the signal of the β particles. The trigger threshold of the scope is set to record only signal from the alpha particles. The ^{90}Sr -source is used to deposit charge in the whole bulk material, which reflects better the situation of the detectors in operation.

7.8. Measurements using the transient current technique (TCT)

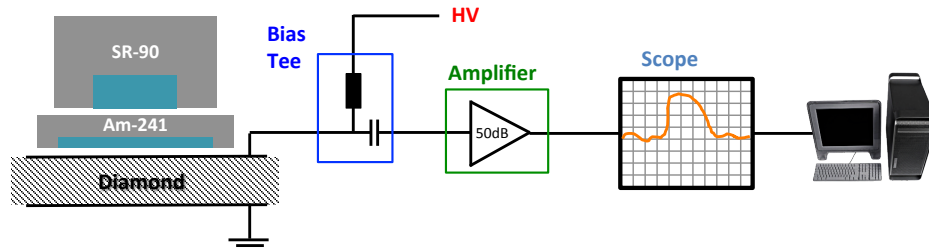


Figure 7.33.: Schematic setup of the TCT measurement. The signals are read out on the HV side, using a Bias-Tee. The amplifier has a 1 GHz bandwidth and 50 dB amplification. Single pulses are recorded with a 5 Gs/s scope and recorded by a PC.

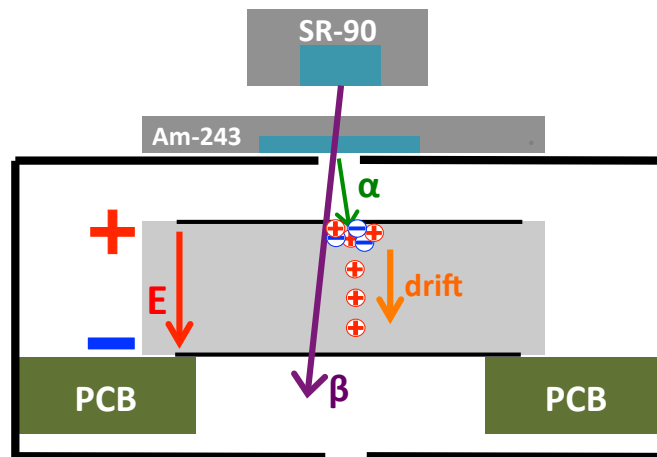


Figure 7.34.: Placement of the sources and flow of particles during TCT measurements. The diamond package is closed with a thin aluminum foil with small a hole in the middle to collimate the α particles. The ^{241}Am α source emits particles directly on the diamond. These are stopped in the first $10\ \mu\text{m}$ of the diamond and the generated charge drifts through the diamond bulk, which is measured. The ^{90}Sr source creates MIP-like β particles, which penetrate the ^{241}Am source and the diamond, leading to a charge deposition similar to operational conditions, where mostly MIP particles are measured.

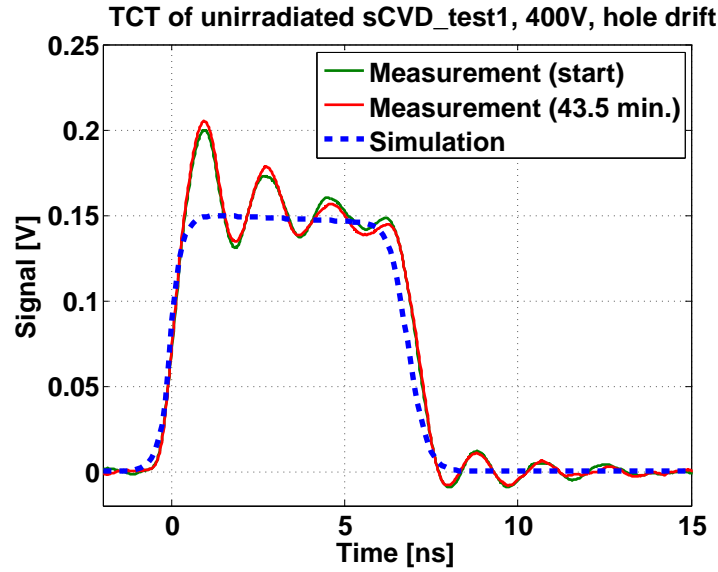


Figure 7.35.: TCT measurement of the un-irradiated diamond sCVD_test1 at 400V. A ^{241}Am α source was used to probe the electric field and a ^{90}Sr was used to create a MIP flux environment. The HV was switched on at the start of the measurement. The pulse shape measured after 43.5 minutes of operation does not differ from the measurement taken immediately after the switch on of the HV. No polarization is observed. The simulated TCT pulse for a constant electric field agrees well with the measurement.

Since α -particles are stopped in any material an external trigger can't be used. The oscilloscope is set to trigger on the pulses directly. About one pulse is stored by the PC per second. The speed of this readout is limited by the GPIB data transfer between the scope and the PC. Later an average over several curves is formed. A time dependence of the signal shape is shown by averaging several groups of traces close in time. For the averaging the curves are realigned using a software discrimination, with a discriminator threshold chosen just above noise level.

At first the HV is switched off, but the sources are applied to pump the diamond. Any residual polarization field is removed. The data taking starts with the switch-on of the HV. TCT pulses measured immediately are taken while the electric field is constant in the bulk, as no charge is trapped yet. Slowly trapped space charge builds up which leads to a deformation of the electric field and a change in shape of the measured pulses. Conclusions on the electric field can be drawn by analyzing the measured pulse shapes.

7.8.2. Un-irradiated diamond

TCT measurements of undamaged detectors have been widely studied. The electric field is constant and, for a sCVD diamond with a MFP much higher than the thickness, one obtains a square TCT signal with a length proportional to the maximum drift time. The diamond sCVD_test1 was measured in the TCT as an example of an un-irradiated diamond. Both, α and β source were applied. Figure 7.35 shows the averaged TCT pulses measured directly after the switch on of the HV of 400V. With the thickness of $530\ \mu\text{m}$ this gives an electric

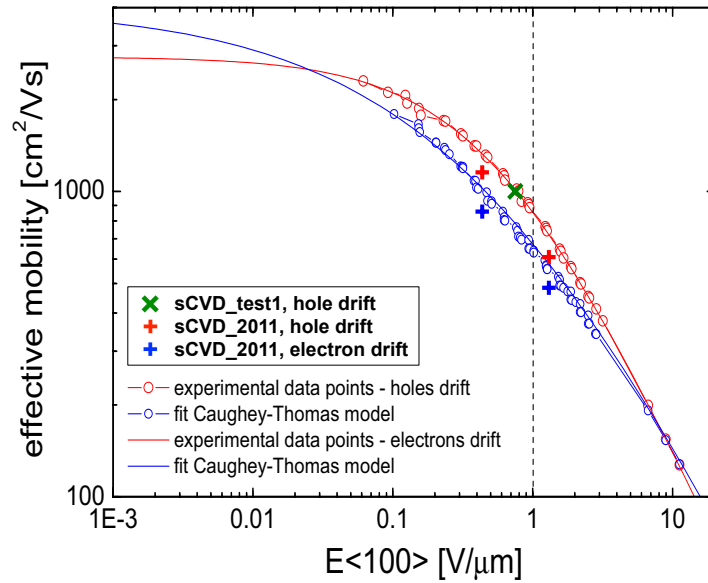


Figure 7.36.: The mobility for electrons and holes in diamond as function of electric field as measured by [Pom08]. The measurement point obtained with sCVD_test1, marked in green, matches the expected curve. The red and blue points from the irradiated sCVD_2011 are consistently below the expectation curve.

field E of $0.75 \text{ V}/\mu\text{m}$. The source was applied at the same side as the positive bias, which means the drift of holes was measured. After 43.5 minutes of applied sources under HV the pulse shape has not changed, showing that there is no buildup of polarization. Also shown is a simulation of the TCT pulse obtained with parameters matching an unirradiated detector, which matches well the measured signal shape.

The measured drift length is 7.06 ns. The average drift velocity v is therefore $75.07 \mu\text{m}/\text{ns}$. The effective mobility μ is defined by $\mu = v/E$ and calculates to $1001 \text{ cm}^2/\text{Vs}$. Figure 7.36 shows this measured value on a plot for the mobility in diamond as function of the electric field, measured by M.Pomorski[Pom08]. The data point matches the expected curve.

7.8.3. Measurements of sCVD_2011 after irradiation

Measurements at 200V

The most tested diamond is the sCVD removed after 2011. Measurements were taken at 200V as this was the operating HV. With the thickness of $460 \mu\text{m}$ the HV creates an electric field of $0.43 \text{ V}/\mu\text{m}$, if the diamond is not polarized, referred to as HV field. Figure 7.37 shows the TCT pulses for electron drift and for hole drift immediately after switch-on of the HV, when the electric field is still constant.

One can clearly see the difference in mobility for electrons and holes. The drift time is taken from the width of the pulses. For holes it is 9.16 ns and 12.33 ns for electrons. The drift velocity for holes (electrons) calculates to $50.2 \mu\text{m}/\text{ns}$ ($37.3 \mu\text{m}/\text{ns}$) and the mobility to $1155 \text{ cm}^2/\text{Vs}$ ($859 \text{ cm}^2/\text{Vs}$). Figure 7.36 shows these data points together with the expectation of un-irradiated diamond. The values measured here are slightly below the data for an un-irradiated detector. This is expected and can be explained by the fact that with a higher

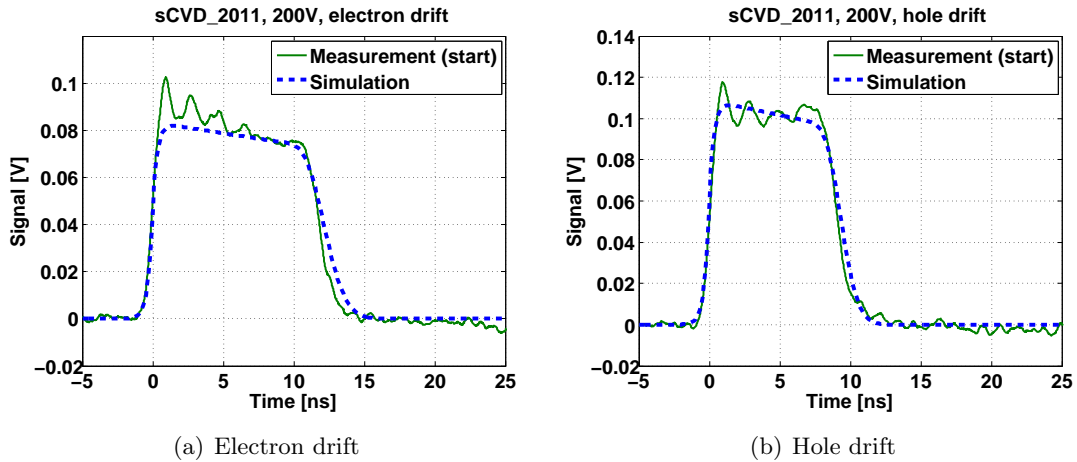


Figure 7.37.: TCT measurements of the diamond sCVD_2011 at 200V after removal from the BCML system. Measurements are taken immediately after the switch-on of the HV, hence the detector was not yet polarized.

trap density there is more elastic scattering of the charge carriers and hence a reduced drift velocity.

Also shown in figure 7.37 is a simulation of the TCT pulse for a unpolarized detector. The measured drift velocity was used in the parameterization of the drift velocity in the simulation (see table 7.1).

With ongoing measurement the signal shape and hence the electric field distribution changes. During the measurement charge carriers are trapped. This fixed space charge deforms the electric field and with it the TCT pulse. The simulation of the electric field assumes a distribution of traps and the relative strength of the trapping. Defects due to radiation damage are equally distributed throughout the bulk. It is assumed that defects trapping holes have a higher trapping probability than defects trapping holes by a factor of three. The de-trapping of holes and electrons is different. A small fraction of the trapped charge is removed every iteration step. The de-trapping for electrons is configured in the simulation to be factor 200 higher than the hole traps. The strong trapping, but also the strong de-trapping leads to a fast buildup of electrons, but this saturates quickly and there is no further increase in trapped electrons.

Figures 7.38 and 7.39 show the simulation of TCT pulses for a polarized diamond together with the measurement for one orientation of the diamond, this orientation is called “side 1”. The simulated amount of trapped charge and the electric field, calculated by integrating over the charge, is shown. The TCT pulse for holes is simulated by injecting charge on the left side, the TCT pulse for electrons is simulated by injecting charge on the right side. In figure 7.38 the diamond is only slightly polarized, where the HV was switched on for about 10 minutes. After about 40 minutes the diamond is more polarized and the pulses are more deformed, shown in figure 7.39. A result of the high number of trapped holes is a high electric field near the cathode, whereas near the anode the electric field is reduced.

The same measurement was taken with the diamond turned over, which will be called “side 2”. In figures 7.40 the measurements and simulations for a small amount of polarization is shown. Figure 7.41 shows the situation at a strong polarization level. The measurements with this diamond orientation show a high initial peak in the measurements of the hole drift.

7.8. Measurements using the transient current technique (TCT)

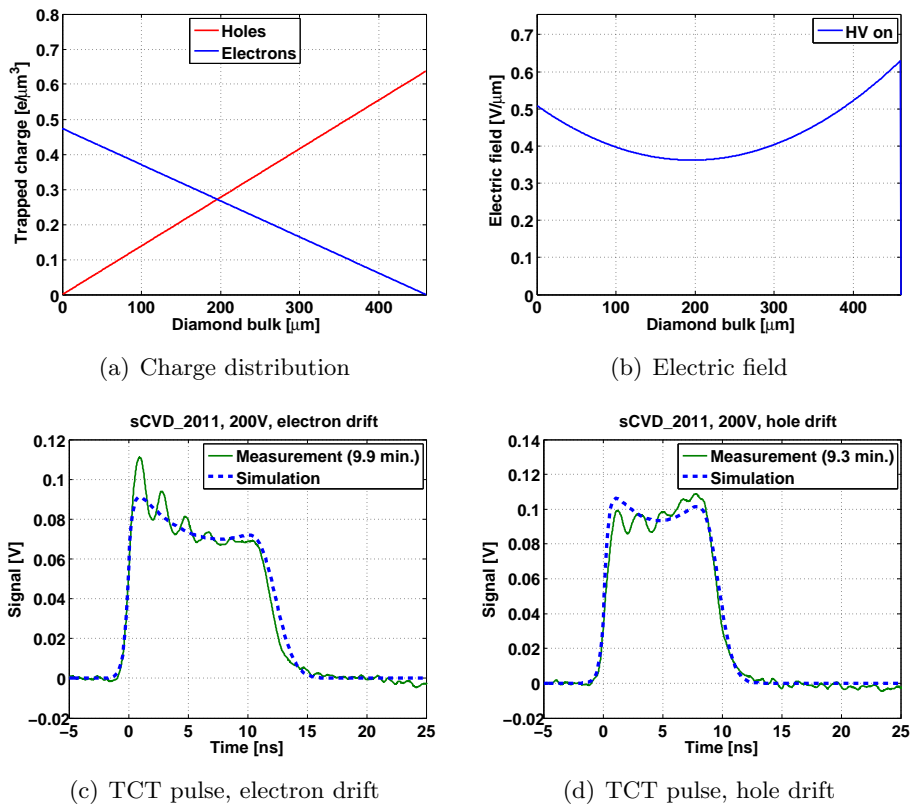


Figure 7.38.: Measured and simulated TCT pulses of sCVD_2011 at 200V. Slightly polarized (~ 10 minutes after HV on), diamond orientation: side 1.

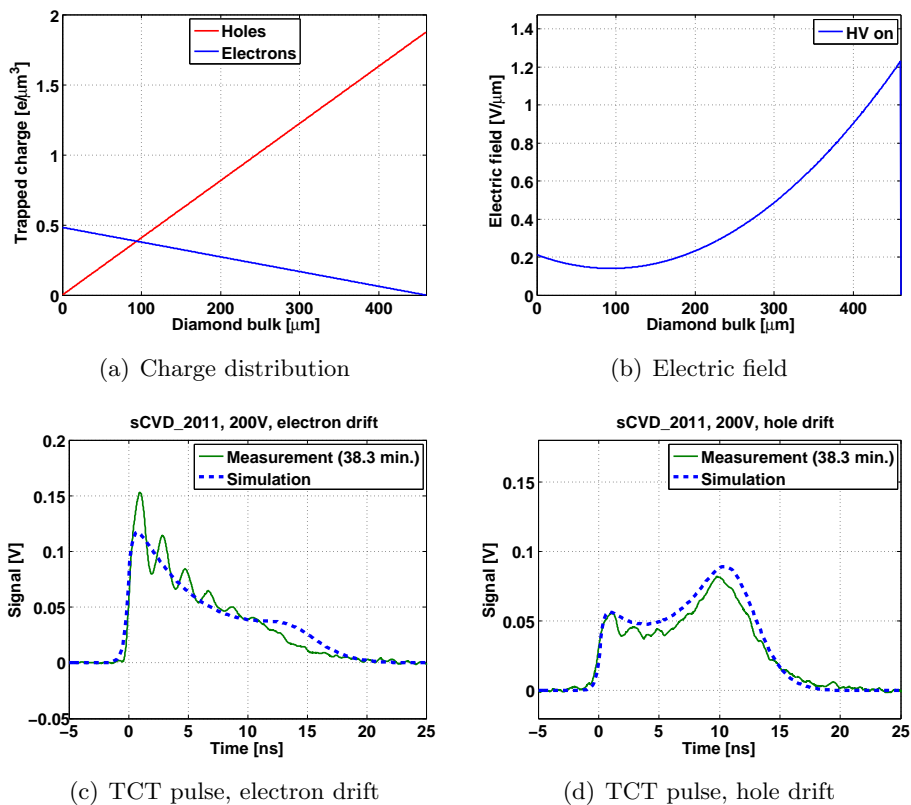


Figure 7.39.: Measured and simulated TCT pulses of sCVD_2011 at 200V. Highly polarized (~ 40 minutes after HV on), diamond orientation: side 1.

This was not observed for the opposite orientation, and it is not well reproduced by the simulation.

Since the traps are distributed homogeneously, one would expect the same behavior of the single crystal diamond for both sides. In reality even a single crystal diamond does have a substrate and a growth side which can result in an inhomogeneity of the material. The used substrate for the CVD growth of single crystal CVD diamonds is a high temperature high pressure (HTHP) diamond, which has high contamination of nitrogen, which could lead to a nitrogen contamination on the substrate side. Also differences could occur during the surface treatment process. It is possible that defects can be created during the mechanical polishing, since lattice dislocations are created in a layer close to the surface. These effects can lead to a different trapping behavior depending on the polarity of the electric field, if the diamond was not treated the same way on both sides. Due to the little knowledge about the initial treatment of the diamond it is only possible to speculate.

Measurements at 600V

The same measurement was performed at 600 V, which corresponds to a HV field of $1.3 \text{ V}/\mu\text{m}$. The pulses measured directly after the start of the measurement are shown in figure 7.42 together with the simulation of a polarization free detector. The drift time is significantly shorter compared to the 200V measurement, as expected at higher HV. The drift time for hole (electrons) is 5.79 ns (7.3 ns), the drift velocity to $79.4 \mu\text{m}/\text{ns}$ ($63.0 \mu\text{m}/\text{ns}$) and the mobility to $1827 \text{ cm}^2/\text{Vs}$ ($1449 \text{ cm}^2/\text{Vs}$). Figure 7.36 shows these data points together with the expectation of un-irradiated diamond. The data points are consistently below the data for an un-irradiated detector, as was the case for the measurement at 200V.

The polarization process happens as well. Figures 7.43 and 7.44 shown simulation and measurements at two different strengths of polarization. No measurement of electron drift is available for the highly polarized situation, and the time it took to polarize it is very long. Likely the source was not placed well in this measurement and the particle environment was not as strong as in the other measurements. The lead to a slower polarization and a low level of saturation polarization. The shape of the signal in the polarized situation shows the same structure as the measurement at 200V. The effect of the strong electron trapping at the surface is less dominant, as it is already saturated. It does take significantly more time to form the same shape of signal. In order to reach the same shape of electric field with higher HV more charge has to be trapped. This takes more time at the same rate of β particles.

Residual polarization field

After the polarization has build up the electric field is deformed. There are regions of decreased, but also areas of increased electric field, since the integral over the field has to be conserved to the externally applied HV. When the HV is switched off, the electric field is reduced by the amount of the HV field. The integral over the residual polarization field must be zero. In the areas where the field was increased the field is still positive, but where the field was decreased the field is now negative. Regions that were field free now have an electric field of the same strength as the HV field, but pointing in the opposite direction.

After the measurements where 600V was applied the switch-off test was performed. The β source was applied (without the α source) under HV for an additional time of about 1 hour to polarize the diamond as much as possible with this source, which would reflect the operational situation. The source was removed and the HV was switched off. Then a measurement was performed where only the α source was applied to probe the residual electric field.

7.8. Measurements using the transient current technique (TCT)

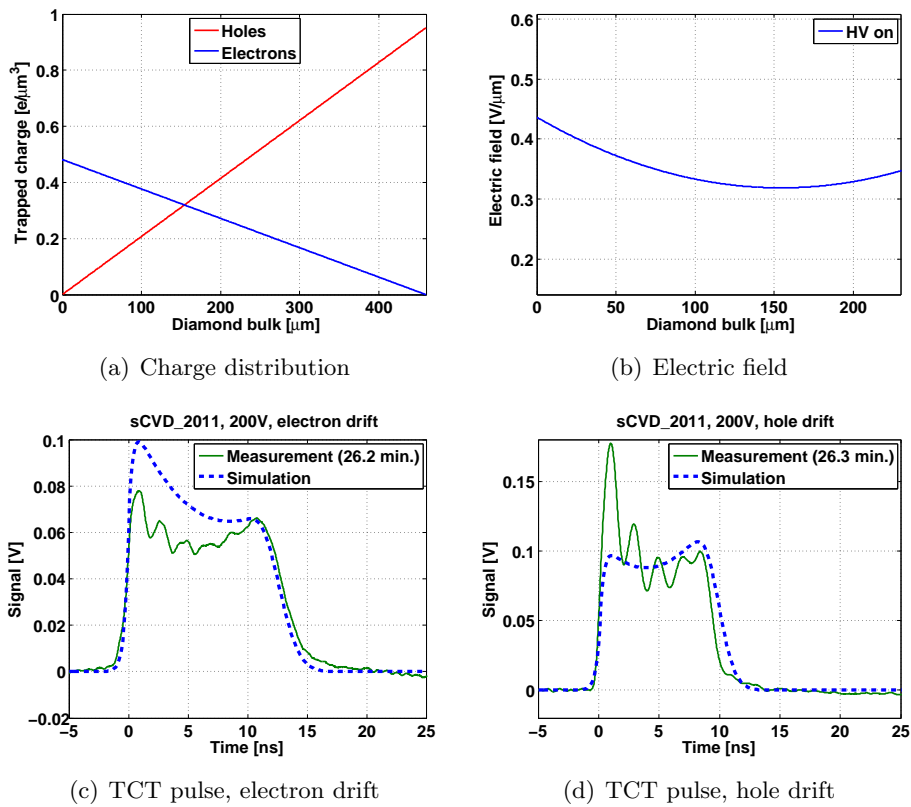


Figure 7.40.: Measured and simulated TCT pulses of sCVD_2011 at 200V. Slightly polarized (~ 25 minutes after HV on), diamond orientation: side 2.

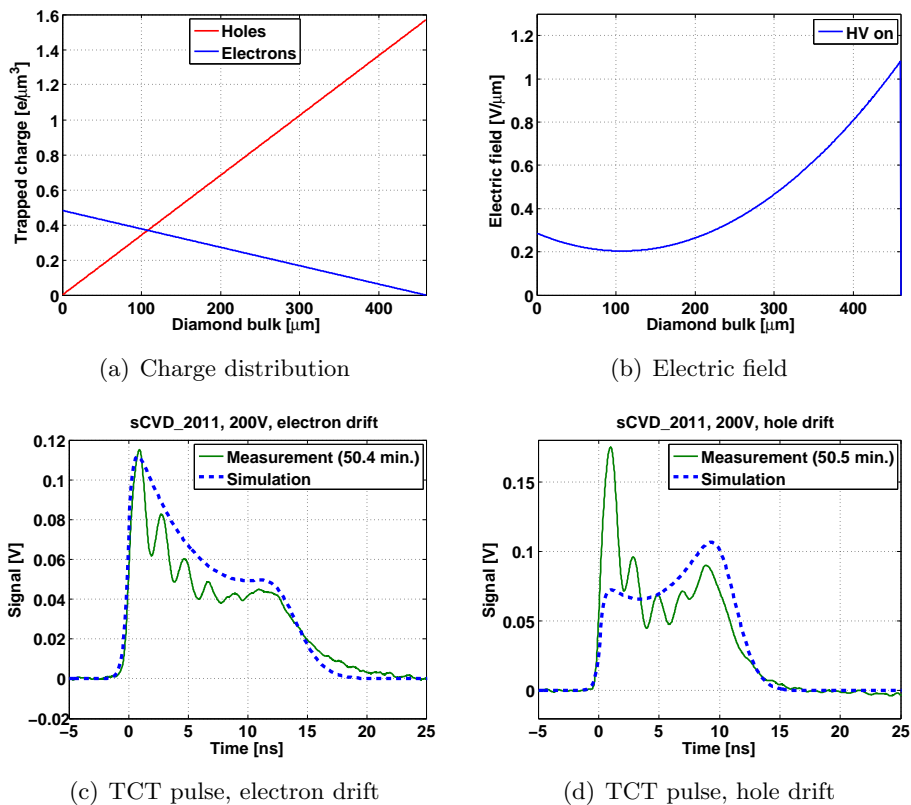


Figure 7.41.: Measured and simulated TCT pulses of sCVD_2011 at 200V. Highly polarized (~ 50 minutes after HV on), diamond orientation: side 2.

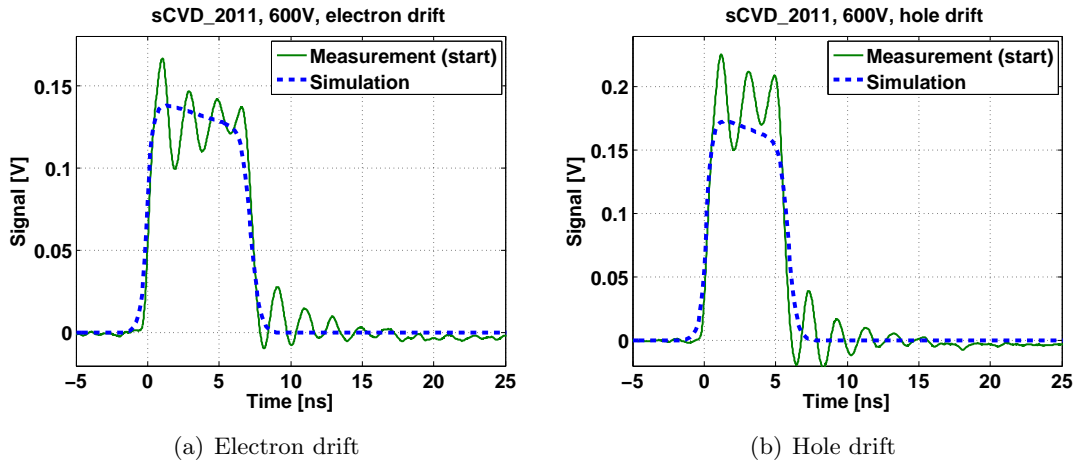


Figure 7.42.: TCT measurements at 600V with the diamond sCVD.2011 after removal from the BCML system. Measurements are taken immediately after the switch-on of the HV, hence the detector is not yet polarized.

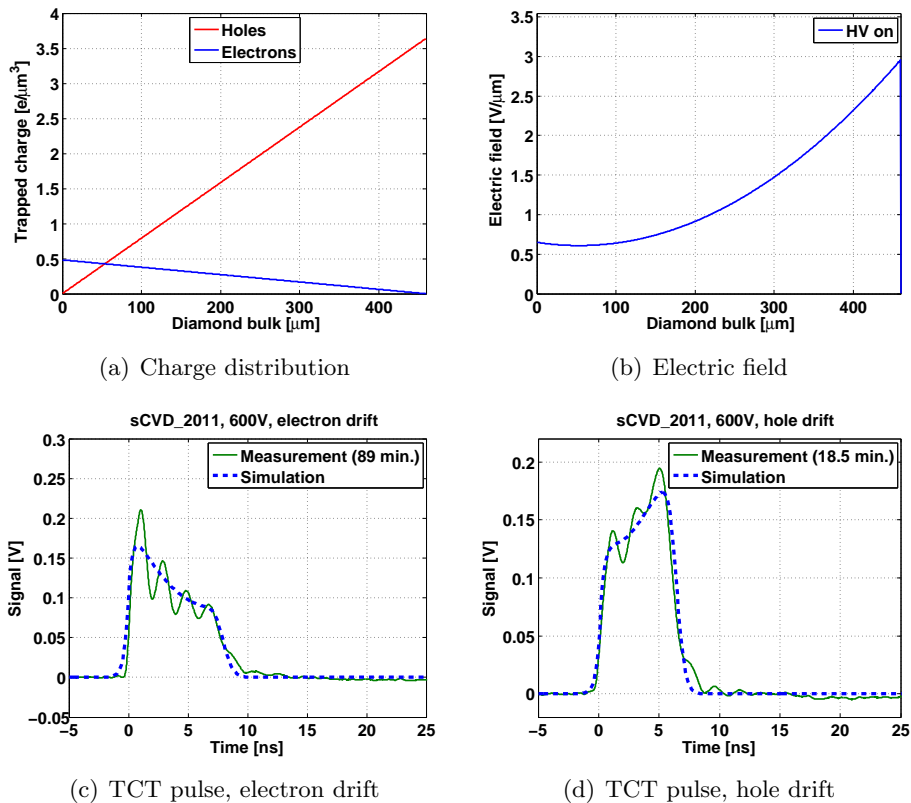


Figure 7.43.: Measured and simulated TCT pulses of sCVD.2011 at 600V, slightly polarized (~ 18 minutes after HV on), diamond orientation: side 1. Measurements of electrons took a much longer time to reach this polarization level, maybe the source was slightly mis-placed and the radiation environment was not strong enough.

7.8. Measurements using the transient current technique (TCT)

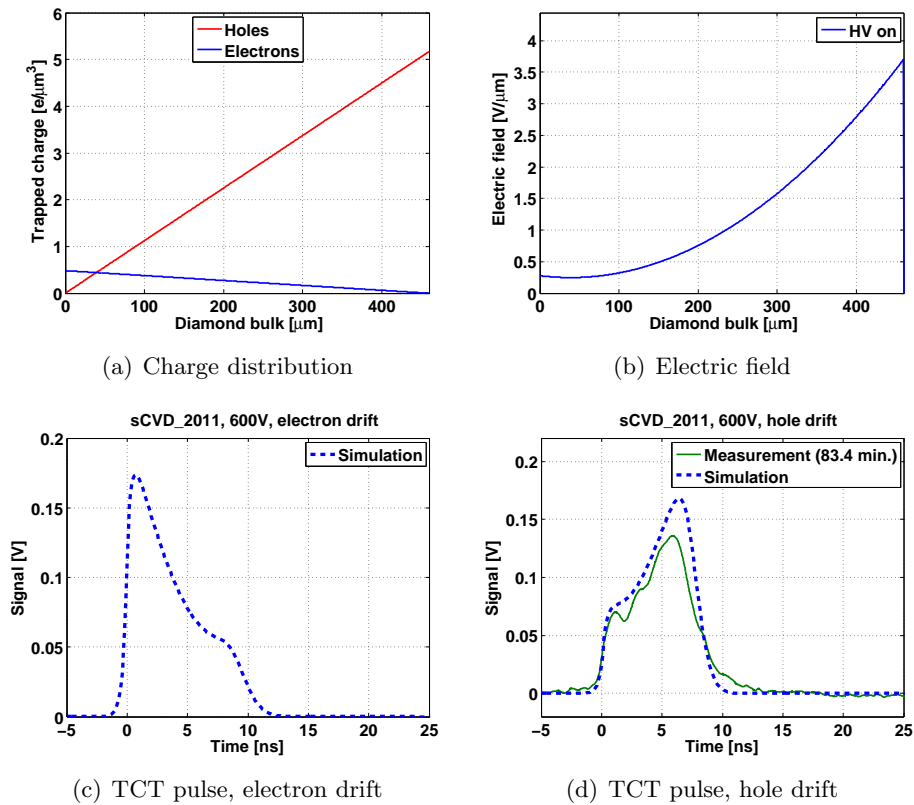
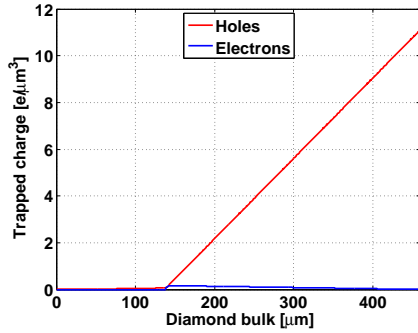
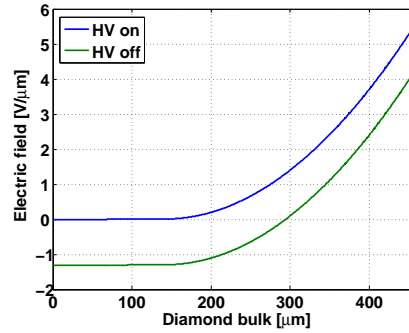


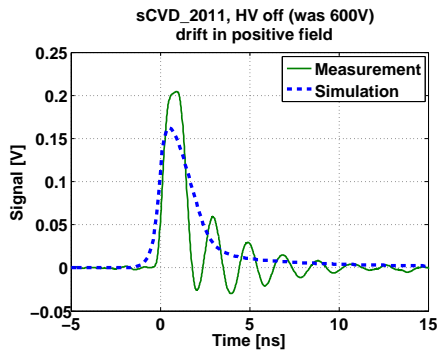
Figure 7.44.: Measured and simulated TCT pulses of sCVD_2011 at 600V, highly polarized (~ 80 minutes after HV on), diamond orientation: side 1. No measurements of electrons are available at this polarization level, maybe the source was slightly mis-placed and the radiation environment was not strong enough.



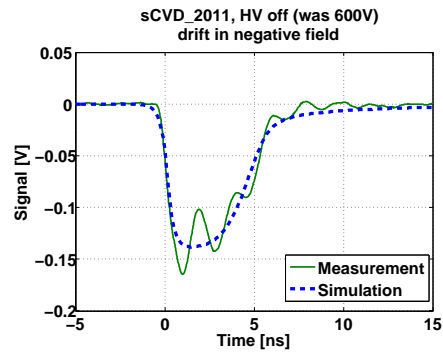
(a) Charge distribution



(b) Electric field



(c) TCT pulse, electron drift in positive field (from right side, cathode)



(d) TCT pulse, electron drift in negative field (from left side, anode)

Figure 7.45.: Measured and simulated TCT pulses of sCVD_2011 after polarizing at 600V. Measurements were taken immediately after the HV was switched off. The electric field is still positive at the cathode, but negative at the anode. In measurements with α particles an electron drift is always measured, for whatever side is used to inject the particles. In the negative field area a negative pulse is measured and expected.

Also the simulation of the electric field was performed for high amounts of induced charge, to obtain the electric field distribution at the situation of a high level of polarization. Figure 7.45(a) shows the distribution of the trapped charge. Figure 7.45(b) shows the electric field while the HV is switched on and the electric field after the HV was switched off. Due to the strong hole trapping, field free regions are created near the anode (left side of the plot).

The type of charge carrier that drifts depends on whether the electric field is positive or negative, and in which direction the charge can drift. On the right side (cathode), where the electric field is still positive, electron drift is expected, since the charge drifts from right to left. The measured pulse would be the same polarity as during the measurement with HV on. On the left side (anode), where the electric field is now negative, also electrons drift is expected, since the charge drifts from left to right. The type of the charge carrier drifting has changed here due to the HV switch-off, and a pulse with the opposite polarity compared to the HV-on measurements is expected.

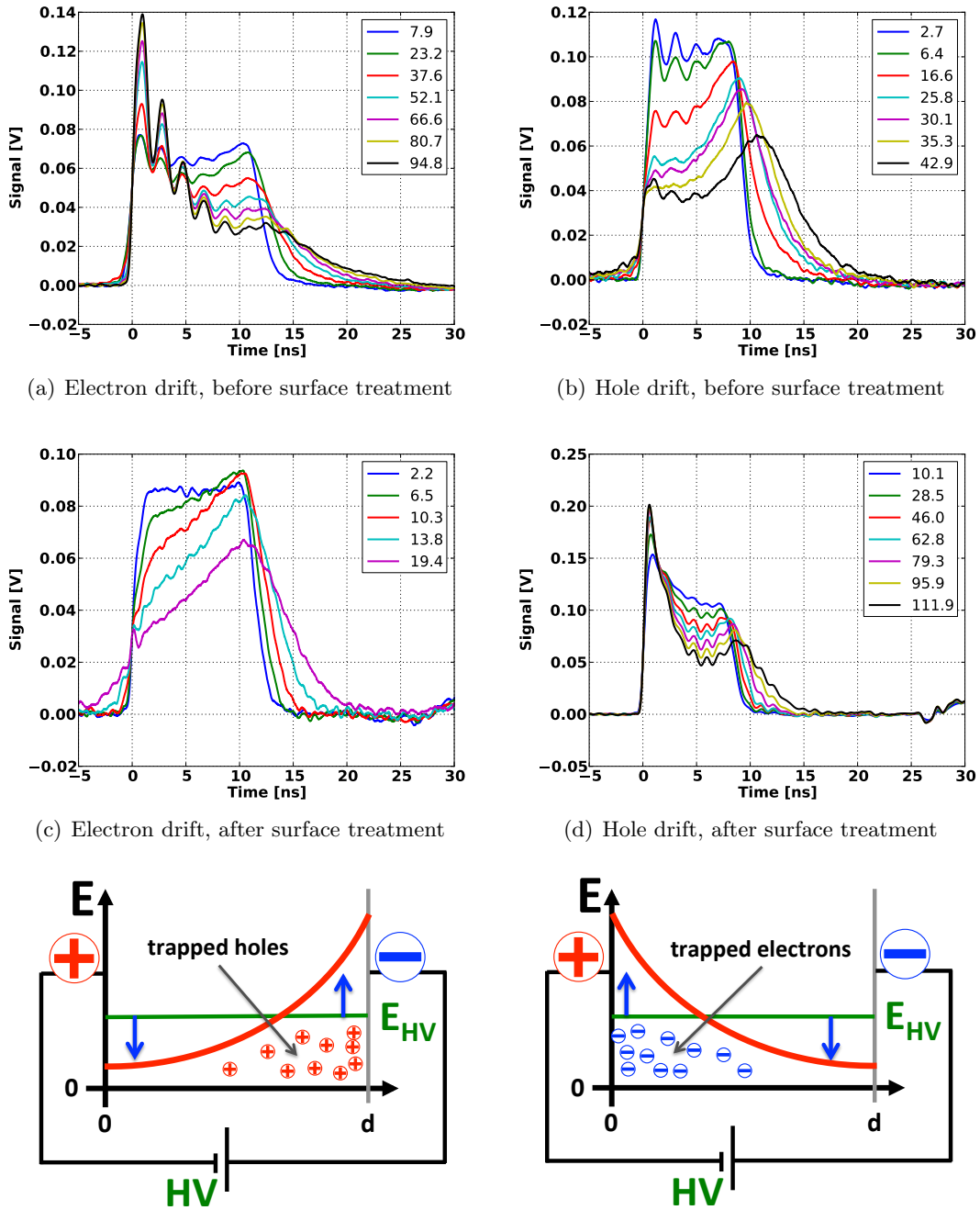
Figure 7.45(c) shows the measurement after the HV was switched off, where the α particle is injected on the cathode, where the electric field is still positive. Figure 7.45(d) shows the measurement, where the α particle is injected on the anode, where the electric field is now negative. The simulated TCT pulses reproduce well the measured signals. The polarity of the measured pulses is as expected. Measurements were done with both orientations of the diamond, which revealed the same results.

This measurement confirms that, even at the relatively low particle rates used for the TCT measurements, regions are created in the diamond, which are completely free of electric field. At the radiation environment where the measurement was performed, the zero field is about $180\mu\text{m}$ wide, which means the diamond is still active in 60% of its volume. In the much more intense radiation environment of CMS, the polarization buildup would be much stronger, which explains the reduced signal strength observed during operation.

7.8.4. sCVD_2011 after surface treatment

The measurement with this diamond clearly shows that the trapping responsible for polarization happens in the bulk, and not at the surface. In order to confirm that the diamond metal contact is not the source of the problems this diamond was processed. The surface was Ar/O plasma etched, about $10\text{-}20\mu\text{m}$ from both side. In order to create a polarization free contact a layer of diamond like carbon (DLC) was sputtered on the diamond surface. The DLC contacts have a high surface resistivity. This would, together with the diamond capacitance, create an RC filter, which destroys the fast signal shape of the TCT. The DLC was coated with a layer of aluminum to remove the surface resistivity of the contacts.

Figure 7.46 shows measurements at 200V for electron drift (figure 7.46(c)) and for hole drift (figure 7.46(d)) after the treatment. The pulses measured before surface treatment are shown as well (figures 7.46(a) and 7.46(b)). The legend indicates the time in minutes since the HV was switched on. Clearly a deformation still takes place after the treatment, which shows that the polarization could not be removed by the surface treatment. The shape of the signals of the polarized detectors changed. Prior to surface treatment hole trapping near the cathode was measured with negligible amount of trapped electrons. The electric field is visualized in the left picture of figure 7.46(e). The measured pulse is increased in height for the measurement of electrons, and a decrease in pulse height for the hole measurement is observed. After the surface treatment, a decrease in pulse height was observed for the measurement of electron drift, and an increase in pulse height measured in hole drift. This indicates a dominant trapping of electrons near the anode, resulting in an electric field as



(e) Sketch of electric field for the cases of pure hole trapping and pure electron trapping. Left plot shows the electric field before edging, right plot shows the electric field after edging.

Figure 7.46.: TCT measurements of the diamond sCVD_2011 at 200V before and after plasma etching of the surface and sputtering DLC electrodes. The legend indicates the time since the start of the measurement. The polarization process happens before and after surface treatment. The measurement before surface treatment (figures (a) and (b)) shows hole trapping at the cathode. The shape of the polarized pulses change after treatment and electron trapping at the anode is measured (figures (c) and (d)). The electric field for both cases is visualized in figure (e).

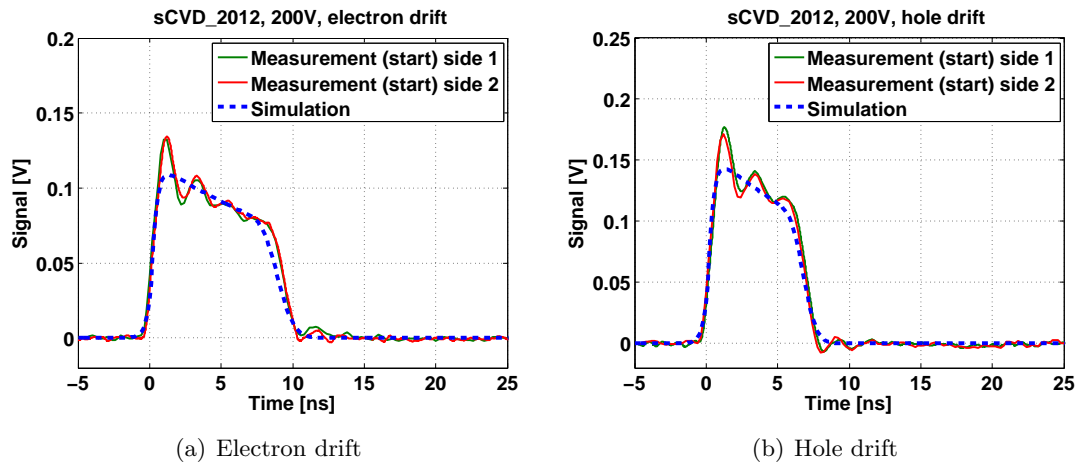


Figure 7.47.: TCT measurements of the diamond sCVD_2012 at 200V after removal from the BCML system. The data was taken immediately after the HV was switched on and no polarization has built up yet.

visualized in the right picture of figure 7.46(e). The reason for the change in signal shape is not understood. It is likely that the hole trapping happens at interstitials. During the acid cleaning processing the diamond was heated up to roughly 250°C. Usually no annealing is expected in diamond at this temperature, but it was shown in [New02] that self-interstitials are mobile at fairly low temperatures of around 550 K. The temperature could have been enough to mobilize and remove the interstitials, leaving only electron traps.

An annealing study where the TCT signals are measured at different annealing temperatures could give further insight into the properties of the defects responsible for polarization.

7.8.5. Measurements of sCVD_2012 after irradiation

The sCVD_2012 was measured with both sources at 200V and a strong polarization was observed, much like the sCVD_2011. Figure 7.47 shows the measurements for both types of charge carrier drifts for both sides of the diamond. A simulation of the TCT measurement was performed using the parameters for the drift velocity as measured by M. Pomorski (see table 7.1), and not the parameters measured with the irradiated sCVD_2011. For the calculation of the trapping, a CCE of 80 % was used, as the measured CCD prior to irradiation was about 83 % (see figure 7.29(b)). The simulation matches well the measured pulse, which leads to the conclusion that drift velocity and mobility are close to the values measured with the unirradiated sCVD_test1 detector and the values of unirradiated sensors published in [Pom08].

The polarization process was simulated as well. Figures 7.48 and 7.49 show the results for two different levels of polarization. This diamond shows very similar curves for both orientations of the diamond, hence two equivalent measurements are shown in one plot together with the simulated pulse. A spike at the start of the pulse in each measurement looks dominant in the plot. However also visible is an oscillation overlaid with this pulse. This peak appears sharper and higher due to these oscillations.

The simulation reproduces the simulation well. Only in the highly polarized state the latter part of the pulse in the hole drift measurement (figure 7.49(d)) is too high and too short. The measurement shows a more smeared out pulse. The general agreement with the simulation

shows that a buildup of positive space charge (e.g. by hole trapping) near the cathode is the dominant reason for the polarization. This result is in good agreement with the result from the sCVD_2011 detector.

The oscillations in the measurements are caused by a resistivity in the connectors at the detector modules. In a new measurement campaign the connection was improved and the oscillations disappeared. One result of these measurements with the sCVD_2012 detector is shown in figure 7.50. The level of polarization in this measurement is comparable to what is shown in figure 7.49(d). As comparison, the simulation of this level of polarization is plotted as well. The peak at the start of the measurements is less pronounced and agrees well with the simulation. As seen in the first measurement campaign, the width of the latter peak is significantly wider in the measurement.

7.9. Limitations of the simulation model, and possible improvements

The model presented in this chapter helps to understand the measured TCT signals with the aim to understand the electric field and the fixed space charge distribution. The two parts of the simulation, estimation of the electric field and estimation of the TCT pulse, have to be reviewed separately.

If no macroscopic defects are present and the edge of the metallization is not taken into account, the trapped charge does not vary in the plane parallel to diamond surface. The electric field vector is always perpendicular to the diamond surface and the distribution of space charge varies only along the electric field. Hence a 1-D calculation of the electric field is possible without the need for assumptions.

The estimation of the TCT pulse for a given electric field is also calculated in 1-D in the model presented here. One component of the drift behavior, however, can't be calculated in 1-D, the coulomb force created by the charge carrier cloud itself. While the charge carrier cloud drifts through the diamond bulk, it expands longitudinally as well as transversally to the drift direction. This leads to a reduced charge carrier density and hence to a reduced coulomb force. In order to estimate this effect correctly, the charge carrier density has to be calculated in 3-D. In the model presented here, the longitudinal drift was artificially blown up to represent this effect, which works sufficiently at high electric fields. When the electric field is reduced due to polarization, the estimation of the TCT pulse is not good any more in low field regions. This is mostly visible in figure 7.49(d). The peak in the latter part of the pulse is wider and lower in the measurement, compared to the simulation. A simulation tool which allows 3-D simulation of charge carrier drift in diamond is Silvaco Atlas[Sil], however 3-D simulations are very computing intense. One way to improve the speed of the simulation, but still obtain results of the same quality as 3-D, would be to use cylindrical coordinates and assume a rotational symmetry around the drift direction.

7.10. Potential defects responsible for trapping

From the TCT measurements it is evident, that both electron and hole trapping is happening. It is possible that the defects trapping electrons are a surface effect, where it is evident that the defects trapping holes are distributed in throughout the bulk, which is expected for traps generated by irradiation.

7.10. Potential defects responsible for trapping

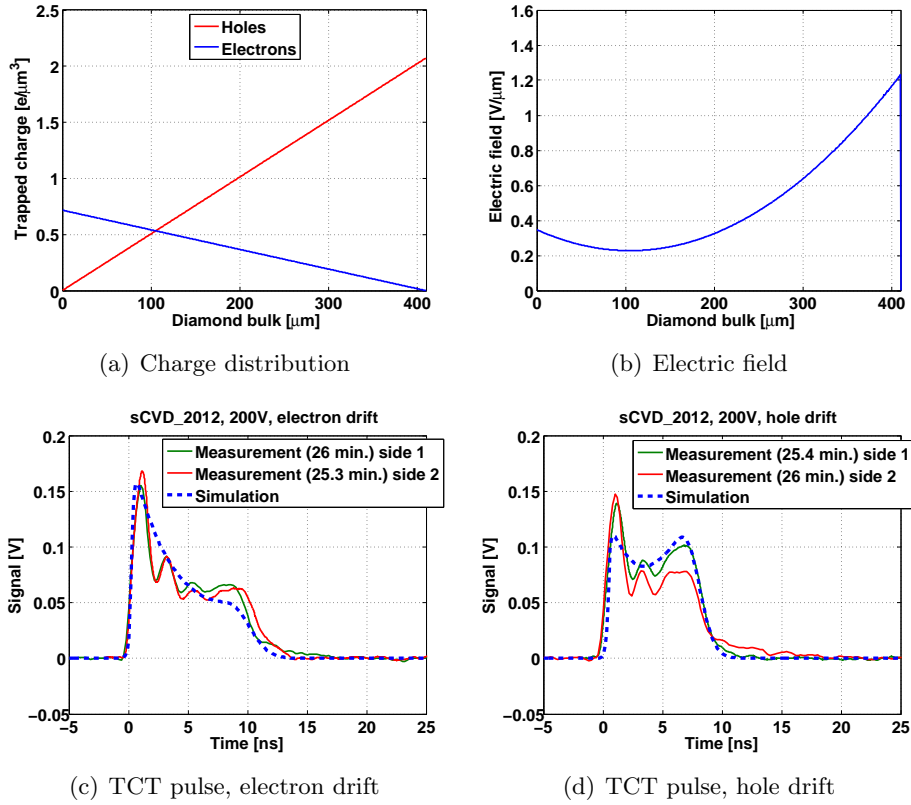


Figure 7.48.: Measured and simulated TCT pulses of sCVD_2012 at 200V. Slightly polarized (~ 25 minutes after HV on). Both diamond orientation are shown.

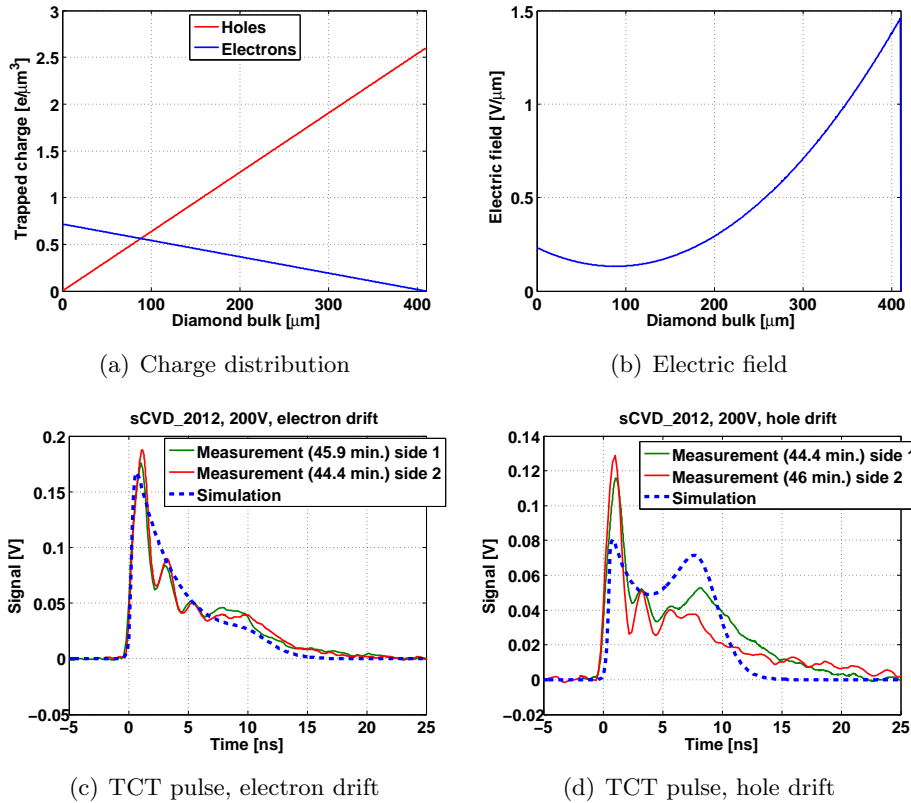


Figure 7.49.: Measured and simulated TCT pulses of sCVD_2012 at 200V. Strong polarized (~ 45 minutes after HV on). Both diamond orientation are shown.

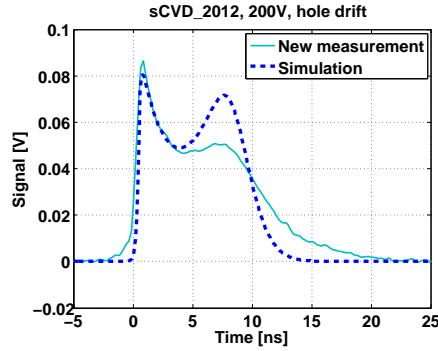


Figure 7.50.: Measured and simulated TCT pulse for hole drift of the sCVD_2012 detector. The simulation is the same as presented in figure 7.49(d), however the measurement was repeated after the bad connection responsible for the oscillations of the first measurements was removed.

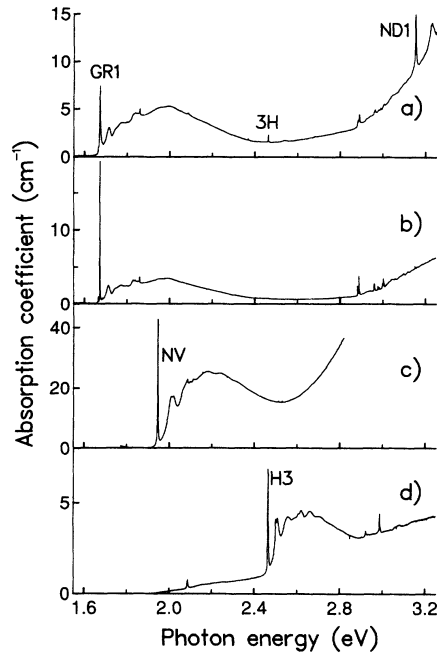


Figure 7.51.: Photo-absorption spectra of irradiated diamond samples [Dav92]. (a) type IaA diamond irradiated, (b) type IIa diamond irradiated, (c) type Ib diamond irradiated and annealed, (d) type IaA diamond irradiated and annealed. Mostly mono-vacancies are created in irradiation (GR1 band). In type Ib diamond nitrogen-vacancies (NV centers) are created during annealing. In type IaA diamonds, where nitrogen is in coupled in pairs (A center), the vacancies are also trapped at the nitrogen centers resulting in the H3 band.

In optical measurement of irradiated diamonds it was shown that mostly mono-vacancies are created, which can be either neutral (V^0) or negatively charged (V^-) [New02]. Figure 7.51 shows the photo-absorption spectra of diamonds irradiated with electrons, before and after annealing [Dav92]. The GR1 band corresponds to the presence of V^0 , which is mostly created in irradiations. In [Pom08] diamonds were irradiated with protons and with neutrons and analyzed with photo-absorption spectroscopy and with photo-luminescence spectroscopy. Also here the most dominant defects created during irradiation are mono-vacancies.

Shown in the TCT measurements is that hole trapping is mostly responsible for the polarization in diamond. Positively charged traps are sought. Vacancies are known to be either neutral or negatively charged, but in [Dan08] evidence for a positively charged state of the mono-vacancy was shown. Also self-interstitials would act as an acceptor and therefore trap holes. Self-interstitials are also found in the neutron and proton irradiation studies of [Pom08], but with much lower significance than the mono-vacancies. The change in charge trapping properties after the surface processing of the sCVD.2011 diamond could be related to the heating during the acid cleaning, where an annealing of the self-interstitials could have occurred. The change in trapping would indicate that indeed interstitials responsible for the hole trapping.

7.11. Conclusions on radiation damage analysis

In this chapter various aspects of radiation damage to diamond detectors were analyzed using data obtained during operation of the BCML system, laboratory analysis of irradiated detectors, and irradiation of diamond detectors in test beams. A model was developed to describe the effects of polarization due to trapped charge in the diamond bulk. A good agreement was found between the model and the measured data, which confirmed that polarization is the major effect responsible for the decrease of detector efficiency in the BCML system with increasing integrated luminosity.

The hyperbolic fit to the data of signal vs. fluence does not describe the decrease well. The hyperbolic fit, which is usually used to describe radiation damage in diamond, is based on a model that takes only efficiency loss due to charge trapping into account. This model is not applicable to a detector that suffers from polarization, which happens at significantly lower fluences than signal reduction due to charge trapping.

By performing TCT measurements to monitor how the diamond polarizes the electric field distribution could be understood. A simulation code was developed, which main input parameters are the distribution of electron and hole traps, their relative strength of trapping, and their relative lifetime. The simulation calculates the space charge distribution in a radiation environment of MIPs, and from this the electric field distribution. Then TCT pulses, equivalent to measurements using a ^{241}Am α source, for electron drift and for hole drift are estimated. Due to the good agreement between simulation and measurement the electric field distribution could be recreated and an insight into properties of the responsible charge traps was found. It is evident that defects trapping holes, which are equally distributed through-out the bulk, are mainly responsible for the buildup of polarization.

Chapter 8.

Summary and outlook

8.1. Summary

The LHC Run 1 was a successful data taking period, both for the CMS experiment and for the Beam Condition Monitor “Leakage” (BCML). The BCML was a key system during the operation of CMS and will continue to remain important for future runs. Without functioning BCML, the Silicon Tracker would not have been permitted to activate its HV during collisions and the status of the beam conditions would be unknown. BCML performed well, only on very few minor incidents the electronics failed and a LHC beam dump was asserted. The important operational points are summarized in the following:

- In the beginning of 2011 the original BCM1L readout system was abandoned and the detector channels were included into the BCM2 readout system, forming the overall BCML system. This extension of BCM2 doubled the amount of abort channels and hence increased the safety and redundancy of the system. The amount of monitoring information increased as well.
- On very few occasions, the electronics showed failure. The tunnel cards spontaneously reset twice and the low voltage failed once, which led to a beam dump, as the protection against beam loss events could not be assured any more. The re-injection of the LHC was permitted immediately by deactivating the involved tunnel cards from the beam dump, and the faulty electronics was replaced during the next possible access to the experimental cavern. In two incidents, a HV power supply failed, which did not lead to a beam abort, since the presence of the HV is not a precondition for the beam permit. No data loss of CMS during collisions was attributed to a failure of BCML, since in a failure case, the LHC beam is dumped.
- On several occasions, beam loss events were measured, but were not significant enough to cause a beam dump. However, they were most useful to better understand the LHC machine and the performance of the BCML system. During LHC machine commissioning beam losses are created artificially, either in a collimator scan or an aperture scan. These losses were interesting to study but never posed any threat to the silicon detectors of CMS, as the intensity was very low and the CMS Tracker was not switched on. During operation, several significant events of unknown falling objects (UFOs) were found. Fortunately, they were not exceeding the abort threshold. These types of events could be of dangerous intensity, and BCML would have the capability to protect the silicon detectors in CMS by dumping the beam. Another type of observed beam loss events were due to bad vacuum, mostly in 2011, where a damaged beam screen connection sparked many times and created an electron cloud. These events are usually of longer duration and are not likely to cause permanent damage. Nevertheless they are unwanted, since the CMS data taking efficiency is adversely affected.

- Two BLM ionization chambers were added to the system in the beginning of 2012. They were each placed on top of the CASTOR table, directly behind BCM2, one tube per end. These detectors provide a good dynamic range and no radiation degradation is expected. The proximity to the BCM2 detectors and the fact that they are in the same readout system as BCM2 makes them ideal to normalize the BCM2 readings and thereby monitor non-linearities and instabilities in the diamond sensors.
- One flaw of the original BCM2 design was the dimensioning of the HV filter. Due to an extremely high filter resistor, the supply of high current could not be ensured over an extended period of time. The danger was having high detector currents just below the beam abort threshold, which would not dump the beam but would drain the filter capacitor and the HV over the diamond would decrease. The full abort functionality would not be assured any more in this case. An additional abort threshold on the 5.2 s integration time window was implemented to avoid this situation. Unfortunately, the detector current during normal operation was close to this level. Therefore, all HV filters were modified by lowering the filter resistor, allowing a higher supply of current. The filter parameters are still very good and all RF noise on the HV line is filtered efficiently. Thus the special abort threshold could be removed.
- One unfortunate issue with the tunnel card electronics are the noise spikes. Occasionally, a very high value is reported, which is much higher than the usual readings during operation. It was shown in this thesis that the maximum height of those spikes does not increase with higher detector currents (except for the increase due to actual detector current). Therefore, these spikes do not impose the threat of a false beam abort. The maximum spike value has to be taken into account when new beam abort thresholds are defined to avoid false beam aborts. The number of spikes increases linearly with the detector current. Unfortunately this cripples the ability of the system of good monitoring for short integration times.

The major observation presented in this thesis was the decrease in signal efficiency. The diamond detectors were not expected to change their efficiency significantly in the first years of LHC operation [Mül11]. By monitoring the signal in comparison with the instantaneous luminosity a change in efficiency was measured. The radiation damage observations in this thesis are summarized as follows:

- The signal measured by the BCML detectors was found to scale linearly to the first order with the instantaneous luminosity, as expected. The ratio of detector signal and instantaneous luminosity showed signs of long term degradation. The amount of signal decrease was correlated with the hadronic particle fluence indicating radiation damage. Especially the BCM2 detectors on the -Z end, which are placed directly in front of the calorimeter CASTOR, showed significant loss in signal efficiency. The heavy CASTOR calorimeter created a strong increase in neutron fluence on the -Z end compared to the BCM2 location at the +Z.
- The radiation damage could be quantified by performing FLUKA Monte Carlo simulations of the CMS detector and obtaining the simulated amount of particle fluence per integrated luminosity. The “displacements per atom” scoring of FLUKA was used to convert the fluence to the newly introduced 24 GeV proton equivalent scaling. Thereby the decrease in signal could be expressed as a function of 24 GeV proton fluence and directly compared with irradiation studies performed by the RD42 collaboration. The

measured radiation damage constant is significantly higher than the RD42 prediction. Moreover, the radiation damage constant reached lower values towards higher levels of irradiation, implying that the damage curve could have an additional non-hyperbolic component. The shape of the decay curve was qualitatively recreated using calculations of the electric field distributions with a fixed space charge buildup. The loss of signal efficiency was thereby shown to be due to field free regions, caused by polarization of the diamond.

- In a test beam irradiation using 23 MeV neutrons and two single-crystalline diamonds in the standard BCM2 readout, a damage curve was measured, confirming the findings of the BCML damage curves. The damage constant of the hyperbolic damage curve decreases in value with higher fluences, but is still significantly higher than the RD42 reference value. The measured range of k-values is consistent with the numbers measured in BCML.
- Several diamonds were removed from BCML after operation and the charge collection distance (CCD) was measured and compared to measurements performed prior to installation. The loss in CCD is consistent with the expectation based on the RD42 irradiations. The decrease of signal efficiency during operation is significantly stronger than the change in CCD. The effect of charge trapping after irradiation therefore does not explain the loss in signal efficiency.
- A special measurement method using the transient current technique (TCT) was prepared. Unlike a measurement with a silicon detector, where the signal shape is stable over time, the diamond changes in signal shape due to build up of polarization. This is investigated by starting to measure with an unpolarized detector. A MIP source is applied next to the α source, which probes the electric field. The charge deposited by the MIP source is comparable to the operational environment and leads to polarization of the detector. The process of the diamond polarizing takes several minutes, which makes it possible to monitor the development and to measure TCT shapes at different levels of polarization. In a high rate environment, as in luminosity production, this would happen in a few seconds.
- A simulation model was developed, where the distribution of traps is configured and the charge build up due to MIP particles is simulated. The electric field is calculated by integrating over the trapped charge. Based on the electric field, TCT pulses can be estimated. By tuning the simulation to the measurements an understanding of the electric field distribution and an approximated trapping distribution was found. All measurements are in support of strong hole trapping throughout the bulk.

8.2. Outlook

Given the experience with the BCML system until now, the system could be improved for further operation. The LHC will deliver during its normal lifetime an integrated luminosity of about 300 fb^{-1} , 10 times more than delivered so far. In the HL-LHC phase, an integrated luminosity of 3000 fb^{-1} is expected. New ways to maintain the BCML system are sought. Planned and potential upgrades are:

- Operating BCM1L with the front-end “tunnel card” electronics being placed in the service cavern and $\sim 100 \text{ m}$ cable between sensor and electronics gave good experiences.

The noise level was almost as low as with BCM2 and several order of magnitude below the more problematic spike noise. The advantage of this design is the placement of the electronics in a radiation-safe and accessible area. Thereby, maintenance is much simplified. It is planned to move the tunnel cards of BCM2 to the service cavern, too. During the long shutdown 1, appropriate cables will be pulled. The change of the system will not be done before the technical stop in 2015, as for the start up of the LHC after the long shutdown, a reliable and tested system is needed.

- The BSC2 scintillating counters were removed from the BCM2 wheel since the particle rates, measured during 2011 and 2012, were above the dynamic range of the detector. This provides a lot of free space inside the wheel and the possibility to install new prototype detectors. One idea is to place a fast particle counting detector as complementary measurement to the leakage current measurement of BCM2. The newly developed BCM1F front-end amplifier is a suitable candidate. As the BCM2 location has a more intense radiation field compared to the BCM1 location this would also be a good test to predict the performance of the BCM1F in the future.

- As shown, the polarization is a significant problem for the BCML detectors. Although the total amount of signal is still sufficient, a constant reconfiguration of the system is needed in order to maintain the same level of protection. A more stable detector technology is sought that still fulfills the requirements of having a fast detector, radiation hard and without the need for cooling. Different types of detector material could now be installed in long shutdown 1 and evaluated as possible replacement of the pCVD for the high luminosity operation of the LHC.

The newly developed heteroepitaxial diamond-on-iridium material [Ber09] is a very potential type of diamond, which can be produced in big wafers like a poly crystal diamond, but provides homogeneity like a single crystal diamond. This material would be ideal for large surface pixel or strip detectors. It has not been tested in a high rate environment yet, however this could be done in BCM2. It would be interesting to investigate if the performance during operation is comparable with single-crystalline or poly-crystalline diamond, and if a signal decrease due to polarization is observed.

Sapphire (Al_2O_3) is also an interesting material for the application as beam loss monitor [Ign10]. This high band gap material is produced in a Czochralski process and is therefore significantly cheaper than diamond. The charge collection efficiency (CCE) is only about 5-10% due to the fairly high number of impurities. This, however, can be compensated by using a higher detector volume. A low CCE leads to a low change of CCE due to irradiation and thus to a higher relative radiation hardness. Sapphire is not a good detector material if a thin sensor with high charge collection is needed, for example in pixel or strip detectors. However in applications where the low CCE can be compensated by using more detector material, like in a beam loss monitor, it is a cheap alternative to diamond.

- Still, diamond is a viable detector material. Methods to avoid or minimize polarization should be developed. Often, the metal electrodes are directly brought on to the diamond surface. A method to reduce the polarization at the surface is to use a graphitic layer. Electrodes made of diamond-like carbon (DLC) coated with metal could reduce the polarization. This has not been tested in a high rate environment yet, but could be done with a prototype detector in BCM2.

A method of actively removing polarization is to apply light on the diamond. Red light

is sufficient to clear the traps responsible for polarization. This was proven effective in low rate environments. Tests at high rates have not been performed yet. It would be interesting to study the signal efficiency at controlled high rates under controlled amount of depolarizing light. This could lead to a polarization free diamond by constant illumination of the diamond.

Another technique is the usage of alternating polarity HV, also used in the work of this thesis to obtain polarization free CCE measurements. By constantly changing the drift direction of the charge carriers the bulk charges up homogeneously and the polarization is much substantially. At high intensity radiation fields, the switching frequency needed to maintain a polarization free detector increases. This has not been tested in a high rate environment yet. A novel detector could be developed and tested in the BCM2 location to show that this method of avoiding polarization is a viable technique in operational conditions.

The TCT measurement technique used in this thesis has high potential to obtain a better understanding of the polarization effects in diamond detectors. Many different aspects could still be improved:

- Due to the different lifetimes of traps they saturate at different levels of occupancy for a given particle rate. At different HV, different amounts of trapped charge is needed to polarize the diamond. If the measurements are performed at many different HV the different types of traps can be separated by their level of saturation.
- Alternating polarity HV is also a viable option to be tested in TCT measurements. The alternating polarity would not completely remove the polarization, since the trapping of electrons and the trapping of holes is different. Nevertheless it would give further insight into the trapping mechanism.
- The method of red light illumination could be tested with the TCT as well. Tests done so far in the scope of this thesis have not revealed useful information, but more detailed testing could show the effectiveness of illumination in avoiding polarization.
- A simultaneous measurement of TCT using α particles and measurement of CCE using MIP particles could connect the pulse shapes to the actual signal performance of the detector. This could be a final proof that the polarization is responsible for the loss of charge collection.
- The model to predict the shapes of TCT pulses presented in this thesis is limited by its one dimensional character. The disturbance of the electric field by the charge carriers themselves can only be calculated, if the charge carrier density is calculated correctly in three dimensions. A compromise to reduce the required computing resources would be a two dimensional calculation in cylindrical coordinates where a rotational symmetry around the direction of the drift is assumed. A software capable of calculating a charge carrier drift through diamond in three dimensions would be Silvaco Atlas[Sil].

Acknowledgements

I wish to thank, first and foremost, my supervisor Prof. Wim de Boer who suggested this interesting topic and convinced me to go to CERN for a PhD thesis. I am greatly thankful for the exceptional support: the correcting of my papers and talks, steering the right path in scientific exploration and the very helpful discussions.

I am very grateful to Prof. Thomas Müller for being my second reviewer, giving valuable input and general support.

I owe deepest gratitude to my CERN supervisor Anne Dabrowski. It was a great pleasure to work together in fighting off the problems we encountered during the operation of the BCM detectors. The biggest challenges as a PhD student are the political decisions, where she guided me very well. I thank her for her assistance in all aspects of the work I was facing and for patiently explaining the things I still had to learn.

Without Richard Hall-Wilton I would not have started to work on this project. I am not only very thankful for him being my supervisor in the early period of my thesis work, but also for all the support he gave me during the whole time.

I am indebted to Steffen Müller, who played a major role in the construction of BCM2. He helped me in many ways to get started with this project and was still supportive even after committing to new tasks. Many fruits I picked were planted by him.

I would like to thank all member of the BRIL project for the great teamwork, helpful discussions, and all the help I was given. Foremost my thanks go to David Stickland, for his support in all matters of BCML operation and diamond research. I deeply thank Alan Bell who went through the same process of writing a PhD thesis shortly before me and was able to help me in many ways.

Great support was given by many people at CMS. I would like to thank in particular Wolfram Zeuner, Austin Ball, Patrice Siegrist and Duccio Abbaneo for their general support. Also I thank Dawn Hudson and Laetitia Guilly for the great assistance with all the paperwork.

Although I only occasionally spent time at my home institute in Karlsruhe, many results of this thesis were acquired there. Robert Eber and Andreas Nürnberg did not only spend considerable amount of time assisting me with the measurements I performed in Karlsruhe, but also helped me numerous times when I had tricky questions or crazy ideas. Also I am grateful for the help with all the bureaucracy from Brigitte Gering, Diana Fellner-Thedens and Bärbel Bäunling. I thank all members of the Institut für Experimentelle Kernphysik for their great support.

A big “Thank you” goes to the technicians at the IEKP in Karlsruhe: Pia Steck, who

Chapter 8. Summary and outlook

always helped me when I needed a diamond glued, cleaned, bonded, packaged or treated in any possible way, Tobias Barvich who always brilliantly came up with ideas how to build the test stands I pictured in my head, and Felix Bögelspacher who was always available for discussions and helped me out with his electronics expertise.

Extremely supportive for the success of this thesis was the CMS group at DESY Zeuthen. I owe deep gratitude to Prof. Wolfgang Lohmann for his support. I also thank Wolfgang Lange and Konstantin Afanaciev for their assistance with the CCD measurements.

From the BLM section of the CERN BE/BI group I thank Ewald Effinger and Christos Zamatzas for the great support with the BLM electronics, and Bernd Dehning and Christoph Kurfürst for the interesting discussions about diamond detectors and polarization.

I would like to thank Heinz Vincke, Christina Urscheler and Igor Kurochkin from the CERN radiation protection group for the help I received concerning the topic of material activation and the nice collaboration regarding FLUKA simulations of CMS.

I owe sincere and earnest thankfulness to Eléni Berdermann from the “Gesellschaft für Schwerionenforschung”, not only for providing some of the diamonds used in this thesis and giving the opportunity to metallize the diamonds. Also the workshops at GSI always were a great pleasure to attend with great and enlightening discussions.

I am very grateful to Michal Pomorski for the surface processing of one of our diamonds and the general discussions about TCT measurements and polarization in general.

Thanks a lot to Martin Husnik from the Institute of Applied Physics at the KIT for providing the possibility to take cross-polarized pictures of diamond.

A big “Thank You” goes to Federico Ravotti for the fruitful collaboration in setting up the updated FLUKA geometry.

I thank Otilia Militaru from the Cyclotron in Louvain-la-Neuve for the support during the irradiation campaign.

A thesis needs a lot of proof reading. For this I thank: Anne Dabrowski, Sophie Mallows, Alan Bell, Michaela Schaumann, Jens Guthoff, Martina Guthoff and Christine Guthoff.

I thank the Wolfgang-Genter-Programme of the Bundesministerium für Bildung und Forschung for the financial support and Michael Hauschild, the coordinator of the program, for his assistance and advice.

Finally I would like to thank all my friends and family for the moral support during this exciting, but stressful times.

Bibliography

- [Aai13] The LHCb Collaboration, R. Aaij et al., “Measurement of the $B_s^0 \rightarrow \mu^+ \mu^-$ Branching Fraction and Search for $B^0 \rightarrow \mu^+ \mu^-$ Decays at the LHCb Experiment”, *Phys. Rev. Lett.* 111, 101805 (2013).
- [Ams09] C. Amsler et al., “Mechanical design and material budget of the CMS barrel pixel detector”, *JINST* 4 (2009), P05003.
- [Ane08] G. Anelli et al., “The TOTEM Experiment at the CERN Large Hadron Collider”, *J. of Instr.*, vol. 3, article S08007, 107 pages, August 2008.
- [Asm02] J. Asmussen, D.K. Reinhard, “Diamond Films Handbook”, Marcel Dekker, Inc. 2002.
- [Bae11] T. Baer et al., “UFOs in the LHC”, *IPAC’11, TUPC137*, 09/2011.
- [Bar07] D. Barney et al., “Implementation of on-line data reduction algorithms in the CMS Endcap Preshower Data Concentrator Cards”, 2007 *JINST* 2 P03001.
- [Barn13] D. Barney et al., “Measurement of the bulk leakage current of silicon sensors of the CMS Preshower after an integrated luminosity of 6.17 fb^{-1} , at $\sqrt{s} = 7 \text{ TeV}$ ”, 2013 *JINST* 8 P02004.
- [Bart13] C. Barth, “Physikalische Analyse des Ansprechverhaltens des CMS Siliziumdetektors beim Betrieb am LHC”, Ph.D. thesis, IEKP-KA/2013-01, 2013.
- [Bat06] G. Battistoni, S. Muraro, P.R. Sala, F. Cerutti, A. Ferrari, S. Roesler, A. Fassò, J. Ranft, “The FLUKA code: Description and benchmarking”, in: M. Albrow, R. Raja (Eds.), *Proceedings of the Hadronic Shower Simulation Workshop 2006*, Vol. AIP Conference Proceeding 896, Fermilab 6–8 September 2006, 2007, pp. 31–49.
- [Bel07] A. J. Bell, “The design & construction of the beam scintillation counter for CMS”, Master’s thesis, Dept. of Physics & Astronomy, University of Canterbury, Christchurch, New Zealand, 2007.
- [Bel10] A. J. Bell et al., “Fast Beam Conditions Monitor BCM1F for the CMS Experiment”, arXiv:0911.2480v3, *Nucl. Instrum. Methods Phys. Res., A* 614 (2010) 433-438.
- [Bel10a] A. J. Bell et al., “Fast Beam Conditions Monitor BCM1F for the CMS Experiment”, *Nucl.Instrum.Meth.A*614:433-438,2010.
- [Bel13] A. J. Bell, “Luminosity, Beam Monitoring and Triggering for the CMS Experiment and Measurements of the Total Inelastic Cross-Section at $\sqrt{s} = 7 \text{ TeV}$ ”, PhD thesis, Faculté de sciences de l’Université de Genève, Thèse N° 4516.

Bibliography

- [Ber09] E. Berdermann et al., “Diamond detectors for hadron physics research”, in: *Diamond and Related Materials* 19 (2010) 358-367, Proceedings of Diamond 2009, The 20th European Conference on Diamond, Diamond-Like Materials, Carbon Nanotubes and Nitrides, Part 1, DOI: 10.1016/j.diamond.2009.11.019.
- [Boe09] W. de Boer et al., “Radiation Hardness of Diamond and Silicon sensors compared.” *Phys. stat. Sol.* 204(2007)3004.
- [Bol06] J. Bol, “Strahlmonitore aus Diamant für primäre Teilchenstrahlen hoher Intensität”, Ph.D thesis, Universität Karlsruhe, IEKP-KA/2006-08.
- [BRM] The CMS Collaboration, “The CMS Experiment at the CERN LHC”, 2008 JINST 3 S08004, p. 290-296.
- [Can79] C. Canali et al., “Electrical properties and performances of natural diamond nuclear radiation detectors”, *Nuclear Instruments and Methods A*, 160:73-77, 1979.
- [Cau67] D. M. Caughey, R. E. Thomas, “Carrier Mobilities in Silicon Empirically Related to Doping and Field”, *Proc. of the IEEE*, vol. 55, p. 2192, 1967.
- [Cha08] The CMS collaboration, S. Chatrchyan et al., “The CMS experiment at the CERN LHC”, 2008 JINST 3 S08004.
- [Cha12] The CMS Collaboration, S. Chatrchyan et al., “Observation of a new boson at a mass of 125 GeV with the CMS experiment at the LHC”, *Physics Letters B*, Volume 716, Issue 1, 17 September 2012, Pages 30-61, ISSN 0370-2693.
- [Cha12a] The CMS Collaboration, S. Chatrchyan et al., “Observation of a New Ξ_b Baryon”, *Phys. Rev. Lett.* 108 (2012) 252002.
- [Cha13] The CMS Collaboration, S. Chatrchyan et al., “Measurement of the $B_s^0 \rightarrow \mu^+\mu^-$ Branching Fraction and Search for $B^0 \rightarrow \mu^+\mu^-$ with the CMS Experiment”, *Phys. Rev. Lett.* 111, 101804 (2013).
- [Dab11] A. Dabrowski, et. al., “The performance of the Beam Conditions and Radiation Monitoring System of CMS”, in: *Nuclear Science Symposium and Medical Imaging Conference (NSS/MIC)*, 2011 IEEE, 2011, pp. 489–495. <http://dx.doi.org/10.1109/NSSMIC.2011.6153979>.
- [Dab11a] A. Dabrowski, M. Guthoff, “Proposed modification to CMS BCM2 RS12 thresholds and preparations for putting CMS BCM1L detector in the LHC machine protection system”, CERN EDMS 1157274 v.3, 12th Sept 2011.
- [Dab12] A. Dabrowski, M. Guthoff, “Proposed modification to CMS BCM2 and BCM1L thresholds for 2012 running”, CERN EDMS 1236236 v.1, 15th Aug 2012.
- [Dan08] S. Dannefaer and K. Iakoubovskii, “Defects in electron irradiated boron-doped diamonds investigated by positron annihilation and optical absorption”, *J Phys Condens Matter*, 2008 Jun 11, 20(23):235225, doi:10.1088/0953-8984/20/23/235225.
- [Dav92] G. Davis et al., “Vacancy-related centers in diamond”, *Physical Review B*, vol. 46, no.20, 1992.

- [Deh02] B. Dehning et al., “LHC Beam Loss Monitor System Design”, 10th Beam Instrumentation Workshop, Upton, NY, USA, 6 - 9 May 2002, AIP Conf. Proc. 648 (2002) pp.229-236.
- [Dem05] W. Demtröder, “Experimentalphysik 4: Kern-, Teilchen- und Atomphysik”, Springer-Verlag, ISBN 3-540-21451-8, 2nd edition, 2005.
- [Dol08] I. Dolenc, “Development of Beam Conditions Monitor for the ATLAS experiment”, Ph.D. thesis, University of Ljubljana, 2008.
- [Ebe13] R. Eber, “Untersuchung neuartiger Sensorkonzepte und Entwicklung eines effektiven Modells der Strahlenschädigung für die Simulation hochbestrahlter Silizium-Teilchendetektoren”, Ph.D. thesis, Karlsruhe Institute of Technology, IEKP-KA/2013-27.
- [Eff06] E. Effinger et al., “The LHC beam loss monitoring system’s data acquisition card”, 12th Workshop on Electronics For LHC and Future Experiments, Valencia, Spain, 25 - 29 Sep 2006, pp.108-112.
- [Eva08] L. Evans and P. Bryant (editors), “LHC Machine”, 2008 JINST 3S08001.
- [Fas10] A. Fasso et al., “FLUKA Realistic Modeling of Radiation Induced Damage”, Proceedings of a Joint International Conference on Supercomputing in Nuclear Applications and Monte Carlo 2010 (SNA + MC2010), Tokyo, Japan, October 17-21, 2010.
- [FBC11] Curse material of the 10th FLUKA Beginners Course, Heidelberg, Germany, 2011, <http://www.fluka.org>.
- [Fer05] A. Ferrari, P.R. Sala, A. Fassò, J. Ranft, “Fluka: a multi-particle transport code”, CERN-2005-10 (2005), INFN/TC_05/11, SLAC-R-773.
- [Gsc02] E. Gschwendtner et al., “The Beam Loss Detection System of the LHC Ring”, 8th European Particle Accelerator Conference, Paris, France, 3 - 7 Jun 2002, pp.1894, CERN-SL-2002-021-BI.
- [Gut11] M. Guthoff, “Design and Experiences with the Beam Condition Monitor as Protection System in the CMS Experiment of the LHC”, proceedings of European Workshop on Beam Diagnostics and Instrumentation for Particle Accelerators, DIPAC’11, Hamburg, Germany, 2011.
- [Gut13] Moritz Guthoff, Wim de Boer, Steffen Müller, “Simulation of beam induced lattice defects of diamond detectors using FLUKA”, Nuclear Instruments and Methods in Physics Research Section A: Accelerators, Spectrometers, Detectors and Associated Equipment, Volume 735, 21 January 2014, Pages 223-228, ISSN 0168-9002, <http://dx.doi.org/10.1016/j.nima.2013.08.083>.
- [Gut13a] M. Guthoff et. al., “Radiation damage in the diamond based beam condition monitors of the CMS experiment at the Large Hadron Collider (LHC) at CERN”, NIM A 730 (2013) 168-173, DOI:10.1016/j.nima.2013.05.041.
- [Huh01] M. Huhtinen, “Simulation of non-ionising energy loss and defect formation in silicon”, ROSE/TN/2001-02.

Bibliography

- [Huh95] M. Huhtinen, P.A. Aarnio, “Neutron and photon fluxes and shielding alternatives for the CMS detector at LHC”, NIMA 363 (1995) 545-556.
- [Ign10] A. Ignatenko, “Test and first application of artificial sapphire sensors”, Nuclear Science Symposium Conference Record (NSS/MIC), 2010 IEEE , vol., no., pp.650,654, Oct. 30 2010-Nov. 6 2010, doi: 10.1109/NSSMIC.2010.5873839.
- [Jon04] R. Jones, “VME64x Digital Acquisition Board for the LHC Trajectory and Closed Orbit System”, LHC Engineering Specification, LHC-BP-ES-0002, EDMS 410295 v.1.1, 2004.
- [Kag10] H. Kagen, “Diamond for High Energy Radiation and Particle Detection”, RESMDD 2010 Florence, Italy, October 15, 2010.
- [Kha10] The CMS Collaboration, V. Khachatryan et al., “CMS Tracking Performance Results from early LHC Operation”, European Physical Journal C, 70:1165-1192, 2010.
- [Kai05] V. Kain et al., “Material damage tests with 450 GeV LHC-type beam”, Proceedings of the Particle Accelerator Conference, 2005, Knoxville, Tennessee, PAC 2005, 16-20 May 2005, doi: 10.1109/PAC.2005.1590851.
- [Koi92] J. Koike, D. M. Parkin, T. E. Mitchell, “Displacement threshold energy for type IIa diamond”, Appl. Phys. Lett. 60, 1450 (1992); doi:10.1063/1.107267.
- [Kur13] C. Kurfürst, “Cryogenic Beam Loss Monitoring for the LHC”, Ph.D. thesis, TU Wien.
- [Kuz06] E. Kuznetsova, “Design Studies and Sensor Tests for the Beam Calorimeter of the ILC Detector”, Ph.D. thesis, Humboldt-Universitaet zu Berlin, 2006.
- [LHC04] O. S. Brüning, P. Collier, P. Lebrun, S. Myers, R. Ostojic, J. Poole, P. Proudlock (editors), “LHC Design Report vol. 1: the LHC Main Ring”, CERN-2004-003-V-1, 2004.
- [May00] P. W. May, “Diamond thin films: a 21st-century material”, In: Phil. Trans. R. Soc. Lond. A 358 (2000), S. 473-495.
- [Mik07] M. Mikuz et al., “Study of Polycrystalline and Single Crystal Diamond Detectors Irradiated with Pions and Neutrons up to $3 \times 10^{15} \text{ cm}^{-2}$ ”, 10.1109/NSSMIC.2007.4436581.
- [Mil] O. Militaru, “High flux neutron irradiation facility at Louvain-la-Neuve Cyclotron”, Technical report, UCL, Louvain-la-Neuve.
- [Mil13] R. Mildren, J. Rabeau (editors), “Optical Engineering of Diamond”, Wiley-VCH, ISBN: 978-3-527-41102-3, April 2013.
- [Mok09] N. V. Mokhov, T. Weiler, “Machine-Induced Backgrounds: their Origin and Loads on ATLAS/CMS”, in: LHC Workshop on Experimental Conditions and Beam-Induced Detectors Backgrounds, CERN, Geneva, Switzerland, 3 - 4 Apr 2008, pp.37-43.
- [Mül11] S. Müller, “The Beam Condition Monitor 2 and the Radiation Environment of the CMS Detector at the LHC”, Ph.D. thesis, IEKP-KA/2011-01, Universität Karlsruhe, CERN-THESIS-2011-085, 2011.

- [Neb11] E. Nebot del Busto et al., “Analysis of fast Losses in the LHC with the BLM System”, IPAC’11, TUPC136, 09/2011.
- [New02] M. E. Newton et al., “Recombination-enhanced diffusion of self-interstitial atoms and vacancy-interstitial recombination in diamond”, *Diamond and Related Materials* 11 (2002) 618-622.
- [Nor75] M. J. Norget, M. T. Robinson and I. M. Torrens, *Nucl. Eng. Design* 33 (1975) 50.
- [Oh99] A. Oh, “CVD Diamant als Material für Teilchendetektoren”, Ph.D. thesis, University Hamburg, Germany, 1999.
- [Ohl10] M. Ohlerich, “Investigations of the Physics Potential and Detector Development for the ILC”, Ph.D. thesis, University Cottbus.
- [Pie13] T. Pierog et al., “EPOS LHC : test of collective hadronization with LHC data”, Jun 2013, arXiv:1306.0121.
- [Pom08] Pomorski M., “Electronic Properties of Single Crystal CVD Diamond and its Suitability for Particle Detection in Hadron Physics Experiments”, PhD Thesis, Universität Frankfurt am Main, 2008.
- [RD42] RD42 Collaboration, W. Adam et al., “Radiation hard diamond sensors for future tracking applications.”, *Nucl. Instrum. Meth. A* 565 (2006) 278.
- [RD42a] The RD42 collaboration, “Development of Diamond Tracking Detectors for High Luminosity Experiments at the LHC”, CERN/LHCC 2008-005, LHCC-RD-016.
- [Roe00] S. Roesler, R. Engel, J. Ranft, “The Monte Carlo Event Generator DPMJET-III”, International Conference on Advanced Monte Carlo for Radiation Physics, Particle Transport Simulation and Applications, Lisbon, Portugal, 23 - 26 Oct 2000, hep-ph/0012252, SLAC-PUB-8740.
- [Sil] Atlas device simulation framework, Silvaco Inc., http://www.silvaco.com/products/tcad/device_simulation/atlas/atlas.html.
- [Sus09] R. Sussmann (editor), “CVD Diamond for Electronic Devices and Sensors”, Wiley, ISBN978-0-470-06532-7, 2009.
- [TOT04] TOTEM collaboration, “Total cross-section, elastic scattering and diffraction dissociation at the Large Hadron Collider at CERN”, TOTEM technical design report, CERN-LHCC-2004-002, Addendum CERN-LHCC-2004-020.
- [TOT11] TOTEM Collaboration, “First measurement of the total proton-proton cross section at the LHC energy of $\sqrt{s} = 7$ TeV”, *EPL* 96 (2011) 21002.
- [TOT12] TOTEM Collaboration, “A luminosity-independent measurement of the proton-proton total cross-section at $\sqrt{s} = 8$ TeV”, TOTEM-2012-005, CERN-PH-EP-2012-354.
- [Wik05] http://commons.wikimedia.org/wiki/File:Diamond_Cubic-F_lattice_animation.gif, 3rd May 2005.
- [Zam06] C. Zamantzas, “The Real-Time Data Analysis and Decision System for Particle Flux Detection in the LHC Accelerator at CERN”, Ph.D. thesis, Brunel University, January 2006.

List of Figures

1.1. Copper targets irradiated with an LHC beam to show the damage potential of the beam.	8
1.2. BCM2 detector package showing the $1 \times 1 \text{ cm}^2$ diamond.	9
2.1. The CERN accelerator complex.	12
2.2. Layout of the LHC.	13
2.3. A beam loss monitor tube installed at a magnet	15
2.4. The CMS experiment and its subdetectors	15
3.1. Energy loss of an electron in diamond and silicon due to ionization and radiative losses	20
3.2. Energy loss of a 5.5 MeV α particle in diamond.	20
3.3. Diamond crystal structure	23
3.4. Schematic representation of the different types of diamond	23
3.5. Phase diagram of carbon	24
3.6. Microwave plasma chemical vapor deposition	25
3.7. Sketch of a pCVD grain structure	25
3.8. Schematic measurement setup for current detectors and MIP counters	26
3.9. Band structure of Schottky- and ohmic contacts.	28
3.10. Examples for different types of defects in diamond	29
3.11. Trapping, recombination and generation of charge at defect levels in a semiconductor	30
3.12. Cross-polarized pictures of sCVD diamonds	32
4.1. Picture of the BCM1 module and its installation location	34
4.2. Picture of the BCM2 module and a half-wheel with installed detectors.	34
4.3. Picture of the installed sCVD	35
4.4. Picture of one of the installed BLM tubes	36
4.5. Overview of the BCML system configuration	37
4.6. BCM1L detector grounding scheme.	38
4.7. BCM2 detector grounding scheme.	38
4.8. Schematic principle of the current to frequency converter (CFC)	39
4.9. Picture of the HV filter boxes installed in the BCM2 tunnel card crate	41
4.10. Electrical circuit of the BCM2 HV filter box with modification	41
4.11. Simulated bias HV at the diamond for old HV filter design	42
4.12. The USB readout together with the tunnel card electronics.	43
4.13. Running sum 1 data of one channel showing noise spikes	44
4.14. Histogram of tunnel card spikes	45
5.1. BCML signals during normal operation	52
5.2. Location of the TCT in the long straight section at IR5	53

List of Figures

5.3.	BCM data during collimator scan, 11th Mar 2011	54
5.4.	X-ray pictures of the RF fingers close to CMS before and after repair	56
5.5.	BCM2 and BCM1L signal during event of bad vacuum.	57
5.6.	Event of worst vacuum observed	58
5.7.	Background calculation shown for an event with bad vacuum.	59
5.8.	Shape of UFO measured with LHC BLM system	60
5.9.	UFO spike in BCM2 data	60
5.10.	UFO timing histogram for UFO detected on 12th Oct 2010 at 22:09:13	61
5.11.	BLM data during UFO event	63
5.12.	UFO timing histogram for UFO detected on 22 nd May 2011 at 13:52:21	64
5.13.	UFO timing histogram for UFO detected on 18 th April 2012 at 09:39:47	65
6.1.	Example of the combinatorial geometry in FLUKA	68
6.2.	NIEL cross sections for various particles in silicon and in diamond.	70
6.3.	DPA for various particles and energies in diamond.	72
6.4.	FLUKA geometry of the CMS detector	73
6.5.	3D representation of the CMS geometry	73
6.6.	TOTEM forward telescopes implemented in the CMS FLUKA model.	74
6.7.	FLUKA geometry of the CMS pixel detector.	76
6.8.	FLUKA geometry of CMS preshower detector.	77
6.9.	Particle Flux of all particles for nominal luminosity.	80
6.10.	The Radiation Simulation online Plotting tool (RSP)	81
6.11.	Particle energy spectra at the BCML locations at 3.5 TeV beam energy, grouped per detector location.	83
6.12.	Particle energy spectra at the BCML locations at 3.5 TeV beam energy, grouped by particle type.	84
6.13.	Simulated 1MeV-n-eq in the Tracker region, 7 TeV beam energy, 3000 fb ⁻¹	86
6.14.	Preshower: leakage current predicted and measured	87
6.15.	Tracker: measured leakage current related to simulated 1MeV-n-eq fluence	87
6.16.	Simulated activation after 10 hours of luminosity and 10 seconds after beam dump.	89
6.17.	Simulated signal in BCML due to activation.	90
6.18.	Present beam pipe geometry and upgrade study	91
6.19.	Electron flux due to MIB old and new beam pipe	92
6.20.	Particle flux as function of R due to MIB for the old and the new beam pipe	93
6.21.	Particle flux as function of Z at inner Pixel layer due to MIB for the old and the new beam pipe	94
7.1.	Calculated decrease of CCD in diamond for different initial CCD	97
7.2.	Decrease of CCD in 24 GeV proton irradiations	97
7.3.	The polarization effect.	98
7.4.	Drift velocity of electrons and holes as function of electric field.	102
7.5.	Simulation of space charge, electric field and TCT pulse.	103
7.6.	Hyperbolic fits to simulated decrease of active detector volume due to polarization.	105
7.7.	Offset to linear fit of BCM data and error estimation on nominal signal extrapolation	106
7.8.	Signal of the BCM2 detectors as function of integrated luminosity, 2011 data	107

7.9. Signal of the BCM1L detectors as function of integrated luminosity, 2011 data	108
7.10. Relative signal strength of BCML detectors as function of integrated luminosity, 2011 data	108
7.11. Relative signal strength of BCML detectors as function of integrated luminosity, full data set	110
7.12. Signal of sCVD detectors as function of integrated luminosity	112
7.13. Fits of hyperbolic damage curve to BCM2 data.	113
7.14. Fits of hyperbolic damage curve to BCM1L data.	114
7.15. k factors measured in partial fits	114
7.16. Fits of hyperbolic damage curve to sCVD data.	115
7.17. Neutron energy spectrum of the Louvain beam line	116
7.18. Measured RAW signal data in 23 MeV neutron irradiations	117
7.19. Hyperbolic fit to the damage curve measured in 23 MeV neutron irradiation. .	118
7.20. Radiation damage constant as function of fluence measured in 23 MeV neutron irradiations	119
7.21. Radiation damage constant as function of fluence summarizing all available measurement.	120
7.22. Signal behavior of BCML detectors at the start of a fill	120
7.23. Linearity of BCM2 detectors measured prior to installation	121
7.24. Instantaneous luminosity of fill 3236 used for rate dependance measurement .	121
7.25. Detector current of BCM2 during fill 3236 used for rate dependance measurement	122
7.26. Relative efficiency during one fill for two BCM2 exemplary inner detectors . .	122
7.27. Relative efficiency during one fill for BCM2 -Z and +Z, averaged per detector group.	123
7.28. Scheme of the CCD measurement setup.[Oh10]	125
7.29. Charge Collection Distance measurements for un-irradiated sCVD diamonds .	126
7.30. CCD measurements of the pCVD diamond from BCM2 outer +Z.	127
7.31. CCD measurements of the pCVD diamond from BCM2 outer -Z.	127
7.32. CCD measurements of the sCVD_2011 from BCM2 inner +Z.	127
7.33. Schematic setup of the TCT measurement.	129
7.34. Placement of the sources and flow of particles during TCT measurements . .	129
7.35. TCT measurement of the un-irradiated sCVD_test1 at 400V	130
7.36. Measured charge carrier mobility in comparison with results from [Pom08] . .	131
7.37. TCT measurements of sCVD_2011 at 200V, detector unpolarized	132
7.38. Measured and simulated TCT pulses of sCVD_2011 at 200V, slightly polarized, side 1	133
7.39. Measured and simulated TCT pulses of sCVD_2011 at 200V, highly polarized, side 1	133
7.40. Measured and simulated TCT pulses of sCVD_2011 at 200V, slightly polarized, side 2	135
7.41. Measured and simulated TCT pulses of sCVD_2011 at 200V, highly polarized, side 2	135
7.42. Measured and simulated TCT pulses of sCVD_2011 at 600V, unpolarized . .	136
7.43. Measured and simulated TCT pulses of sCVD_2011 at 600V, slightly polarized, side 1	136
7.44. Measured and simulated TCT pulses of sCVD_2011 at 600V, highly polarized, side 1	137

List of Figures

7.45. Measured and simulated TCT pulses of sCVD_2011 after polarizing at 600V and HV switched off.	138
7.46. TCT measurements of sCVD_2011 before and after plasma etching of the surface	140
7.47. TCT measurements of the diamond sCVD_2012 at 200V, unpolarized	141
7.48. Measured and simulated TCT pulses of sCVD_2012 at 200V, slightly polarized	143
7.49. Measured and simulated TCT pulses of sCVD_2012 at 200V, highly polarized	143
7.50. Measured and simulated TCT pulse of sCVD_2012 with improved measurement	144
7.51. Photo-absorption spectra of irradiated diamond samples	144
B.1. Alternative fits to decrease of active detector volume due to polarization. . .	170
B.2. Different fits to the data of the sCVD diamonds	171
B.3. Signal prediction of abort channels to 300 fb^{-1}	173

List of Tables

2.1.	A selection of the LHC beam parameters, design parameters and values of Run 1	14
3.1.	Material properties of diamond and silicon	24
4.1.	All running sums calculated in the DAB cards [Zam06].	43
4.2.	Maximum height of spikes for the tunnel cards installed in BCML.	46
5.1.	Properties of measured signals during UFO event on 12 th Oct 2010 at 22:09:13.	63
5.2.	Properties of measured signals during UFO event on 22 nd May 2011 at 13:52:21	65
5.3.	Properties of measured signals during UFO event on 18 th April 2012 at 09:39:47	66
6.1.	Expected signal of the BCML detectors at nominal luminosity	85
6.2.	Equivalent fluence of 24 GeV protons at the locations of the BCML detectors	86
7.1.	Parameters for the parametrization of the drift velocity	101
7.2.	Results of the hyperbolic fit to the simulated signal decrease	104
7.3.	Results of all hyperbolic fits on signal decrease of pCVD and sCVD detectors in BCML	115
7.4.	24 GeV proton equivalent fluence received by the analyzed diamonds and pre- diction of CCD decrease	126
A.1.	Running Sum 12 abort thresholds	168
B.1.	Results of different fits to the simulated signal decrease	171
B.2.	Results for the fit parameters of all three fit functions for sCVD 2011.	172
B.3.	Results for the fit parameters of all three fit functions for sCVD 2012.	172

Appendix A.

Beam abort thresholds

The beam abort thresholds of running sum 12 (83.9s) integration time for all channels included in the abort are given in table A.1. The abort thresholds were updated twice. The BCM1L channels were activated in the abort with the first threshold update.

Appendix A. Beam abort thresholds

Detector	DAB card	channel	Initial thresholds		Thresholds since 29.08.2011		Thresholds since 15.08.2012	
			[ADC]	[nA]	[ADC]	[nA]	[ADC]	[nA]
BCM1L -Z far	2	1	—	—	87873922	204.6	73553177	171.3
BCM1L -Z up	2	2	—	—	135960561	316.6	98918337	230.3
BCM1L -Z near	2	3	—	—	129644221	301.9	92825886	216.1
BCM1L -Z down	2	4	—	—	104286111	242.8	77693456	180.9
BCM1L +Z far	2	5	—	—	98240648	228.7	77951616	181.5
BCM1L +Z up	2	6	—	—	89607286	208.6	69826315	162.6
BCM1L +Z near	2	7	—	—	132339414	308.1	92275981	214.8
BCM1L +Z down	2	8	—	—	196930210	458.5	127051318	295.8
BCM2 -Z inner top	3	1	126000000	290	390527041	909.3	238698554	555.8
BCM2 -Z inner far	3	2	126000000	290	199123384	463.6	135160926	314.7
BCM2 -Z inner near	3	9	126000000	290	263300833	613.1	126145384	293.7
BCM2 -Z inner bottom	3	10	126000000	290	240163762	559.2	123210182	286.9
BCM2 +Z inner near	4	1	126000000	290	716178979	1667.5	413980118	963.9
BCM2 +Z inner top	4	2	126000000	290	906825226	2111.4	520634850	1212.2
BCM2 +Z inner far	4	9	126000000	290	709923318	1652.9	409761176	954.0
BCM2 +Z inner bottom	4	10	126000000	290	899393726	2094.1	434497063	1011.6

Table A.1.: Running Sum 12 abort thresholds

Appendix B.

Parametric fits to signal decrease

B.1. Alternative fit functions

As seen in chapter 7, the hyperbolic fit is not a good description of the decrease in signal efficiency due to polarization. A parametric function is sought, which provides a better fit for the purpose of extrapolating to higher fluences. In addition to the normal hyperbolic curve, two modified fit functions are justified here and tested against the data:

1. The hyperbolic fit corresponds to the decrease of the charge collection distance (CCD) as derived in chapter 7.1, equation 7.7. CCD and Φ are not measured directly, hence equation 7.7 cannot be fitted directly. One can assume that the measured signal S is proportional to the CCD and the integrated luminosity L is proportional to the fluence. In case of the simulation, the signal S is replaced with the size of the active volume, and L is given by the simulation steps. The fit equation is given by:

$$S(L) = \frac{S_0}{1 + S_0 \cdot k' \cdot L} \quad (\text{B.1})$$

k' is the radiation damage constant, but in different units, and S_0 the signal of the un-irradiated detector. k' is not comparable with k of equation 7.7, since the proportionality between Φ and L depends on the detector location.

2. A hyperbolic fit with an offset c : It was suggested by M. Pomorski [Pom08], that the damage curve converges against an offset. This was explained by the fact that polarization squeezes the electric field out of the bulk, leaving a small active volume, which does not change in size significantly.

$$S(L) = \frac{S_0}{1 + S_0 \cdot k' \cdot L} + c \quad (\text{B.2})$$

3. A hyperbolic fit with an exponent e : The fit of the hyperbolic curve to parts of the data showed a decrease in k-factor with higher fluence. This was also seen in test beam irradiations by C. Kurfürst, where the exponent was suggested [Kur13]. The exponent was just added to L of equation B.1. For the fits here, a slightly different function is used. A hyperbolic function with exponent is used, where the function is infinite at $L = 0$:

$$S(L) = \frac{1}{k' \cdot L^e} \quad (\text{B.3})$$

A shift to the left, L_0 , is introduced to facilitate the starting conditions:

$$S(L) = \frac{1}{k' \cdot (L + L_0)^e} \quad (\text{B.4})$$

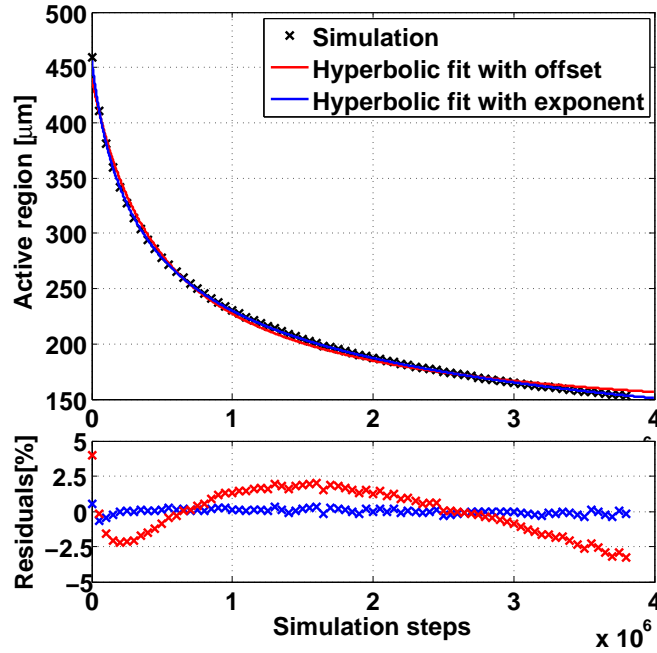


Figure B.1.: Alternative fits to decrease of active detector volume due to polarization. The decrease is best described by a hyperbolic function with exponent (equation B.7).

S_0 is the signal of the un-irradiated detector, which can be used to calculate L_0 :

$$S_0 = \frac{1}{k' \cdot L_0^e} \Rightarrow L_0 = \frac{1}{\sqrt[e]{k' \cdot S_0}} \quad (\text{B.5})$$

From equation B.5 in equation B.4 follows:

$$S(L) = \frac{1}{(\sqrt[e]{k' \cdot L} + \frac{1}{\sqrt[e]{S_0}})^e} \quad (\text{B.6})$$

The final fit function has an exponent over the whole denominator:

$$S(L) = \frac{S_0}{(\sqrt[e]{k' \cdot S_0} \cdot L + 1)^e} \quad (\text{B.7})$$

As the exponent e is a free parameter, but included in the unit of k' . Hence it is not possible to compare k' parameters of fits on different data sets. Of interest is the value of the e , which defines the shape of the curve.

B.2. Fit to simulated decrease of active volume

The alternative fit functions are applied to the simulated decrease of active detector volume as presented in chapter 7.2.3. In figure B.1 the results of the fit of equations B.2 and B.7 to the simulated data is shown. Although the residuals of the fit using the hyperbolic with offset is significantly smaller than the standard hyperbolic (seen in figure 7.6), a pattern can

B.3. Fit to decrease of sCVD detector signal of BCML

Fit function	hyperbolic + offset	hyperbolic with exponent
CCD ₀ [μm]	320	457
k' [steps ^{-e} μm^{-1}]	6.3×10^{-9}	4.5×10^{-5}
offset [μm]	121	0
exponent	1	0.33

Table B.1.: Results for the fit parameters obtained in the fits to the simulated decrease of active detector volume.

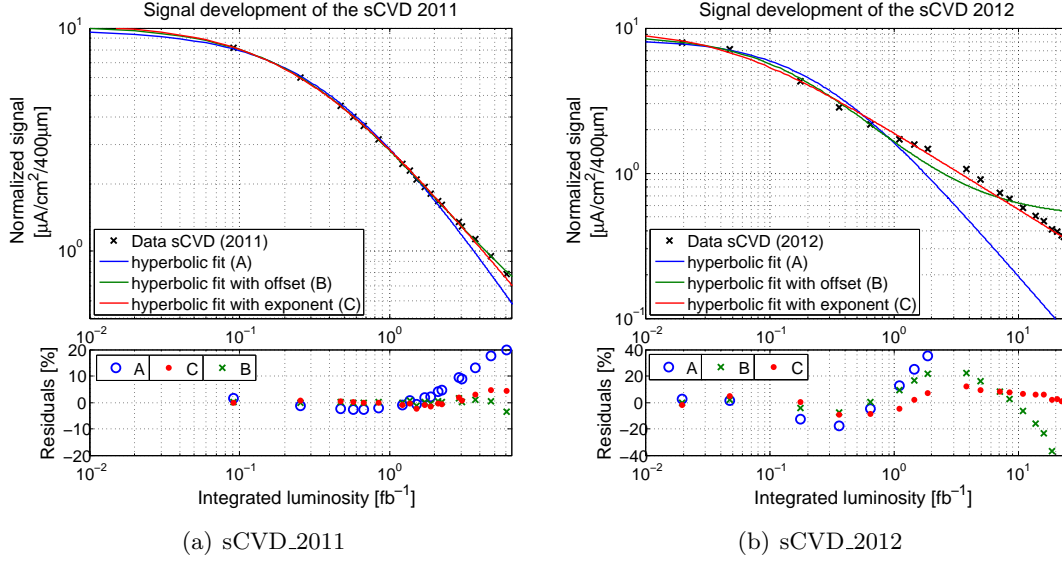


Figure B.2.: Different fits to the data of the sCVD diamonds. A hyperbolic function is not a good fit to the data. A hyperbolic fit with exponent provides the best parameterization.

be seen in the residuals, showing that this is not an ideal function. The hyperbolic function with exponent show the best fit to the simulated decrease in signal strength. The result parameters for the fits are presented in table B.1.

B.3. Fit to decrease of sCVD detector signal of BCML

As seen in chapter 7.3.3, the hyperbolic fit is not a good description of the damage curve measured with the BCML detectors. For the extrapolation of the signal efficiency towards higher fluences a good fit function is need. It was shown in simulations that a hyperbolic function with exponent could be a better fit function (section B.2). A fit using a hyperbolic function with offset (equation B.2) and a fit using a hyperbolic function with exponent (equation B.7) is tested against the signal data obtained with the sCVD diamonds installed in BCM2.

Figure B.2 shows the different fits for both diamonds. The normal hyperbolic fit, equation B.1, shown is blue, shows generally the worst fit. The fit with offset (equation B.2, shown in green), and the fit with exponent (equation B.7, shown in red) work comparably well, when fitted to the sCVD_2011 data (figure B.2(a)). The sCVD_2012 received an about 4 times higher fluences than the sCVD_2011 and more data is available in the flat part of

Appendix B. Parametric fits to signal decrease

Fit function	hyperbolic	hyperbolic + offset	hyperbolic with exponent
S_0 [nA]	9.83 ± 0.34	9.71 ± 0.02	10.5 ± 0.08
k' [fb ^e /nA]	0.25 ± 0.01	0.29 ± 0.00	0.29 ± 0.00
offset [nA]	0	0.28 ± 0.01	0
exponent	1	1	0.83 ± 0.01

Table B.2.: Results for the fit parameters of all three fit functions for sCVD 2011.

Fit function	hyperbolic	hyperbolic + offset	hyperbolic with exponent
S_0 [nA]	8.4 ± 0.87	8.4 ± 0.46	9.8 ± 0.7
k' [fb ^e /nA]	0.50 ± 0.12	0.75 ± 0.12	0.52 ± 0.03
offset [nA]	0	0.49 ± 0.12	0
exponent	1	1	0.53 ± 0.05

Table B.3.: Results for the fit parameters of all three fit functions for sCVD 2012.

the curve. Here, the fit using the offset diverges from the slope of the data, but the fit using an exponent gives a qualitatively good result. The parameters for each fit is given in table B.2 and B.3. The exponent obtained in the measurement (0.33) is higher than in the result from simulation (0.53 and 0.83). It is yet unclear, what influences the exponent. The exact level of polarization is a stabilized condition of trapping and de-trapping it strongly depends in the number of traps and on the particle environment. A more detailed model is needed to predict the exact shape of the damage curve.

B.3.1. Prediction of signal strength at 300 fb⁻¹

Important for the operation is whether the signal strength of the diamond detectors is sufficient to survive until long shutdown 3. It is expected that the LHC will deliver an integrated luminosity of 300 fb⁻¹ until then. A good fitting function is needed for a reliable prediction. Although it is only an empirical function, the hyperbolic curve with exponent is the fit function which gives the lowest residuals and is the best available description to make an extrapolation towards higher integrated luminosities.

Equation B.7 is fitted to the data of BCM1L and BCM2 inner on +Z, shown in figure B.3(a). The fit is extrapolated to an integrated luminosity of 300 fb⁻¹, shown in figure B.3(b). For BCM1L it predicts a relative signal strength of about 29 % and for BCM2 inner about 6.7 % at 300 fb⁻¹.

If the abort threshold cannot be lowered any more to compensate for the loss in signal efficiency, it is considered the limit for the detector not properly working any more. The limit for lowering the abort thresholds is given by the maximum height of the noise spikes, which are different for each channel (see chapter 4.3). To include enough safety margin, a minimal abort threshold of 700 ADC counts is proposed, which corresponds to a detector current of 3.4 μA. The abort threshold at full signal efficiency is 30.2 μA, hence the minimum signal strength for a detector is 11.3 %. This limit is shown in figure B.3(b). BCM1L should survive 300 fb⁻¹ without any problems. The BCM2 inner detector would hit this limit around 127 fb⁻¹. The abort threshold can still be reduced, if the tunnel cards are checked for the exact number of the maximum height of the noise spikes. The thresholds have to be chosen carefully enough, so that a false beam abort due to spikes will not happen. Additionally, the HV can be increased. The calculations shown here are based on data with 200 V. The signal increase

B.3. Fit to decrease of sCVD detector signal of BCML

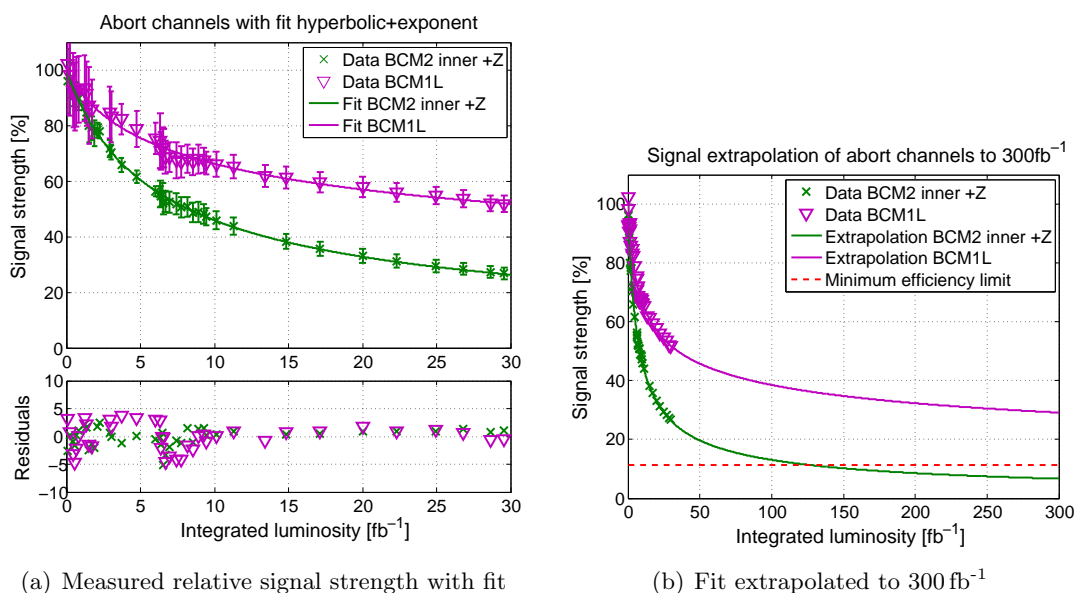


Figure B.3.: Signal prediction of abort channels to 300 fb⁻¹. Figure (a) shows the quality of the fit using the hyperbolic with exponent (equation B.7). In figure (b) the fit is extrapolated to 300 fb⁻¹. The minimal signal strength required for a proper abort functionality is shown. BCM1L will stay above the minimal level until LS3. The BCM2 inner detectors would hit the minimum level at about 127 fb⁻¹, if the signal loss is not compensated by increasing the HV.

is almost linear with HV, if the reduction of signal is due to polarization. The HV can be increased up to 500V, but the chance of erratic dark currents increases. Raising the HV should only be done, if the diamond is removed from the abort system and monitored for several days of operation for erratic dark currents, before the abort functionality is reactivated.

On the other hand, these predictions are based on data from the 3.5 and 4 TeV era. Post LS1, with 6.5 or 7 TeV beam energy, the damage per unit of luminosity will be slightly higher. The exact moment for the failure of parts of the system is difficult to predict, but the system has enough reserves to survive until up to long shutdown 3.

B.3.2. Operation up to 3000 fb⁻¹ (HL-LHC)

BCML does have enough reserve to provide a proper abort functionality until LS3. For the HL-LHC phase fresh detectors should be installed, where the mode of operation has to be reevaluated. The target luminosity of 3000 fb⁻¹ puts high requirements on the radiation hardness of the BCML detectors. A possibility would be to increase the detector signal, by using several diamonds in parallel for one readout channel. Also the tunnel card electronics is currently being redeveloped. If the spike problem can be solved, much lower abort thresholds would be possible.